FABRICATION OF LEAD-FREE PIEZOELECTRIC COMPOSITE VIA COLD SINTERING PROCESS

JITRAWAN NOISAK

A THESIS SUBMITTED IN PARTIAL FULFILLMENT OF THE REQUIREMENT FOR THE DEGREE OF MASTER OF SCIENCE IN APPLIED CHEMISTRY

DEPARTMENT OF CHEMISTRY SCHOOL OF SCIENCE
KING MONGKUT'S INSTITUTE OF TECHNOLOGY LADKRABANG

2024

KMITL-2024-SC-M-012-007

Thesis Title	Fabrication of Lead-Free Piezoelectric Composites via Cold Sintering Process
Student Name	Miss Jitrawan Noisak
Student ID	64605022
Degree	Master of Science (Applied Chemistry)
Department	Chemistry
Year	2024
Thesis Advisor	Prof. Dr. Naratip Vittayakorn

Abstract

The cold sintering process (CSP) emerges as a promising technique for the low-temperature fabrication of ceramics and composites, enabling high-density formation under mild conditions. This study explores the application of CSP in two parts: firstly, the fabrication of γ-Glycine (γ-GC) ceramic, and secondly, the development of γ-GC composite with ferroelectric materials ($BaTiO_3$; BT). For the γ-GC ceramic, we investigated the influence of sintering temperature and duration on microstructure and electrical properties. Higher sintering temperatures and longer holding times promoted grain growth. Notably, the inclusion of transient solvent (DI water) aided in achieving a compacted microstructure conforming to CSP mechanisms. Incorporating bacterial cellulose (BC) as a filler enhanced the hardness of the γ-GC ceramic by 10%. A relative density of 97% was achieved at 120°C/24h, preserving the γ polymorph of glycine without undesired transformations. Ferroelectric analyses revealed a remanent polarization of 0.004 μC/cm^2 and a coercive field of 1.201 kV/cm.

Subsequently, leveraging γ-GC as a transient liquid phase, we fabricated high-density composites with BT powder via CSP. A γ-GC/BT composite with a density of 96.7% was attained at 120˚C for 6 h under 10,000 kPa uniaxial pressure. SEM-EDS

mapping indicated complete precipitation-dissolution of γ-GC within the CSP mechanism, filling the interstices between BT particles. XRD and FTIR analyses confirmed the absence of phase transformation in γ-GC. Dielectric measurements revealed a high dielectric constant (ε_r) of 3600 and low dielectric loss (tan δ) of 1.20 at 200°C, 100 kHz, for the composite. Hysteresis loop analysis displayed a remanent polarization (P_r) of 0.55 μC/cm^2 and a coercive field (E_c) of 7.25 kV/cm. This research underscores CSP's potential for low-temperature fabrication of γ-GC ceramics and its capability to utilize γ-GC as a transient liquid phase for crafting high-performance composites at reduced temperatures.

Keywords: Bacterial cellulose, Barium titanate, Cold Sintering Process, γ-glycine

Acknowledgements

This thesis was accomplished due to the support and kindness of everyone. Including various agencies involved for which the researcher would like to thank.

Firstly, I would like to thank Prof.Dr. Naratip Vittayakorn, my research supervisor, for the topic assigned to me as well as waiting for close supervision, provide good advice to improve problems, helping to check this thesis to be completer and more accurate in the thesis and honor is thesis professor consultant, so thank you very much here.

I would like to thank Dr. Thitirat Charoonsuk, Advance Material Research Unit (AMR) research team for helping to educate. Providing advice, and suggestions on ways to solve problems.

I would like to thank Dr. Nattapong Pinpru, AMR researcher team and researcher from national nanotechnology center (NANOTEC) for support in the Secondary Electron Microscope (SEM) analysis.

I would like to thank Dr. Phakkhananan Pakawanit, the AMR researcher team and researcher from Thai Synchrotron National Lab for support in the X-ray Tomographic Microscopy (XTM) analysis.

I would like to thank our supervisory committee members, Dr. Sitthisuntorn Supothina and Assoc.Prof.Dr. Panpailin Seeharaj, for their questions and recommendations during the test.

I would like to thank the AMR research team, professors of the department of chemistry, school of science including staff of chemistry lab for teaching and facilitate the use of chemical equipment chemicals and analytical instruments.

Finally, I would like to express my gratitude to my parents and family for allowing me to study and be the encouragement and motivation to complete the research successfully.

Jitrawan Noisak

TABLE OF CONTENTS

TABLE OF CONTENTS (II)

TABLE OF CONTENTS (III)

TABLE OF CONTENTS (IV)

LIST OF TABLES

LIST OF FIGURES (I)

LIST OF FIGURES (II)

LIST OF FIGURES (III)

LIST OF FIGURES (IV)

Figure **Page**

LIST OF FIGURES (IV)

LIST OF FIGURES (V)

LIST OF FIGURES (VI)

ABBREVIATIONS AND SYMBOLS

γ-GC	Gamma Glycine
β-GC	Beta Glycine
α-GC	Alpha Glycine
BC	Bacterial Cellulose
BT	Barium Titanate
°C	Degree Celsius
h	Hours
cm	Centimeter
min	Minute
CSP	Cold Sintering Process
TSP	Traditional Sintering Process
RT	Room Temperature
ε_r	Dielectric Constant
Tanδ	Dielectric Loss
P_r	Remnant Polarization
P_s	Saturation Polarization
E_c	Coercive Field
ρ_r	Relative density
ρ_t	Theoretical density

CHAPTER 1

Introduction

1.1 Research Motivation

Piezoelectric materials have a non-centrosymmetric crystal structure that can generate displacement between anions and cations, thus producing surface charge when exposed to dimension change caused by mechanical stress. This change, known as the piezoelectric effect, was discovered in 1880 by Jacques and Pierre Curie [1]. When piezoelectric materials, such as quartz, tourmaline, and Rochelle salt, are mechanically stressed, they polarize along the stress direction. Likewise, under the action of an external electric field, piezoelectric materials can produce a geometric deformation proportional to the external electric field. The discovery of piezoelectricity was significantly applied to electronic devices such as piezoelectric ultrasonic transducers during World War I [2].

In general, most piezoelectric materials used in electronic devices are synthesis piezoelectric materials such as lead titanate ($PbTiO_3$) [3], lead lanthanum zirconate titanate (PLZT) [4], and lead zirconate titanate (PZT) [5]. These exhibited very high dielectric and piezoelectric properties. However, these materials contain lead, and toxic lead is further enhanced due to its volatilization at higher temperatures, particularly during calcination or sintering, thus affecting the environment and the human body [6]. Consequently, the European Union implemented the Restriction of Hazardous Substances Legislation (RoHs), and there has been a push to develop lead-free piezoelectric materials [7].

Among the lead-free piezoelectric ceramics, three main groups of lead-free perovskite ferroelectric oxides have henceforth been considered environment-friendly alternatives. Mainly include potassium sodium niobate [$(K, Na)NbO_3$; KNN] based-, barium titanate ($BaTiO_3$, BT) based-, bismuth titanate [$Bi_{1/2}Na_{1/2})TiO_3$; BNT] based-ceramic systems material [8]. Barium Titanate (BT) is a widely used material in

transducers due to its high dielectric constant, good thermal stability, low dielectric loss, and stable electric properties. Perovskite-type BT-based Multilayer Ceramic Capacitors (MLCC) are particularly useful. However, conventional MLCCs require the use of noble metals such as platinum (Pt) or palladium (Pd) as internal electrodes, and they must be fired in the air at temperatures of 1300 ˚C or higher. It is important to control the sintering temperature precisely during MLCC fabrication to prevent metal diffusion into the dielectric layer, which may cause stress and cracks [9]. However, to sinter BT-based ceramics, very high temperatures are required, leading to high energy costs which can make the process economically unfeasible [10-13].

A new approach to sintering high-density ceramic materials has been discovered. This innovative technique is called the cold sintering process (CSP) and was developed by Randall *et al* [14] at the Pennsylvania State University. The CSP method involves uniformly moistening ceramic powder with a specific transient solution and then sintering it at low temperatures (below 300 ℃) under pressure to achieve the dissolution-precipitation phenomenon. Researchers have successfully used CSP for water-soluble materials such as sodium chloride (NaCl). The NaCl particles diffuse throughout the water film, filling voids and precipitating through the dissolution-precipitation process inherent to CSP. This process can achieve high relative densities exceeding 90% after 24 hours at room temperature and 75% relative humidity[15]. CSP has also been effectively employed with various ferroelectric or piezoelectric materials, including KH_2PO_4, $NaNO_2$, CeO_2, and BT [16, 17]. CSP can deliver high relative densities (>98%) of potassium dihydrogen phosphate (KH_2PO_4) below 300 ˚C, with a processing duration of around 1 h [15]. This finding highlights the potential of CSP as a promising alternative for sintering at low temperatures. However, CSP cannot be available in one step for all types of materials. Especially, materials with limited solubility such as BT due to perovskite structure [18]. Heat treatment is required to assist the CSP in removing the amorphous phase that forms into dense crystals.

In traditional sintering methods, it is usually difficult to produce uniform microstructure dense ceramic/ceramic or ceramic/polymer composites. However, Cold

Sintering Process (CSP) can perform this task effectively. One of the important pre-conditions for cold sintering is that at least one composite material must have the ability to dissolve in a transient liquid phase. This is necessary for the dissolution-precipitation process to occur according to the CSP mechanism.

NaCl is often used as a soluble additive to improve the density of Al_2SiO_5 ceramic. In a study by I.j. Induja and M.T. Sebastian [19], Al_2SiO_5/NaCl was subjected to CSP at 120 °C under 200 MPa for 50 minutes, resulting in a density of 91.2%. This is higher than the density of monolithic Al_2SiO_5ceramic produced by traditional sintering at 1525 °C, which is only 64.5%. It should be noted that NaCl acts as a new transient liquid phase and does not form a new phase at grain boundaries. However, the addition of NaCl does affect the dielectric property of Al_2SiO_5.

A new transient liquid phase must not only be soluble in water but also should not compromise the properties of the pre-existing material. Glycine (GC) has gained significant attention as it is the simplest amino acid found in proteins. It can be crystallized in three polymorphic phases (α, β, and γ) under ambient conditions [20, 21]. γ-GC and β-GC are known to have piezoelectric properties due to a non-centrosymmetric polar structure [22]. Among all the phases, γ-GC is the most stable and polarization is about five times larger than that for β-GC [23]. However, it could dissolve quickly in aqueous solution [24]. But for CSP, the glycine can be used as a new liquid phase to fabricate composites between γ-GC and BT through CSP.

This research employed the CSP method instead of the conventional sintering process to produce high-density ceramic composites of γ-GC and BT at lower temperatures. γ-GC, which acts as a new liquid phase, was used to accomplish the dissolution-precipitation phenomenon based on the mechanics of CSP. The objectives of the study can be categorized into two types: 1) To create high-density γ-GC ceramics using the CSP method, and 2) To produce γ-GC/BT composites with varying ratios of γ-GC using CSP and investigate the relationship between γ-GC content, morphology, grain growth characteristics, and processing ability, which includes the electrical properties of all samples.

1.2 Objective of the study

1.2.1. To investigate the transformation of α-GC to γ-GC through the recrystallization process.

1.2.2. To investigate the sintering parameter required to achieve a densely packed γ-GC ceramic via CSP.

1.2.3. To understand the mechanism involved in achieving a high-density ceramic in CSP.

1.2.4. To investigate the cubic-tetragonal phase in BT through the thermal treatment process.

1.2.5. To determine the optimal sintering parameter necessary to attain a densely packed composite of γ-GC/BT at varying γ-GC ratios via CSP.

1.2.6. To investigate the crystal structure, morphology, and uniqueness of γ-GC ceramic and composite between γ-GC and BT at different γ-GC ratios.

1.2.7. To investigate the dielectric and ferroelectric properties of γ-GC ceramic and composite between γ-GC and BT with varying γ-GC ratios.

1.3 Scopes of the study

1.3.1. Study the preparation process of γ-GC from α-GC solution by using sodium chloride (NaCl) powder as an activator through a recrystallization process.

1.3.2. Fabricate high-density γ-GC ceramics with varying sintering temperatures and holding times via CSP.

1.3.3. Investigate the effect of treatment temperature on the transformation of BT ceramics from cubic to tetragonal phase.

1.3.4. Fabricate high-density composites between γ-GC and BT by adding γ-GC at different weight ratios (15%, 30%, 50%, and 90%) through the CSP process.

1.3.5. Study the correlation between the changing amount of γ-GC and relative density at various weight ratios (15%, 30%, 50%, and 90%) using CSP.

1.3.6. The properties of γ-GC ceramic and its composites with BT were thoroughly characterized using Fourier Transform Infrared Spectroscopy (FTIR), X-ray diffraction (XRD), Scanning Electron Microscopy (SEM), and X-ray Tomographic Microscopy (XTM).

1.3.7. Investigate the temperature and frequency-dependent dielectric properties (dielectric constant and dielectric loss) of γ-GC ceramic and composites formed between γ-GC and BT at weight ratios of 15%, 30%, 50%, and 90% γ-GC.

1.3.8. Investigate the ferroelectric properties of γ-GC ceramic and γ-GC/BT composites with varying weight ratios (15%, 30%, 50%, and 90%) by measuring their polarization-electric field (P-E) hysteresis loops.

1.4 Benefits of the study

1.4.1. Understand the phase transition of α-GC to γ-GC by using NaCl powder as an activator through a recrystallization process.

1.4.2. Understand the important factors (sintering temperatures and holding times) of the CSP to achieve a densely packed γ-GC ceramic.

1.4.3. Understand the mechanism for CSP related to the densification process, sliding and rearrangement of particles, dissolution-precipitation process, and crystal growth.

1.4.4. Understand the relationship between varying sintering temperature and holding time on the microstructure and relative density of γ-GC ceramic via CSP.

1.4.5. Understand the relationship between the microstructure of γ-GC ceramic at varying sintering times and temperature to dielectric property and ferroelectric property.

1.4.6. Knowing the optimum sintering conditions to fabricate a high-density γ-GC ceramic via CSP.

1.4.7. Understand the relationship between the microstructure of γ-GC ceramic under varying sintering conditions on their dielectric and ferroelectric properties.

1.4.8. Understand the cubic tetragonal phase transition of BT ceramic under thermal treatment process.

1.4.9. Understand the microstructure of composites between γ-GC and BT composites through CSP that changes upon the varying amounts of γ-GC.

1.4.10. Understand the relationship between the changing amount of γ-GC on the relative density of composites between γ-GC and BT composites via CSP.

1.4.11. Knowing the appropriate amount of γ-GC for fabricating high-density composites between γ-GC and BT.

1.4.12. Understand the relationship between the changing amount of γ-GC on dielectric property and ferroelectric property of composites between γ-GC and BT.

CHAPTER 2

THEORY AND LITERATURE REVIEWS

Piezoelectric materials were applied in various applications, such as sensors for gas igniters, accelerometers, microphones, and actuator devices, including liquid inkjet printers. Generally, the piezoelectric materials applied in various applications are synthetic materials containing many leads. However, it is toxic-enhanced due to its volatilization at higher temperatures particularly during calcination or sintering, thus affecting the environment and the human body. Thus, this chapter will mention lead-free piezoelectric material, sintering at low temperatures, and preparing composite base lead-free piezoelectric at low temperatures.

2.1 History of Piezoelectricity

Piezoelectricity is an effect related to the change in electric potential created when a piezoelectric substance is deformed. This was first observed by Carl Linnaeus and Franz Aepinus in the mid-1800s, but it was not truly understood until it was demonstrated by two French physicists, Jacques and Pierre Curie, in 1880. They discovered an unusual characteristic of certain crystalline minerals such as tourmaline, quartz, topaz, cane sugar, and Rochelle salt. It was found that tension and compression generated voltages of opposite polarity proportional to the applied load. This phenomenon is called the piezoelectric effect [25]. The at-first-discovered direct piezoelectric effect is shown schematically in Figure 2.1a, b. This direct effect is used in sensor applications such as gas igniters, and accelerometers. The word piezoelectricity comes from Greek and means electricity resulting from pressure. Lippman predicted the existence of the converse effect based on fundamental thermodynamic principles [26], saying that a crystal will deform when an electric voltage is applied to certain opposite faces of the crystal. Before the end of 1881, the brothers Curies confirmed experimentally the existence of the converse effect. They show that if one of the voltages generating crystal was exposed to an electric field, it lengthened or shortened according to the polarity of the field and in proportion to its

strength, as shown in Figure 2.2a, b. This converse effect is applied in actuator devices including liquid inkjet printers, camera shutters, etc.

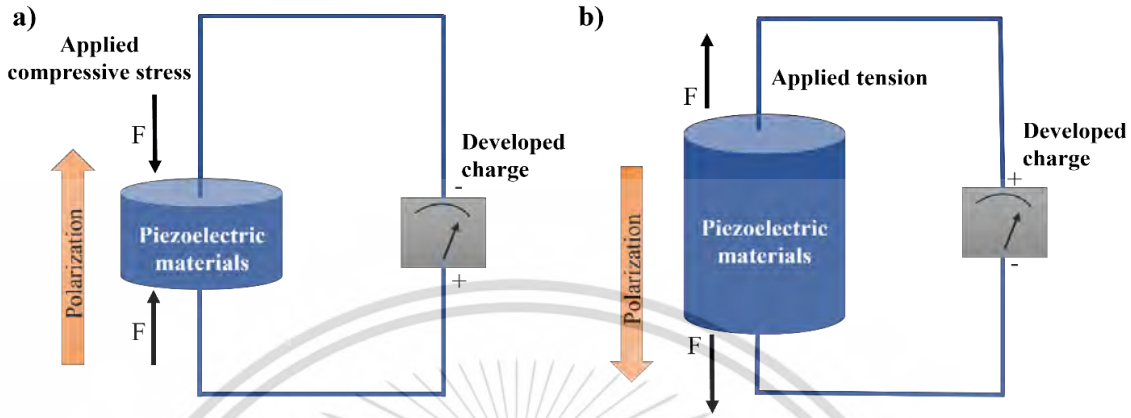

Figure 2.1 shows the direct piezoelectric effect at a) applied compressive stress, and b) applied tension modified from [27].

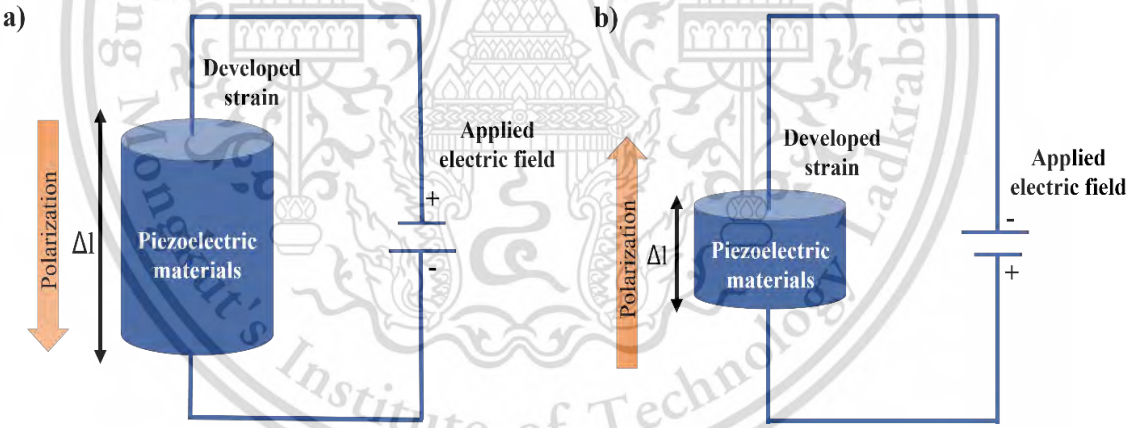

Figure 2.2 shows the converse piezoelectric effect at a) and b) are applied electric field modified from [27].

Piezoelectricity is the coupling between electrical and mechanical displacements in a material. The direct and converse piezoelectric effect can be described by basic Equations 2.1 and 2.2 respectively [28].

Direct piezoelectric effect:

$$D = d_1 T + \varepsilon^T E \tag{2.1}$$

Where D is dielectric displacement (C/m^2), T is the mechanical stress (N/m^2), ε^T is the permittivity at constant stress, E is the electric field (V/m) and d_1 is piezoelectric charge coefficients direct piezoelectric effect.

Converse piezoelectric effect:

$$S = s^E T + d_2 E \tag{2.2}$$

Where S is mechanical strain, S^E is mechanical compliance, T is mechanical stress (N/m^2), E is the electric field (V/m) and d_2 is piezoelectric charge coefficients for the converse piezoelectric effect.

The discovery of piezoelectricity generated significant interest in the European scientific community, and it developed as a new field of research in the last quarter of the 19th century. This research, published in 1910, described the 20 natural crystal classes in which piezoelectric effects occur.

2.1.1 Crystal classes

The crystals can be divided into 32 symmetry point groups. Out of these 32-point groups, 21 groups are non-centrosymmetric with one or more crystallographic unique directional axes and 11 groups are centrosymmetric with non-piezoelectric, meaning the center of positive and negative charge coincides with each other. Out of these 21-point groups, 20 belong to the class of piezoelectric. Out of these 20-point groups, 10 of these represent the polar crystal classes, which show a spontaneous polarization without mechanical stress due to a non-vanishing electric dipole moment associated with their unit cell, and which exhibit pyroelectricity. If the dipole moment

can be reversed by applying an external electric field, the material is ferroelectric, as shown in Figure 2.3.

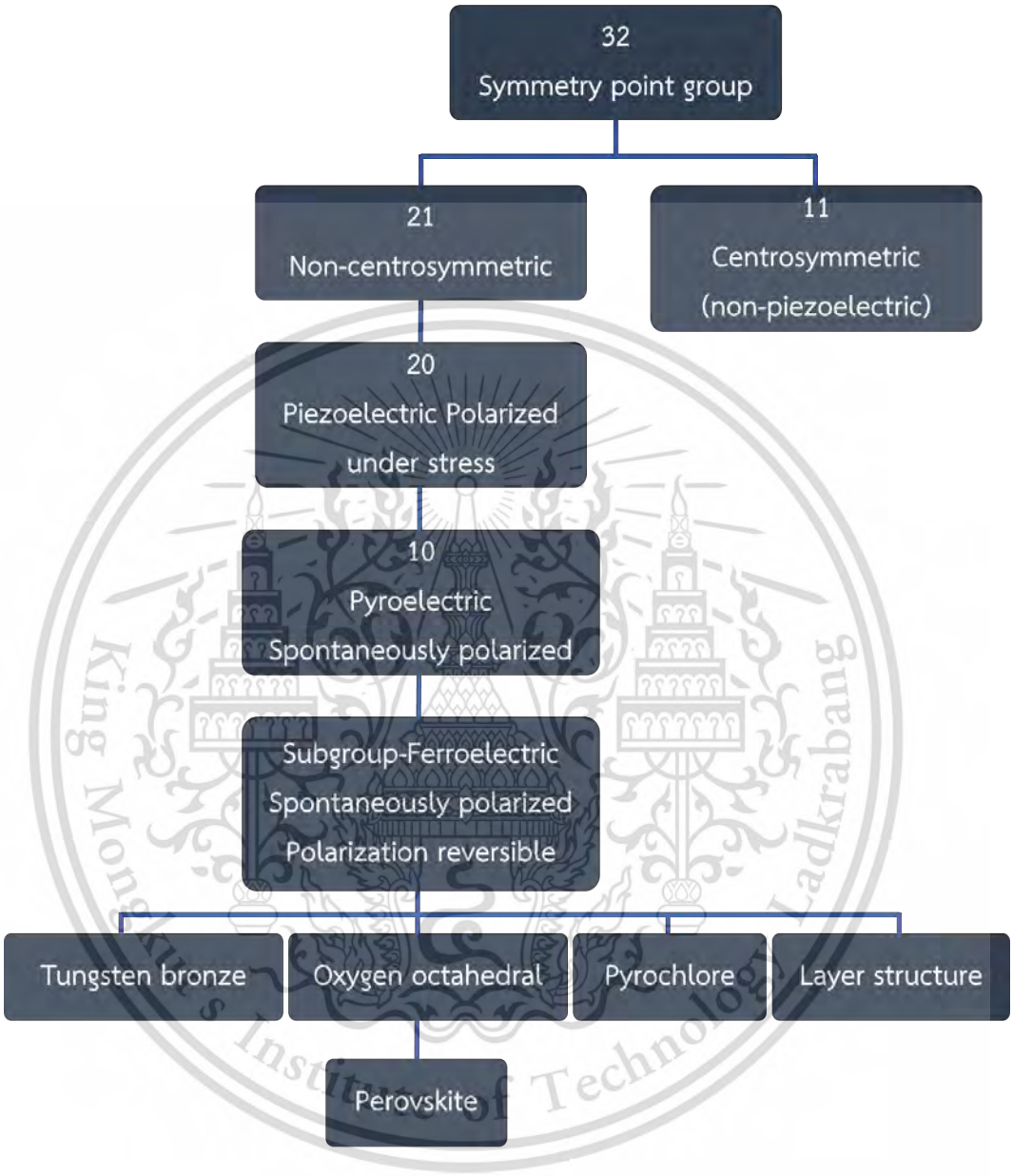

Figure 2.3 shows the piezoelectricity and its subdivisions with symmetry groups (modified form [29]).

2.2 Perovskite Structure

In general, perovskite is an important class of piezoelectric materials. Originally, perovskite referred to the mineral calcium titanate, with the chemical formula $CaTiO_3$ [30]. The mineral was discovered in the Ural Mountains of Russia by Gustav Rose in 1839 and name after Russian mineralogist Lev Perovskite 1792-1856. An ideal perovskite structure can be described as a simple cubic unit cell with a closed-packed face center cubic (FCC) structure. The perovskite structure is written as ABO_3, where A is a cation with a larger ionic radius on the comers, and B is a cation with a smaller ionic radius in the body center or octahedral interstitial site and O is oxygen in the center of the faces. as shown in Figure 2.4. The A site is in 12-fold coordination, the B site is in 6-fold coordination, and the O site is in 6-fold coordinated anions.

The ideal perovskite structure is a simple cubic lattice. The simple geometrical relationship between cations and anions can be used to describe the stability of the perovskite structure proposed by Goldschmidt in early 1920. The stability of the perovskite structure is the tolerance factor which can be expressed as following Equation 2.3 [31].

$$t = \frac{(R_A + R_O)}{\sqrt{2}\,(R_B + R_O)} \tag{2.3}$$

where t is the tolerance factor, R_A,R_B,and R_O are the ionic radius of the large cation occupying the A-site, small cation occupying the B-site, and anion (oxygen) respectively. For ideal cubic symmetry, the tolerance factor is 1. The stable perovskite structure and tolerance factor should be in the range of $0.8 \leq t \leq 1$. If $t > 1$, this indicates the A site cation is too large and generally precludes the formation of a perovskite, and if $t < 0.8$, the A cation is too small, again often leading to alternative structures [32]. The tolerance factor has been very successful in describing and predicting oxide and fluoride perovskite stability, i.e., ABX_3 compounds where X= O^{-2} or F^- [33].

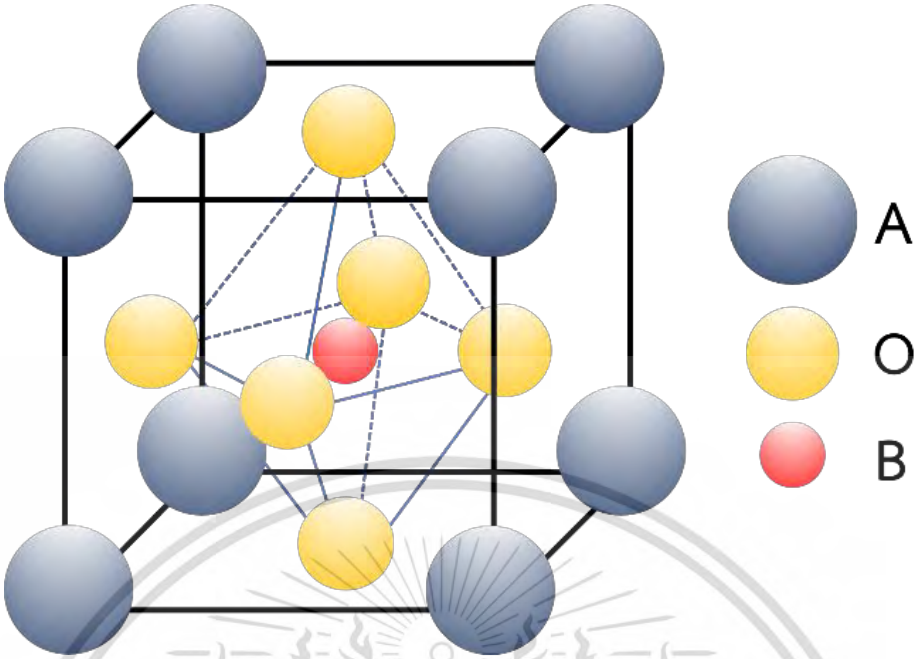

Figure 2.4 ABO_3 perovskite type unit cell (Modified from [34]).

2.3 Lead-based piezoelectric materials

The lead zirconate titanate ($PbZr_{1-x}Ti_xO_3$; PZT) piezoelectric material is a crystalline substance that exhibits the piezoelectric effect, which means it generates an electrical charge when subjected to mechanical stress. A group of researchers led by T. Sawaguchi discovered this material in the late 1950s.[35]. Lead zirconate titanate is a solid solution of lead zirconate ($PbZrO_3$) and lead titanate ($PbTiO_3$) which is a perfect sample of polycrystalline ceramics. Currently, PZT is the most widely used piezoelectric material for numerous electric devices utilizing actuators, sensors, and transducers [36]. Above the curie temperature (T_c) [37], PZT obtains a cubic perovskite structure where the A-site is Pb^{2+} (large cation) on the comers, B-site is Zr^{4+}

and Ti^{4+} in the body center and O is oxygen in the face centers, as shown in Figure 2.5a.

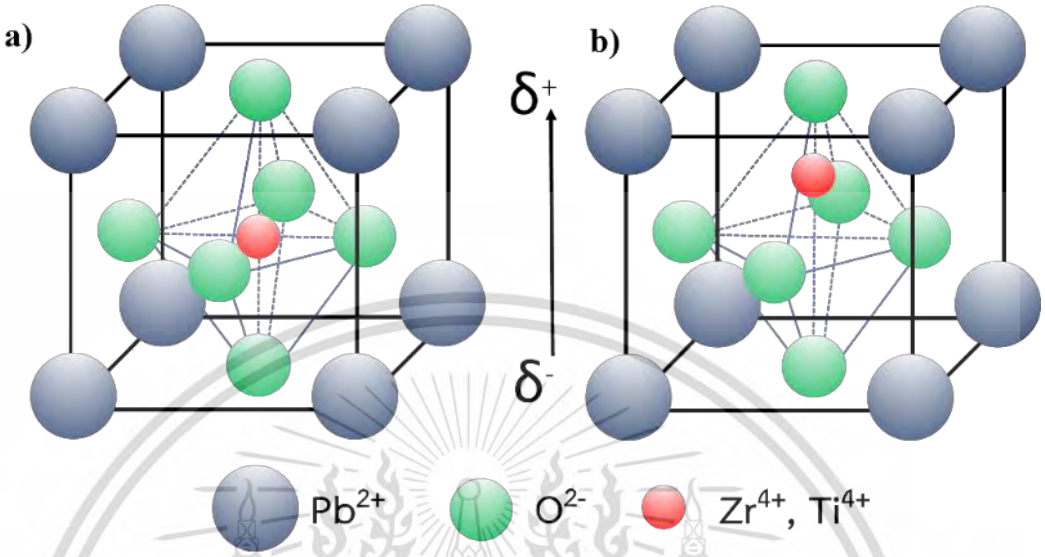

Figure 2.5 a) Perovskite structure of PZT and b) Structure of PZT under an electric field (Modified from [38, 39]).

The rigid lattice structure of atoms and their bonding affinity allow positive ions to move within the structure under external forces, including force, pressure, stress, strain, heating, and electric or magnetic fields. In the case of the PZT unit cell structure, an external electric field causes the B-type atom to move from its original position, resulting in polarization within the crystal. This movement generates a charge deviation, which produces electricity in piezoelectric materials. Under the influence of an electric field, the material expands slightly along the axis of the electric field and contracts a little in the perpendicular direction. Figure 2.5b shows the PZT unit cell structure under the influence of an external electric field. There are so many developments in phase diagram of PZT crystals. The form of the crystalline structure exhibited by PZT is dependent on the percentage concentration of metal oxides. The phase diagram of the PZT system as a function of temperature and

chemical composition is shown in Figure 2.6a. A generally accepted phase diagram of PZT says that the ferroelectric compositions with rhombohedral and tetragonal symmetry on the two sides of the morphotropic phase boundary (MPB) on the polar axis are <111> and <001>, respectively. The MPB, which separates rhombohedral Zr-rich from tetragonal Ti-rich PZT, has a very narrow composition range. Under loading conditions, the ferroelectric rhombohedral phase is transformed into the ferroelectric tetragonal phase, which is mainly responsible for the changes in charges or polarizations at the piezoelectric crystal surface. The compositions in the MPB region are commercially interesting because they have shown high dielectric permittivity and piezoelectric electromechanical coupling factors, as shown in Figure 2.6b [40]. The enhanced dielectric and piezoelectric properties of the commercial composition are generally associated with a large ionic displacement upon field application due to the rotation of the polar axis. Furthermore, other systems of lead base systems exhibit excellent piezoelectric and dielectric properties such as $Pb(Mg_{1/3}Nb_{2/3})O_3$-$PbTiO_3$ [41] and $Pb(Zn_{1/3}Nb_{2/3})O_3$-$PbTiO_3$ [42].

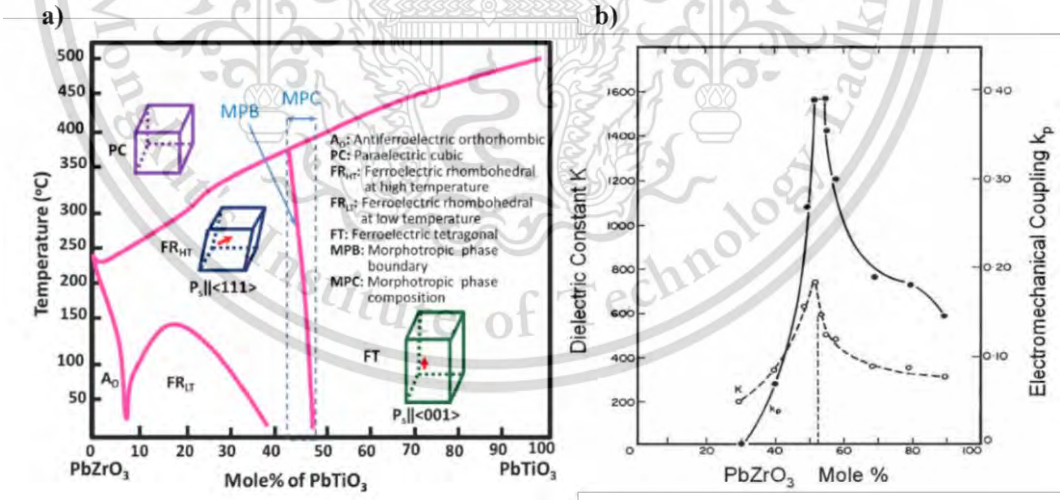

Figure 2.6 a) shows a Phase diagram for PZT, with relevant regions labeled, and b) enhanced dielectric and piezoelectric properties in PZT. [40, 43].

However, lead-based piezoelectric materials contain lead, which affects the environment and human health because of the toxicity of lead oxide in volatile during processing, including sintering and calcination process. Therefore, legislation of the European Union, such as Waste from Electrical and Electronic Equipment (WEEE) and Restriction of Hazardous Substances (RoHS) directives and End-of-Life Vehicles (ELV), restrict the use of six hazardous substances, including the lead, in electronic equipment. To prevent toxicity, lead-free piezoelectric materials have been receiving considerable attention to replace lead-based piezoelectric materials.

2.4 Lead-free piezoelectric materials

Since the early 2000s, researchers have been working to develop a new generation of lead-free piezoelectric materials. Piezoelectric materials can convert mechanical stress into electrical energy, and they are widely used in various industries, including sensors, actuators, energy harvesting devices, and communication technologies. However, lead-based piezoelectric materials have been under scrutiny due to their harmful effects on the environment and public health. Therefore, the development of lead-free piezoelectric materials has been a crucial research area in recent years. Among the lead-free piezoelectric materials, potassium sodium niobate [$(K,Na)NbO_3$, KNN], bismuth sodium titanate [$(Bi,Na)TiO_3$, BNT], and barium titanate ($BaTiO_3$, BT) have gained the most attention. These materials have shown promising properties, such as high piezoelectric coefficients, good thermal stability, and mechanical strength. The successful development and commercialization of lead-free piezoelectric materials would have significant economic and environmental benefits.

2.4.1 Potassium sodium niobate (KNN)

KNN materials are extensively studied piezoelectric systems due to their large d33 and high temperature curie (T_C) over the last decade. [44]. KNN is a solid solution of ferroelectric $KNbO_3$ and the antiferroelectric $NaNbO_3$. The phase diagram of $KNbO_3$-$NaNbO_3$ is exhibited in Figure 2.7. The MPB at near the 50:50 ratio of $KNbO_3$-$NaNbO_3$

separates two tetragonal phases at high temperatures and two orthorhombic phases at room temperature, with different tilting of the oxygen octahedral [45]. Moreover, (K0.5Na0.5) NbO3 is a good candidate for high-temperature piezoelectric applications because it has a high Curie temperature (T_c) of about 420 ˚C. Nevertheless, it's difficult to obtain fully dense ($K_{0.5}Na_{0.5}$) NbO_3 ceramics by ordinary sintering.

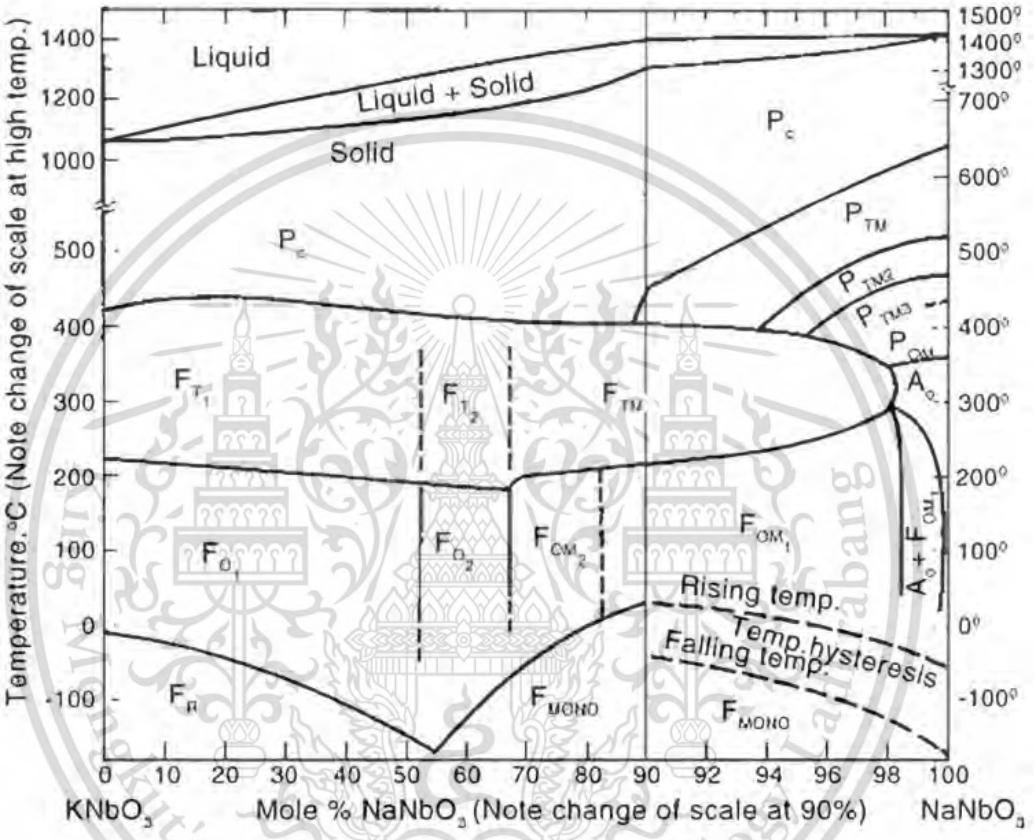

Figure 2.7 Phase diagram of $KNbO_3$-$NaNbO_3$ [46].

2.4.2 Bismuth Sodium Titanate (BNT)

Bismuth Sodium Titanate (BNT) or $(Bi_{0.5}Na_{0.5})$ TiO_3 was first reported by Smolenskii et al. In 1961 [47]. BNT ceramic is one of the ABO_3-type ferroelectric perovskites with a rhombohedral crystallographic structure at room temperature, which is replaced by Na+ and Bi3+ complex ions at the A-site. The A-site ions of BNT ceramics are located at the eight corner positions of the octahedron, and the B-site ions are at the body center of the octahedral structure [48], as shown in Figure 2.8a.The high curie temperature (T_c) 320 °C and a phase transition point from ferroelectric to antiferroelectric T_p= 200 °C. However, data on piezoelectric properties of BNT ceramic are scarce because it is difficult to pole this ceramic due to a large coercive field (E_c) is 73 kV/cm, a large saturation polarization (P_s) 45 μC/cm^2 and high remanent polarization (P_r) is 35 μC/cm^2 [48] as shown in Figure 2.8b, which seriously hinder its practical application. However, the comprehensive properties of BNT system can be significantly improved by doping or by incorporation with other components to form solid solutions. In addition, BNT ceramics need sintering temperature (>1200 °C) to obtain the dense body.

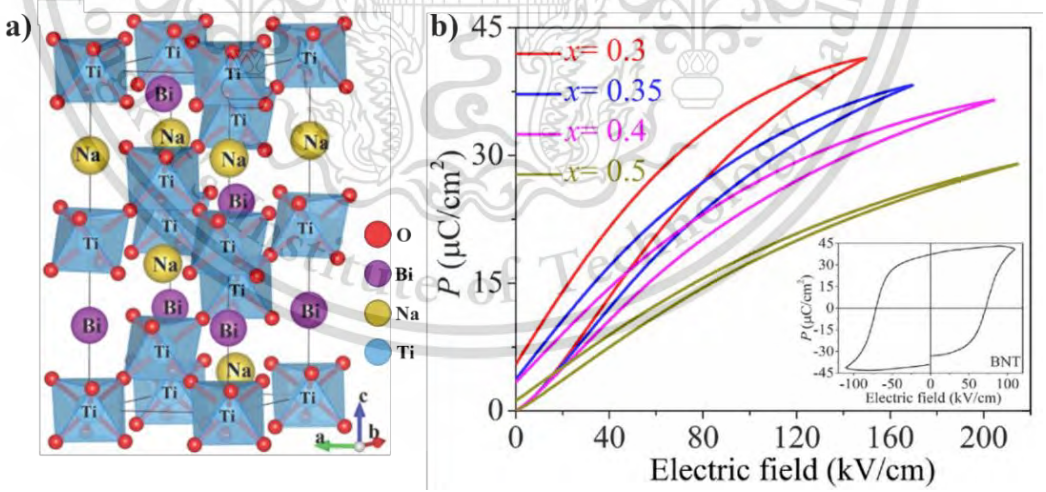

Figure 2.8 a) Schematic of the BNT perovskite structure [49] and b) The polarization-electric field (P-E) loops of BNT [48].

For application, BNT base multilayer ceramic capacitors (MLCCs) have attracted comprehensive attention due to the characteristics of small equivalent series resistance (ESR), high-rated ripple current, complete varieties and specifications, small size, and low leakage current. Jia et al. [50] conducted a study on $0.9[0.94(Bi_{0.5}Na_{0.5}TiO_3\text{-}0.25NaNbO_3)\text{-}0.06BaTiO_3]\text{-}0.1CaZrO_3$ MLCCs. The study found that these MLCCs exhibited excellent temperature stability in a recoverable energy storage density (W_{rec}) at the E_c of 120 kV/cm, even in temperature ranges as low as -55˚C to -175˚C. This indicates that the MLCCs have the potential to be used as high-temperature ceramic capacitors, as shown in Figure 2.9.

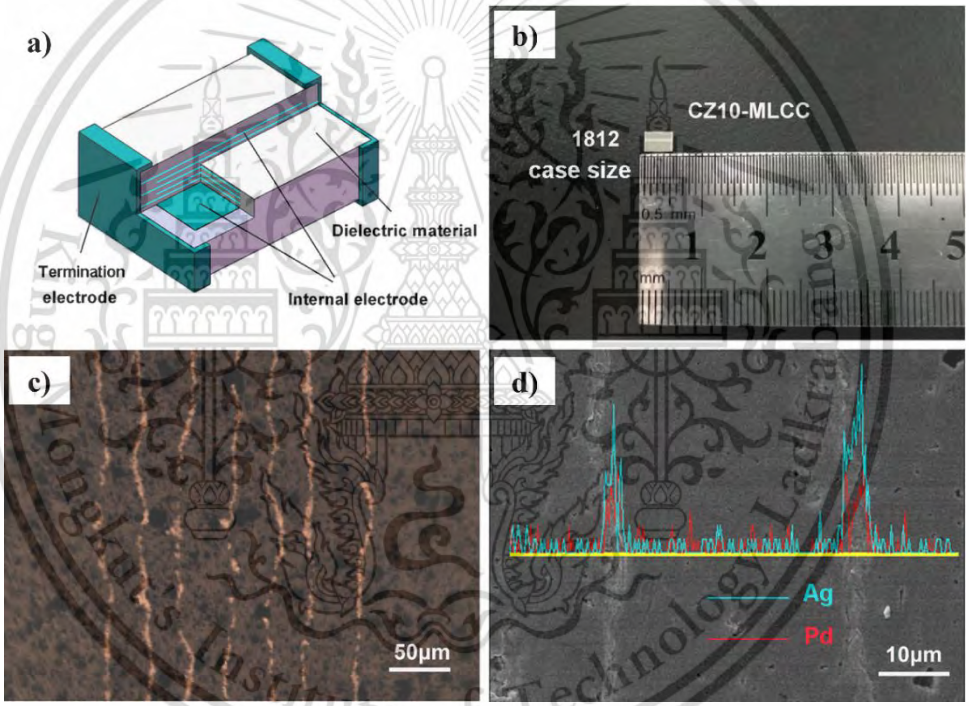

Figure 2.9 a) A schematic of multilayer ceramic capacitor architecture, b) view of CZ10-based MLCC chip of 1812 case size, c) cross-sectional microstructure of CZ10 MLCCs, and d) EDS analysis performed across two internal electrodes [50].

2.4.3 Barium Titanate (BT)

Barium Titanate (BT), with the chemical formula $BaTiO_3$, was discovered in 1946 by Wul and Goldman [51]. BT was the first ferroelectric material due to its high dielectric constant and low loss characteristics. It finds wide applications in capacitors and multilayer capacitors (MLCs), and as a piezoelectric material for microphones and other transducers [52]. Furthermore, BT belongs to the class of perovskites, like the mineral $CaTiO_3$, with the general formula of ABO_3, where the A-site is Ba^{2+} on the corners, the B-site is Ti^{4+} in the body center, and O is O^{2-} in the face centers.

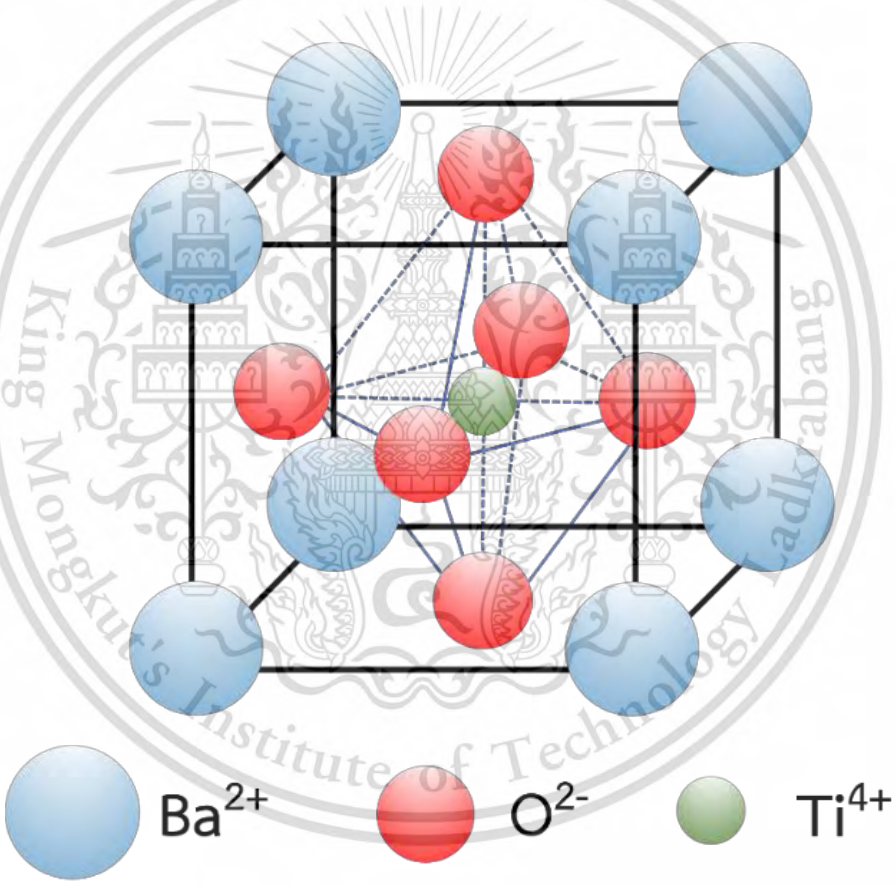

Figure 2.10 The Ba^{2+} cations are located on the A-sites and Ti^{4+} on the B-sites (modifies from [53]).

2.4.3.1 Structural phase transitions in barium titanate

BT is the first discovered ferroelectric perovskite. Its ferroelectric properties relate to a series of four structure phase transitions. These four structure phases of BT are rhombohedral, orthorhombic, tetragonal, and cubic as a function of the temperature. The Curie point (T_c) of BT is 120 °C. Above 120 °C, it has an original cubic structure, which is Centro-symmetric and possesses no spontaneous dipole. It is stable up to 1460 °C and above this temperature a hexagonal structure is stable [54]. When the temperatures are below the Curie point, crystallographic changes in BT occur; first, at about 120 ° C, a ferroelectric transition between the cubic, paraelectric, and ferroelectric phases of the tetragonal structure takes place. At 5 °C, the transition to a phase of the orthorhombic structure goes on and at -90 °C to the low-temperature phase having a trigonal structure [55]. The crystallographic changes of BT are shown in Figure 2.11.

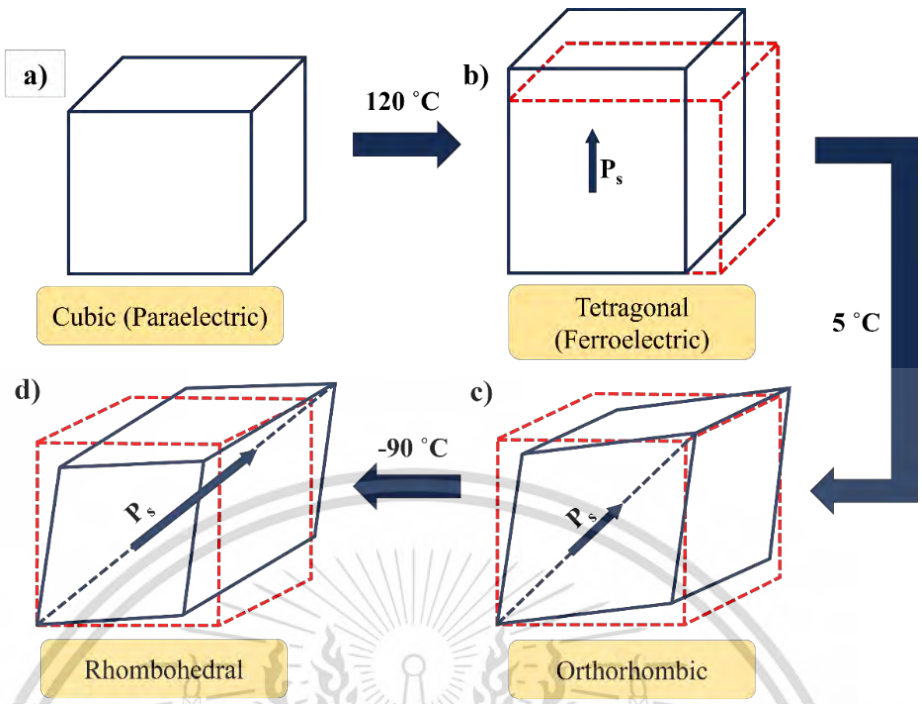

Figure 2.11 shows the unit cell of the four phases of BT a) Cubic structure, stable above 120 °C, b) Tetragonal structure, stable between 120 °C and 5 °C, c) Orthorhombic structure, stable between 5 °C and -90 °C and d) Rhombohedral structure, stable below -90 °C, the dotted lines in (b,c, and d) delineate the original cubic cell. Arrows indicate the direction of the spontaneous polarization, P_s, in each phase. (modified from [56]).

Moreover, the phase transition of BT corresponds to a change in the values of the lattice parameter [57]. These changes can be related to structural distortion, lengthening of the bonds, or their shortening, so crystallographic dimensions of the BT lattice change with temperature. For the tetragonal phase, polarization (P) is parallel to the edge of the crystal unit cell, while for the orthorhombic (a=c<b) and rhombohedral phases (a=b=c), it becomes parallel to the face diagonal and the body diagonal, respectively, as shown in Figure 2.12.

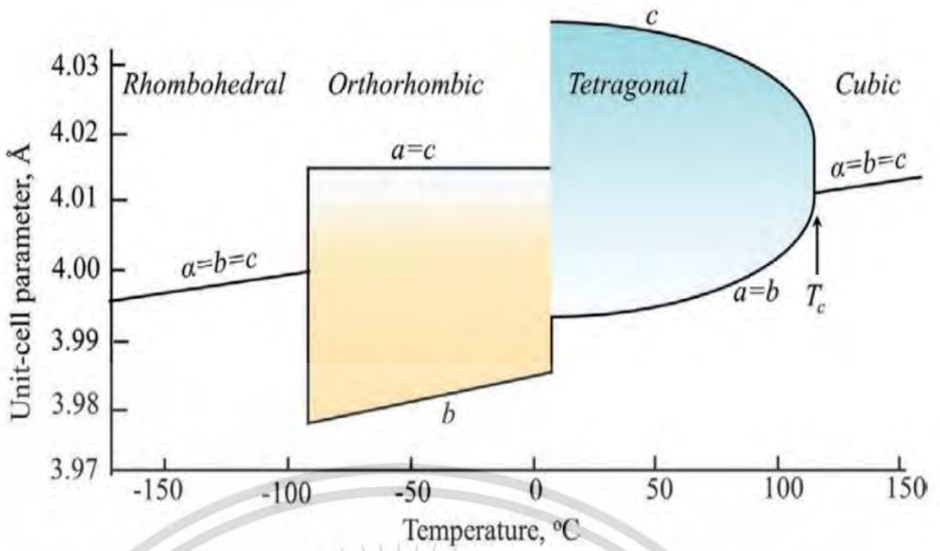

Figure 2.12 Lattice parameters as a function of temperatures [57].

2.4.3.2 Dielectric Properties of BT

BT was the first material used to manufacture dielectric ceramics capacitors, multilayer capacitors, etc. It is used for this application due to its high dielectric constant and low dielectric loss. The values of the dielectric constant depend on the synthesis way, which means purity, density, grain size, etc. [58]. The dielectric constant is also dependent on temperature, frequency, and dopants. The temperature dependence of the dielectric constant is measured with a small field along the pseudo-cubic edge, as shown in Figure 2.13. The BT has a phase transition from tetragonal to cubic (Tc) that occurs at 120 ° C with the highest dielectric constant. It was also a transition point from the ferroelectric to the paraelectric phase [52]. In addition, the temperature dependence of the dielectric constant was reported in several papers, where BT was prepared by different types of synthesis. For example, Kim et al. [11] prepared BT powder by the Pechini process, they reported that the influence of grain size on the dielectric constant value. The various grain sizes were obtained from 0.86 to 10 μm and measured the temperature dependence of the dielectric constant. At room temperature, the dielectric constant was 4500 and 1800 at the Curie points 6200 and 7000, for 0.86 μm and 10 μm grains, respectively. They concluded that as the grain size increased, the dielectric constant decreased at

most studied temperatures, and they determined that the specimen with grain sizes of 0.86 μm exhibited the highest dielectric constant for the temperature range below the Curie point, as shown in Figure 2.14.

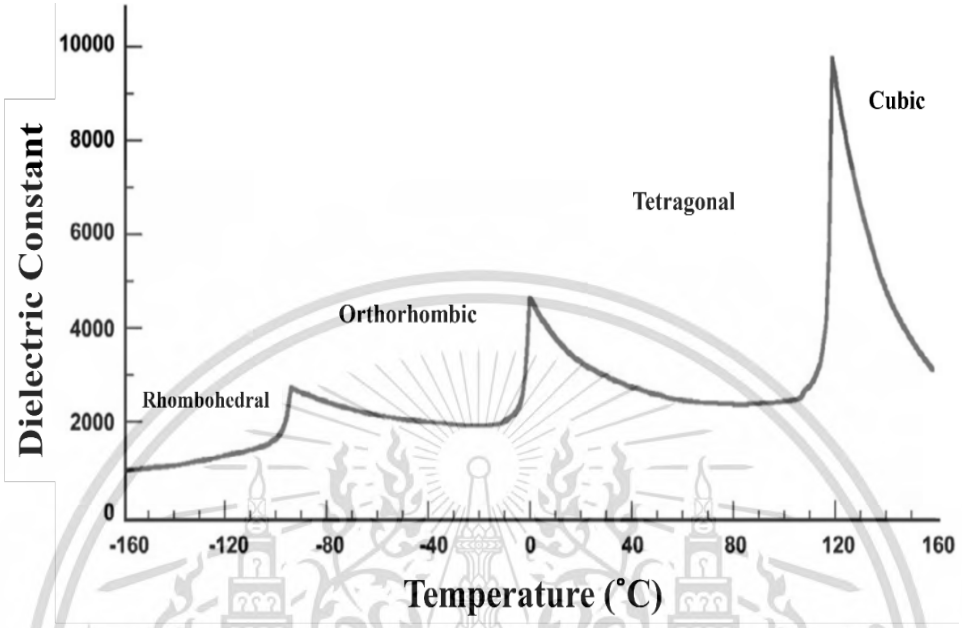

Figure 2.13 Dielectric constants of BT as a function of temperature [59].

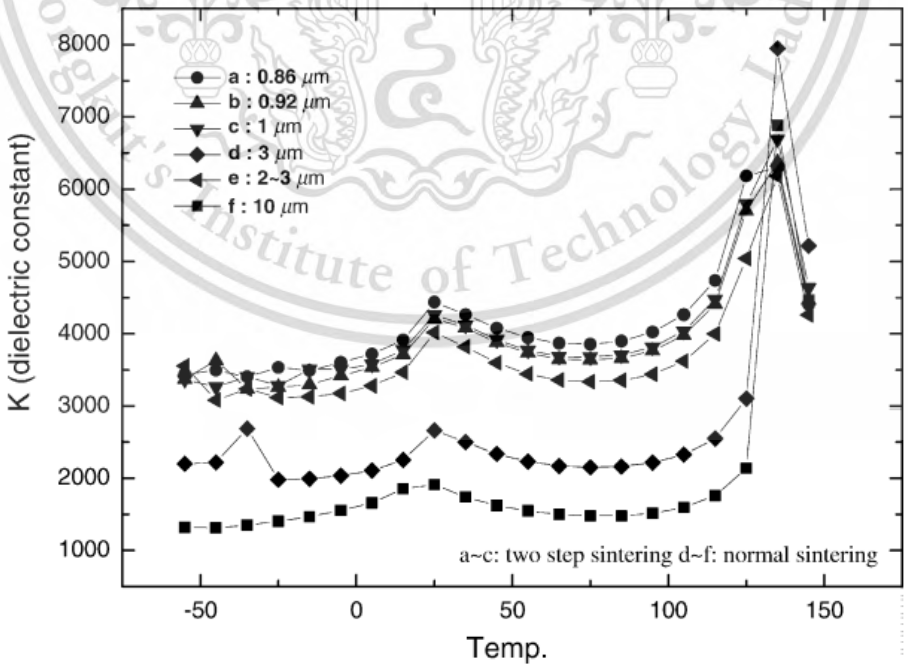

Figure 2.14 The temperature dependence of dielectric constant in various grain sizes [11].

Benlahrache et al. [60] prepared pure barium titanate (BT) using the conventional method of milling and calcination. They conducted measurements by examining the frequency dependence of the dielectric constant, as shown in Figure 2.15. The samples were sintered at a temperature of 1500 °C for 2 hours with an applied bias of 100 V. At room temperature, the dielectric constant decreases for frequencies below 1 kHz. However, for higher frequencies, the dielectric constant changes slightly and tends towards a constant value. The dielectric constant of BT remains constant at normal temperatures, but at higher temperatures, it behaves differently and requires further investigation. Many works have mentioned the preparation of pure BT, and the method chosen for its synthesis depends on the cost and, more importantly, the final application. In the following paragraphs, we will discuss the process of preparing pure BT.

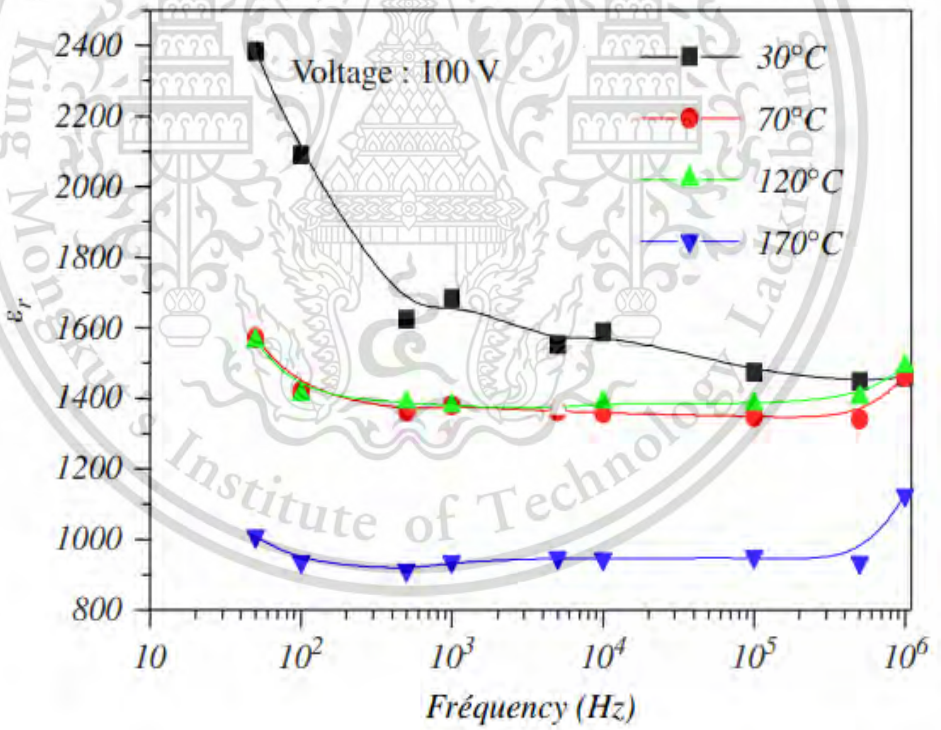

Figure 2.15 Frequency dependence of relative dielectric constant at various temperatures, when polarized at 100 V. Pure BT sintered at 1500 °C/2h [60].

2.4.3.3 BT synthesis methods

2.4.3.3.1 Chemical methods for BT synthesis

Chemical synthesis has grown through techniques such as hydrothermal methods. The advantage of chemical methods is the quasi-atomic dispersion of constituent components in a liquid precursor, which facilities the synthesis of crystallized powder with submicron particles and high purity at low temperatures. The properties of the powder may vary as different preparation methods are used.

2.4.3.3.1.1 Hydrothermal Method

The hydrothermal method is attractive for synthesizing BT powder, because the combined effects of solvent, temperature, and pressure on the reaction equilibrium can stabilize desirable products while inhibiting formation of undesirable compounds. In addition, hydrothermal synthesis also makes it possible to prepare BT powder in a single processing step. Boulos et al. [61] synthesized BT powders by the hydrothermal method using two different titanium sources $TiCl_3$ and TiO_2. The barium source was $BaCl_2 \cdot H_2O$. Synthesis was performed at 150 ˚C and 250 ˚C. SEM micrographs of BT powders show spherical highly crystallized elementary grains with size in the range 40-70 nm for samples prepared from $TiCl_3$ at 150 ˚C and 80-120 nm at 250 ˚C. the average particle size for powders obtained from TiO_2 at 150 ˚C or 250 ˚C was 40-70 nm as show in Figure 2.16.

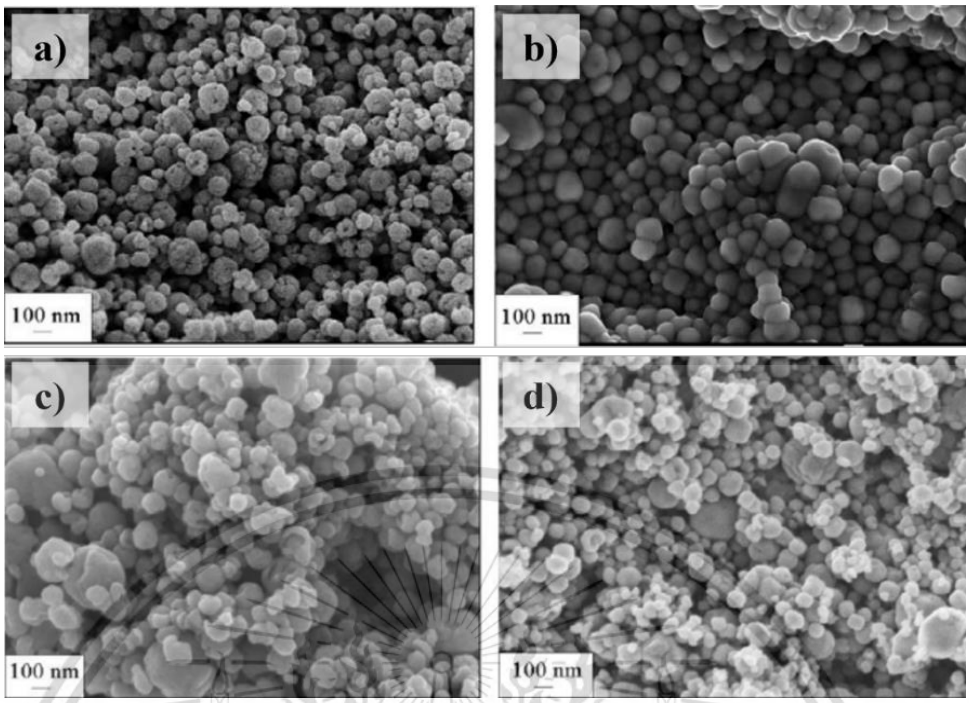

Figure 2.16 SEM image of BT powders prepared from $TiCl_3$ a) at 150 ˚C b) at 250 ˚C, prepared from TiO_2 c) 150 ˚C and b) 250 ˚C [61].

Figure 2.17 TEM images showing the typical shape of a particle from the a) as-synthesized powder and b) powder obtained after calcination at 1000 ˚C for 4 hours [62].

Norfarina et al. [62] They synthesized BT nanoparticles through the hydrothermal method and calcined them at 1000 ˚ C. After calcination, they found

that highly crystalline BT was obtained. The particle size of the BT-calcined powder increased to 11.66 nm, indicating crystal growth. Moreover, the shape of the particles for the as-synthesized powder changed from ellipsoid-like to cube upon calcination, as shown in Figure 2.17.

2.4.3.3.2 Conventional solid-state reaction

Barium Titanate (BT) is usually produced by a solid-state reaction, which involves ball milling of Barium Carbonate (BaCO3) or Barium Oxide (BaO) and Titanium dioxide (TiO2). The mixture is then calcined at high temperature. However, in some reports, the required calcination temperature was as high as 800 ˚C to 1200 ˚C, while in others, it was 1300 ˚C. The BT powders produced by this method are highly agglomerated, have a large particle size (2-5 μm), and high impurity contents, which result in poor electrical properties of the sintered ceramics. These issues arise due to inherent problems such as high reaction temperature and heterogeneous solid-phase reaction.[63]

L. Simon-Severat et al. [64] synthesized a BT powder through a solid-state reaction. The BT powder was prepared by heating a mixture of $BaCO_3$ and TiO_2 at high temperatures. The processing steps involved ball milling for 2 hours, calcining at 1150°C for 4 hours, and then mixing the calcined product for 3 hours. The precursor solid-state powder was studied by XRD, and the results showed that the BT perovskite phase started to appear at temperatures between 780°C and 800°C. At 950°C, both orthorhombic and rhombohedral $BaCO_3$ phases were observed. At 1050°C, there was no $BaCO_3$ present, but only a small amount of rhombohedral $BaCO_3$ and well-formed $BaTiO_3$, as shown in Figure 2.18.

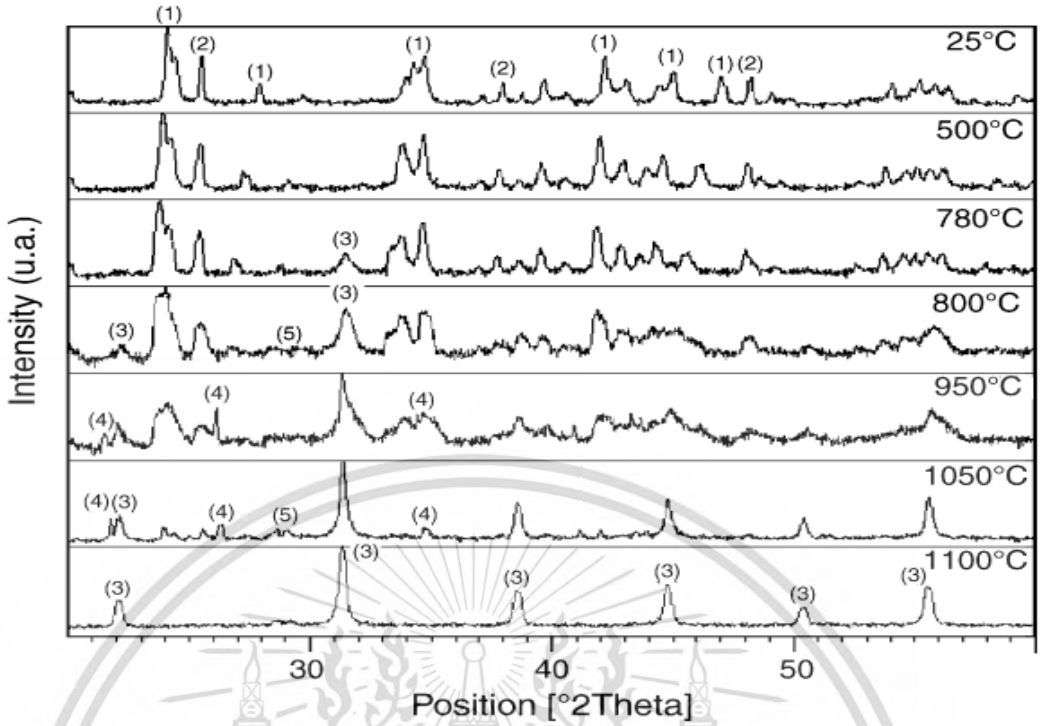

Figure 2.18 XRD results in the temperature of the precursor solid-state reaction powder: (1) $BaCO_3$; (2) TiO_2; (3) $BaTiO_3$; (4) rhombohedral $BaCO_3$; and (5) Ba_2TiO_4. [64].

2.4.3.4 Applications

BT was the first polycrystalline ceramic material ever discovered that exhibited ferroelectricity, During the 1950s, it was considered a serious candidate for piezoelectric transducer application [65], actuator [66], especially, the main application of BT-based ceramic is in multi-layer ceramic capacitors (MLCCs) [67].

2.4.3.4.1 Multi-layer ceramic capacitors (MLCCs)

Multi-layer ceramic capacitors (MLCCs) are highly regarded for their superior frequency characteristics, high reliability, excellent volumetric efficiency, and high breakdown voltage. The demand for MLCCs in the smartphone, portable PC and the automotive industry has led to a global shortage of these capacitors. MLCCs consist of multiple dielectric layers and inner electrodes that are stacked in parallel. Figure 2.19 depicts a schematic diagram of the detailed structure and fabrication procedure

of MLCCs. MLCCs are typically manufactured through the following process. Firstly, fine ceramic powders for dielectric layers are mixed with a binder, solvents, and additives such as dopants and sintering aids. This mixture is made into a slurry and cast into thin sheets using a tape-casting method. Once dried and cut into equally sized sheets, the green sheets are screen-printed with a metal paste. The required number of green sheets are stacked with inner electrodes slightly offset from each other. Pressure is then applied to the stacked green sheets to laminate them. The laminated sheets are cut into the desired chip size. After cutting, the binder in chips is burned out and then sintered. To connect the internal electrodes in parallel, termination is made on the chip through tumbling, dipping, and firing processes. After the completion of electrical testing for quality, the fabrication of MLCC chips is completed.

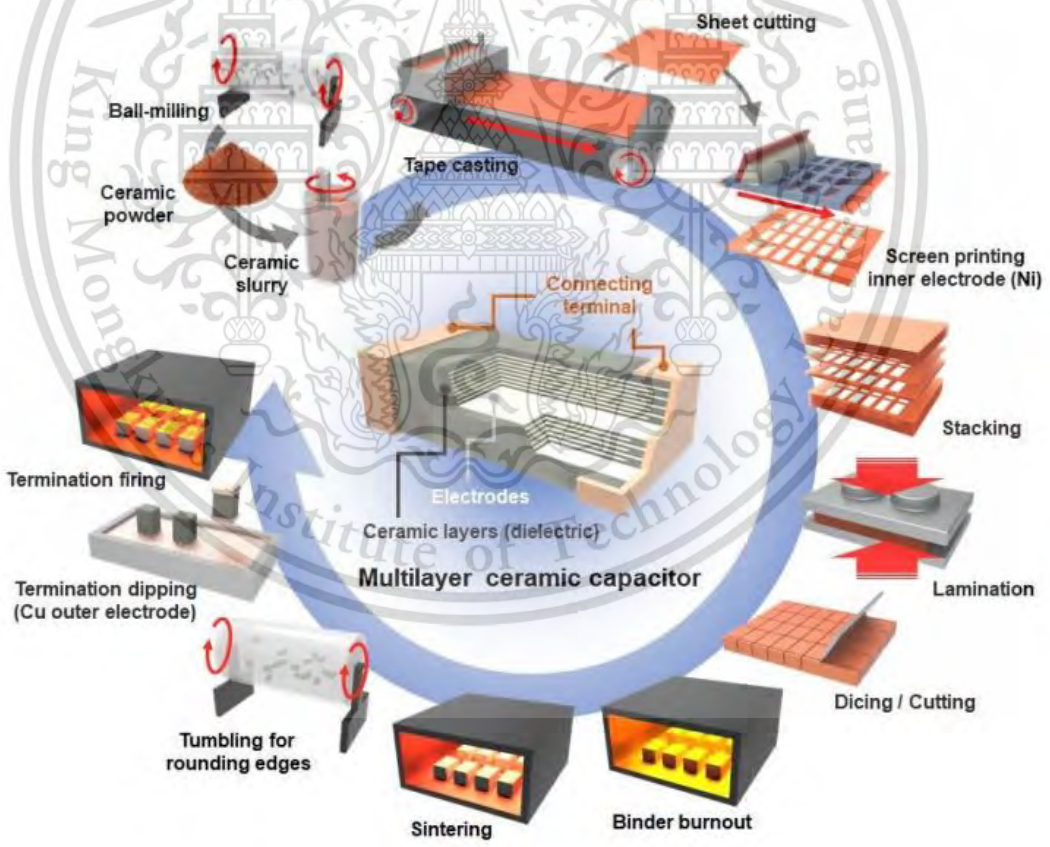

Figure 2.19 shows the MLCCs architecture and its fabrication process [9].

However, there are several issues in the fabrication process of high capacitance MLCCs. The sintering temperature control is important to fabricate MLCCs. Because high sintering temperature (>1200 °C) of dielectric materials causes the metal diffusion into the dielectric layer, residual stress, and mechanical crack due to sintering shrinkage, which result in poor performance and malfunction. To solve this problem, a new sintering process to lower the sintering temperature was developed.

The oldest manufacturing technique that has been documented back to 25,000 BC is the sintering of ceramic materials. Sintering is still a crucial process in the manufacturing of advanced ceramic products today, despite its ancient beginnings. However, the material to migrate between solid-solid interfaces, and conventional sintering procedures call for high temperatures and prolonged holding times. As a result, sintering procedures are always changing to accommodate brand-new industrial and technological demands. Creating high-quality products through sustainable production without harming the environment is currently the key challenge. Alternative sintering techniques have developed as a result, which lowers the time, temperature, energy, and prices compared to conventional sintering processes.

2.5 Sintering Process

The sintering process is the process of compacting and forming a solid mass of material by pressure and heat without melting it to the point of liquefaction. Sintering process as part of a manufacturing process used with metal, ceramics, plastics, and other materials. The atoms in the materials diffuse across the boundaries of the particles, fusing the particles, reducing porous, and creating one solid piece as shown in Figure 2.20. The sintering process consists of three stages. Before sintering, in the first stage called initial stage grains were contacted with each other, grain boundary areas grew, and grains started to merge. In this stage, grains were smaller than merged grains formed. However, pores were larger than before the sintering process. In the second stage, the neck was formed between adjacent grains. There were small numbers of large grains instead of large numbers of small grains. Pores

were smaller than pores before sintering. Grain growing was continued in this stage. Therefore, this stage is called intermediate stage. In the final stage, merging was completed. The grains were larger than calcined ceramic grains. Small pores were formed, and the surface area was decreased. It is smaller than the surface area in the other two stage [68]. However, the sintering temperature does not have to reach the melting point of materials, sintering is often chosen as the shaping process for materials with extremely high melting points such as barium titanate, tungsten, or molybdenum.

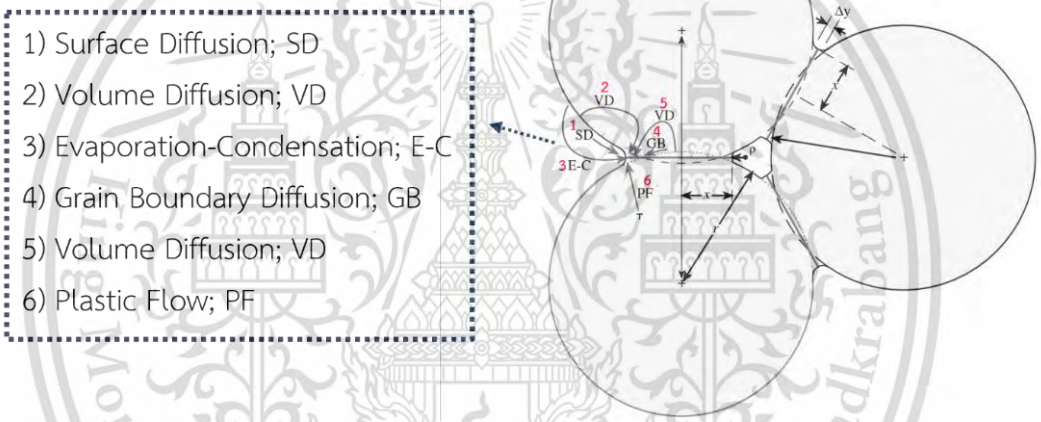

Figure 2.20 shows the sintering effect (modified from [69]).

To understand the sintering process, the sintering process can be understood by the mass transport mechanism (Figure 2.21). The atomic materials will be diffused by the drive force. The driving force is therefore a part that results in the reduction of the free energy in the system. It is a help atomic diffuses from a point of high concentration to a point of low concentration. As sintering progresses, the two spheres move together.

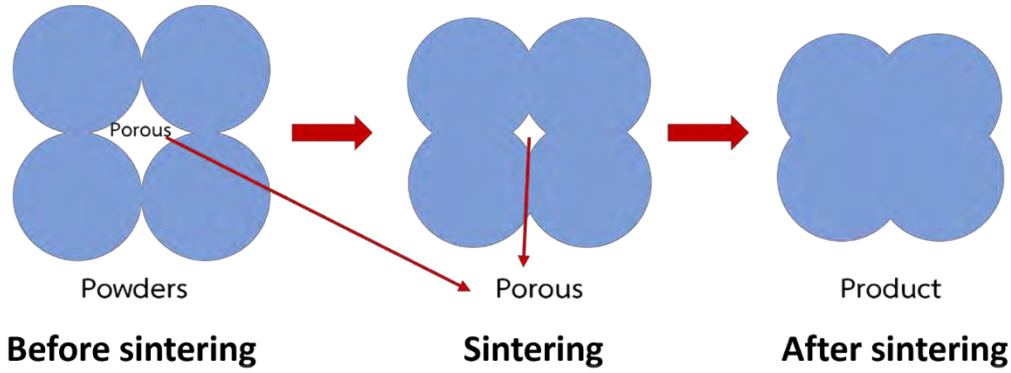

Figure 2.21 showing the diffusion paths from the GB to the neck surface and the development of a pore (2D projection) modified from [70].

This movement is an essential step in densification, which proceeds through six mechanisms: Surface Diffusion (SD), Volume Diffusion (VD), Evaporation-Condensation (E-C), Grain Boundary Diffusion (GB), and Plastic Flow (PF). Especially, the mechanism of GB is the most important mechanism to facilitate material compaction. The diffusion from the grain boundaries to the pores contributes to neck formation. At the same time, it causes densification. There are six mechanisms for material transfer and some of the processes are listed in Table 2.1.

Table 2.1 Mechanism and Transport in sintering (Diffusion to the Neck) (modified from[70])

Mechanism	Transport path	Source
1	Surface Diffusion; SD	Surface
2	Volume Diffusion; VD	Surface
3	Evaporation-Condensation; E-C	Surface
4	Grain Boundary Diffusion; GB	GB
5	Volume Diffusion; VD	GB
6	Plastic Flow; PF	Dislocations

2.5.1 Grain growth

Grain growth is used to describe grain size enlargement. Grain growth occurs in dense materials or in porous materials at high temperatures. The larger grain size is accompanied by the disappearance of some small grains. In porous materials, the grain size increases while the number of grains and pores decreases.

Grain growth and grain size are related to relative density. Initially, the particles are randomly aggregated and when heated in the sintering process, the grain growth is limited by porosity. As the sintering process progresses until the density reached 92%, the porosity was eliminated. Thereafter, rapid grain growth takes place in areas of particle density during continuous sintering. The final porosity will be eliminated. After that, the final product is characterized by highly dense ceramic particles.

The average grain size increases during the grain growth, the amount of grain boundaries in the system are decreased to maintain the overall volume. Grain boundaries of equal energy and colliding at exactly the three-grain boundary form an angle of 120° to each other. This can be explained by Figure 2.22, which can be seen that if all interlocking grain boundaries form an angle of 120°, hexagonal grain is obtained. Grain with grain boundaries on more than 6 sides, when grain boundaries are displaced, these grains expand. The size of the grain has grown. But if the grain with the number of grain boundaries is less than 6 sides, when the grain boundaries move towards to the center of curvature, these grains shrink until they disappear.

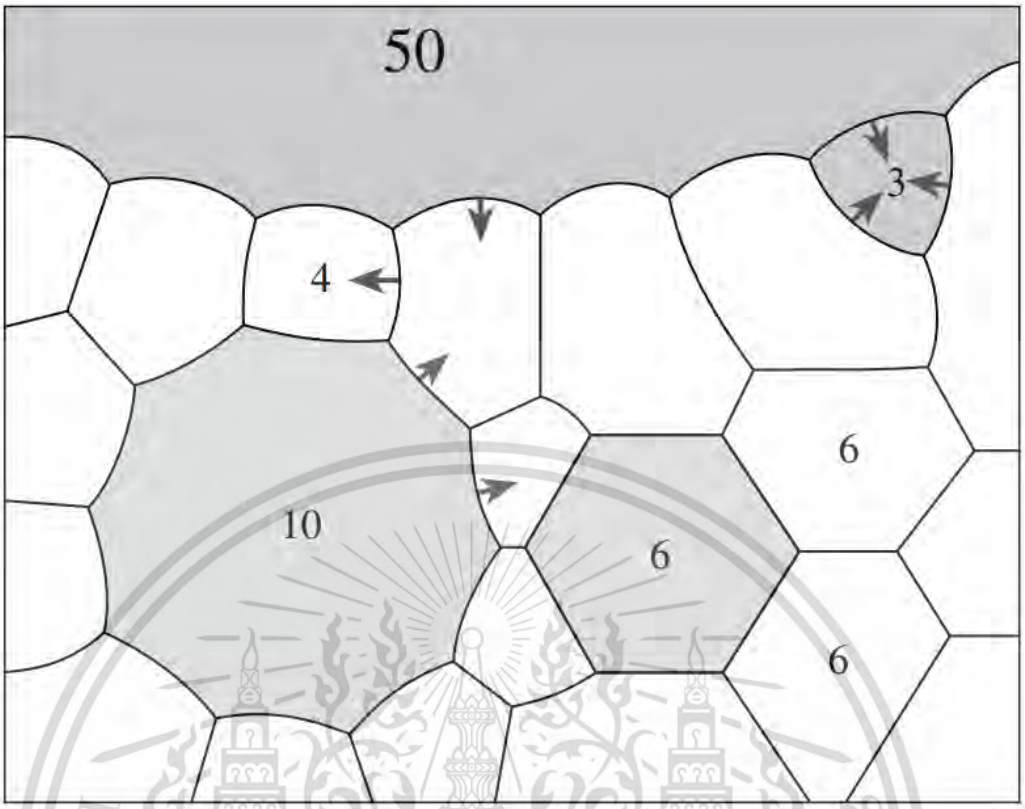

Figure 2.22 shows the complex microcrystalline structure in two dimensions with an arrow showing the direction in which the grain boundaries are moving [71].

2.5.2 Stage of sintering

The stage of sintering can be divided into 3 stages: Initial stage, Intermediate stage, and Final stage. These three steps affect the density and microstructure as shown in Figure 2.23. The density increases progressively as the particles move into each other. The other factors occurring in the sintering process can be summarized as shown in Table 2.2.

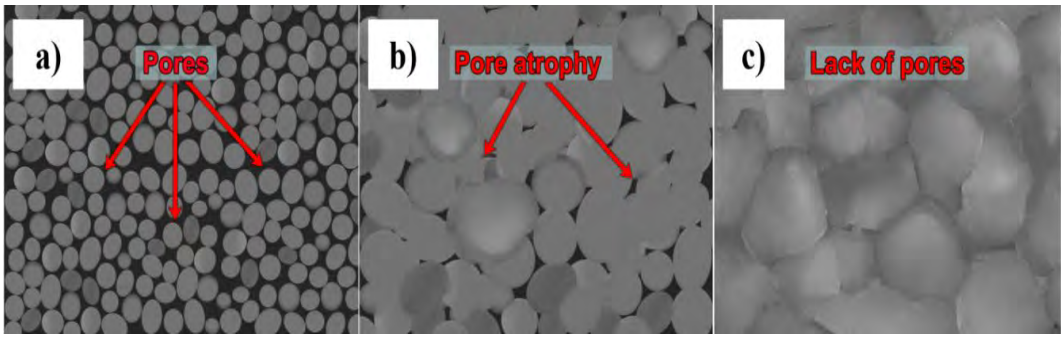

Figure 2.23 shows the example of microstructure characteristics of ceramics produced can be divided into 3 stages: a) initial sintering, b) intermediate sintering, and c) final sintering, [72].

2.5.2.1 Initial sintering

It involves the movement of powder particles into contact with each other by diffusion without changing their shape. It can be observed that the curvature of the particle surface breaks away at this stage and the neck grows at the point of contact between the powder particles. The relative density of this early specimen may increase from 50% to 60%, due to the increase packing of the powder particles, as shown in Figure 2.23a.

2.5.2.2 Intermediate stage

During this period of sintering, it was found that the size of the neck began to grow and the porosity in the sample began to decrease rapidly. As particles move closer to each other causing the specimen to shrink significantly. There is grain growth going on, the shrinkage of the specimen that occurs the most during this period causes the relative density of the specimen to be as high as 90%, as shown in Figure 2.23b.

2.5.2.3 Final stage

The last stage of sintering is when the pores in the specimen begin to close themselves and are gradually eliminated from the specimen by relying on the diffusion mechanism of air from the pores out along the grain boundary and then fall

off the surface of the specimen. This will increase the density a little more from 95% to 99%, and the grain size will increase in the final sintering stage, as shown in Figure 2.23c.

Table 2.2 summarizes characteristics that occur in each stage of the sintering process.

Sintering stage	Characteristic of microstructure	Relative density	Characteristic that changes or occur
Initial	The neck of each particle encounters each other	an increase of 50% to 60%	The moving particles encounter each other
Intermediate	various pores are reduced	increase to a maximum value of 90%	neck enlargement, grain enlargement, porosity
Final	Grain boundaries are clearly visible	Over 90%	full grown grain and porosity closed

2.5.3 Temperature zone in the sintering process

According to the temperature period, the sintering temperature is divided into 3 periods: preheat/pre-sintering zone, Sintering zone, and Cooling zone, which affects the density of the ceramic.

2.5.3.1 Preheat/Pre-sintering zone.

Because forming ceramics often adds fillers or lubricants. Therefore, during the initial sintering preparation is the removal of all fillers, lubricants, and other organic contaminants. Elemental decomposition and oxidation of transition metals occur if present in the specimen. The temperature in the kiln of this zone slowly increases.

2.5.3.2 Sintering zone

Once the liquid phase has been removed at first zone, the ceramic specimen will enter the sintering. This is an important period that causes the ceramic density

process because particles move towards each other through diffusion and then connect to each other. This is when porosity decreases will cause changes in the microstructure.

2.5.3.3 Cooling zone

When the ceramics are fully solidified from the sintering, the temperature will drop in the cooling zone. This is the time when trying to maintain the ceramic condition to prevent cracks and involves phase transitions in the structure. If the material has already undergone a phase change during de-tempering, the material has a rapid phase change and will cause cracks in the ceramic specimen.

2.5.4 Liquid phase sintering (LPS)

Liquid Phase Sintering (LPS) is a process used in powder metallurgy or ceramic processing to bond particles together to form a solid material. In LPS, a liquid phase is introduced to the powder mixture, typically through the addition of a sintering aid or a eutectic composition. During sintering, the powder particles are heated to a temperature where the liquid phase forms. This liquid phase facilitates the movement of particles, promoting particle rearrangement and neck formation between adjacent particles. As the temperature continues to rise, the liquid phase helps in the redistribution of mass, leading to densification and the formation of a solid structure. Liquid phase sintering offers several advantages, including enhanced densification, improved mechanical properties, and the ability to produce complex shapes. It is commonly used in the production of various materials, including ceramics, metal alloys, and composites.

The classic stages of liquid phase sintering (LPS) involving mixed powder that forms a liquid on heating typically include the following steps: 1) Particle rearrangement: Initially, the powder mixture is compacted into a green body with loosely packed particles. During the early stages of heating, the particles begin to rearrange themselves due to surface energy minimization and the application of heat. 2) Formation of liquid phase: As the temperature increases, certain components

within the powder mixture reach their respective melting points or eutectic compositions, leading to the formation of a liquid phase. This liquid phase is often generated by the presence of sintering aids or impurities intentionally added to the powder mixture. 3) Capillary action and particle coalescence: The formation of the liquid phase enables capillary action, which draws the liquid into the interparticle voids. This capillary action helps in the wetting of particle surfaces by the liquid phase, promoting particle coalescence and neck formation between adjacent particles. The liquid bridges between particles act as a temporary bonding agent during sintering. 4) Densification and mass transport: With further heating, the liquid phase facilitates mass transport mechanisms such as diffusion, viscous flow, and surface diffusion. These mechanisms lead to the rearrangement of particles and the densification of the material. The liquid phase aids in the removal of pores and voids, resulting in increased density and improved mechanical properties. 5) Final solidification: As the sintering process progresses and the temperature reaches the solidus temperature of the liquid phase, the liquid begins to solidify. At this stage, the necks formed between particles become more rigid, contributing to the development of a solid structure. 6) Cooling and final properties: Once the sintering process is complete, the material is allowed to cool down gradually. During cooling, the solidified microstructure is stabilized, and the final properties of the sintered material, such as density, microstructure, and mechanical properties, are determined.

These classic stages of liquid phase sintering are crucial for achieving desired densification, microstructure, and properties in the final sintered product, as shown in Figure 2.24. The process parameters, composition of the powder mixture, and characteristics of the liquid phase play significant roles in controlling the kinetics and outcomes of liquid phase sintering.

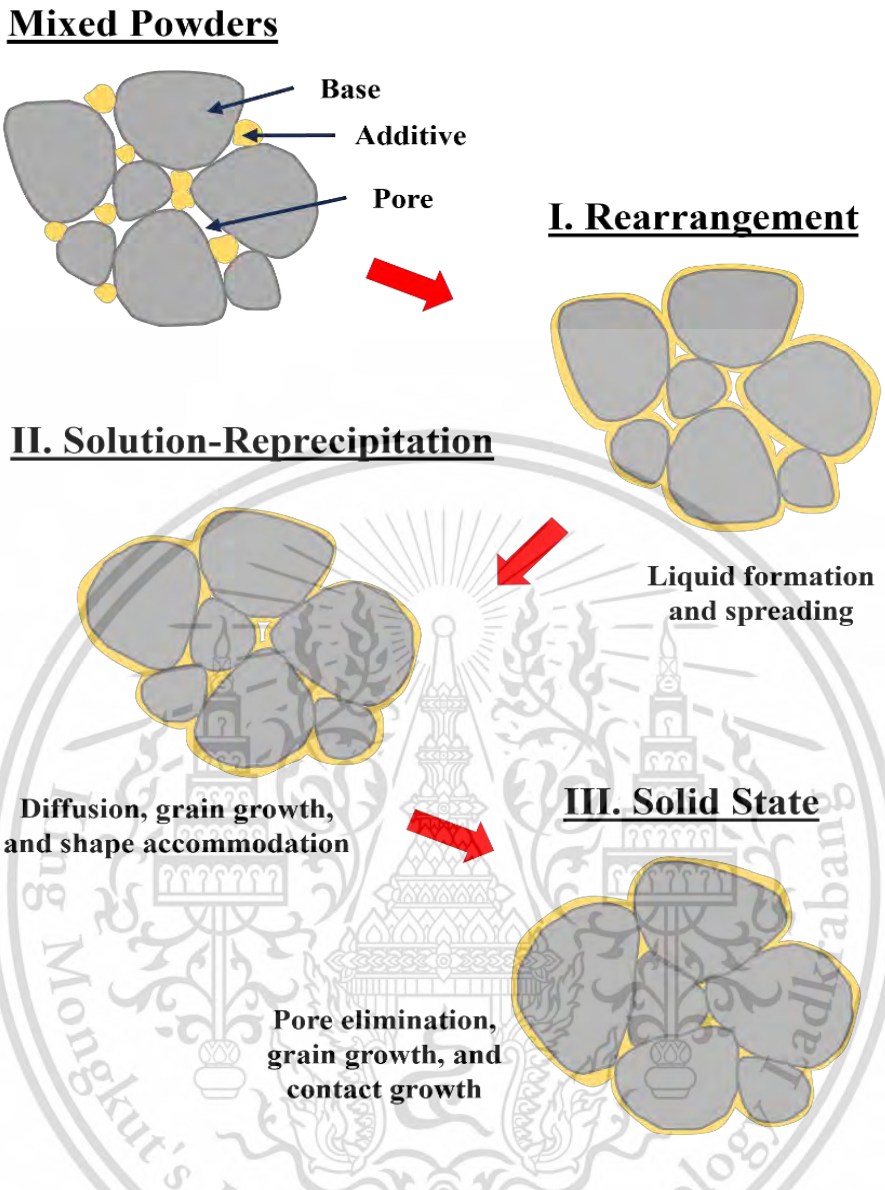

Figure 2.24 The classic stages of liquid phase sintering involving mixed powder which form a liquid on heating (modified from [73]).

2.5.5 Other types of sintering

Traditional sintering is a process that requires high temperature above 1000 °C and takes a long time, resulting in significant energy consumption. Therefore, a new sintering method was developed between 1976 and 2016 to address this issue. The different types of sintering methods can be seen below.

2.5.5.1 Hydrothermal reaction sintering

Hydrothermal Reaction Sintering (HRS) is a highly effective method for producing ceramic materials with very high relative density. According to Equation 2.4, the reaction between highly pure metal powder or chips and water at a specific temperature (500-1000°C) and pressure (100 MPa) leads to the formation of sintered metal oxide (MeO) and hydrogen (H_2) gas [74].

$$Me + H_2O \longrightarrow MeO + H_2 \quad (2.4)$$

The H_2 gas leaving the system induces the reaction to proceed more efficiently, resulting in better compression of the component.

Hirano and Somiya [75] demonstrated a method for producing pure chromium oxide (Cr_2O_3) tablets using chromium (Cr) powder, as illustrated in Figure 2.25a. The process involved mixing chromium powder and water, which were then placed in a platinum capsule. The capsule was sealed with an electric arc and placed in a test tube pressure vessel (Figure 2.25b). Applying a pressure of 98 MPa at 1000°C for 3 hours resulted in a relative density of 99.2%. The sintered specimen had an average grain size of 10 μm with a range of 3 μm. Figure 2.26 shows a scanning electron micrograph of the fracture surface of the specimen, which mostly occurred through grains with typical brittle fracture cleavage steps and river patterns.

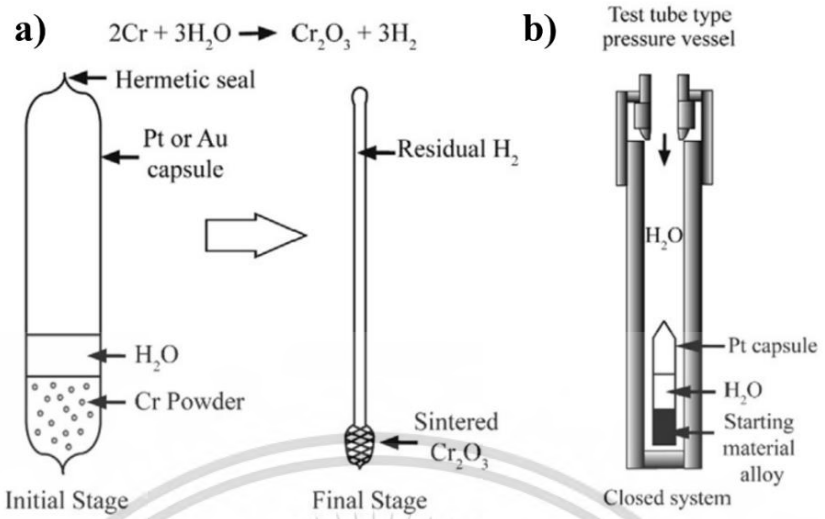

Figure 2.25 a) HRS stages of Cr_2O_3, and b) apparatus used for hydrothermal reaction sintering [74].

Figure 2.26 shown scanning electron micrograph of fracture surface of pure Cr_2O_3 specimen sintered under hydrothermal conditions, 1000 °C, 100 kg/cm^2, 3h [75].

2.5.5.2 Hydrothermal hot pressing

Hydrothermal hot pressing (HHP) [76] is a process for sintering inorganic powders under hydrothermal conditions but at lower temperatures (below 500 °C) compared to HRS. HHP is similar to the natural process of lithification in geology, as the processing temperatures are as low as those seen in geological environments. It can also be referred to as a geo-mimetic process. For HHP to be successful, two prerequisites must be met. Firstly, the sample needs to be compacted under hydrothermal conditions. Secondly, there should be a way for water to escape. Compression helps to pack the initial powder, preventing the development of shrinkage cracks. The speed at which water is removed from the powder mixture affects compaction. Without a way for water to escape, it remains in the pores and prevents densification. The final density achieved in HHP depends on processing temperature, pressure, time, and the amount of water used. The schematic drawing of the HHP equipment and the autoclave detail are shown in Figure 2.27a and b, respectively.

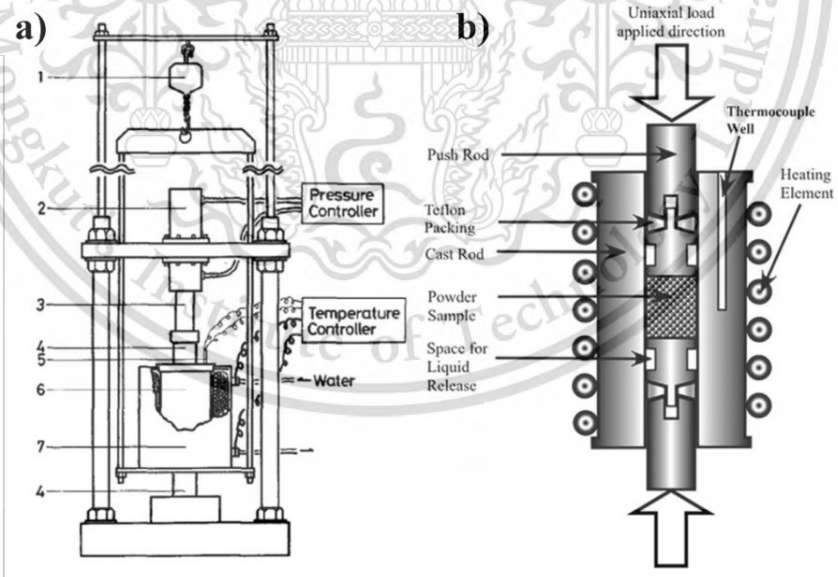

Figure 2.27 shown a) HHP equipment details 1: crane for adjusting the furnace position, 2: pump, 3: ram, 4: autoclave push rod, 5: thermocouple, 6: autoclave, 7: induction furnace [77]. b) hydrothermal hot pressing autoclave [78].

The first application of HHP was conducted on a mixture of α-quartz and amorphous silica. After the addition of NaOH, including aqueous solutions, the blend was pressed under 180 MPa pressure. The sample was then placed in an autoclave which was heated in between 120 and 350 °C under 27 MPa pressure for 30 min [77]. In other studies, $CaCO_3$ and, subsequently, TiO_2 were formed. In the process, TiO_2 (800 nm average particle size) was mixed with water, placed in an autoclave, and compressed by the push rod to 200 MPa pressure while heated to 350 °C for 30 min. The shape of the $CaCO_3$ powder surface showed some change after hot-pressing. The original shape of the $CaCO_3$ powder remained in an experiment consisting of only preliminary compression at ambient temperature (Figure 2.28a). the shape of the $CaCO_3$ hot-pressing at 200 °C (Figure 2.28b). the shape of the $CaCO_3$ powder surface became smoother and rounder after hot-pressing at 300 °C, and the formation of necks and deformation of some particles were also observed (Figure 2.28c).

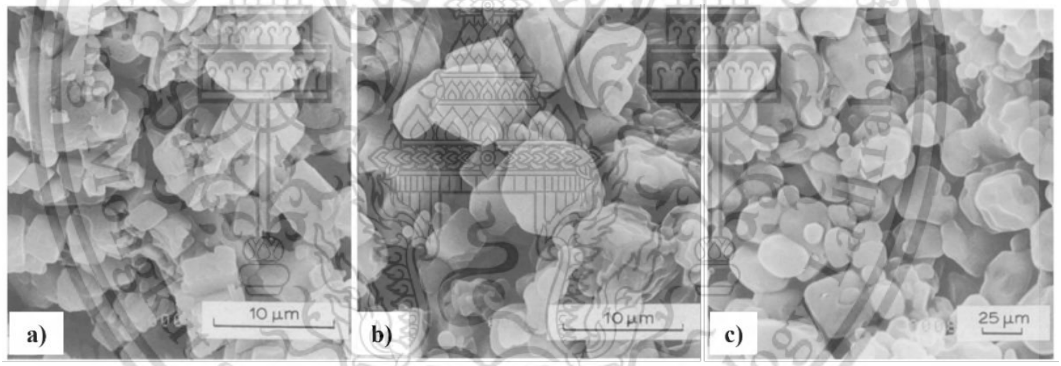

Figure 2.28 Scanning electron micrographs of a) fractured surface of compressed starting sample, and HHP sample at b) 200 °C and c) 300 °C [79].

2.5.5.3 Spark plasma sintering

Spark Plasma Sintering (SPS) is a sophisticated powder metallurgy technique used to consolidate powders into dense materials with tailored microstructures and enhanced properties. In SPS, a pulsed direct current and pressure are applied

simultaneously to the powder compact. This process facilitates rapid heating due to the joule heating effect, which occurs when an electrical current passes through the powder bed, generating localized heating at the particle interfaces. The simultaneous application of pressure ensures uniform densification and helps to eliminate porosity. SPS offers advantages such as shorter processing times, lower sintering temperatures, and the ability to process a wide range of materials, including ceramics, metals, and composites, making it a versatile technique in materials science and engineering. The working principle of the spark plasma machine (Figure 2.29) is to fill the powder of material into the graphite crucible. The direct current power supply system directs a direct current pulse through the specimen to rapidly heat it up while the pressure system applies pressure through the graphite core to the workpiece. Therefore, the specimen is obtained with high density in a short time by using lower temperatures than traditional sintering.

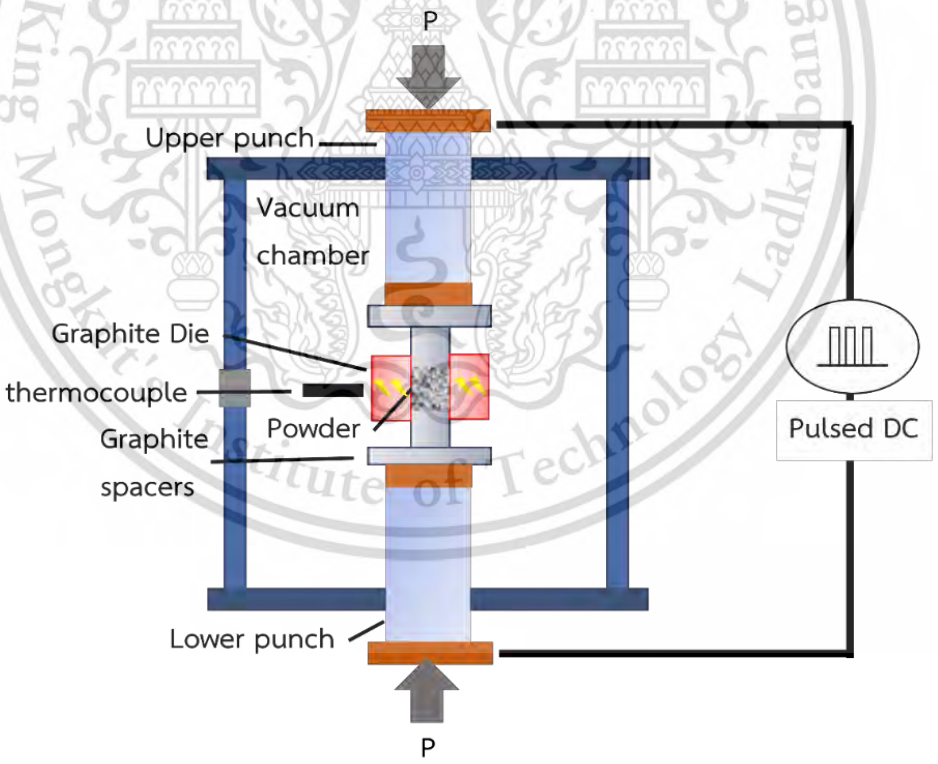

Figure 2.29 shows a typical SPS system (modified form [80]).

Compared to traditional sintering methods, Spark Plasma Sintering (SPS) offers significant advantages, including much shorter sintering times (typically 1-20 minutes per cycle) and lower sintering temperatures (approximately 200-500°C). These lower temperatures contribute to better material properties compared to traditional methods. However, challenges arise during specimen forming, which can be quite complex, and although the sintering temperature can be reduced, there may still be limitations in achieving significant reductions [81].

The structure depicted in Figure 2.30a-d illustrates a titanium alloy (Ti-6Al-4V) reinforced with nanoscale TiN particles. The sintering process occurred at a temperature of 1,100°C, under a pressure of 50 MPa, and with a heating rate of 100°C/min under vacuum conditions. In Figure 2.30a, the alternating alpha and beta phases are evident in the pure alloy. In contrast, the alloy reinforced with nanoscale TiN particles exhibits a relatively homogeneous distribution of TiN particles throughout the titanium alloy matrix, achieved during plasma spark sintering [82].

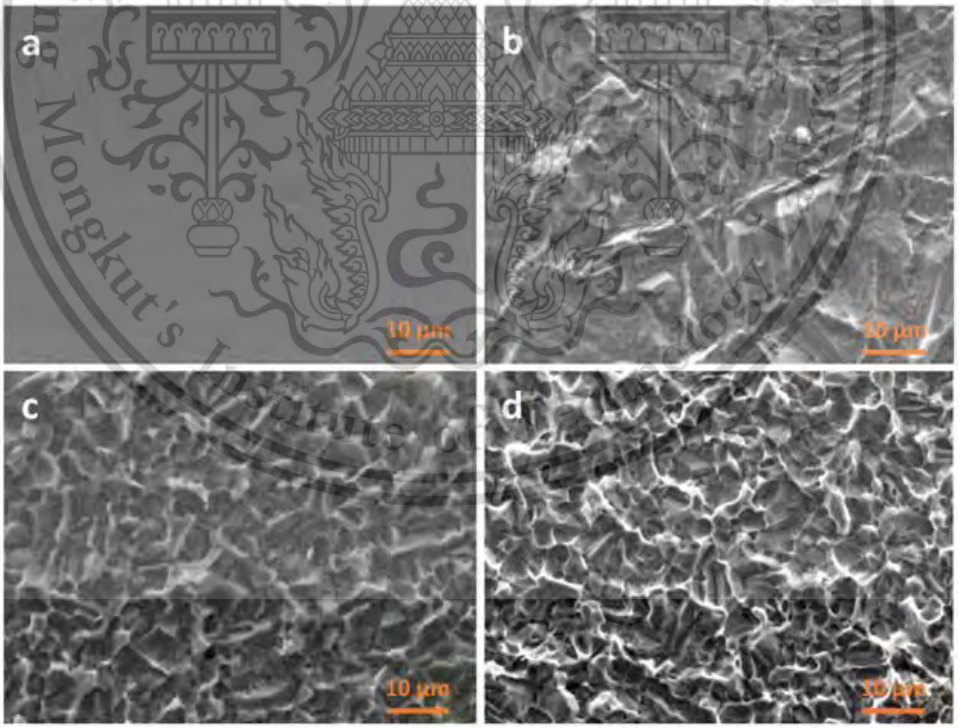

Figure 2.30 shows the structure of a titanium-based sintering compound with TiN nanoparticles. a) pure titanium alloy (Ti-6Al-4V) does not contain TiN particles, b) 2%Vol TiN, c) 4%Vol TiN, and d) 6%Vol TiN [82].

Aluminum-silicon carbide composites with ratios of 50% and 70% were fabricated using a plasma-sintering process at a temperature of 600˚C, under pressures of 50 and 80 MPa, with a heating rate of 100˚C. The structure post-sintering is depicted in Figure 2.31, revealing an even distribution of silicon carbide particles serving as reinforcement, without agglomeration due to the particles of the reinforced phase. The particles exhibit nearly the same size as the matrix material, particularly noticeable in composites containing 70%wt silicon carbide. However, some porosity or gaps may be present, and chipping of silicon carbide particles can occur, potentially due to specimen preparation regardless of pressure and compaction [83].

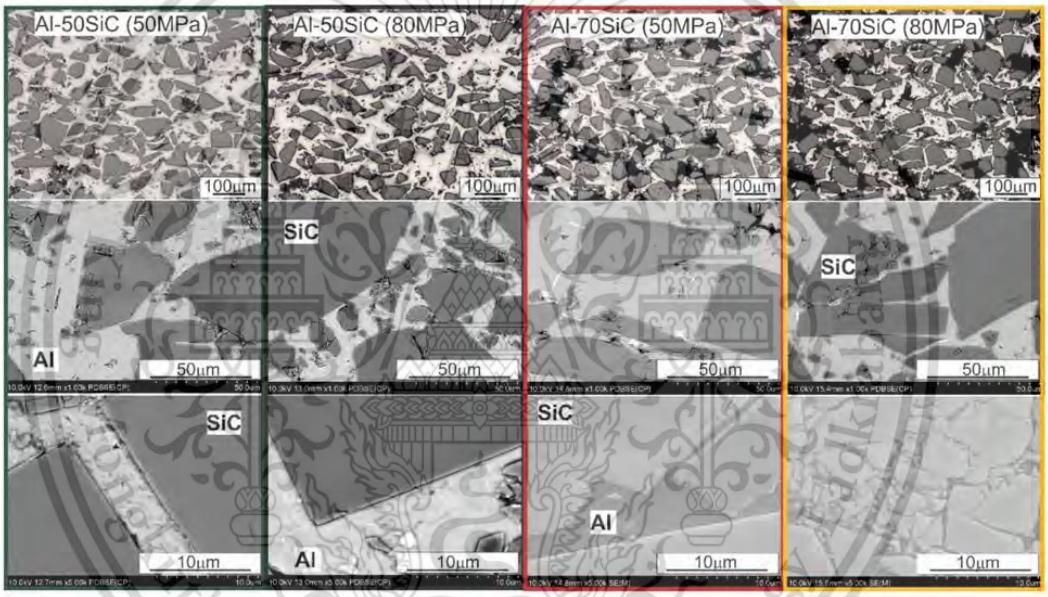

Figure 2.31 illustrates the microstructure of aluminum-silicon carbide composites post-spark plasma sintering, featuring compositions of 50wt% and 70wt% silicon carbide[83].

2.5.5.4 Microwave sintering

Microwave sintering (MW) is an advanced processing technique used to consolidate powders into solid materials by applying microwave radiation as the primary source of heat. This method operates on the principle of electromagnetic radiation in the microwave frequency range (typically 300 MHz to 300 GHz) interacting with the material being sintered. During microwave sintering, the material is exposed to microwave radiation, which penetrates the material and rapidly heats it volumetrically. Unlike conventional heating methods that primarily heat the material's surface, microwave radiation can heat the material from within due to the interaction with polar molecules or ions present in the material. This volumetric heating leads to uniform temperature distribution throughout the material, promoting rapid and efficient sintering. The main component of a microwave sintering process, as shown in Figure 2.32, is the microwave sintering furnace. It includes a microwave generator to produce radiation, a waveguide system to direct the radiation, a sintering chamber where materials are placed, temperature control systems, cooling mechanisms, and safety features. These components work together to efficiently sinter materials using microwave radiation, offering advantages such as faster heating rates and improved material properties [84].

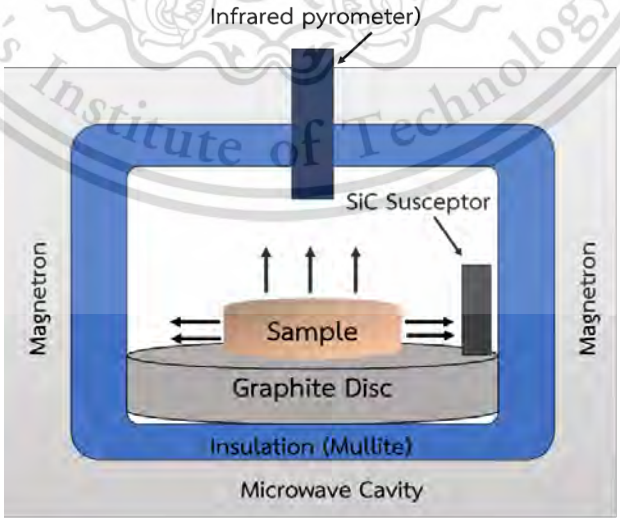

Figure 2.32 shows sketch of the microwave sintering process (modified from [85]).

Hirofumi Takahashi et al. [86] conducted a study on the piezoelectric properties of $BaTiO_3$ ceramics using hydrothermally synthesized $BaTiO_3$ powders with nanoscale-size particles, densified through microwave sintering. The SEM microstructures (Figure 2.33 a-c) depict specimens fabricated by a) hydrothermal synthesis and microwave process (H-MW), b) hydrothermal synthesis and conventional process (H-CV), and c) solid-state reaction and CV process (S-CV). The H-MW specimens, sintered at 1,320˚C with a heating rate of 600˚C/h and maintained for 30 minutes, exhibit the smallest average grain size. Notably, the maximum piezoelectric constant d_{33} value observed for specimens processed via microwave sintering reaches 350 pC/N.

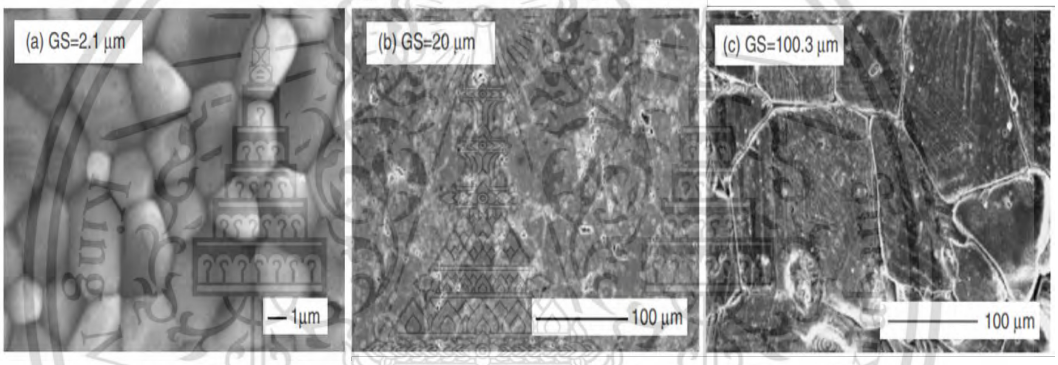

Figure 2.33 shows SEM micrographs comparing the microstructures of specimens produced by different processes: a) hydrothermal synthesis with MW, b) hydrothermal synthesis with CV, and c) solid-state reaction with CV. [86].

S.D. Ramarao et al. [87] conducted research on the microwave sintering and microwave dielectric characteristics of $ZnWO_4$ ceramic compounds. They sintered $ZnWO_3$ ceramic pellets in both a normal resistive heating furnace and a multi-mode microwave furnace. The research team sintered the samples at 1,100 ˚C for 1 h, 2 h, and 3 h to understand the impact of the duration of microwave sintering. These samples were identified as ZnW-MS-1h, ZnW-MS-2h, and ZnW-MS-3h respectively. Figure 2.34 shows the microstructure of both conventionally sintered (ZnW-CS) and

microwave sintered $ZnWO_4$ compounds. It is evident from the figure that the microwave sintered compounds (ZnW-MS-1h, ZnW-Ms-2h, ZnW-MS-3h) have a uniform, smaller grain size in comparison to the conventional sintered compound (ZnW-CS). The average grain size of the microwave sintered compound is smaller than that of the conventionally sintered compound, indicating that the microwave sintered compound has a lower and more uniform grain size distribution than ZnW-CS.

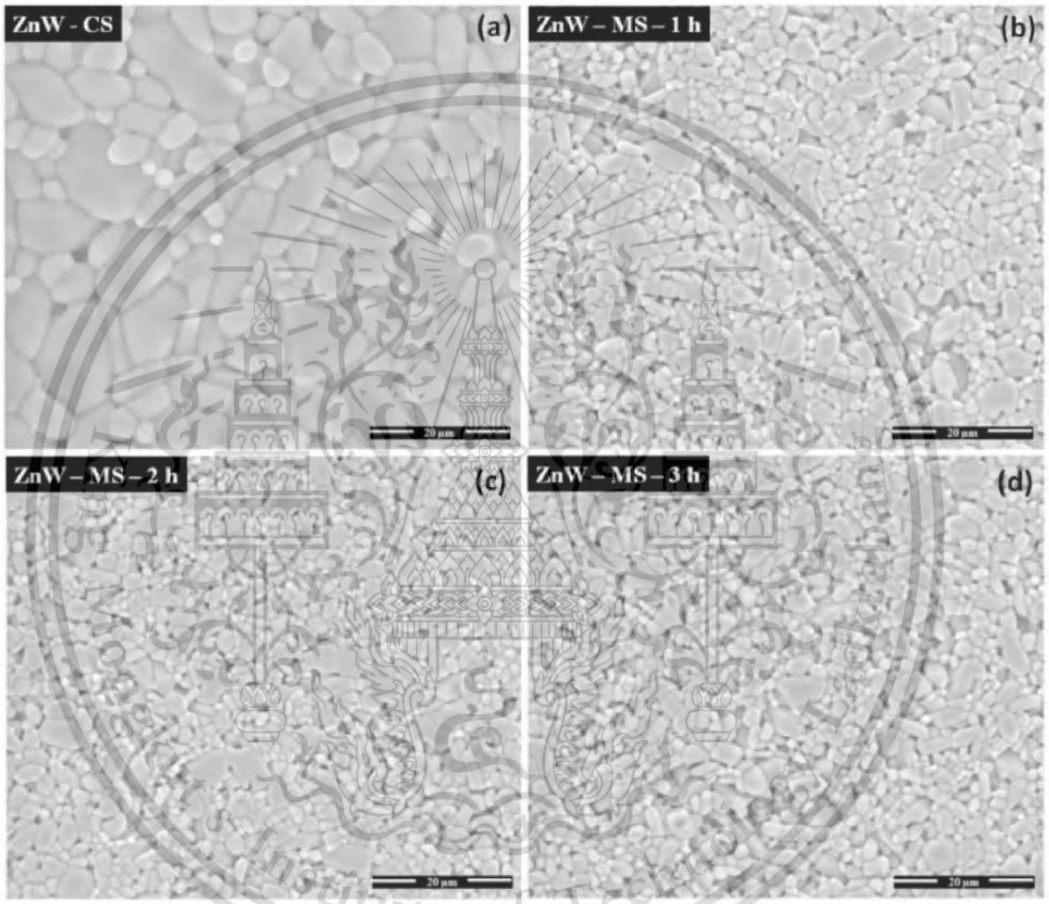

Figure 2.34 depicts the surface morphology of $ZnWO_4$ compounds, comparing conventional sintering a) with microwave sintering b), c), d). Microwave sintered compounds exhibit a more uniform grain distribution and smaller grain size compared to conventionally sintered ones. [87].

2.6 Cold Sintering Process (CSP)

Cold sintering process or CSP is a new process that is instead of the traditional sintering process. Such processes still require high temperatures due to the slow solid state diffusional processes, or high temperature needed to form a liquid. Therefore, CSP has become a new alternative and demonstrates for the first time that a wide range of inorganic materials and ceramic-based composites can be sintered at much lower temperatures than previously thought possible by using either an acidic or basic aqueous solution as a low-temperature solvent for the solution-precipitation process.

CSP can be defined as the process where an inorganic powder is densified in the presence of a transient typically between 1 and 10 vol%. During cold sintering, the liquid phase becomes the medium for mass transport. Water is the most common cold sintering liquid; many other organic and ionic liquids can be used depending on the solubility of the materials. The moist powder is subsequently loaded into a conventional pellet die to which mechanical force and heat are applied. Pressures and temperatures typically span the range between 100 and 500 MPa and room temperature to 300 °C, respectively. The details of CSP mechanism are described below.

2.6.1 Mechanism of CSP

The mechanism of CSP is depicted in Figure 2.35, consisting of two stages. At stage I, the homogenized ensembles the powders were added with a liquid phase, which can be water or water with volatile solute [15, 88]. The liquid phase serves as a lubricant and smooths the particle surface. The added liquid is beneficial to particle rearrangement as it partially dissolves sharp particles edges, leading to spaces for particles sliding. The densification at this stage is mainly through the external pressure (i), where the liquid phase readily redistributes itself and fills into particle interstitials. Accordingly, this early stage of sintering results in the initial particle compaction, contributing mostly to the total sample shrinkage (S_1).

Next, stage II begins at the solid-solid interface, involving dissolution at intergranular interfaces and mass transport through diffusion. Here, the ion dissolved from the particles diffuse through the water film, causing gradual dilution of solute concentration away from the solid surfaces. Subsequently, precipitation occurs in pores and lead to neck growth at grain-grain interstitials. As a result, the sample undergoes a slight shrinkage. When the temperature and time are raised, the liquid volume is substantially reduced. Once precipitation is completed, the number of particle-particle contacts is significantly increased; crystal growth may occur via the coalescence of small crystallites into relatively larger ones. Notably, the crystal growth stages are strongly dynamic in nature, being driven by water evaporation and a supersaturated liquid at the temperature right above its boiling point. This triggers a large chemical driving force for the solid and liquid phases to reach an equilibrium state. Accordingly, temperature and time play a crucial role in this stage, as they enhance solubility while speeding up dissolution and grain growth. During the grain growth state, the initial grain undergoes a gradual and controlled increase in size, influenced by factors such as temperature and time. Throughout this process, the average size transitions from an initial value of D_0 to the final value of D_1. The densification rate varies with temperature, initially rising rapidly before becoming constant. The densification process may slow down at high temperatures due to evaporation [89, 90].

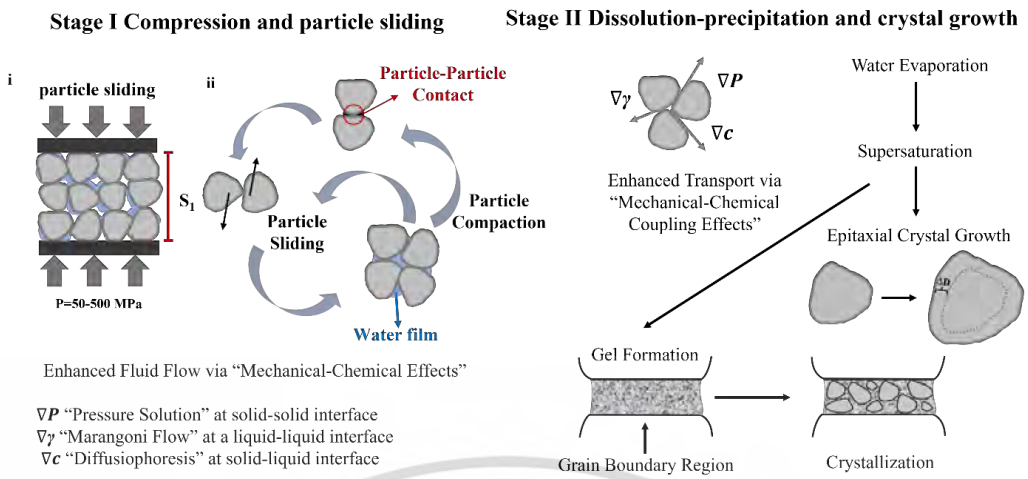

Figure 2.35 Schematic illustration of microstructure and major mechanisms during the Cold Sintering Process. (modified from [14]).

From the CSP stages above (Figure 2.35), since a liquid phase is introduced into the solids at this stage, three types of interfaces are hence considered here:

1. Pressure solution or liquid-enhanced creep at the solid-solid interface, performance-enhancing liquid creep is generally related to dissolution at the inter-grain interface and diffuse mass transport. The dissolution occurs at the contact between grain-grain with solute dispersed along the water film, and then it will precipitate into the pores space and fill into the grain-grain interstitials. The pressure dissolution should take place in the particle ensembles, since the particle-particle contacts become more prevalent under applied pressure, especially in the materials with limited or negligible solubility.

2. Marangoni flow at the liquid-liquid interface. The Marangoni effect was first realized in the phenomenon of "tears of wine" in 1855 [91]. From the fluid flow perspective, it describes a mass transport along the liquid-liquid interface due to a surface tension gradient between them; this surface tension gradient can arise from a gradient of chemical concentration or a gradient of temperature. In a fixed temperature environment, the dissolving of materials takes place at the water film layer close to

the solid surface. Marangoni flow could be generated by a concentration gradient, where the solute concentration in the aqueous solution gradually dilutes as it moves away from the solid surface. Additionally, the above-mentioned or==pressure enhanced dissolution between grains could be another source to yield a concentration gradient, in which case a local nonuniform solute distribution is manifested at the particle-particle contact region.

3. Diffusionphoresis at the solid-liquid interface. Diffusiophoresis describes the transport of colloidal particles driven by a chemical concentration gradient of solute, and it does so by producing a slip velocity at the solid-liquid interface to drive colloids migrating through fluids. Generally, there are two types of diffusiophoresis: electrophoresis, involving electrolyte systems, and chemiphoresis, in nonelectrolyte systems. In the case of electrophoresis, the particle movement is caused by a spontaneous electric field, whereas for chemiphoresis the transport is driven by a pressure gradient across the particle owing to particle-fluid interactions, such as repulsive steric exclusion or attractive van der Waals interaction.

In thermodynamics, the wet particle compact and its ambient surroundings form an open system. As the temperature is raised, the subsequent dissolution-precipitation and crystal growth stages are primarily governed by a strong dynamic process that is created through water evaporation that enables a supersaturated state of the liquid phase at a low temperature right above the boiling point of the liquid, triggering a large chemical driving force for the solid and liquid phases to reach an equilibrium state. Specifically, two possible routes could be adopted to serve the same purpose.

1. The first one takes place through direct precipitation, where ionic species and/or atomic clusters diffuse into the liquid and then precipitate on crystal sites with lower chemical potential, as they are thermodynamically more favorable. The mass transport during this process minimizes the excess free energy of the surface area and removes surface and porosity as the material forms a dense solid. Simultaneously, the shape of the crystallite accommodates when the epitaxial crystal growth proceeds: a

rounded configuration is generally manifested when the liquid phase is prevalent, while polyhedron with flat facets is normally developed when the volume of liquid is substantially reduced. Once a thorough precipitation is done, the particle-particle contacts are significantly increased, and further Ostwald Ripening crystal growth may occur via the coalescence of small crystallites into relatively larger ones if the dynamic driving force is still strong enough to trigger this process.

2. The second route is taken in a step manner, where a metastable glass phase or intermediate compound is formed to bridge the initial solutes and final product. This process is well known in geochemistry and is referred to as Oswald Step Rule. Under this process, a supersaturated solution often nucleates an amorphous phase with least stable state, especially when its nucleation rate is larger than that of the more stable phases; and then the target crystal is achieved through a recrystallization of the glass phase. This route offers an alternative pathway to lower the free energy of the system, but it also creates metastable phases that may limit the desired driving force for crystallization, since the grain-boundary diffusion activity is significantly suppressed by the viscous amorphous phase. However, this problem can be solved by heating it to help crystallize it or the growth of the crystal.

The precipitation process is largely affected by the mass transport, hence enhanced transport via above-mentioned mechanical-chemical effects (namely pressure dissolution, Marangoni effect, and diffusiophoresis transport) should also contribute to the precipitation or crystal growth stage.

At the CSP can produce dense ceramics at substantially reduced temperatures, the requirement for Gibbs free energy reduction in the ceramic ensemble system during CSP should be less compared to that in conventional sintering routes as show in Figure 2.36. CSP is performed in a multistep manner; for each step, the free energy barrier is relatively lower and could be easily overcome with the assistance of various mechanical-chemical coupling effects or hydrothermal reactions.

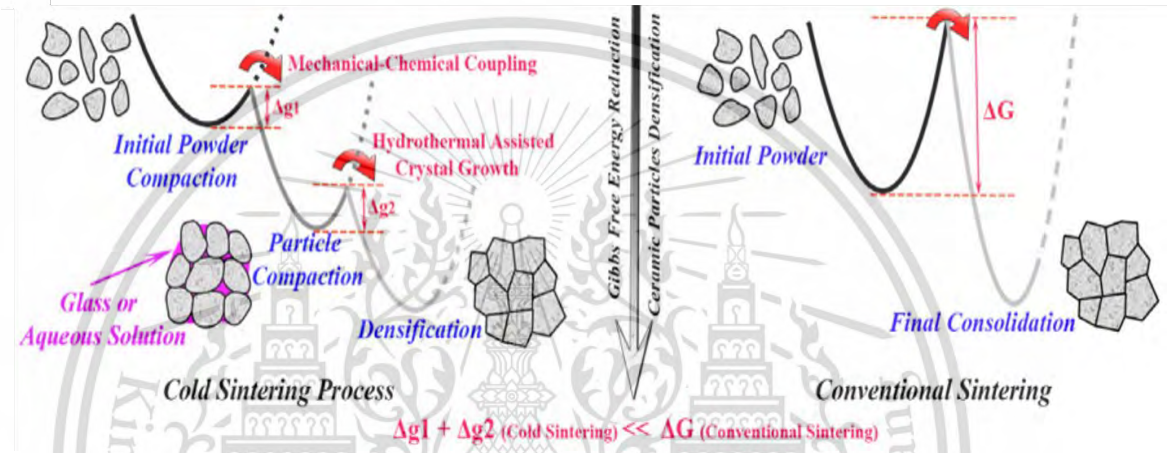

Figure 2.36. Corresponding Gibbs free-energy evolution compared to conventional sintering [14].

2.6.2 Related High-density Materials using CSP.

The Cold Sintering Process (CSP) offers versatility in terms of the types of materials that can be processed. Some of the materials commonly used in CSP include: 1) Ceramics: CSP has been applied to various ceramic materials, including oxides (such as alumina, zirconia, and titania), nitrides (such as silicon nitride), and carbides (such as silicon carbide). CSP enables the consolidation of these ceramic powders at much lower temperatures compared to conventional sintering methods. 2) Polymers: Polymer-based materials, such as thermoplastics and elastomers, can also be processed using CSP. The low processing temperatures of CSP are particularly advantageous for polymers, as they prevent thermal degradation and enable the

incorporation of temperature-sensitive additives or reinforcements. 3) Composites: CSP has been used to fabricate composite materials by combining ceramics, polymers, metals, or other materials. These composites can exhibit tailored properties, such as enhanced mechanical strength, thermal stability, or electrical conductivity, depending on the combination of constituents and processing parameters. 4) Biological Materials: CSP has shown promise in processing biological materials, such as proteins, enzymes, and nucleic acids, which are typically sensitive to high temperatures. By using mild processing conditions, CSP allows for the fabrication of biomaterials with preserved bioactivity and functionality. 5) Functional Materials: CSP has been explored for the fabrication of various functional materials, including piezoelectric ceramics, ferroelectrics, thermoelectric materials, and photocatalysts. The ability to process these materials at low temperatures enables the retention of their unique functional properties. 6) Glass and Glass-Ceramics: CSP has been applied to the consolidation of glass and glass-ceramic materials, offering advantages such as improved transparency, tailored microstructures, and reduced processing costs compared to conventional glass-forming techniques. Overall, the versatility of CSP allows for the fabrication of a wide range of materials with tailored properties and functionalities. This makes CSP a promising technique for various applications, including electronics, energy storage and conversion, biomedical devices, and environmental remediation. Table 2.3 lists various materials for which CSP is used that have different mechanical and electrical functions after CSP.

Table 2.3 displays several complex oxide that are available through the Cold Sintering Process (CSP). [92]

Binary Compounds	Ternary Compounds	Quaternary Compounds	Quinary Compounds
MoO_3	Li_2CO_3	$LiFePO_4$	$LiAl_{0.5}Ge_{1.5}(PO_4)_3$
WO_3	$CsSO_4$	$LiCoPO_4$	$Li_{0.5x}Bi_{1-0.5x}Mo_xV_{1-x}O_4$
V_2O_3	Li_2MoO_4	KH_2PO_4	
V_2O_5	$Na_2Mo_2O_7$	$Ca_5(PO_4)_3(OH)$	
ZnO	Li_2WO_4	$(LiBi)_{0.5}MoO_4$	
Bi_2O_3	Na_2WO_4		
C_5Br	$BaTiO_3$		
MgO	Na_2ZrO_3		
PbTe	$Mg_2P_2O_7$		
Bi_2Te_3	Cs_2WO_4		
NaCl	KPO_3		
ZnTe	$Ca_3Co_4O_9$		
$CuCl_2$	$BaMoO_4$		

In 2016, much research studied the CSP and successfully applied it to various materials as follows.

1. The CSP of sodium chloride (NaCl) [92], NaCl powder was compressed using a uniaxial compressor with a 12.5 mm of die with a pressure of 5 MPa. At room temperature sintering kinetics of a 55% dense NaCl compact held at either 75% or 85% relative humidity (RH) for up to 24 h as shown in Figure 2.37a. The salt samples densify from 55% to 69% in 5 h and to 90% relative density after 24 h in 75% RH air. The sample sintered at room temperature and 85% RH densify to 64% and 90% density after 2 h and 10 h, respectively, the microstructures of the 90% dense at RT sintered NaCl consist of grains of approximately 20 to 30 μm in average size as show in Figure 2.37c, d. The grain growth is like that observed in many liquid phase thermally sintered ceramics because of the high solubility and long holding time. In Figure 2.37b, they

compare the densification kinetics of NaCl when thermally sintered at 600 °C and 700 °C. Even though these samples were heated at 600 °C and 700 °C they are only 84% dense after 50 min and 10 min, respectively. The microstructure shows little grain growth relative to the initial NaCl powder around 3 μm because of the large amount of porosity in Figure 2.37 e, f. With high aqueous solubility at room temperature, salts like NaCl can easily densify with a small fraction of uniformly distributed water, thus demonstrating the power of the proper solvent for cold sintering. In the case of sparingly soluble materials, like ceramics, the cold sintering temperature and pressure are raised to enhance solubility and the process of densification.

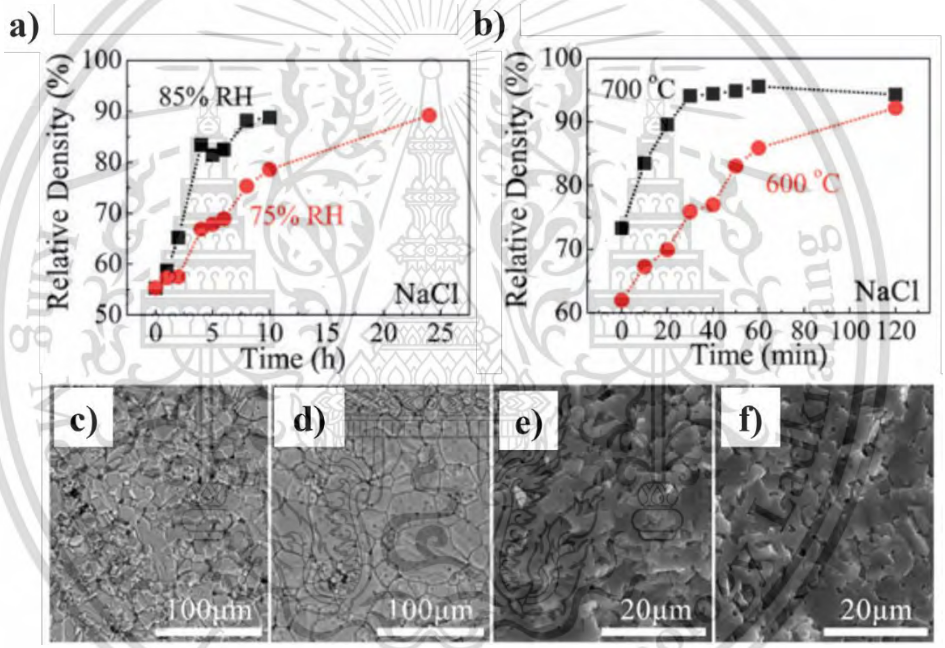

Figure 2.37 Comparison of relative densities of ≈ 3 μm diameter NaCl under a) cold and b) conventional thermal sintering conditions. Microstructures of NaCl sintered at c) room temperature and 75% relative humidity (RH) for 24h, d) room temperature and 85% relative humidity for 10 h, e) 600 °C for 50 min, and f) 700 °C for 10 min [92].

2. The CSP of Sodium Nitride ($NaNO_2$), $NaNO_2$ powder was mixed with 7 wt% of deionized water for 1-2 min and then uniaxially pressed under 350 Mpa at 120 °C for

1 min to 3 h in a steel die to achieve dense pellets. The die was preheated at 120 °C more than 1 h before hot pressing. The as-prepared ceramic pellets were then baked at 120 °C for 6-12 h to remove possible water residue. They found the cold-sintered $NaNO_2$ ceramics reach a 98% relative density [14].

3. The CSP of potassium hydrogen phosphate (KH_2PO_4) [14], the CSP was performed at a temperature of 120 °C right above the boiling point of water, with the assistance of an external uniaxial pressure of 350 MPa. Figure 2.38 displays the density evolution of cold-sintered KH_2PO_4 ceramics as a function of cold sintering time. It is interesting to notice that highly dense ceramics, >98% of relative density, can be even achieved in an extraordinary short time of 1 min. After a mechanical polishing, the cold-sintered pellet looks semi-transparent (image inset). Correspondingly, the SEM image of the fractured surface also demonstrates a dense micromorphology (micrograph inset).

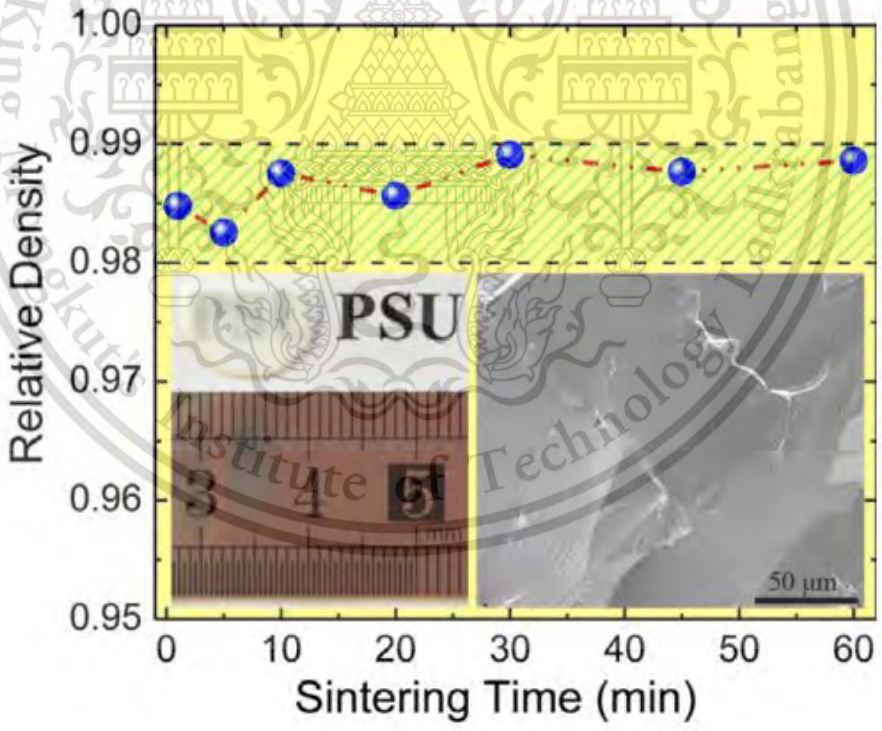

Figure 2.38 Density evolution of KH_2PO_4 as a function of Cold Sintering time at 120 °C and 350 MPa. The inset shows a photograph of the cold-sintered transparent KH_2PO_4 with a thickness of 0.43 mm, as well as a SEM micrograph for the dense micromorphology. A theoretical density of 2.338 g/cm^3 was adopted for KH_2PO_4 [14].

4. The CSP of barium titanate ($BaTiO_3$) [14], $Ba(OH)_2/TiO_2$ suspension was made by mixing corresponding chemical with deionized water. Ba $(OH)_2/TiO_2$ suspension 25wt% was added to $BaTiO_3$ nanoparticles. The mixtures were ground using pestle and mortar. The mixture was uniaxially pressed under 430 MPa first at room temperature for 10 min, and then the temperature was ramped up to 180 °C with a rate of 9 °C/min. The temperature was isothermally kept for 1 min to 3 h to obtain a series of samples. The as-prepared ceramic pellets were first baked at 200 °C overnight to remove possible water residue, and then further annealed at 700 °C-900 °C for 3 h with a temperature ramp rate of 5 °C/min in air. Figure 2.39 shows the densification curve as a function of cold sintering time, the bulk ceramics with up to 90% relative density are achieved after isothermally sintering the ceramics at an extraordinarily low temperature of 180 °C for a short time of 30 min. On the other hand, the $BaTiO_3$ ceramics are prepared via the conventional thermal sintering route where dense solids are generally obtained at much higher temperatures of 1,200 °C-1,400 °C for several hours. After annealing the corresponding ceramics cold sintered at each time interval, another densification curve is obtained and has been found to exhibit a similar tendency with the cold sintered one. The density is slightly improved by a few percent and the presented densification curves clearly indicate that this hydrothermal-assisted CSP is feasible to obtain dense ceramic solids, and the resulting density is decisive to the final density after heat treatment.

In the case of desiccants such as NaCl, $NaNO_2$, and KH_2PO_4, the structure of these substances can easily react with water. For this reason, the solution-precipitation process can occur easily. However, for substances with low solubility, water cannot be used as a solvent, such as $BaTiO_3$. Therefore, it is necessary to select the solution appropriately to occur in the solution-precipitation process. In this work, we will choose gamma-glycine and will discuss it further.

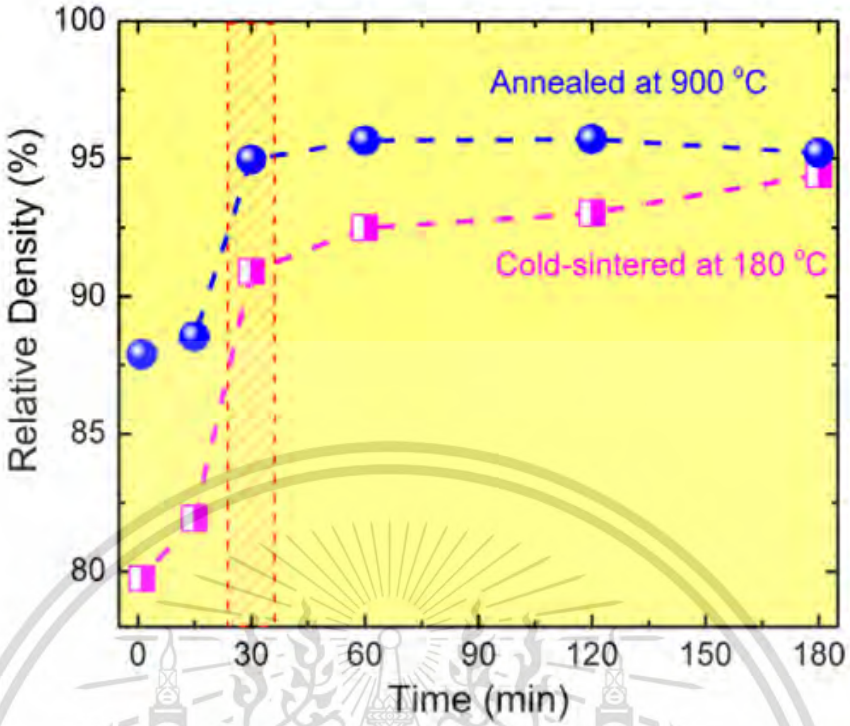

Figure 2.39 Density evolution of cold-sintered and subsequently annealed $BaTiO_3$ ceramics as a function of cold-sintering time [14].

2.7 Amino acid

Amino acid is a biomolecule that has both amino and carboxyl functional groups as components. Amino acids are the building blocks of protein, the building blocks that are present in all living things. Proteins have different biological functions, such as being enzymes and hormones that help speed up reactions within living things. These properties depend on the type and sequence of amino acids in a protein. In general, an amino acid structure formula consists of as amino group at the alpha position of the carboxyl group and a side chain or R substituent, which is different in each type of amino acid [93].

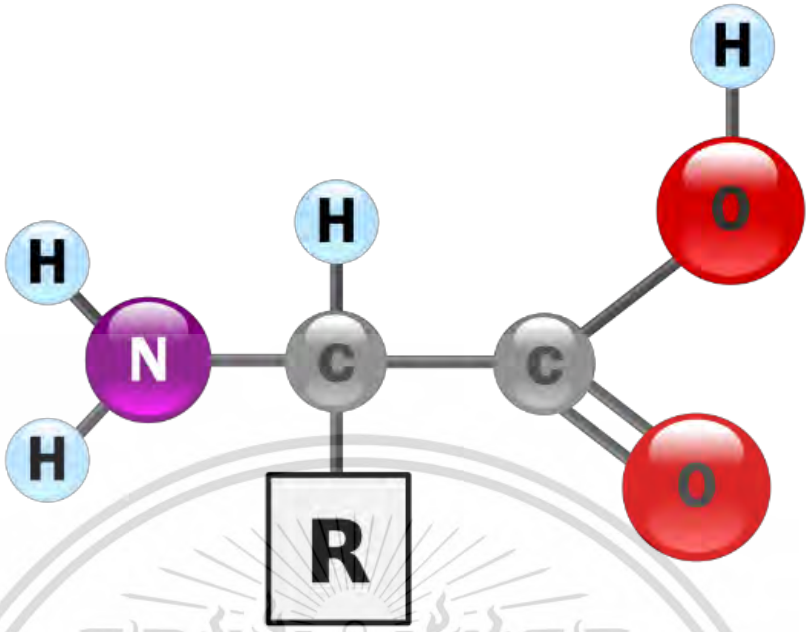

Figure 2.40 General structural formula of amino acids [94].

The structure of amino acids (Figure 2.40) consists of base amino groups and acidic carboxyl group. In aqueous solution at pH close to neutrality, amino acids exist as zwitterions, i.e., as dipolar ions with both NH_3^+ and CO_2^- in charged states. Thus, the overall structure is NH_3^+-CHR-CO_2^-.

2.8 Glycine

Glycine is the simplest amino acid, both in terms of its chemical structure and its role in biological systems. Glycine is extensively utilized in various domains including biological functions, food and beverage production, pharmaceuticals, cosmetics, and industrial processes. However, its application in electronics is somewhat limited. Although it demonstrates promise in areas such as dielectric materials, semiconductor doping, surface passivation, and bioelectronics, challenges such as limited conductivity and compatibility with electronic materials impede its widespread adoption. Additionally, concerns arise regarding glycine's biological origins and potential interactions with electronic components, impacting device reliability and long-term stability. Nonetheless, ongoing research endeavors aim to leverage glycine's distinctive

properties for specialized electronic applications. Glycine, with the chemical formula NH_2CH_2COOH, crystallizes into three polymorphs α, β, and γ depending on crystallization conditions [21]. The metastable α-glycine (α-GC) lacks piezoelectric properties, while the unstable β-glycine (β-GC) exhibits piezoelectricity due to its non-centrosymmetric structure. Furthermore, the addition of inorganic salts like NaCl significantly enhances the secondary nucleation of the piezoelectric γ-glycine (γ-GC) while inhibiting α-GC primary nucleation, facilitated by ion-glycine interaction and the formation of linear head-to-tail glycine chains [95].

In 2012, Heredia et al. [96] reported robust and continuous nanoscale ferroelectricity in piezoelectric γ-GC for the first time. Additionally, Hu et al. [23] found that the polarization of γ-GC is about five times stronger than that of β-GC due to spirally aligned dipoles along the axis, as opposed to randomly oriented dipoles in β-GC as shown in Figure 2.41 [97].

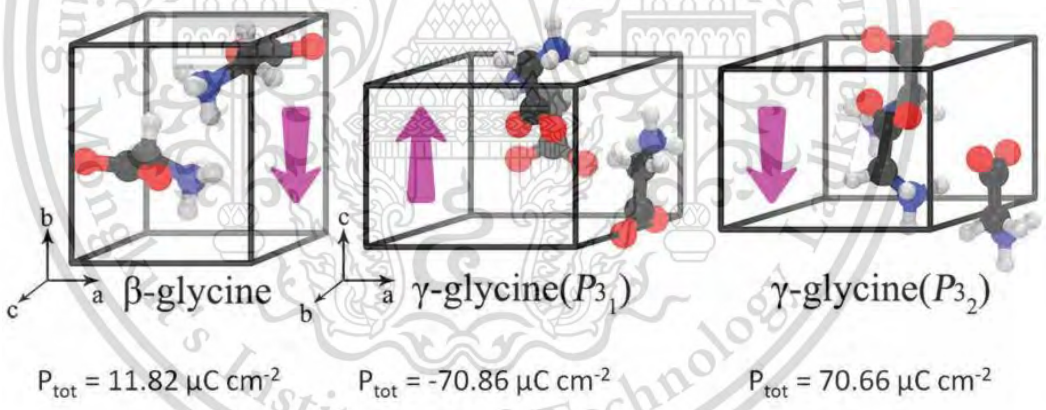

Figure 2.41 Calculation polarization and structure of β-glycine, γ-glycine (P_{31}), and γ-glycine (P_{32}) [23].

2.8.1 Effect of common inorganic salts on glycine polymorphic transformation

The formation of the thermodynamically stable γ-GC phase typically involves careful preparation methods that often include the use of acids, bases, and inorganic

salts. This process is crucial for obtaining the desired phase of glycine, as different conditions can lead to the formation of alternative phases such as α-GC or β-GC. In Inorganic salts, it was found that various monovalent cation salts (e.g., NaCl and KNO_3, which do not cause solution pH to shift) effectively induce γ-GC, while typical divalent cation salts (e.g., $MgSO_4$, Ca $(NO_3)_2$, and Mg $(NO_3)_2$) hardly induce γ-GC. Among a few studies, NaCl was particularly chosen to examine its effect on glycine polymorphic crystallization. It was observed experimentally that NaCl promotes the nucleation of γ-GC during solution-mediated transformation from α-GC to γ-GC, which was attributed to a particular salt ion-glycine ordering in solution [98].

2.8.1.1 Solution-Mediated Polymorphic Transformation

After introducing α-GC crystals into the α-GC saturated solution at 23°C, the glycine concentration in the liquid phase remained virtually unchanged, and the solid phase retained its α-GC form until the onset of secondary nucleation, initiating the formation of stable γ-GC. The induction time for γ-GC secondary nucleation was calculated based on this onset. As the process progressed, the presence of γ-GC increased while α-GC decreased in the solid phase. Eventually, α-GC disappeared entirely, and only γ-GC remained in the solid phase even before the solution concentration reached α-GC solubility, as illustrated in Figure 2.42.

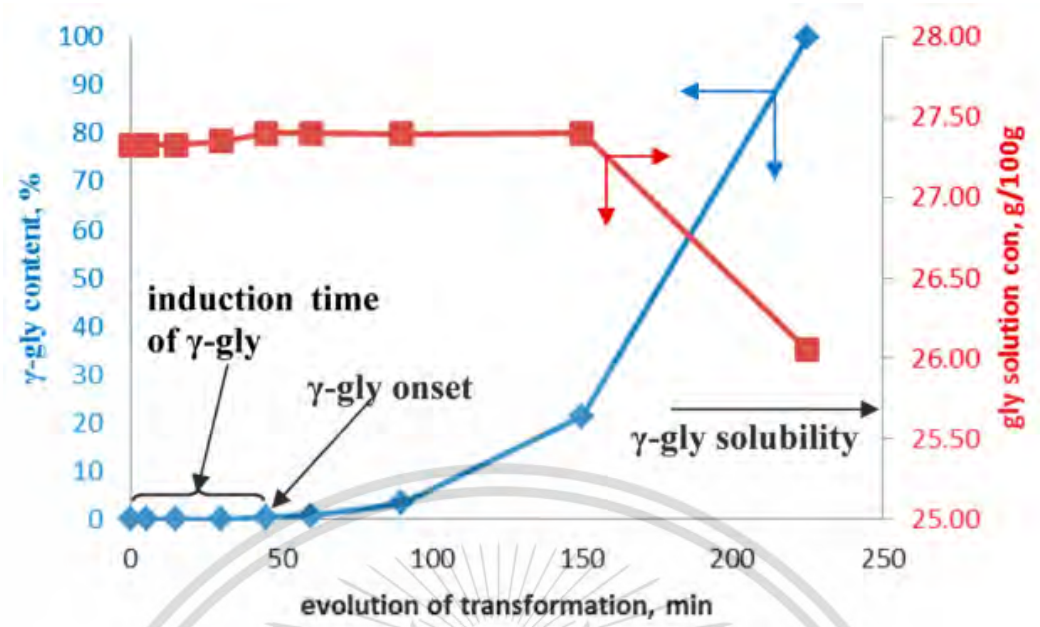

Figure 2.42 Illustration of the evolution of a typical solution-mediated glycine transformation in the presence of 2.5 m NaCl, highlighting the onset and the corresponding induction time of γ-GC secondary nucleation [98].

2.8.2 Growth of nonlinear optical γ-GC crystals

M.Narayan Bhat and S.M. Dharmaprakash [99] grew γ-GC from α-GC solution. This solution was distributed in various beakers. Pre-determined amounts of analytical grade sodium chloride (NaCl) were added to these beakers to obtain solutions having glycine and sodium chloride in the ratio 1:1 to 6:1. The resulting solution was filtered twice and then heated on a water bath maintained at constant temperature until the volume was sufficiently reduced. A small quantity of each sample was allowed to evaporate in a dish to obtain seed crystals. It was observed that the sample containing glycine and NaCl in the ratio 3:1 gave good bulk crystals of larger dimensions 12 mm x 11 mm x 11 mm with perfect external morphology in Figure 2.43.

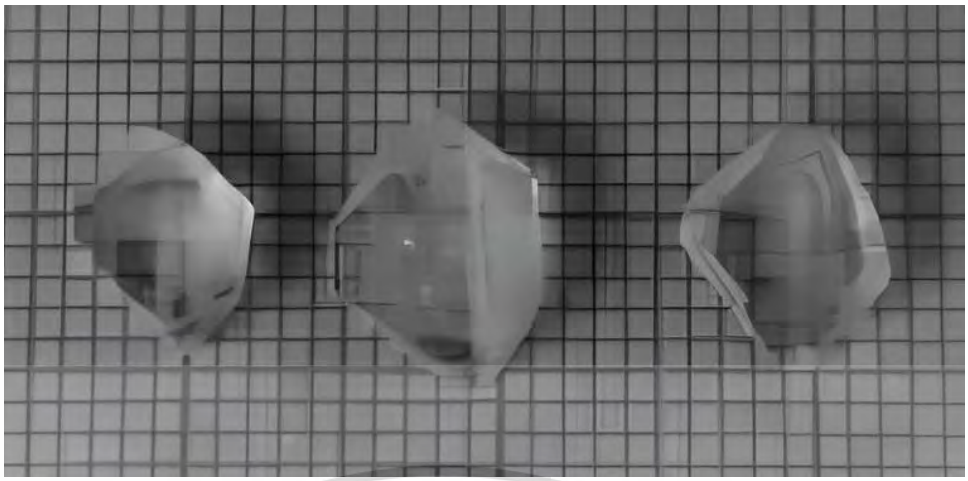

Figure 2.43 photograph of γ-GC crystal with containing glycine and NaCl in the ratio 3:1 [99].

The γ-GC crystal underwent primary characterization through chemical analysis, X-ray diffraction (XRD), and Fourier-transform infrared spectroscopy (FTIR) to determine the crystal and its phase purity. Elemental analysis of the γ-GC was done using HERAUS Carbon, Hydrogen, and Nitrogen analyzer, and the results are displayed in Table 2.4.

Table 2.4 CNH analysis of γ-GC crystal

Element	Composition (%)	
	Experimental	Theoretical
Carbon	31.80	32.05
Hydrogen	6.40	6.67
Nitrogen	18.20	18.67

The functional groups in γ-GC crystal were analyzed by the Fourier transform infrared (FTIR) technique and recorded in the range 400-4,000 cm^{-1}; the characteristic absorption peaks are observed in the range from 400 to 1,600 cm^{-1} and shown in Figure 2.44a. The peaks observed at 504.2, 607, and 694 cm^{-1} are attributed to carboxylate

groups, while the absorption peaks at 1,111, and 1,131 cm^{-1} are attributed to the NH_3^+ group. Thus, the carboxyl group is present as a carboxylate ion, and the amino group exists as an ammonium ion in γ-GC. Of the remaining peaks, those at 893 and 1,033 cm^{-1} are attributed to the CNN group, and the peak at 910 cm-1 is assigned to the CH_2 group. The XRD pattern helps to identify the phases of glycine. For γ-GC, the position of the peaks was found to be in good agreement with the data available in JCPDS files, as shown in Figure 2.44b. The highest intensity peak is at plane 110. The cell parameters were found to be a=b=7.04065 Å, c= 5.4842 Å space group $P3_1$ [100].

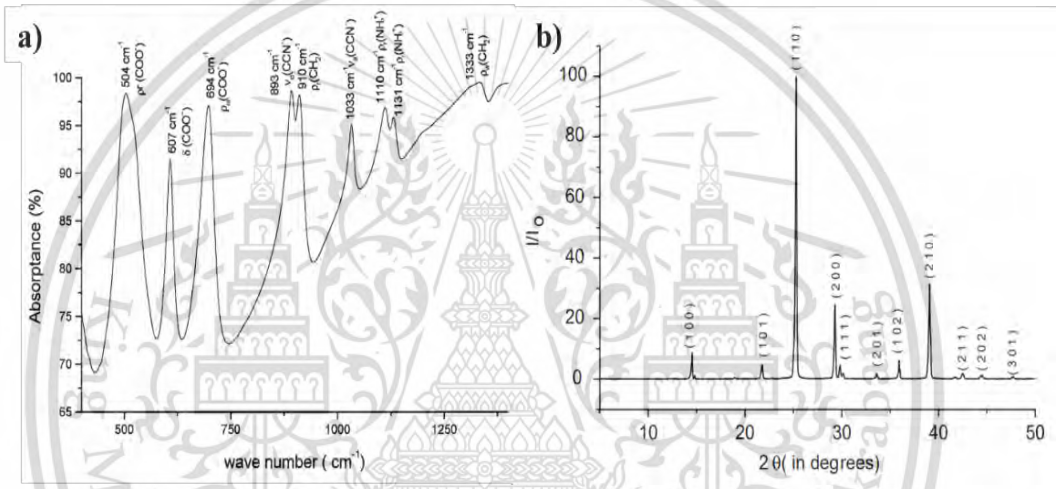

Figure 2.44 a) IR spectra and b) powder XRD pattern of γ-GC [101].

In addition, γ-GC crystals were also used to analyze the weight change of the substance based on its thermal properties via Thermogravimetric analysis (TGA). The analysis was performed under a Nitrogen atmosphere in the temperature range of 40-300 ˚C. it was found that at approximately 215 ˚C, the γ-GC crystals begin to endow heat, causing a phase change back to α-GC. When the temperature is raised to about 256 ˚C, the weight of the γ-GC crystal decreases rapidly. It results from the thermal decomposition of γ-GC crystals at that temperature. The analysis results are shown in Figure 2.45.

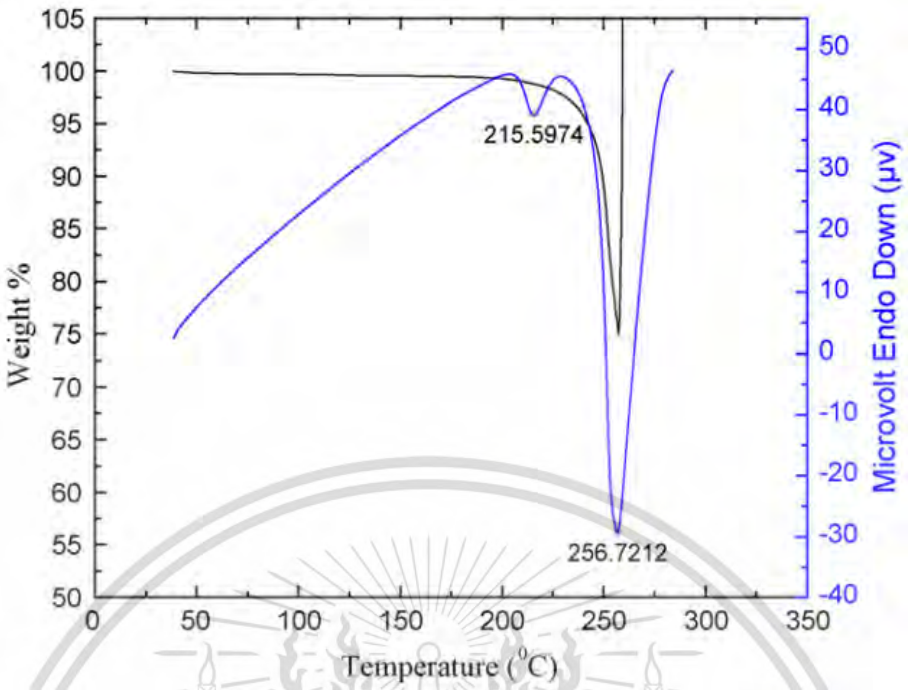

Figure 2.45 TGA/DTA curves of γ-GC [101].

2.8.3 Control of piezoelectricity in amino acids by super-molecular packing

Previous research has found that there are many other biological materials that have piezoelectric properties. As mentioned in section 2.1, piezoelectric materials are materials that can generate electric current through mechanical stress. Conversely, by applying an electric field, the material structure will be deformed. Guerin et al. [102] studied the piezoelectric properties of amino acids, and they found that out of 20 amino acids, only glycine had no chiral properties. Glycine crystallizes in three different crystal forms: α, β, and γ. The crystallization of α-GC occurs in the centrosymmetric space group $P2_1/c$, which precludes piezoelectricity. On the other hand, β-GC and γ-GC belong to the non-centrosymmetric space groups $P2_1$ and $P3_2$, respectively and so should exhibit a non-zero piezoelectric response. In addition, the density functional theory (DFT) was used to predict piezoelectric coefficients in the three ambient polymorphs of glycine. The result shown in Table 2.5 is the elastic stiffness constants calculated using DFT. It is worth noting that all but the longitudinal shear stress coefficient c_{66} computed for achiral α-GC are very similar to those of β-GC, even though

α-GC is centrosymmetric and thus non-piezoelectric. The value of c_{66} in α-GC is four times larger than that in β-GC. The computed c_{44} and c_{66} values for β-GC are relatively low, which suggests a high shear compliance and potentially high shear piezoelectricity in this polymorph. On the other hand, γ-GC shows higher values of c_{44} and c_{66} indicating a lower shear compliance. In addition, the relative permittivity of glycine polymorphs is shown in Table 2.6. The DFT-computed relative permittivity tensors of the three glycine polymorphs. The values calculated for glycine polymorphs are consistent with those of other amino acids (relative permittivity of 2.13-2.39) calculated using density functional perturbation theory (DFPT). The average dielectric constant calculated in this study is 2.5 for γ-GC.

Table 2.5 Computed electric constants of the three ambient polymorphs of glycine with and without dispersion corrections (modified from [102])

		GGA	GGA-D3
α-GC	C_{11}	53.7	49.3
	C_{22}	21.7	19.2
	C_{33}	71.5	69.7
	C_{44}	7.5	6.0
	C_{55}	16.3	15.6
	C_{66}	6.9	4.97
	Young's modulus	30	26 (33/40)
β-GC	C_{11}	55.5	69.2
	C_{22}	23.0	32.1
	C_{33}	69.3	85.4
	C_{44}	7.6	8.8
	C_{55}	15.6	18.6
	C_{66}	1.3	3.1
	Young's modulus	15	26
γ-GC	C_{11}	25.0	42.8
	C_{22}	27.4	42.8
	C_{33}	77.8	91.5
	C_{44}	12.0	16.2
	C_{55}	12.5	16.2
	C_{66}	5.4	8.7
	Young's modulus	28	49 (28/19)

Table 2.6 Computed relative permittivity and dielectric constant of the three ambient polymorphs of glycine. (modified from [102])

Polymorph	ε_{11}	ε_{22}	ε_{33}	ε_r
Alpha	2.74	2.19	2.60	2.51
Beta	2.71	2.17	2.58	2.49
Gamma	2.46	2.46	2.58	2.50

Under the influence of mechanical stress, a crystal undergoes deformation, causing ions in the crystal to shift from their equilibrium positions. This creates electrical dipole moments. For a net polarization to develop, the dipoles formed within the unit cell of the crystal must not cancel each other out. Centrosymmetric crystals such as α-GC experience symmetrical movements of ions. The dipoles in the unit cell cancel each other, resulting in no net polarization (Figure 2.46a). When a crystal lacks center of symmetry, any mechanical deformation will cause the ions to move in a non-symmetrical manner. This results in the creation of a net polarization, as shown in Figures 2.46b-e. The Figure displays molecules with their carbon, hydrogen, oxygen, and nitrogen atoms colored in cyan, white, red, and navy blue, respectively. It is worth noting that the crystallographic a, b, and c axes of the crystals have been aligned with arbitrarily chosen 1-, 2- and 3-axes, respectively.

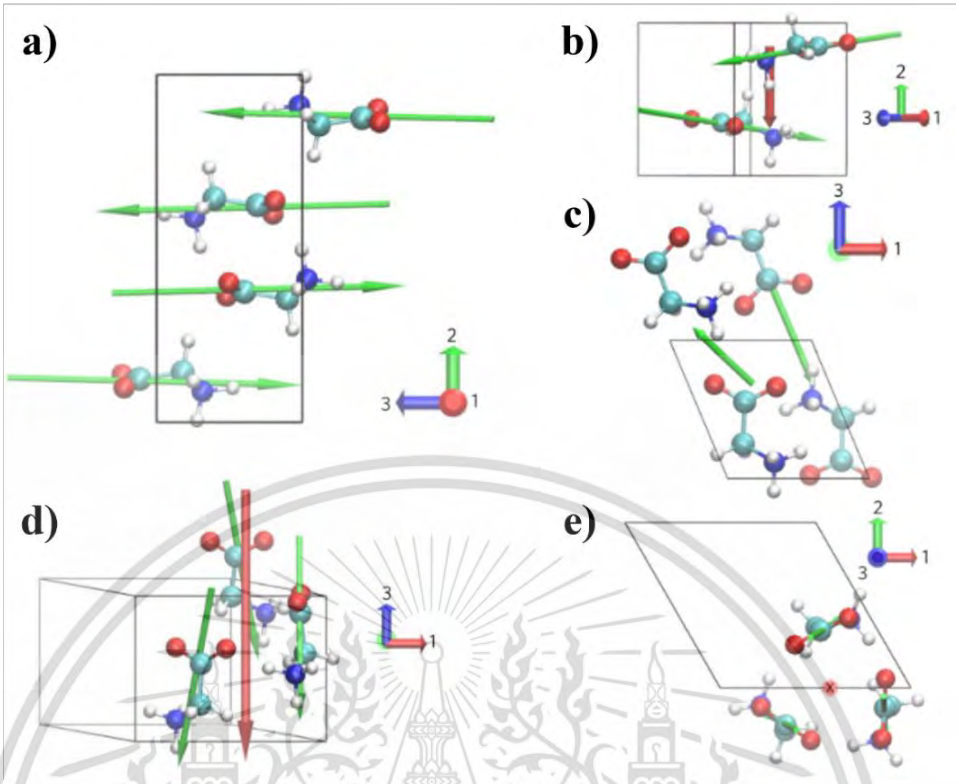

Figure 2.46 Supramolecular packing directs piezoelectric response in glycine amino acid crystals. a) Computed molecular dipoles (green arrows) in the centrosymmetric α-GC preclude piezoelectricity. The molecular dipoles in α-GC sum to zero and produce no net polarization. b) Molecular dipoles in β-GC sum to a spontaneous polarization (red arrow) along the 2-axis. c) Molecular dipoles contributing to the experimentally observed high shear piezoelectricity in β-GC. When strained in the shear plane normal to the 3-axis the distance between glycine molecules increases. d) Molecular dipoles in the unit cell of γ-GC sum (red arrow) to a spontaneous polarization along the 3-axis. e) A top-down view of the γ-GC unit cell along the [001] crystallographic direction [102].

2.9 Composite

Composite materials are fabricated from two or more constituent materials, each possessing notably disparate chemical or physical properties, which are amalgamated to yield a material with properties distinct from those of its individual components. Throughout the completed structure, the constituent elements retain their separate and discernible identities, thus demarcating composites from mere mixtures and solid solutions. A composite material comprises a matrix phase, within which the reinforced phase materials are uniformly dispersed and integrated.

2.9.1 Types of composite materials

Composites are categorized into three primary types: 1. Polymer matrix composites (PMCs), 2. Metal matrix composites (MMCs), and 3. Ceramic matrix composites (CMCs). These categories can be further subclassified based on the nature of the reinforcing agents, which include particles, fibers, and whiskers, as depicted in Figure 2.47.

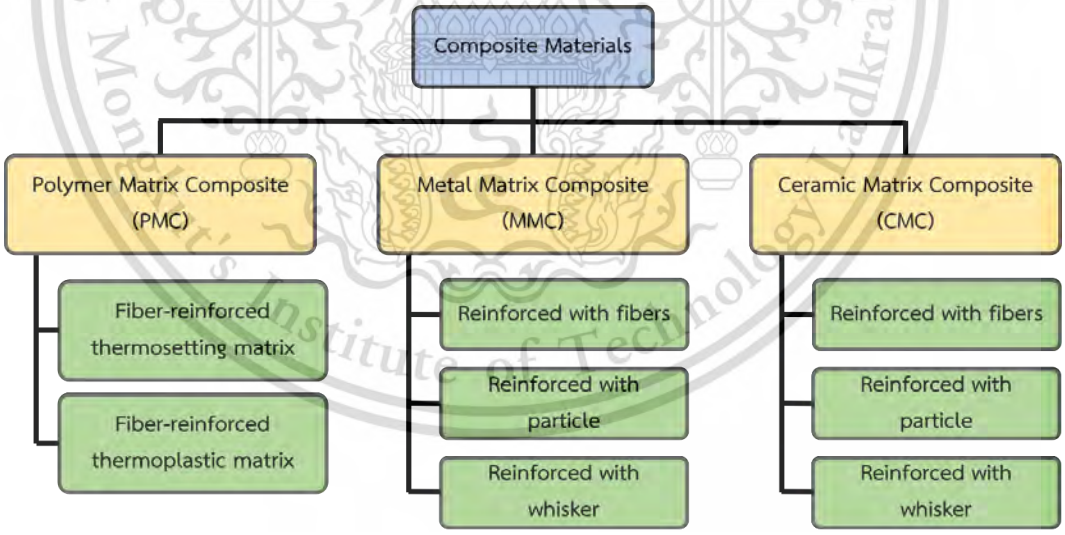

Figure 2.47 Classification of composite materials according to the type of matrix and their characteristics reinforcing substances. (Modified from [103]).

2.9.1.1 Polymer matrix composite (PMC) [104]

Polymer matrix composites (PMCs) utilize high-strength reinforcement fibers to effectively absorb and distribute forces, thereby enhancing the material's ability to withstand higher loads without deformation. This reinforcement mechanism is illustrated in Figure 2.48, depicting the basic mechanical properties of polymer composites under force application along the fiber orientation.

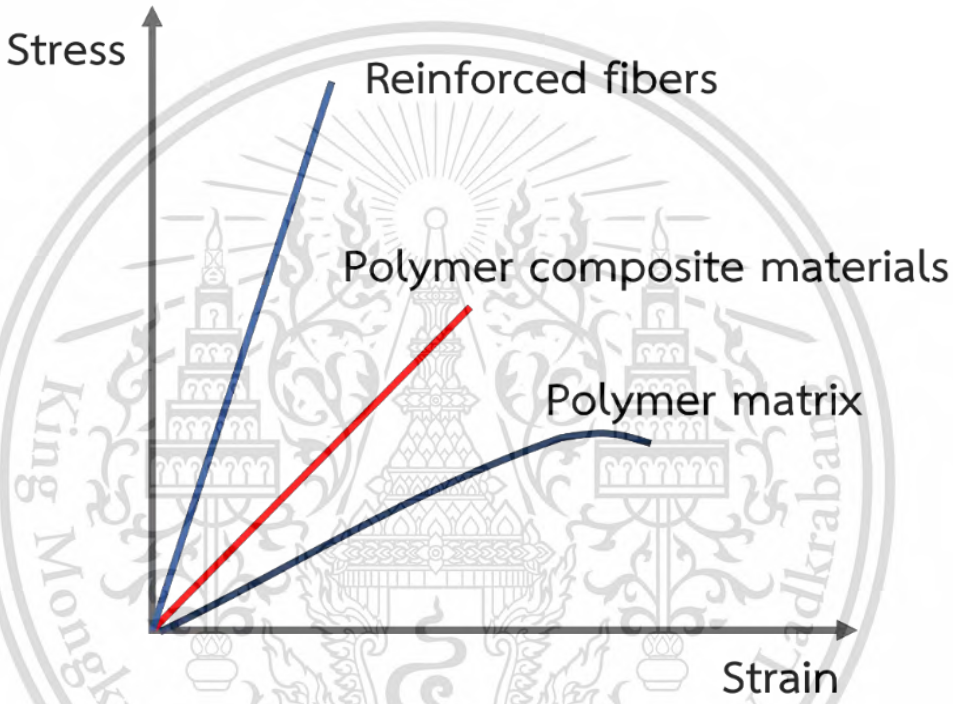

Figure 2.48 Mechanical properties of polymer composites are compared with component materials (modified from [105]).

Within the polymer matrix category, there are two primary subdivisions: thermosetting matrix and thermoplastic matrix, each exhibiting distinct thermal behaviors. Thermosetting polymers feature a crosslinked molecular structure, rendering them rigid and brittle. Conversely, thermoplastic polymers possess a linear or branched molecular arrangement, enabling them to soften and flow upon heating

beyond their melting temperature. Additionally, thermoplastics exhibit adhesive properties and demonstrate environmental durability.

2.9.1.2 Metal matrix composite (MMC) [106]

Metal matrix composites (MMCs) have been engineered to enhance the fatigue resistance of metals, notably aluminum and titanium. Reinforcement within MMCs can take the form of particles, fibers, or whiskers. It is imperative that the reinforcing agents for metals exhibit both high strength and high heat resistance, as metal fabrication typically involves exceedingly high temperatures. Furthermore, it is essential that the reinforcement materials do not induce corrosion within the metal matrix. This ensures the integrity and longevity of the composite material in demanding applications.

2.9.1.3 Ceramic matrix composite (CMC) [107]

Ceramic matrix composites (CMCs) address the inherent brittleness of ceramic materials, which are prone to fracture and lack repairability once cracks occur. The incorporation of reinforcements into the ceramic matrix significantly enhances the mechanical properties of the composite, imparting greater stiffness and durability. Reinforcements play a crucial role in mitigating crack propagation during operation, thereby preventing catastrophic failure. Utilized in various forms such as particles, fibers, or whiskers, reinforcements for CMCs encompass a range of materials including alumina, silica, silicon carbide, and carbon. These reinforcements, when combined with ceramic matrices such as cement, carbon, or silicon carbide, contribute to the overall strength and resilience of the composite material.

CHAPTER 3

EXPERIMENTAL PROCEDURES

This section explains experimental procedures used for the preparation of powders ceramic processing and characterization of γ-GC powder, BT powder, and γ-GC ceramic and γ-GC/BT composite ceramics. The characterizations of γ-GC ceramic and γ-GC/BT composite-based ceramics describe physical and electrical properties.

3.1 Chemicals

The chemical purity, solutions, and supplier of raw materials used for preparations γ-GC ceramic and γ-GC/BT composite ceramics are listed in Table 3.1.

Table 3.1 Specifications of the starting precursors and solutions used in this study.

Chemical and Solutions	Purity (%)	Suppliers
Commercial-grade glycine (NH_2COOH)	99	Sigma-Aldrich
Barium titanate	99.95	Inframat Advanced Materials, LLC
Sodium chloride (NaCl)		Carlo Erba
Nata de coco		Bifern, ASP Inter Food Co., Ltd
Absolute ethanol (C_2H_5OH)	95	Liquor distillery organization
Acetic acid solution (CH_3COOH)	99.7	J.T.Baker
Benedict solution		J.J.M.I. Co., Ltd
De-ionized water (DI water)		

3.2 Equipment

1. Beaker sizes 100, 250, 500, and 1,000 ml
2. Cylinder size 100 ml
3. Glass stirrer
4. Magnetic stir bar
5. Plastic scoop and metal scoop
6. Filter paper (Whatman, England)

7. Pressure-reducing filter
8. Weighing paper
9. Digital scale
10. Hot plate
11. Petri dish
12. Oven
13. Thermometer
14. Dropper
15. Blender
16. Centrifuge machine
17. Test tube
18. Pipette size 1 ml
19. Freeze-dry machine
20 Pestle and Mortar
21. Ball mill and ball mill grinding bottle
22. Tungsten carbide block
23. Heat jacket
24. Hydraulic press
25. Temperature controller

3.3 Powder preparation

3.3.1 Powder preparation of γ-GC

In this study, γ-GC powder was prepared using a recrystallization process by mixing glycine commercial powder 56 g and sodium chloride 15 g in 100 ml DI water. The glycine solution was stirred at 200 rpm for 5-6 h before being filtered with a

pressure-reducing filter to remove any residual sediment from the solution. Then the solution is left in an oven at 35 °C for 25 days (Figure 3.1).

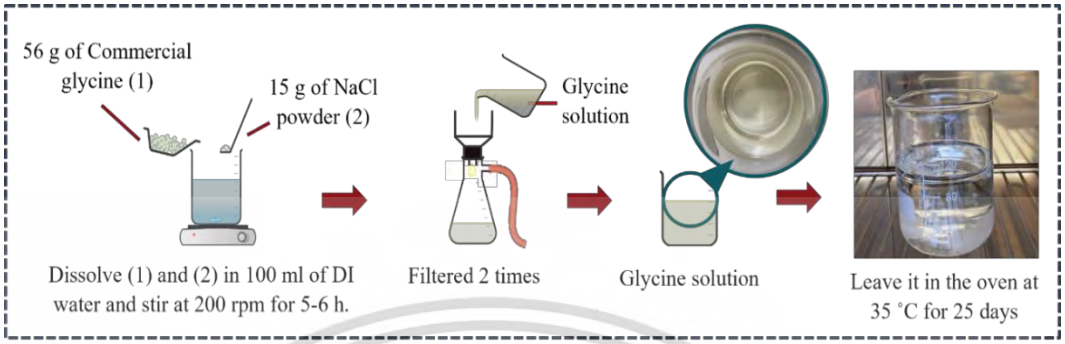

Figure 3.1 Procedure for growing gamma glycine crystals using sodium chloride.

After 25 days, remove the glycine crystal from the solution with tweezers and place it on a pressure-reducing filter to spray with a saturated glycine solution to wash the residual salt. The preparation of saturated glycine solution is shown in Figure 3.2. The glycine crystals were rinsed around 3-4 times. After washing the crystals, the crystals were placed on a petri dish and dried at 35 °C for 2 days.

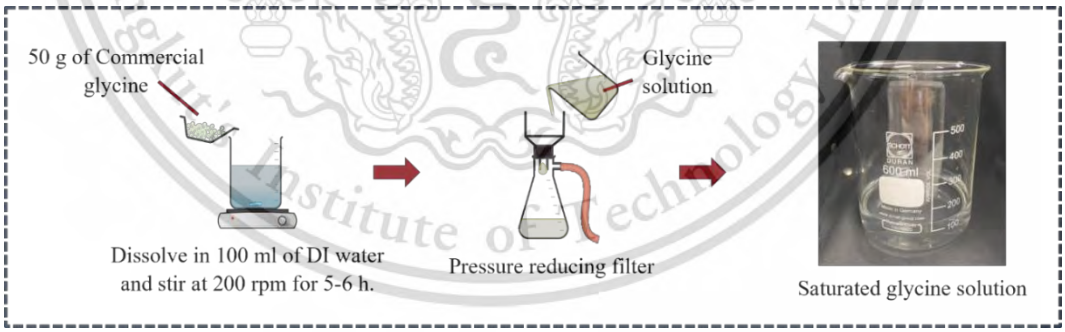

Figure 3.2 The preparation of saturated glycine solution.

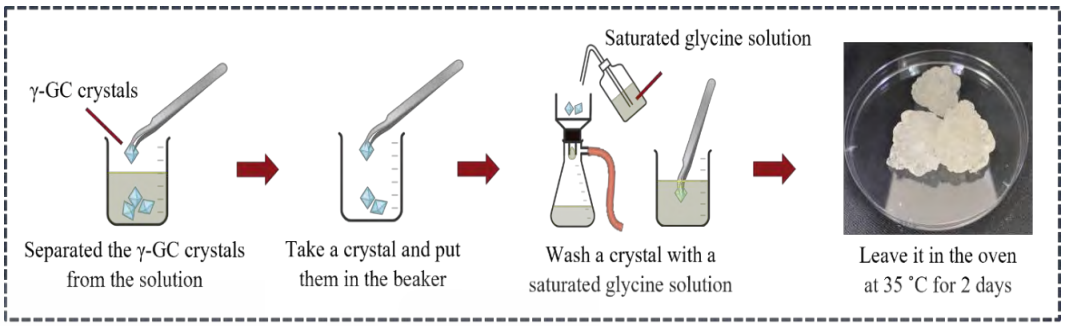

Figure 3.3 Procedure for collecting and washing γ-GC crystals.

After passing 2 days, 20 g of γ-GC crystals were coarsely ground with a pestle and mortar before the ball milling, as shown in Figure 3.3. Prepare 100 ml of 95% ethanol by volume in a cylinder and pour into a 250 ml beaker. Then, about half of the ball mill grinding was added into the ball mill bottle, and 20 g of γ-GC powder was poured into the ball mill bottle, followed by 100 ml of ethanol. The ball mill bottle was tightly closed and placed in a ball mill machine for 3 h. After 3 h, the ball mill bottle was removed from the ball mill machine, and the γ-GC powder was separated by a steel sieve, placed on a 250 ml beaker, and all the ingredients in the bottle were poured onto the steel sieve. The sieve will filter the ball mill granules, while the ethanol and γ-GC powder will pass into the bottom beaker. Use the ethanol contained in the ethanol cylinder to spray the ball mill bottle, ball mill grinding, and sieve until clean without γ-GC powder remaining. After that, the ethanol mixed with γ-GC powder

was filtered with a pressure-reducing filter to separate the γ-GC powder from the ethanol. The γ-GC powder was baked at 60 °C for 2 days.

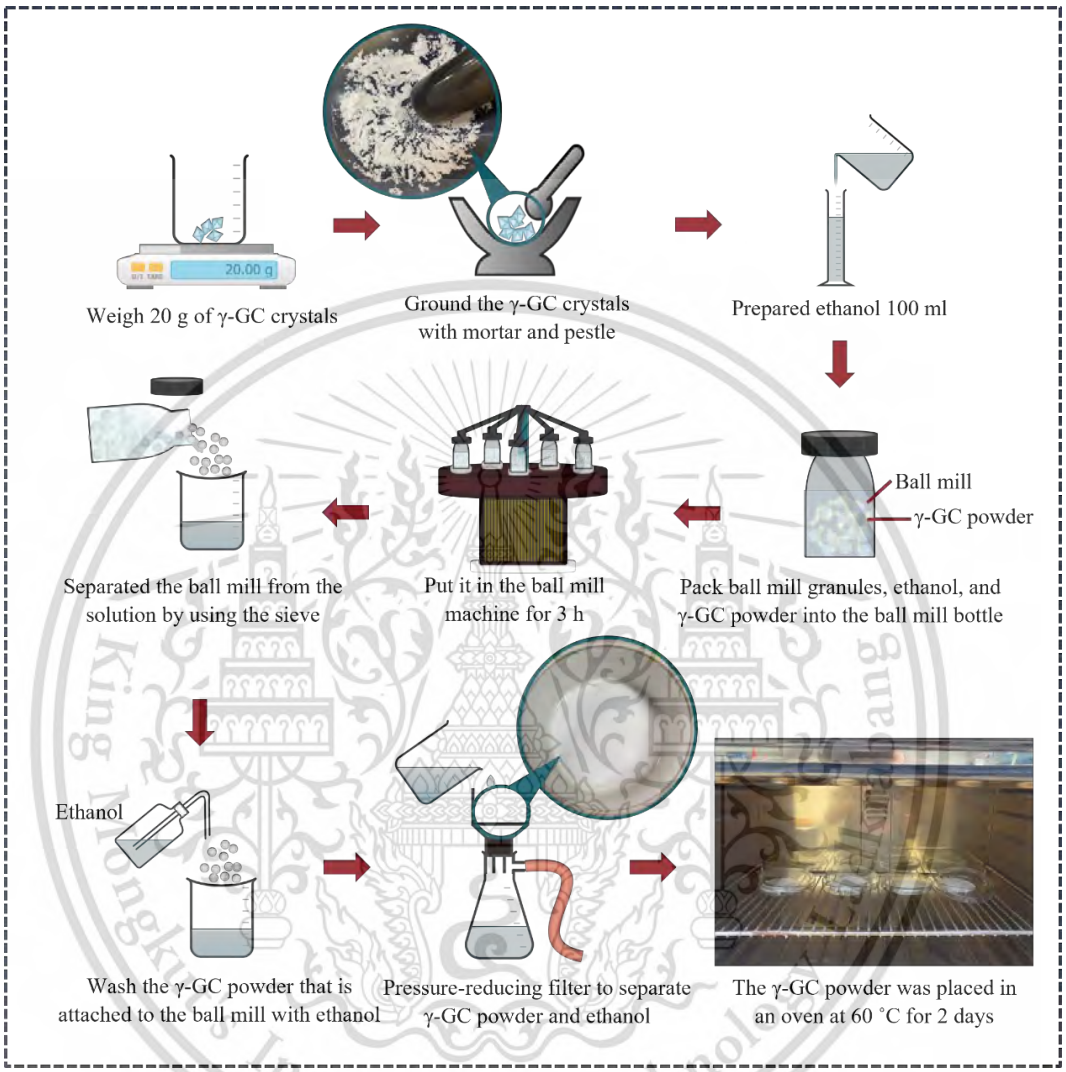

Figure 3.4 The process of grinding γ-GC crystals with a ball mill machine.

3.3.2 Powder preparation of bacterial cellulose (BC)

Take 1000 g of coconut jelly in syrup and pour into a sieve to remove coconut jelly from the syrup: rinse with DI water 3-4 times (Figure 3.5). After that, coconut jelly was boiled in DI water using a 1000 ml beaker. A magnetic stirrer was inserted into the beaker and put on the stirrer with a heat of 70-80 ˚C for 30 min. Repeat about 10-15 times. Before freeze-drying, take boiled water to sugar test with benedict in a 1:1 ratio, i.e., 1 ml of boiled water per 1 ml of benedict was pipetted into the test tube and brought to heat. Note that the benedict color must not change. If Benedict's color changes from blue to brown, coconut jelly must be boiled in DI water continuously until the Benedict test does not change color. After removing all the sugar in the coconut jelly, rest the coconut jelly until it cools down. Then, weigh 200 g of coconut jelly and blend with a blender until fine. 50 g of finely spun coconut jelly was freeze-dried at -40 ˚C for 24 h to prepare the bacterial cellulose powder.

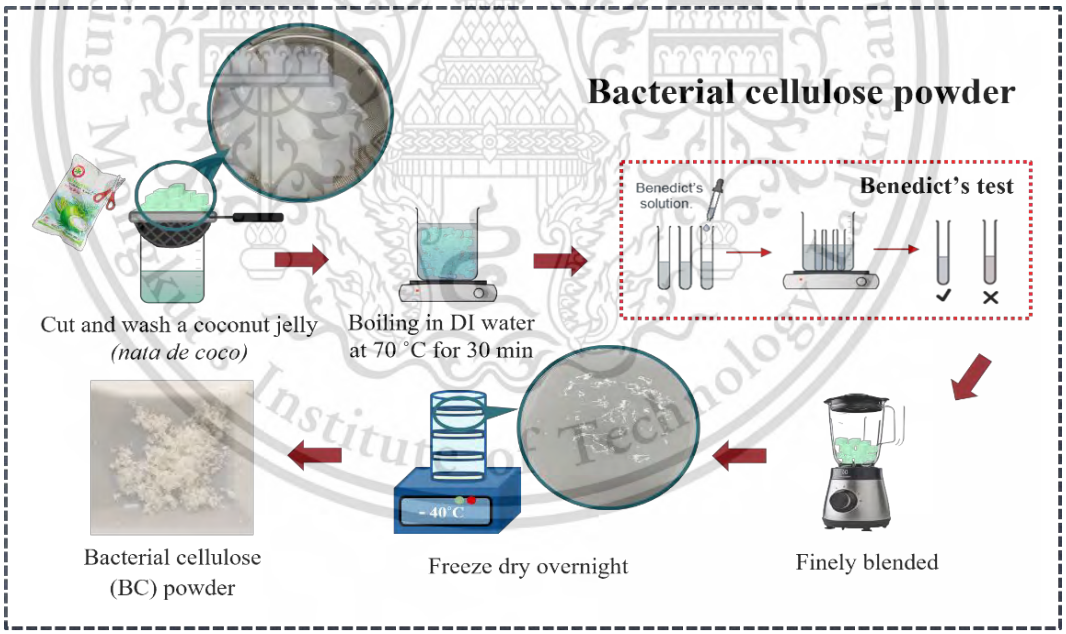

Figure 3.5 The preparation of bacterial cellulose powder with freeze-dry process.

3.3.3 Powder preparation of barium titanate (BT)

In this part, weigh 10 g of barium titanate (BT) powder commercially by weight boat, pour the BT commercial powder into the crucible, and close the crucible lid tightly before entering the muffle furnace (Figure 3.6). Next, put the crucible into the muffle furnace and heat it to 1200 °C for 12 h, 10°C/min.

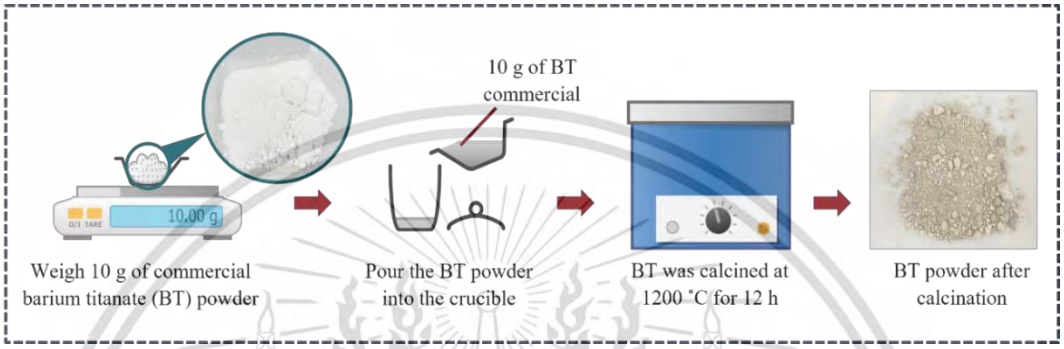

Figure 3.6 The preparation of barium titanate (BT) powder

After that, BT was prepared via acid treatment by weight BT commercial 5 g and weight BT after calcined at 1200 °C/12 h for 5 g. The acid solution was prepared by pipetting 5.73 ml of 99% by weight of acetic acid solution into a 100 mL volumetric flask and adjusting the volume with deionized water (DI water) to 100 ml, as shown in Figure 3.7.

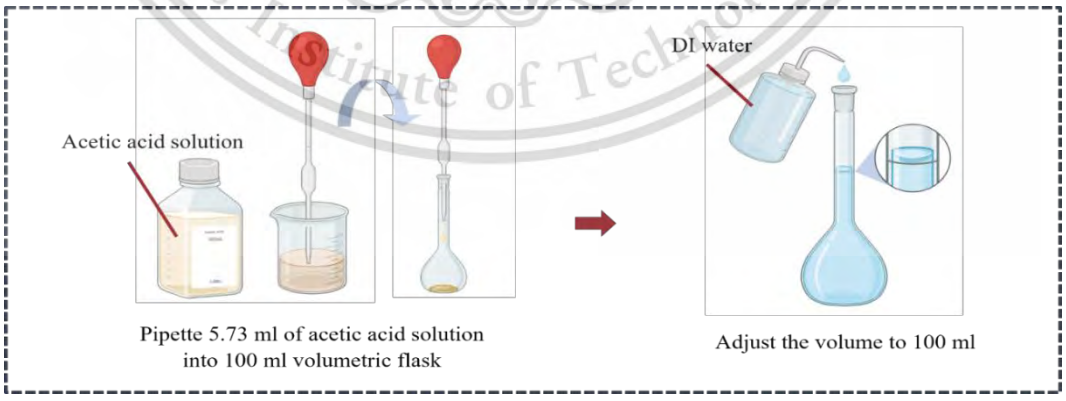

Figure 3.7 The preparation of 1M acetic acid

Pipette 25 ml of 1M acetic acid solution into 50 ml of the beaker, as shown in Figure 3.8. The acid solution was prepared in 2 lots for BT commercial and BT after calcined at 1200 °C/12 h. Then, pour 5 g of BT commercial into beaker 1 and pour 5 g of BT after calcined at 1200 °C/12 h into beaker 2 and then stir for 1 h at a temperature of 80 °C. After treatment, the BT powder was washed with DI water until the pH is neutral. Filter the solution with a pressure-reducing filter and put it in the oven at 60 °C for 24 hours before use. Before use, 3.68 g of BT calcined after acid treatment and 1.32 g of BT commercial after treatment were ground well in a mortar and grinder for 5 min, as shown in Figure 3.9.

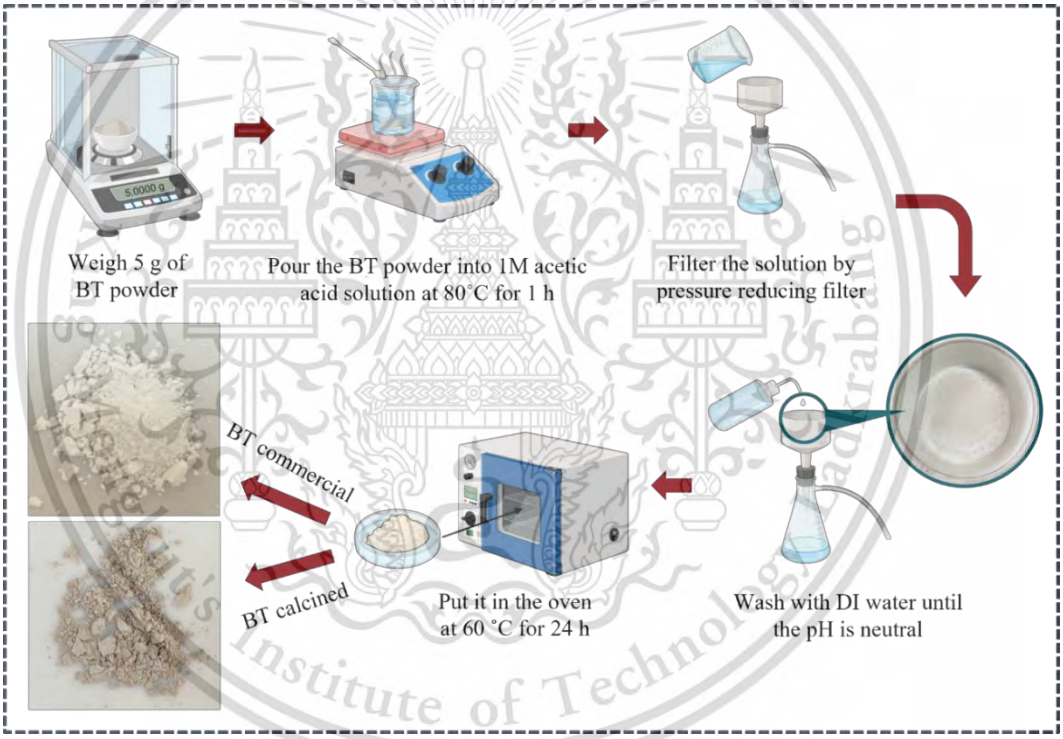

Figure 3.8 The preparation of BT powder via acid treatment.

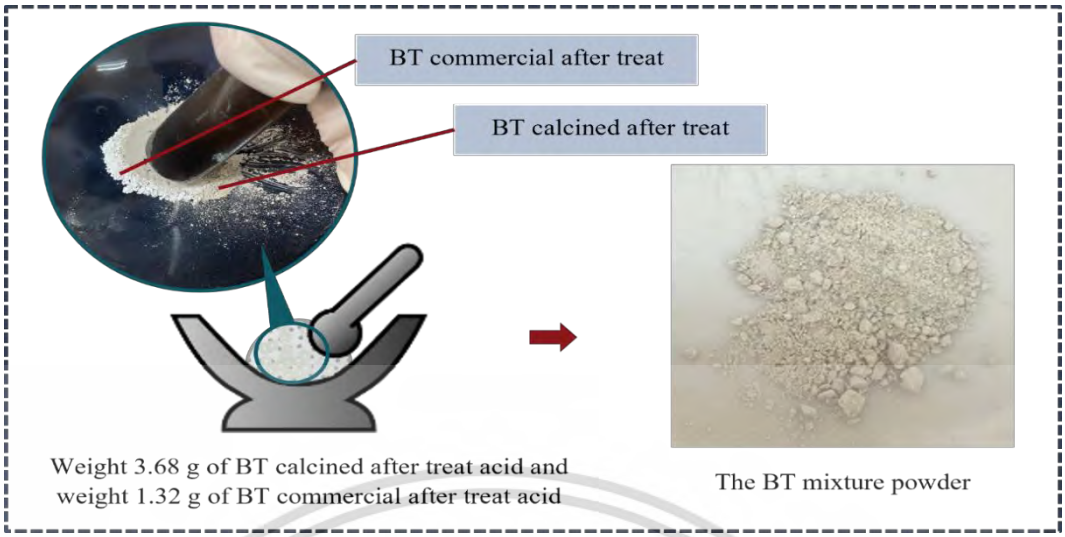

Figure 3.9 Preparation of the mixture between BT commercial and BT calcined at 1200 °C/12h after acid treatment.

3.4 Ceramic via a cold sintering process

3.4.1 γ-GC ceramics

Weight 0.9207 g (92wt%) of γ-GC powder and 0.0093 g (1wt%) of BC powder and mixed in a mortar for 2 min. Then, 7wt% (0.07 g) of DI water was added and ground in a pestle and mortar for 2 min. Next, 0.1 g of the mixture was load in a tungsten carbide block before placed on a hydraulic pressure machine and applied pressure of 2,000 kPa at varying sintering temperature and holding time (0 °C/0h, RT/6h, RT/12h, RT/24h, 60°C/6h, 60°C/12h, 60°C/24h, 120°C/6h, 120°C/12h, and 120°C/24h) for densification. After cooling, the cold-sintered γ-GC ceramic was removed from the block for characterization. The detail is shown in Figure 3.10.

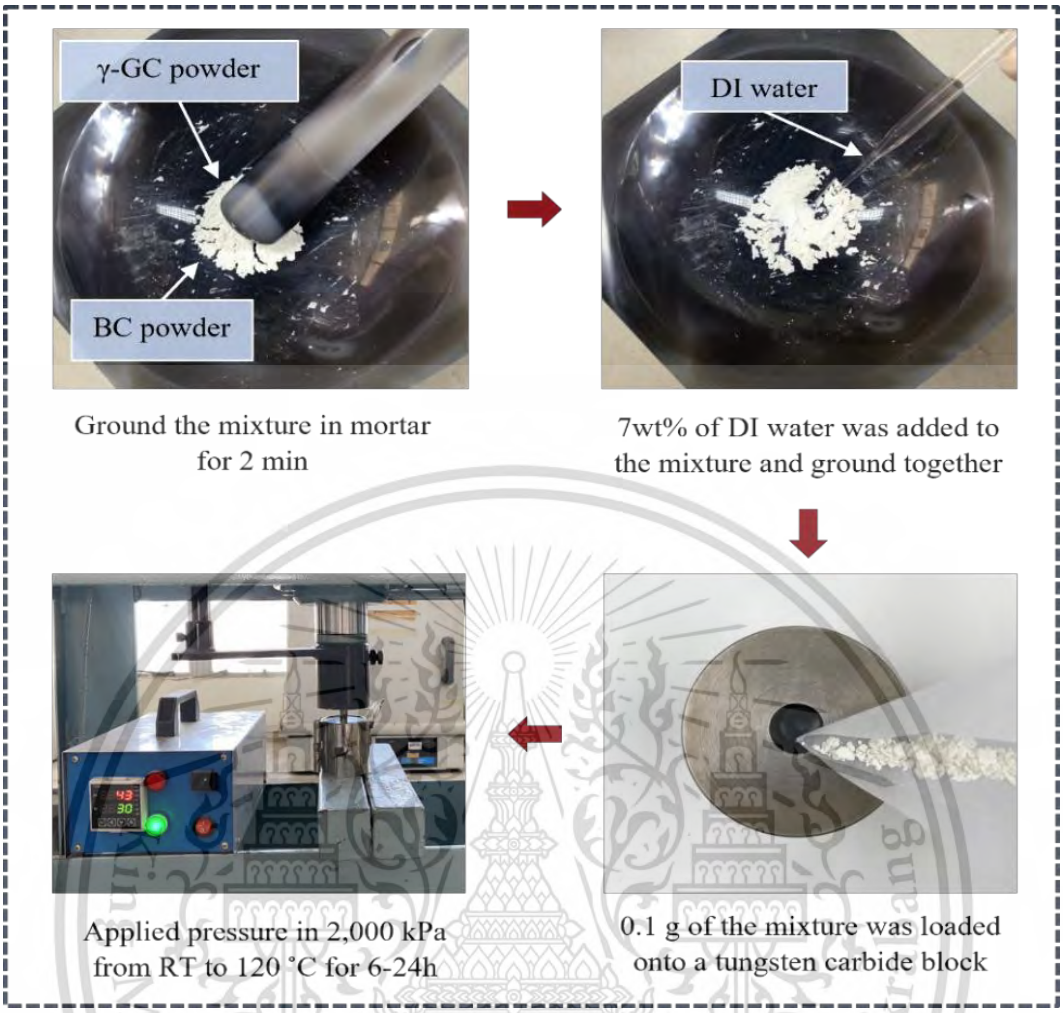

Figure 3.10 The preparation of γ-GC ceramic via cold sintering process

3.4.2 γ-GC/BT composites ceramics

Weight 0.14 g, 0.28 g, 0.46 g, and 0.84 g of a γ-GC according to the ratio of 15wt%, 30wt%, 50wt%, and 90wt%, respectively. Mix with BT powder and ground in a pestle and mortar for 5 min. Then, 7wt% (0.07 g) of DI water was added to the mixture by using a pestle and mortar for 5 min. Next, 0.3 g of the γ-GC/BT mixture was loaded in a tungsten carbide block and placed on a hydraulic pressure machine and applied pressure of 10,000 kPa at a holding time of 6 h and sintering temperature of 120 °C for 1 h for densification. After cooling, the cold-sintered γ-GC/BT composite ceramics were removed from the block for characterization. The detail is shown in Figure 3.11.

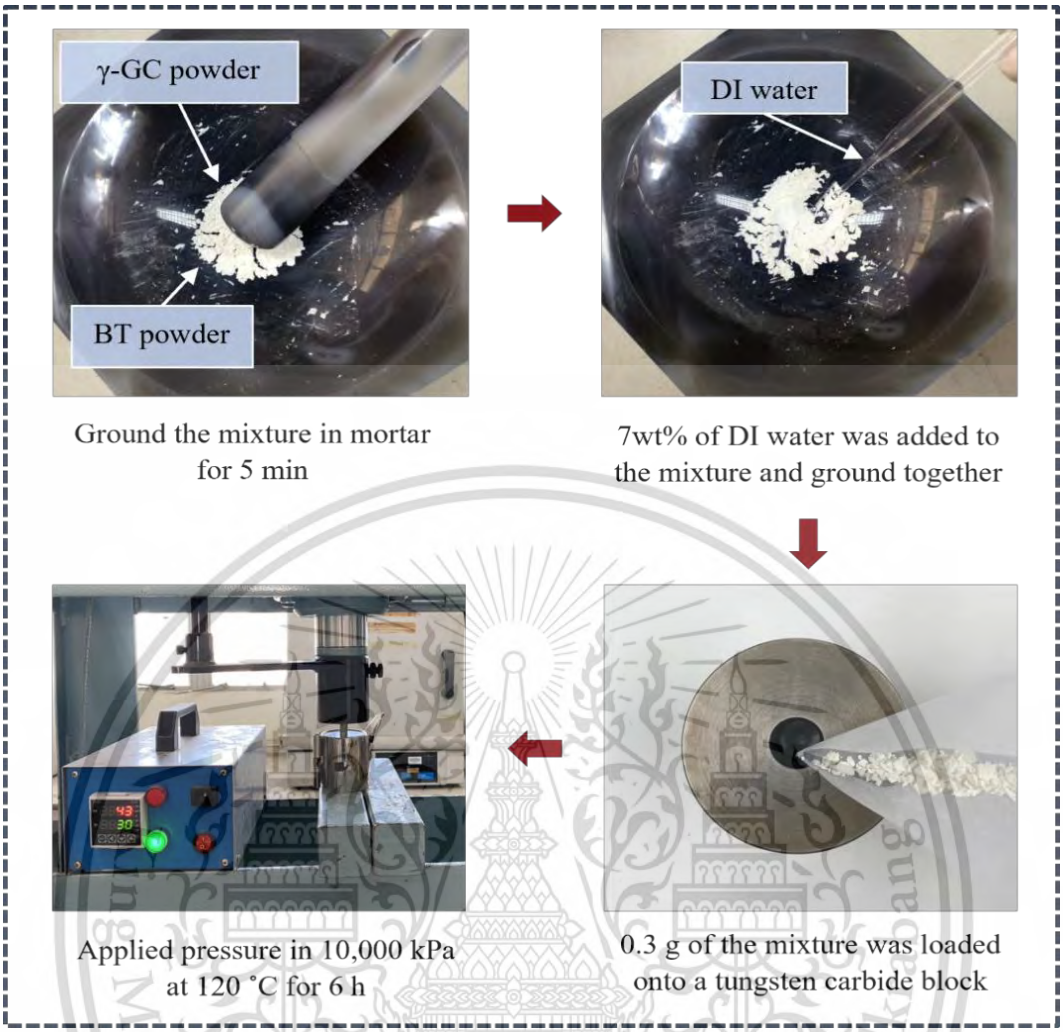

Figure 3.3 The preparation of γ-GC/BT composites via cold sintering process

3.5 Characterization of ceramics

3.5.1 Physical properties and structure determination

3.5.1.1 Density measurement

The density of γ-GC ceramic pellets and γ-GC/BT composite pellets is an index of their quality, which is dependent on impurities and pores. It was determined by measuring the pellets' mass and dimensions. The degree of densification, or the ratio of actual density to theoretical density, was calculated using Equation 3.1 [108].

$$\rho_r = \frac{4m}{(\pi d^2 h \rho_t)} \times 100\% \quad (3.1)$$

where ρ_r is the relative density (%), m is a mass of the cold-sintered pellet (g), d and h are the diameter (cm) and thickness (cm) of the cold-sintered pellet, respectively; and ρ_t is the theoretical density (g/cm^3) of composites which was calculated using Equation 3.2.

$$\rho_t = \frac{\mathrm{m}}{\left(\frac{m_1}{\rho_1}\right)+\left(\frac{m_2}{\rho_2}\right)} \quad (3.2)$$

Where m = 1 and m_1 is the mass fraction of γ-GC and m_2 are the mass fraction of BC, and BT, respectively; ρ_1 is the theoretical densities (g/cm^3) of γ-GC and ρ_2 are theoretical densities of BC, and BT, which were calculated according to the Equation 3.3.

$$\rho = \frac{nA}{V_c N_A} \quad (3.3)$$

when n is the number of molecules per unit cell, A is the formula weight (g/mol), V_c is the volume per unit cell (cm^3/unit cell), and N_A = 6.023 x 10^{23} / mol. In addition, a mass fraction can be calculated according to Equation 3.4.

$$m_{fraction} = \frac{m_i}{m_{tot}} \quad (3.4)$$

When $m_{fraction}$ is a mass fraction, m_i is a mass of γ-GC, BC, and BT, m_{tot} is the mass of the mixture.

3.5.1.2 X-ray diffraction analysis (XRD)

After sintering of γ-GC ceramics and γ-GC/BT composites ceramics, the crystal structure and phase transition of all ceramics was carried out using the X-ray diffraction (XRD) technique. XRD is a versatile, non-destructive analytical technique used to analyze physical properties such as phase composition, crystal structure, and orientation of powder, solid, and liquid samples. X-ray scattering is caused by the interaction of X-rays and crystal lattices in materials, in which X-rays scattered from distinct lattices interfere with one another and generate a diffraction pattern when the incident angle of the X-ray beam changes. The interaction of the incident rays with the

sample produces a diffracted ray when conditions satisfy Bragg's Law as an Equation 3.5.

$$n\lambda = 2d\sin\theta \quad (3.5)$$

Where n is the diffraction order (n=1 is first order, n=2 is second order, n=3 is third order), λ is the wavelength (nm), d is a lattice spacing (nm), and θ is an angle (degrees). This process is like matching fingerprints in a crime scene investigation. The most comprehensive compound database is maintained by the ICDD (International Center of Diffraction Data) and JCPDS (Joint Committee on Powder Diffraction Standard).

In these studies, the x-ray diffraction results of γ-GC powder, γ-GC ceramic, BT powder, and γ-GC/BT composites were obtained from a Smart Lab X-ray diffractometer, as shown in Figure 3.12. The source of the X-ray used Cu-K_α radiation with λ= 1.5418 Å. The data of X-ray diffraction were collected in the 2θ scan range of 5-50˚ for γ-GC powder and γ-GC ceramic. However, BT powder and γ-GC/BT composites were collected in the 2θ scan range of 10-80 ˚C. The phase was determined by comparing the major peaks to the values listed on the JCPDS data. In addition, the instrument merges a heat-flux type DSC with an XRD, which was measured to investigate the temperature of the transformation of γ-GC to α-GC.

3.5.1.2.1 In-situ X-ray diffraction

In-situ X-ray diffraction is one of the operating modes of an X-ray diffraction analyzer with an auxiliary device, namely a cold-heat device. This makes it possible to study changes in crystal structure and composition as test conditions change. In addition, the addition of such equipment makes it possible to analyze changes in substances from room temperature up to 1,500 ˚C. It is also possible to study the thermal behavior of sample substances.

In this work, the γ-GC ceramic at condition 120 °C/24 h was investigated in the 2θ = 10-40°. The composite was placed on an aluminum square-shaped stage (8 mm * 8 mm), and the temperature was increased from RT to 300 °C at a heating rate of 40°C/min.

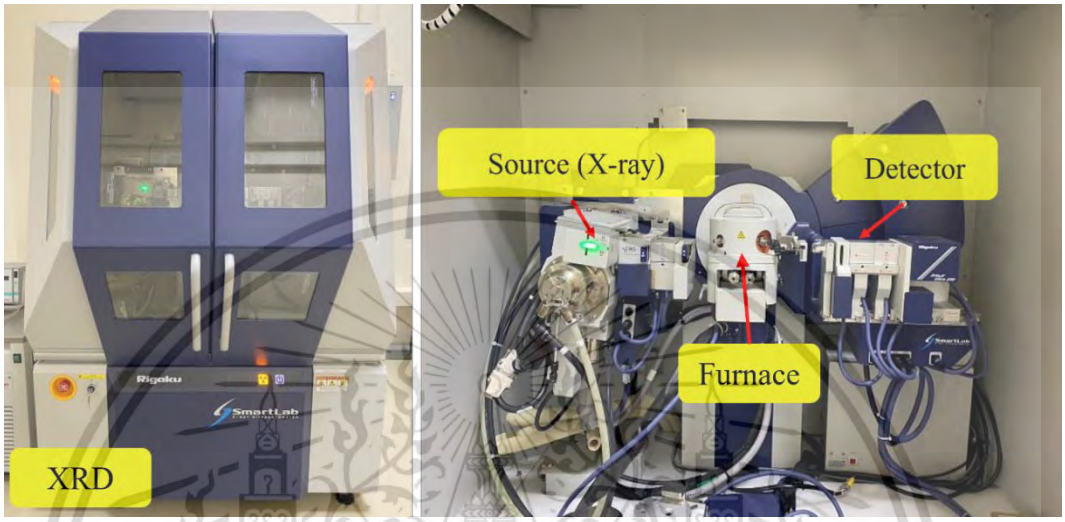

Figure 3.12 X-ray diffractometer, RIGAKU smart lab

3.5.1.3 Transform Infrared Spectrometer (FTIR)

FTIR is a common form of infrared spectroscopy. All infrared spectroscopies act on the principle that when infrared (IR) radiation passes a sample, some of the radiation is absorbed. The radiation that passes through the sample is recorded. Because different molecules with their different structure produce different spectra, the spectra can be used to identify and distinguish among molecules. The advantage of this technique is it does not destroy the sample, it is significantly faster than older techniques, and it is much more sensitive and precise. A molecule's covalent bonds will selectively absorb radiation of specific wavelengths, which changes the vibration energy in the bond. The type of vibration (stretching or bending) induced by the infrared radiation depends on the atoms in the bond. Because different bonds and functional groups absorb different frequencies, the transmittance pattern is different for different molecules. The output of the FTIR spectrum was recorded on a graph

known as an interferogram with wavenumber (cm^{-1}) recorded on the X-axis and transmittance recorded on the Y-axis. In this study, FTIR was studied to examine the functional group of materials. The γ-GC powder and γ-GC ceramic were used in an attenuated total reflectance (ATR) mode and recorded between 700-4000 cm^{-1}. However, the BT powder and γ-GC/BT composites sample will be used in the FTIR transmittance mode for recording between 400-4,000 cm^{-1}. The FTIR detector is shown in Figure 3.13.

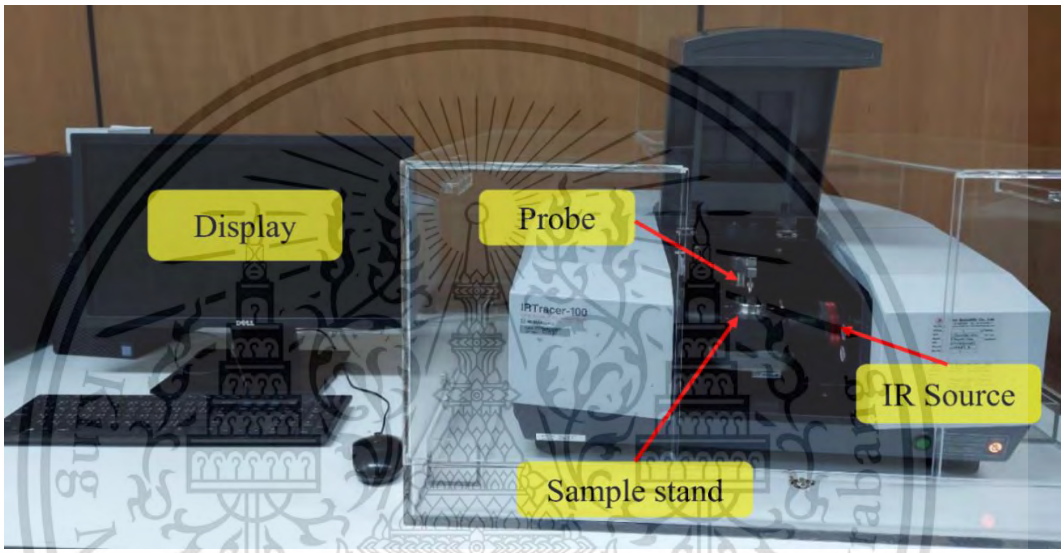

Figure 3.13 Fourier transform Infrared (FTIR), SHIMADZU, IR Tracer-100.

3.5.1.4 Scanning Electron Microscopy (SEM)

SEM is a highly versatile technique used to obtain high-resolution images and detailed surface information of samples. It is a type of electron microscopy that uses a focused beam of electrons to scan the surface of a specimen and generate images at a much greater resolution compared to optical microscopy. The resolution of SEM instruments can range from < 1 nanometer up to several nanometers. SEM uses an electron beam that is produced at the top of the column in the electron gun and accelerated through the column at a specified accelerating voltage (1 keV-30 keV). Condenser lenses and apertures act to reduce the beam diameter. The final lens in

the column is the objective lens, which focuses the beam on the sample surface. The diameter of the beam in an SEM can range from <1 nanometer up to 20 nanometers, depending on the type of electron gun, accelerating voltage, and lens configuration (Figure 3.14).

In this study, the surface morphology of ceramic was observed using SEM (Quanta FEG-250, FEI), as shown in Figure 3.15. The γ-GC powder, BT powder, and all ceramic were attached on stainless steel stubs and using carbon adhesive tape. After that, the top surface of the sample was coated by a gold layer.

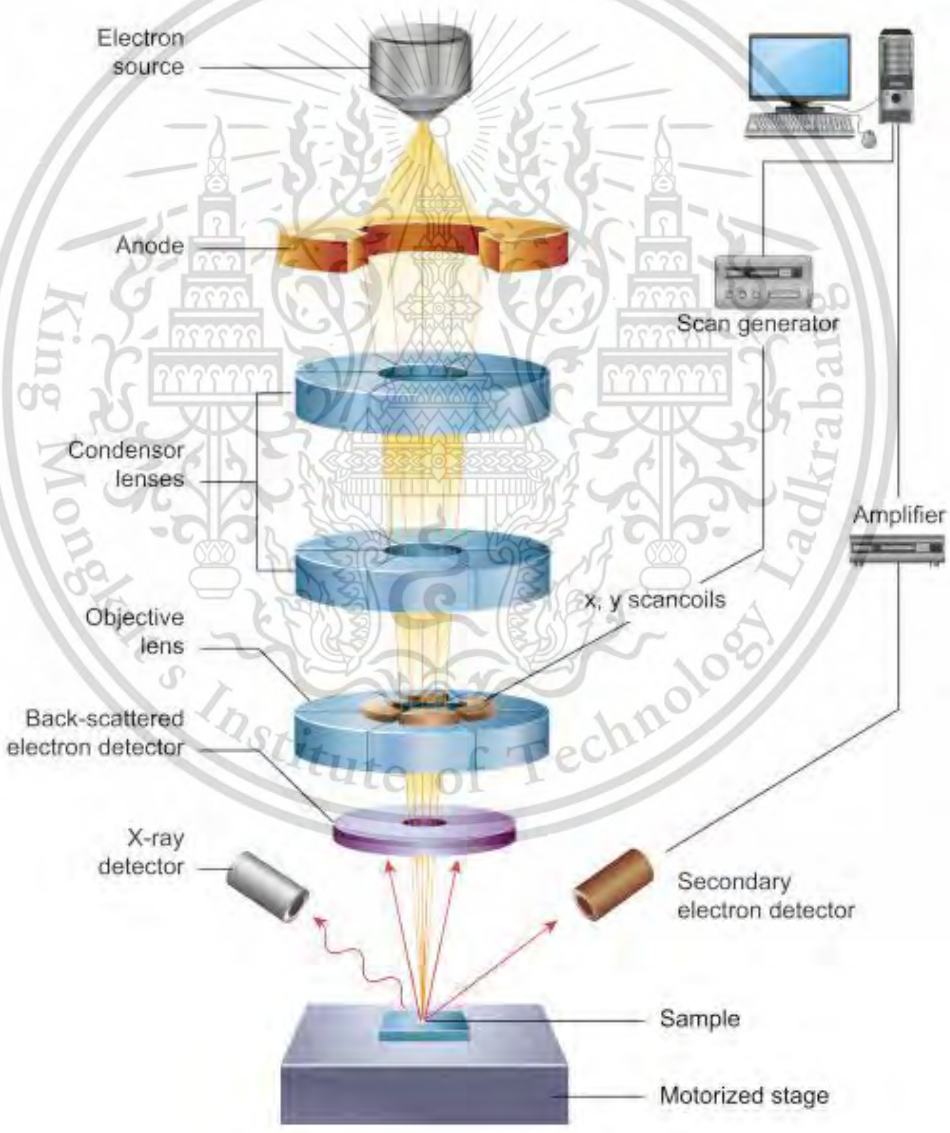

Figure 3.14 The component and operation of SEM [109].

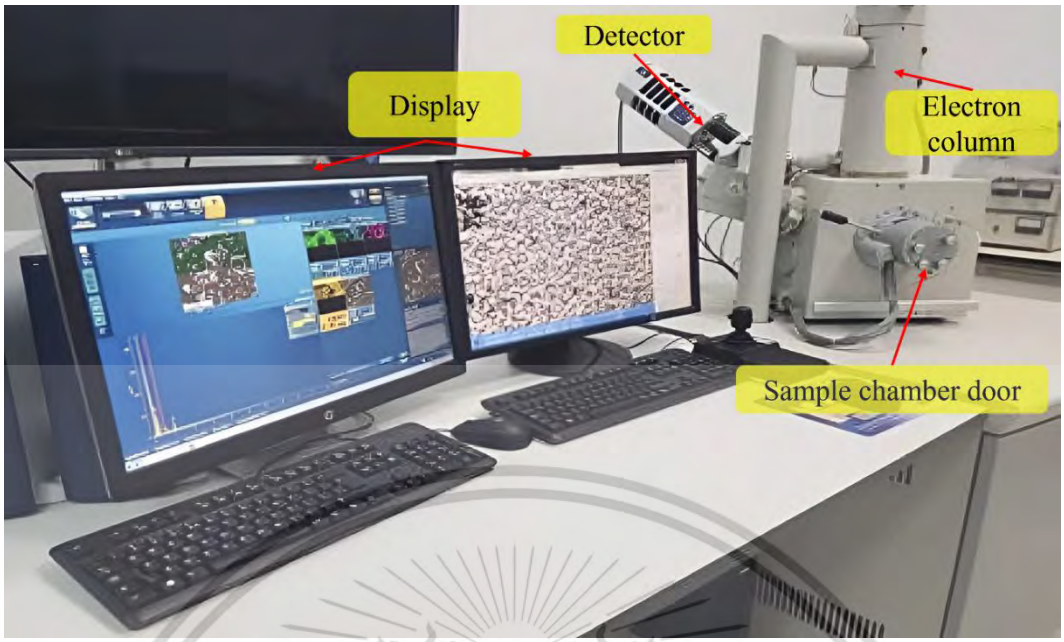

Figure 3.15 Scanning Electron Microscope (SEM, Quanta FEG-250, FEI).

3.5.1.4.1 Energy dispersive X-ray spectroscopy (EDS)

EDS is an analytical technique used for the elemental analysis or chemical characterization of a sample. The EDS analysis can be used to determine the elemental composition of individual points or to map out the lateral distribution of elements from the image area. The EDS has an analytical capability that can be coupled with several applications, including SEM and TEM.

In this work, the γ-GC/BT composites at various γ-GC content (15wt%, 30wt%, 50wt%, and 90wt%) were performed to analyze the chemical components of materials.

3.5.1.5 Transmission Electron Microscopy (TEM)

TEM is a technique of imaging the internal structure of solids using a beam of high-energy electrons transmitted through the solid. This technique is unlike optical microscopes, which rely on light in the visible spectrum. TEM can reveal stunning

details at the atomic scale by magnifying nanometer structures up to 50 million times.

In this work, the size and shape of the BT commercial powder and BT after calcined at 1,200 °C/12 h were measured and analyzed by TEM (FEI, Model: TECNAI G2 20, Netherlands). The TEM is shown in Figure 3.16.

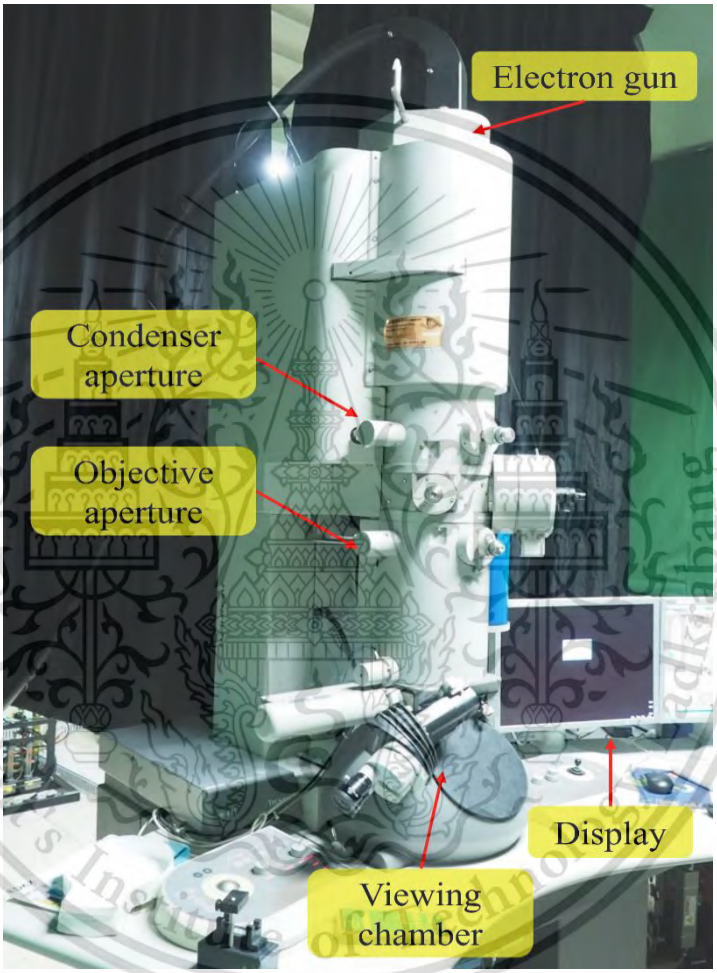

Figure 3.16 Transmission electron microscopy (TEM, FEI, Model: TECNAI G2 20, Netherlands).

3.5.1.6 Synchrotron X-ray Tomographic Microscopy (SR-XTM)

SR-XTM utilized the X-ray beam generated from the synchrotron light source in the X-ray imaging. When the X-ray beam is projected onto the sample, the X-ray beam that passes through the sample creates an X-ray pattern from the differential

absorption of the sample. The scintillator is used to convert the transmitted X-ray to visible light to acquire the X-ray image. Then, it is magnified by the objective lens coupled microscope and finally recorded by the high-resolution camera (sCMOS camera). A typical SR-XTEM scan is carried out by acquiring the X-ray images around the sample for at least 180°. After the scan, all X-ray images are calibrated by flat-field correction with bright and dark current images. The resulting X-ray images are inputted in computational processing to obtain the sinograms and the reconstructed tomographic images based on the filtered back-projection algorithm. The collection of reconstructed images (also referred to as tomograms) reflects the cross-sectional details of the sample in three dimensions. The SR-XTM is shown in Figure 3.17.

In this work, γ-GC ceramic at condition 120 °C/24h and γ-GC/BT composites at varying γ-GC content of 5wt%, 30wt%, and 90wt% were conducted by SR-XTM at beamline 1.2W, Synchrotron Light Research Institute (SLRI), Thailand. X-ray projections of the sample were collected for a complete dataset, spanning 180° with 0.1-degree increments. Artifacts were minimized by attenuating polychromatic X-rays with a 350-micron-thick aluminum foil, averaging 11.5 keV. Projections were captured using an sCMOS camera with a 1.44-micrometer pixel size. Data was pre-processed and reconstructed in 3D using the Octopus Reconstruction software. The reconstructed images were visualized using Drishti software.

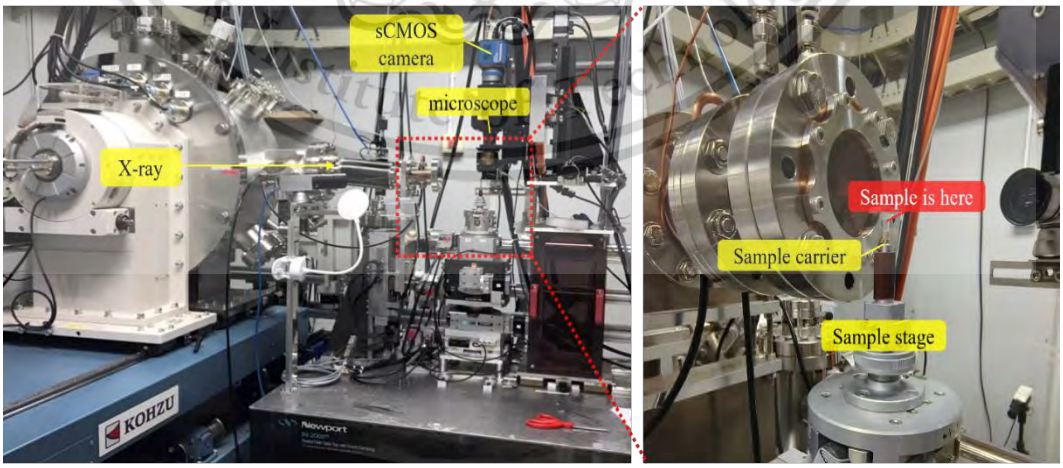

Figure 3.17 Synchrotron X-ray Tomographic Microscopy (SR-XTM)

3.5.1.7 Vickers hardness test

Vickers hardness test determines hardness in materials within the microhardness test load range. This approach employs force to assess sagging markings on the material's surface. Vickers uses a diamond square-based pyramid-shaped indenter and a microscope to observe the impression and diagonals. The measuring pressure ranges from 10 gram‧ force (gf) to 100 kilogram‧force (kgf). If the measuring pressure is less than 1 kgf, it must be polished using a machine or electric polisher before testing to obtain the most accurate test results. It is suitable for measuring the hardness of steel.

In this study, the γ-GC ceramic was measured by a Vickers hardness tester (Figure 3.18) to confirm the improvement in the hardness properties of the material when bacterial cellulose was added. The γ-GC ceramic was placed on the sample stand under the press. The diamond indenter was moved down slowly until it touched the sample, applied 1 kg of force, and held for 5 min before removing it from the sample. In this test, the samples were repeated 5 times.

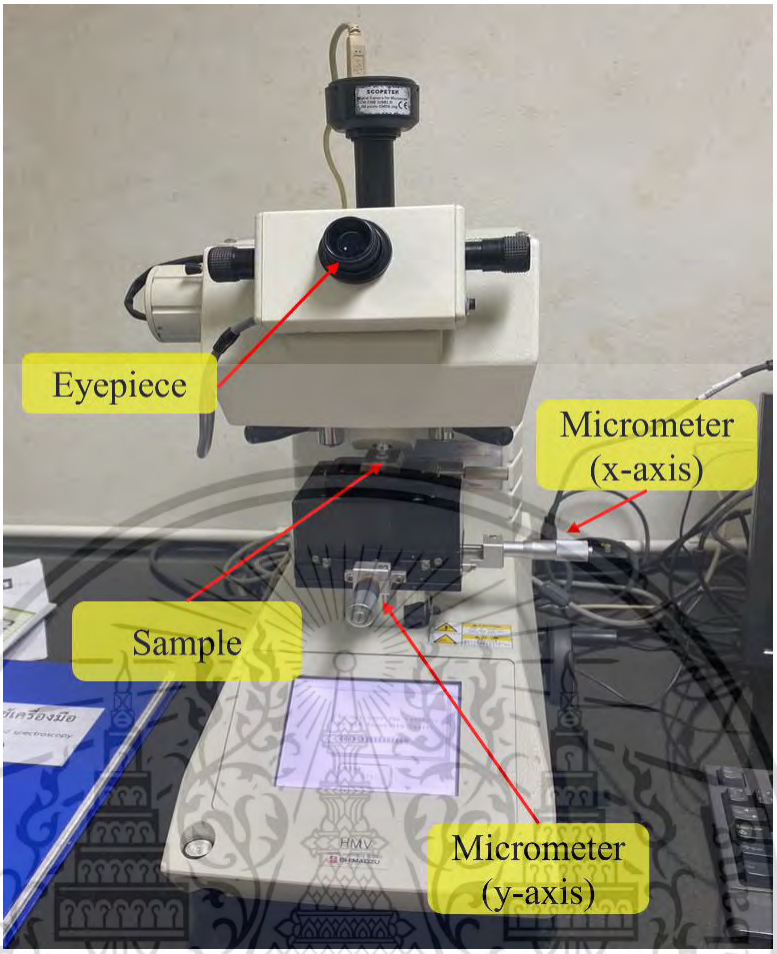

Figure 3.18 Hardness tester (Shimadzu, Model: HMV-2T).

3.5.2 Electrical Analysis

3.5.2.1 Sample preparation

Before measuring electrical properties, all ceramic samples were polished for both sides and made parallel. Then, the cold-sintered pellet's top and bottom surfaces were coated with silver paste and dried in air at 100 ˚C for 30 min before measurement.

3.5.2.2 Ferroelectric property measurement

The ferroelectric material measures polarization as a function of the electric field (P-E hysteresis loop). The P-E hysteresis loop describes the dynamic nonlinear

polarization switch behavior as a function of the field. The saturation polarization (P_s), remnant polarization (P_r), and coercive field (E_c) can be obtained from the ferroelectric hysteresis loop.

In this study, the polarization-electric field (P-E) hysteresis loop was determined at room temperature using a standard ferroelectric test system (RT66A) from Radiant Technologies (Figure 3.19), for γ-GC ceramic at condition RT/24h, 60°C/24h, and 120°C/24h were measured at an electric field of -5 to 5 kV/cm. For γ-GC/BT composites, varying γ-GC from 15wt%, 50wt%, and 90wt% were measured at an electric field of -20 to 20 kV/cm. During the measurement, the ceramic sample was immersed in silicone oil to prevent the breakdown from the side area of the samples.

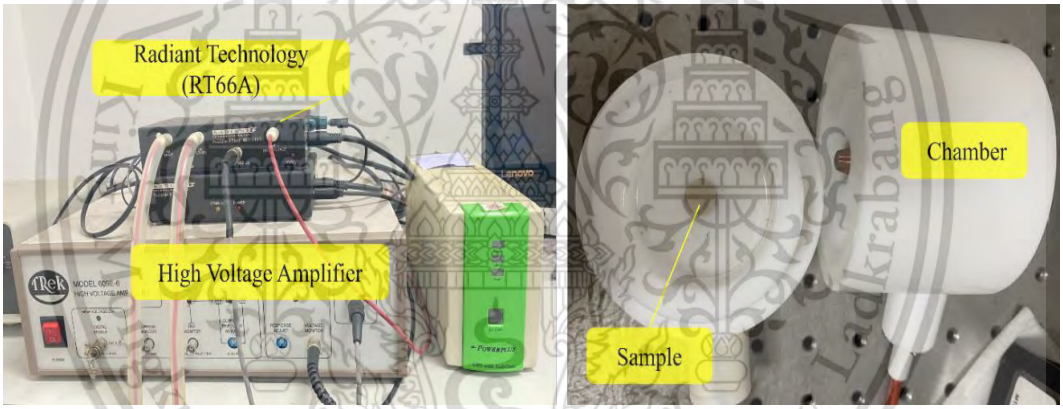

Figure 3.19 Ferroelectric Tester

3.5.2.3 Dielectric property measurement

The dielectric property measurement is mentioned in the determination of the phase transition temperature, relative permittivity (ε_r) or dielectric constant, and loss tangent ($\tan\delta$). The capacitance measurements determined the relative permittivity and loss tangent value based on the following Equation 3.6.

$$C = \frac{\varepsilon_0 \varepsilon_r A}{d} \tag{3.6}$$

Where C is the capacitance (Farad), d is the ceramic thickness, A is the surface area of the sample, and ε_0 is the permittivity of free space, 8.854 x 10^{-12} F/m. In this study, the dielectric property measurements of γ-GC ceramic and γ-GC/BT composites were recorded using an LCR meter (Agilent E4908A), as shown in Figure 3.20, for γ-GC ceramic at condition 120 °C/24h were measured from 100 Hz to 1 MHz at RT to 150 °C. γ-GC/BT composites were measured from 100 Hz to 2 MHz at RT to 200 °C.

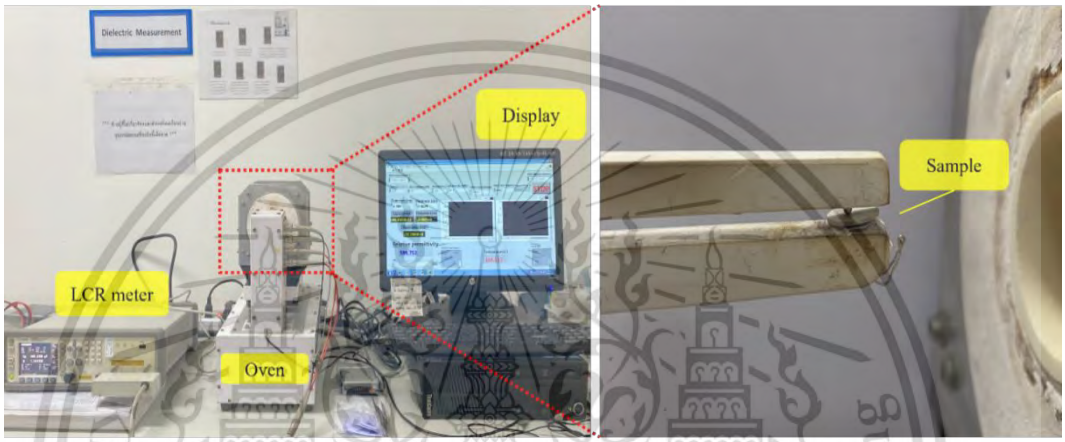

Figure 3.20 LCR meter (Agilent E4908A)

CHAPTER 4

TOWARDS THE PREPARATION OF ORGANIC FERROELECTRIC COMPOSITES: FABRICATION OF A GAMMA-GLYCINE-BACTERIAL CELLULOSE COMPOSITE VIA COLD SINTERING PROCESS

Based on article published in journal of Materials Research and Technology

The cold sintering process (CSP) has emerged as a revolutionary technique for low-temperature processing of ceramics and composites, enabling high-density fabrication at low temperatures. In this study, we demonstrated the implementation of CSP in fabricating the γ-glycine (γ-GC)-bacterial cellulose (BC) composite and evaluated the effect of sintering temperature and holding time on the microstructure and electrical properties. Our findings revealed that an increase in sintering temperature and holding time leads to grain growth, as the transient solvent (water) facilitates the closely-packed microstructure. Moreover, the addition of BC as a filler into the γ-G matrix leads to a composite with a 10% increase in hardness when BC was uniformly distributed in γ-GC. The composite with a relative density of 97% was successfully obtained at 120°C/24 h, preserving the γ polymorph of glycine without the unwanted transformation commonly observed with traditional sintering. We also reported the dielectric and ferroelectric properties of the γ-G-BC composite, exhibiting a remanent polarization of 0.004 μC/cm^2 and a coercive field of 1.201 kV/cm. Our findings suggest that CSP is a promising approach for low-temperature processing and fabrication of ceramics, especially when incorporating structurally sensitive filler such as organic ferroelectric, to achieve high-performance composites.

4.1 Introduction

Piezoelectric materials have the unique property of converting mechanical forces into electricity and vice versa. Inorganic piezoelectric materials, such as lead zirconated titanate (PZT) [110], aluminum nitride (AIN) [111], zinc oxide (ZnO) [112],

and barium titanate ($BaTiO_3$) [113, 114], exhibit this effect due to ions rearrangement within their crystal structures which lack the inversion symmetry [115, 116]. These materials are commonly used as ultrasonic motors and actuators, precision motion control and positioning devices, microfluidics, implantable medical devices, and piezoelectric nanogenerators [115-118]. However, inorganic piezoelectric materials have some drawbacks, including limited strength and durability, poor temperature stability, high cost and difficulty of processing, inflexibility, poor biocompatibility, potential toxicity to the environment and human health, making them less attractive for biomedical and related applications [115],[116].

Recently, organic piezoelectric materials, including glycine [119], collagen [120], silk [121], self-assembled diphenylalanine peptide nanotubes (PNTs) [122], graphene [123], and chitosan [124], are attracting increasing attention due to their notable advantages [125] such as such as high biocompatibility, flexibility, and processability. However, they have relatively low piezoelectric coefficients and poor mechanical properties. Despite these limitations, organic piezoelectric materials hold great promise in the field of biomedicine, particularly for implantable devices and sensors, due to the reduced risk of adverse biological responses. Improvements in the fabrication techniques, molecular design, and characterization methods are necessary to address these challenges and to expand their potential applications in various fields [126, 127]. Among organic piezoelectric materials, glycine has gained considerable attention due to its simplicity as the simplest amino acid found in proteins [20, 127]. It crystallizes into three polymorphs depending on crystallization conditions: α, β, and γ. The metastable α-glycine (α-GC) phase has a centrosymmetric structure and possesses no piezoelectricity, while the unstable β-glycine (β-GC) phase has a non-centrosymmetric structure and consequently shows piezoelectricity [128]. The addition of inorganic salts (such as NaCl) significantly promotes the secondary nucleation of the piezoelectric γ-GC while simultaneously inhibiting the α-G primary nucleation. This is possible due to ion-glycine interaction and the formation of linear head-to-tail glycine chains [129]. Despite initial reports of low piezoelectric coefficients, recent studies [23, 130] have shown that glycine exhibits strong piezoelectric properties, with piezoelectric coefficients comparable to or better than those of conventional organic piezoelectric materials [119]. In 2012, Heredia et al. [131] reported robust and continuous nanoscale

ferroelectricity in piezoelectric γ-GC for the first time. Additionally, the polarization of γ-GC is about five times stronger than that of β-GC due to spirally aligned dipoles along the axis, as opposed to randomly oriented dipoles in β-GC [97]. However, when compared to inorganic piezoelectric materials, γ-GC still possess a lower piezoelectric output.

However, the synthesis of γ-GC crystals through traditional re-crystallization processes does not allow doping or compositing. While the properties could be improved when γ-GC ceramics is composited with other materials, the transformation of γ-GC at high temperatures remains a challenge that affects its piezoelectric and ferroelectric properties. The current limitation regarding the densification of ceramics can be addressed by utilizing the cold sintering process (CSP) [132-135]. This innovative low-temperature sintering approach has proven to be effective in densifying ceramic materials. The recent study conducted by Randall et al. [14] reported that the CSP is capable of delivering high relative densities (>98%) of potassium dihydrogen phosphate (KH_2PO_4) below 300 °C, with a processing duration of around 1 h. This finding highlights the potential of CSP as a promising alternative, based on the "dissolution-precipitation" phenomenon, to conventional high-temperature sintering methods [136, 137]. Accordingly, CSP is an innovative, promising approach for the preparation of γ-G composites by utilizing the low-temperature processing conditions which could impede the conventional γ-GC transformation typically at >200 °C [20, 128]. This research seeks to improve the density, mechanical, piezoelectric, and ferroelectric properties of γ-GC, an organic piezoelectric/ferroelectric material. Additionally, the study aims to explore new methods for the fabrication of high-performance composites using biomaterial-based fillers such as bacterial cellulose, thereby expanding the range of their potential applications.

4.2 Experimental procedure

4.2.1 Gamma glycine (γ-GC) preparation

Figure 4.1a Shows a schematic illustration of the γ-GC synthesis via a recrystallization process. An amount of 56 g of commercial-grade glycine (NH_2COOH, 99% purity from Sigma-Aldrich) and 15 g of sodium chloride (NaCl, analytical-grade from Carlo Erba) in a 3:1 mol ratio were dissolved in 100 mL deionized water (DI water),

stirred for 5 h at room temperature (RT), then filtered with a vacuum filtration twice. The obtained liquid was kept in an oven at 35 °C for 25 days for the α- to γ-transformation. The γ-GC crystals were obtained after 25 days, which were ground using a ball mill apparatus for 3 h to make the γ-GC powder.

4.2.2 Bacterial cellulose (BC) preparation

BC powder was prepared by washing and soaking 700 g of nata de coco from the local manufacturer (Bifern, ASP Inter Food Co., Ltd) in 1000 mL of boiled water, with the water replaced every 30 min until pH 5. Then, the obtained nata de coco paste was blended in a wet blender, poured into trays, and freeze-dried at -40 °C for 24 h.

4.2.3 Fabrication of γ-GC/BC composites via CSP

Figure 4.1b Illustrates the fabrication of γ-GC/BC composite via CSP. γ-GC powder and BC powder were mixed in a mortar for 2 min. Then, DI water was added, and the mixture was ground in a pestle and mortar for 2 min. The weight ratio of γ-GC: BC: DI water was 92: 1: 7. Next, 0.1 g of the γ-GC-BC mixture was placed in a tungsten carbide block and subjected to uniaxial pressure of 2,000 KPa at RT-120 °C for 6-24 h for densification. After cooling, the cold-sintered γ-GC/BC composites was removed from the block for characterization. For comparison, the traditional sintering process (TSP) was also employed. The γ-GC powder underwent uniaxial pressing at pressure of 2000 KPa followed by sintering in air at a temperature of 200 °C for a duration of 24 h.

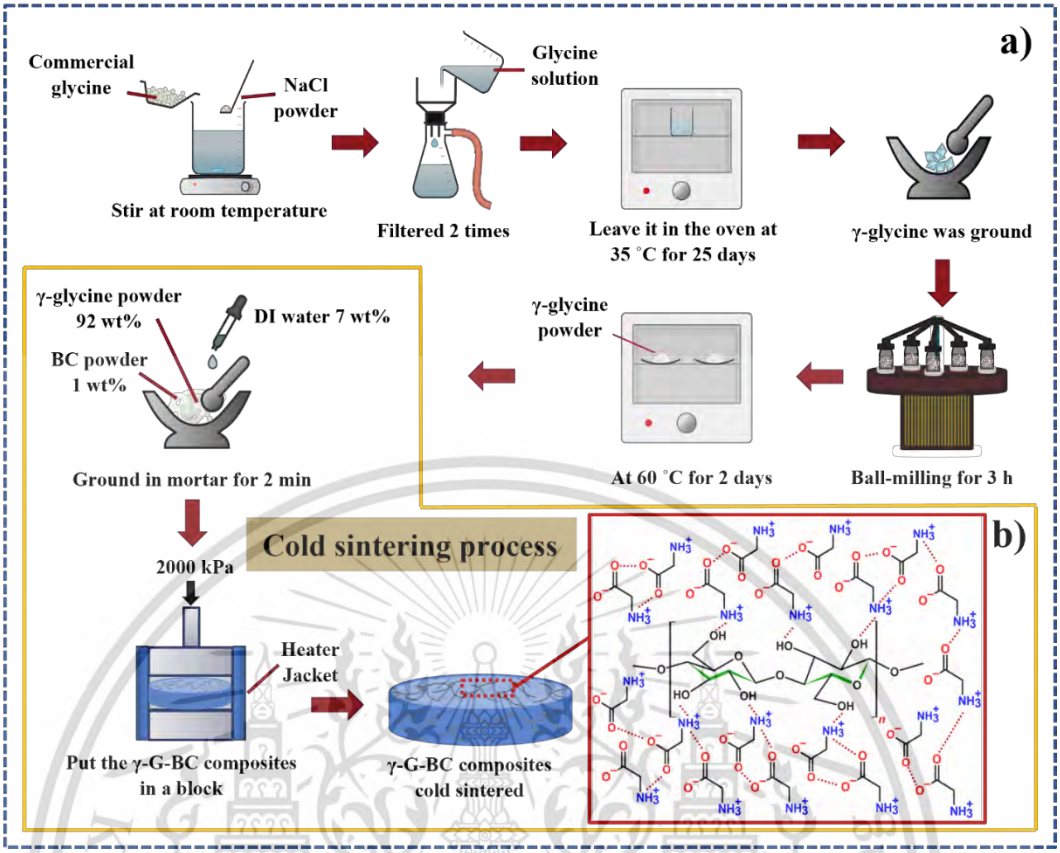

Figure 4.1 Schematic illustration of a) preparation of γ-GC, and b) fabrication of the γ-GC-BC composites via CSP.

4.2.4 Characterization

The relative density of γ-GC-based composites was calculated by measuring mass and dimensions of the cold-sintered pellet. The degree of densification, or the ratio of actual density to theoretical density, was calculated using Equation 4.1 [108]

$$\rho_r = \frac{4m}{(\pi d^2 h \rho_t)} \times 100\% \quad (4.1)$$

where: ρ_r is the relative density (%), m is mass of γ-GC-BC composites (g), d and h are diameter (cm) and thickness (cm) of the pellet, respectively; and ρ_t is the theoretical density (g/cm^3) which was calculated using Equation 4.2

$$\rho_t = \frac{\mathrm{m}}{\left(\frac{m_1}{\rho_1}\right)+\left(\frac{m_2}{\rho_2}\right)} \quad (4.2)$$

where $\mathrm{m} = 1$, m_1 and m_2 are the masses of γ-GC and BC, respectively; ρ_1 and ρ_2 are the theoretical densities (g/cm^3) of γ-GC and BC, respectively, which were calculated according to Equation 4.3.

$$\rho = \frac{nA}{V_c N_A} \quad (4.3)$$

where n is the number of molecules per unit cell, A is the formula weight (g/mol), V_c is the volume per unit cell (cm^3/unit cell), and $N_A = 6.023 \times 10^{23}$/mol.

Fourier-transform infrared spectroscopy (FT-IR, SHIMADZU, IRTracer-100) in an attenuated total reflectance (ATR) mode was recorded between 700-4000 cm^{-1} and the resolution 4 cm^{-1} with 45 accumulation scans. Crystal structure of the composite was characterized by X-ray diffraction (XRD, RIGAKU smart lab, 2θ = 5-50˚) and compared to the JCPDS database. LeBail refinement of the unit cell parameters was performed using JANA2006 software. The average crystallite size of γ-GC-BC composites was calculated using Debye Scherrer Equation 4.4.

$$D = \frac{K\lambda}{\beta cos\theta} \quad (4.4)$$

Where D is the crystallite size, K is known as the Scherer's constant (K = 0.94), λ is wavelength of X-ray radiation (1.5418 Å), β is a full width at half maximum (FWHM) of the diffraction peak, and θ is the angle of diffraction [138]. A simultaneous XRD-DSC instrument (Rigaku Co., Tokyo, Japan) was also utilized to further characterize the γ-GC-BC composite. The instrument merges a heat-flux type DSC with an X-ray diffractometer (Cu K_α, 40 kV, 30 mA; and 2θ = 10-40˚) to obtain accurate readings. The composite was placed on an aluminum square-shaped stage (8mm x 8mm), and the temperature was increased from RT to 300˚C at a heating rate of 40˚C/min. The morphology and grain size of the γ-GC-BC composite were observed using an SEM (Quanta FEG-250, FEI). SR-XTM was conducted at beamline 1.2W, SLRI, Thailand. X-ray projections of the sample were collected for a complete dataset, spanning 180 ˚with 0.1-degree increments. Artifacts were minimized by attenuating polychromatic X-rays with a 350-micron-thick aluminum foil, averaging at 11.5 keV. Projections were

captured using an sCMOS camera with 1.44-μm pixel size. Data was pre-processed and reconstructed in 3D using the Octopus Reconstruction software. The reconstructed images were visualized using Drishti software. The Vickers test was examined using a micro hardness tester (Shimadzu HMV-2T, 1 kg load). Hardness values were calculated using Vickers hardness Equation 4.5.

$$HV = \frac{1.854 \times F}{d^2} \quad (4.5)$$

where *HV* represents a Vickers hardness (kg/mm^2), F is the applied load (g), and d is the diagonal length (mm) of the indentation cavity. To determine the dielectric properties of the γ-GC-based composite, top and bottom surfaces of the pellet were coated with silver paste and dried in air at 100 °C for 30 min. The dielectric constant (ε_r) and loss tangent (tan δ) of the γ-GC-BC composites were recorded using an LCR meter (Agilent E4908A) from 100 Hz to 1 MHz at RT, 50, 100 and 150 °C. Polarization versus electric field hysteresis loops of selected samples were recorded at RT using a standard ferroelectric test system (RT66A) from Radiant Technologies.

4.3 Results and discussion

Figure. 4.2 is the SEM image showing the microstructure of the γ-GC-BC composites compressed at 2,000 kPa and sintered at varying temperatures (RT, 60, and 120 °C) for a duration of 6-24 h. After removal from the tungsten carbide block, the composites appeared as white pellets with a diameter of 1 cm and a thickness of approximately 1 mm. Firstly, at the fixed holding time of 24 h, the γ-GC-BC composite sintered at RT had a porous and uneven surface, with a small grain size of approximately 1.45 ± 0.73 μm (Figure 4.2a). With increasing sintering temperature to 60 °C (Figure 4.2b) and 120 °C (Figure 4.2c), the surface became smoother, and the grain size increased to 1.76 ± 1.20 μm and 2.27 ± 0.99 μm, respectively. In other experiments where the temperature was fixed at RT and the time was varied, the composite sintered for 6 h had a small grain size of 1.42 ± 0.81 μm (Figure 4.2d) and a porous surface. The grain size increased with increasing holding time to 2.01 ± 1.02 μm (12 h, Figure 4.2e) and 2.39 ± 1.48 μm (24 h, Figure 4.2f). Clearly, the sintering temperature

and holding time both affect the grain size and densification, as they play important roles in accelerating the density and the densification process.

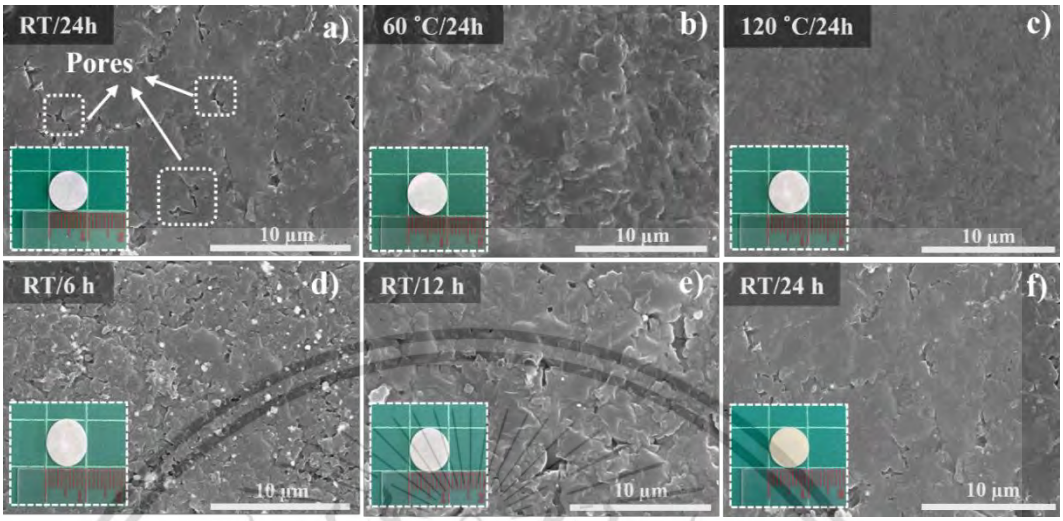

Figure. 4.2 SEM images of the cold-sintered γ-G-BC composites prepared at different conditions: (a) RT/24h (b) 60 ̊C/24h (c) 120 ̊C/24h (d) RT/6h (e) RT/12h and (f) RT/24h. The insets show the corresponding digital of the pellet.

The mechanism of CSP is depicted in Figure 4.3, consisting of two stages. At stage I, the homogenized ensembles of the γ-GC/BC composite was added with a liquid phase, which can be water or water with volatile solute (i) [15, 139]. The liquid phase serves as a lubricant and smooths the particle surface. The added liquid is beneficial to particle rearrangement (ii) as it partially dissolves sharp particles edges, leading to spaces for particles sliding. The densification at this stage is mainly through the external pressure, where the liquid phase readily redistributes itself and fills into particle interstitials. Accordingly, this early stage of sintering results in the initial particle compaction (yellow frame), contributing mostly to the total sample shrinkage (S1) [140].

Next, stage II begins at the solid-solid interface [141], involving dissolution at intergranular interfaces and mass transport through diffusion. Here, the ions (dissolved from the particles) diffuse through the water film (iii (a-ii)), causing gradual dilution of solute concentration away from the solid surfaces. Subsequently, precipitation occurs in pores (iii(a-iii)) and lead to neck growth at grain-grain interstitials. As a result, the

sample undergoes a slight shrinkage (S2). When the temperature and time are raised, the liquid volume is substantially reduced. Once precipitation is completed, the number of particle-particle contacts is significantly increased; crystal growth may occur via the coalescence of small crystallites into relatively larger ones. Notably, the crystal growth stages (iv-b) are strongly dynamic in nature, being driven by water evaporation and a supersaturated liquid at the temperature right above its boiling point. This triggers a large chemical driving force for the solid and liquid phases to reach an equilibrium state. Accordingly, temperature and time play a crucial role in this stage, as they enhance solubility while speeding up dissolution and grain growth. During the grain growth state, the initial grain undergoes a gradual and controlled increase in size, influenced by factors such as temperature and time. Throughout this process, the average grain size transitions from an initial value of D_0 to a final value of D_1. The densification rate varies with temperature, initially rising rapidly before becoming constant. The densification process may slow down at high temperatures due to evaporation [89, 90].

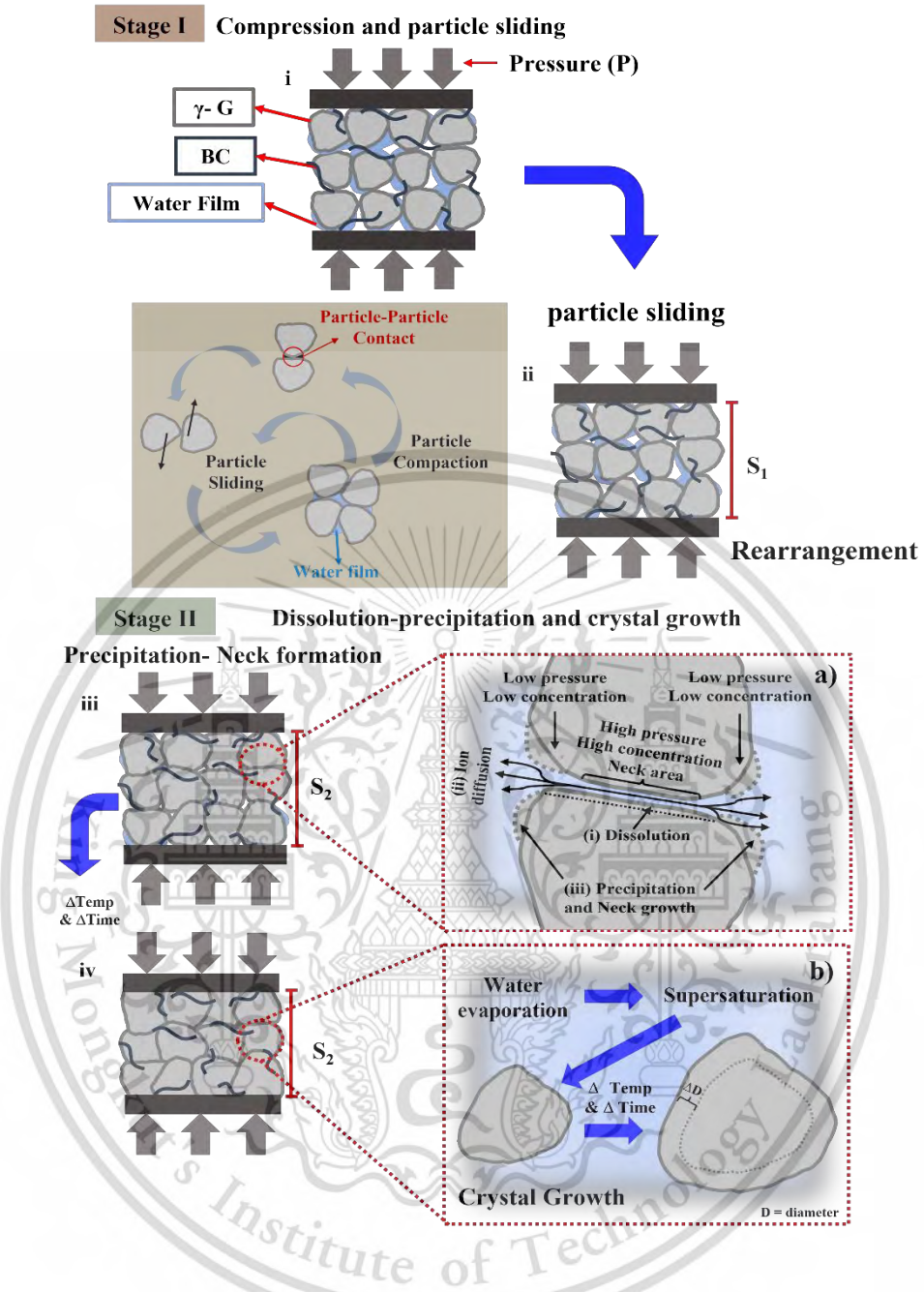

Figure 4.3 Schematics of CSP mechanism at various stages adapted from ref. [14],[139],[142]. Stage I involves compression and particle sliding: i) particle compaction, ii) particle sliding and rearrangement. Stage II involves the dissolution-precipitation and crystal growth shown in iii) and iv). Details of these two steps of Stage II are shown in a) incorporating dissolution, ion diffusion, precipitation-neck formation; and b) water evaporation and crystal growth.

The relative density of the γ-GC/BC composites was plotted in Figure 4.4a and b, illustrating its dependence on CSP parameters such as sintering temperatures and holding times. The results revealed that increasing the sintering temperature in CSP from RT to 120 °C (Figure 4.4a) increased the relative density from 93.9 ± 1.8% to 97.4 ± 1.5%. This is attributed to the improved mass transport and composite deformation at elevated temperature, leading to the improved bonding between particles and elimination of pores. The holding time also affected the relative density, as shown in Figure 4.4b. It is rationalized that a longer holding time allows for the enhanced dissolution of ions into DI water, and for a greater amount of precipitates around grain boundaries, thereby decreasing the local distance between particles and promoting mass transport The relative density of γ-GC/BC composites via CSP (97%, 120 °C, 24 h) was found to be higher than that from the traditional sintering process (TSP, 85%, 200 °C, 24 h).

The densification of the γ-GC/BC composite was also correlated with hardness, as seen from the micro-hardness test (Figure 4.4c) which is suitable for small scale samples. We observed an increase in hardness value from 58.2 ± 0.56 (TSP) to 78.1 ± 1.88 (CSP) for γ-GC. However, these values are smaller than 86.3 ± 0.66 for the γ-GC/BC composites prepared via CSP, presenting an increase of approximately 10%. The Vickers hardness of the γ-GC can be attributed to the H-bonded chains of which are interconnected by lateral NH···O H bonds, resulting in a three-dimensional network. However, the brittle γ-GC is prone to cracking by pressure as depicted in Figure 4.4d [143]. The addition of BC filler increased the hardness of the γ-GC/BC composite due to strong crosslinking between the amine groups of γ-GC and the hydroxyl groups of BC as demonstrated in Figure 4.4e-f. The 3D distribution of the γ-GC/BC composite on a macroscale was confirmed using Synchrotron Radiation X-ray Tomographic Microscopy (SR-XTM), which showed that BC was evenly distributed over the γ-GC surface (Figure 4.5a).

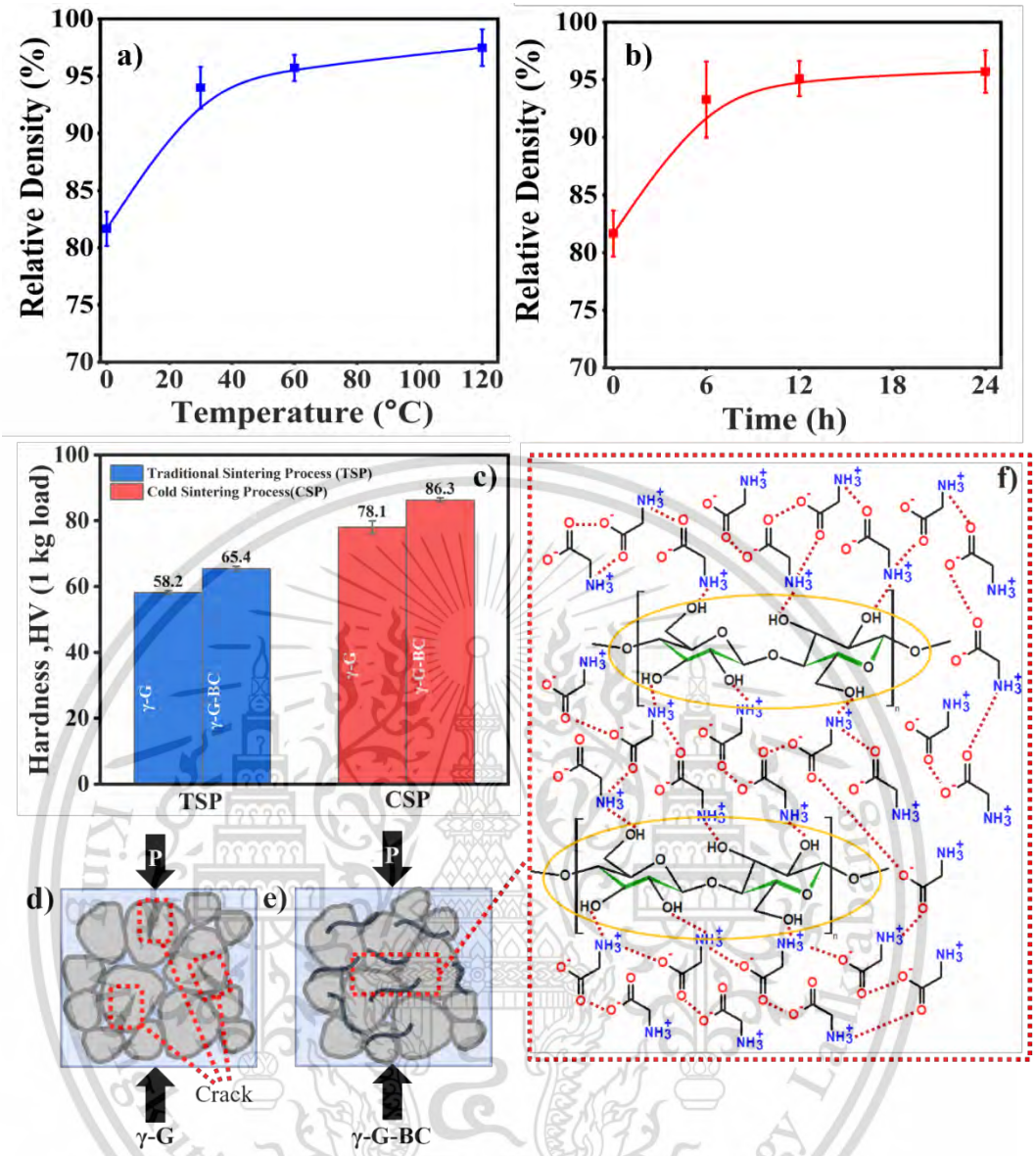

Figure 4.4 The relative density of γ-GC/BC composite after CSP at a) various sintering temperatures and b) various holding times. c) Vickers hardness number (HV, 1 kg load) of the γ-GC/BC composite via TSP (blue) and the 120 °C/24h via CSP (red). CSP diagram of d) γ-GC via CSP, and e) after adding BC; f) the chemical structure showing hydrogen bonds between amino groups of γ-GC and hydrogen groups of BC.

The different γ-GC/BC composites were also characterized using ATR-FTIR. The NH_3^+ stretching vibrations were observed in all spectra as the broad band at 3091 cm^{-1}, as depicted in Figure 4.5b-i. The zoom-in in Figure 4.5b-ii shows a strong

asymmetrical (C=O)O stretching with the highest intensity at 1573 cm^{-1} (peak 1), NH bending vibration of NH_3^+ at 1492 cm^{-1} (peak 2), (C=O)O symmetrical stretching at 1390 cm^{-1} (peak 3), and CH_2 wagging with the lowest intensity among four peaks at 1328 cm^{-1} (peak 4). The ratio of the intensity (I) of these four peaks, where $I_3 > I_4 > I_2 > I_1$, and $I_2/I_1 = 1.27$ is unique to α-glycine [144]. For β-GC, the characteristics intensity sequence is $I_1 > I_2 > I_4 > I_4$, and $I_2/I_3 = 1.02$ [145]. Lastly, the characteristics intensity sequence for γ-GC is $I_1 > I_3 > I_2 > I_4$, with $I_2/I_3 = 0.96$ [101]. Therefore, if I_1 is maximum, and I_2/I_3 ratios are between 0.96 and 1.02, glycine is presumably a mixed phase between β-GC and γ-GC. Note that β-GC can rapidly transform to α-GC and γ-GC in the presence of moisture at room temperature, but it is metastable in dry air. It is deduced from the sequence of intensities and the calculated I_2/I_1 of 1.36, that the glycine in the γ-GC/BC (TSP) composite is α-GC. On the other hand, the ATR-FTIR results of the γ-GC/BC composite prepared via CSP indicated that glycine is in the γ-GC form ($I_2/I_3 = 0.76$) without phase transformation commonly observed with the TSP employing higher temperatures (>200 °C). The presence of the carboxylic acid group resulted in the donation of its proton to the amino group, forming a dipolar ion with a strong hydrogen bond viz. H_3N^+ CH_2COO. These zwitterions adopt an antiparallel arrangement and subsequently the non-centrosymmetric cell with piezoelectric/ferroelectric properties.

The X-ray diffraction (XRD) patterns of the γ-GC/BC composites prepared through TSP and CSP are presented in Figure 4.5c. Consistent with ATR-FTIR results, all peaks of the sample prepared through TSP corresponded to the standard data in JCPDS number 32-1702 of α-GC. This contrasts with the γ-GC phase (JCPDS 06-230) for the composites prepared through CSP. In addition, LeBail refinement using the JANA2006 software was performed, and the results are shown in Figure 4.5c (calculated peak, black line; observed peak, +; shift patterns, green line; and the Bragg peak positions, black). The refinement parameters are selectively tabulated in Table 4.1. The lattice parameters obtained for the sample prepared through TSP were a = 5.492(5) Å, b = 11.704(9) Å, and c = 5.125(4) Å, confirming the monoclinic structure of the α polymorph. The lattice parameters of the sample obtained from CSP were a = b = 7.031(1) Å and c = 5.478(1) Å, indicating a hexagonal structure characteristic of the γ polymorph. Accordingly, XRD analysis confirmed that the CSP successfully preserved

the γ polymorph of glycine which would provide the piezoelectric properties. The crystalline size, estimated using Equation 4.4, is not significantly different between CSP (23.8 nm) and TSP (21.4 nm).

To further investigate the temperature-dependent phase transformation of the γ-GC/BC composite, the simultaneous differential scanning calorimetry (DSC) and XRD analyses were performed. The heat flow curve, as depicted in Figure 4.5d, show three distinct steps at 160, 190, and 225 °C. The first one corresponds to the melting of BC [146]. Next, the other two steps reflect the γ-GC transformation. At 190 °C, the mixture of γ-GC and α-GC was formed, resulting from the breaking of the 3D network of H-bonds in the crystal lattice [128, 147]. This temperature is comparable to 185.5 °C [148] and 187 °C [149], in the literature, and is complete at 215 °C, as confirmed by X-ray diffraction. Accordingly, the third DSC peak at 225 °C indicates the decomposition of glycine [150] . The temperature dependence of the phase transformation explains why TSP which requires a higher sintering temperature of >200 °C will not preserve the γ polymorph of glycine.

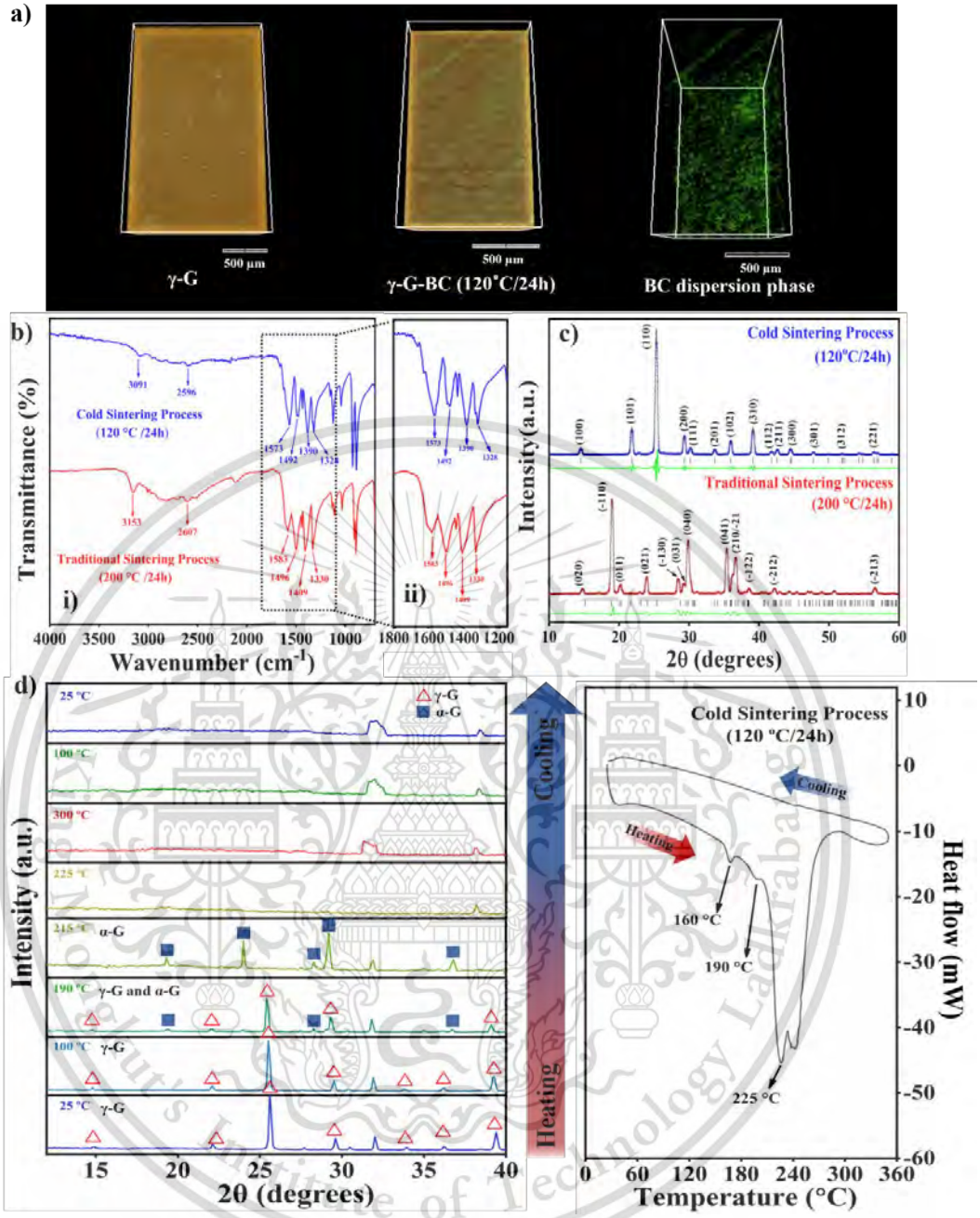

Figure 4.5 a) X-ray tomographic 3D visualization of γ-GC/BC composites via TSP and the 120 ๐C/24h via CSP and BC dispersion phase b) i. ATR-IR spectrum and ii. The zoom-in; c) LeBail refinement of the XRD patterns of the γ-GC/BC composites via TSP and the 120 ๐C/24 h via CSP; and d) in-situ XRD patterns and the simultaneous heat flow curve of the 120 ๐C/24 h γ-GC/BC composites.

Table 4.1 LaBail refinement parameters and calculated data from XRD pattern using JANA2006 software.

Samples	Lattice parameters				structure	polymorph	R-parameters
	a (Å)	*b* (Å)	*c* (Å)	Angles (°)			
TSP	5.492 (5)	11.704 (9)	5.125 (4)	$\alpha = 90.0$ $\beta = 111.3$ $\gamma = 90.0$	Monoclinic	Alpha (α)	R_p = 9.12 R_{wp} = 16.76 R_{exp} = 5.61 GOF = 2.26
CSP	7.031 (1)	7.031 (1)	5.478 (1)	$\alpha = 90.0$ $\beta = 90.0$ $\gamma = 120.0$	Hexagonal	Gamma (γ)	R_p = 7.92 R_{wp} = 10.47 R_{exp} = 7.87 GOF = 1.33

The dielectric responses of the γ-GC/BC composites were investigated as a function of temperatures and frequencies. The temperature dependences of the ε_r and tan δ for the 120 °C/24 h γ-GC/BC composites from RT to 150 °C at selected frequencies are shown in Figure 4.6a-b. Figure 4.6a indicated that ε_r increases gradually with increasing temperature due to the increased mobility of the polar segments. Specifically, the cellulose sub-unit comprises of polar -OH groups in glucopyranose rings oriented in the equatorial direction. Meanwhile, γ-GC exists as a dipolar ion as discussed above. The alignment of these polar groups from two components contributes to an increase in orientation polarization, resulting in a higher dielectric constant of the composite. Figure 4.6b Illustrates the temperature-dependence of tan δ at different frequencies. At 100 Hz, the tan δ peak is observed at 105 °C, with the peak shifting to higher temperatures as frequency increases. The maximum tan δ values are found to be 123 °C and 140 °C for 1 kHz and 10 kHz, respectively. The tan δ peak

corresponds to the transition from a crystalline to an amorphous phase of BC. The results agree well with the DSC results shown in Figure 4.5d. However, the different temperature occurrence may be attributed to the use of different measurement techniques.

Figure 4.6c Illustrates the frequency-dependent variation of the ε_r at different temperatures ranging from RT to 150 °C. At low frequencies, the ε_r value is high, typical for space charge polarization at the grain boundaries. As the frequency increases, the ε_r decreases for all temperatures, indicating a decrease in polarization due to the dielectric dispersion behavior. This behavior is influenced by the distribution of charges and the statistical motion of interfacial polarization effects. Figure 4.6d demonstrates the effect of frequency on tan d at different temperatures. At 50 °C, the tan δ peak is identified around 103 Hz. This peak shifts to higher frequencies as the temperature increases. The maximum is formed due to the dielectric relaxation, which is mainly found in organic molecules through ionic motion and molecular dynamic motion. It is noteworthy that at 150 °C, a rapid increase in tan δ is observed at low frequencies, suggesting the onset of direct current conduction.

An electric field can induce polarization reversal/switching in ferroelectric materials, which is one of their most significant characteristics. This switching of domains within ferroelectric materials is responsible for the occurrence of ferroelectric hysteresis loops. Figure. 4.6e shows the polarization-electric field (P-E) hysteresis loops of the γ-GC-BC composites prepared under different conditions, i.e., RT/24 h, 60 °C/24 h, and 120 °C/24 h, where the voltage ranges from -5 to 5 kV. The polarization (P_r) is similar in the RT/24 h and 60 °C/24 h samples, but it significantly increases in the 120 °C/24 h sample. In contrast, the coercive electric field (E_c) remains constant for the RT/24 h and 60 °C/24 h samples but significantly decreases for the 120 °C/24 h sample (Figure 4.6f). It can be observed that the hysteresis loop is saturated, especially for the 120 °C/24 h γ-GC-BC composite, indicating good ferroelectric characteristics with saturated polarization (P_s), P_r and E_c of 0.013 μC/cm^2, 0.004 μC/cm^2 and 1.201 kV/cm, respectively. Table 4.2 presents a comprehensive comparison between the ε_r, P_r and E_c of diverse piezoelectric biomaterials and the γ-GC-BC composite. The experimental results provide evidence of a direct relationship between the density of the sample

and its mechanical, dielectric, and ferroelectric properties, substantiating the successful fabrication of high-density γ-GC/BC composite ceramics by CSP.

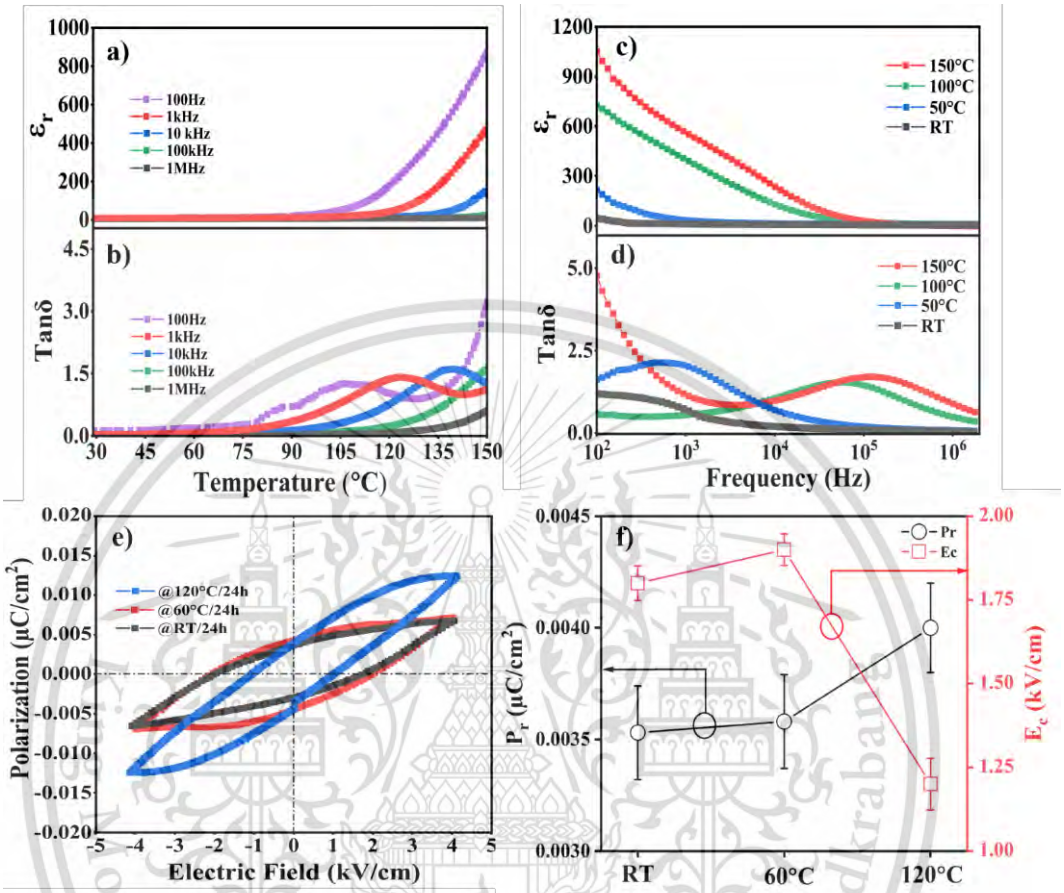

Figure 4.6 Temperature dependence of a) the dielectric constant and b) loss tangent; and the frequency dependence of c) the dielectric constant and d) loss tangent of the 120 ℃/24 h γ-GC-BC composite; e) the ferroelectric properties of γ-GC/BC composites prepared at the conditions RT/24 h, 60 ℃/24 h and 120 ℃/24 h, at the electric field of 5 kV/cm. And f) the corresponding P_r and E_c values.

Table 4.2 A comparison of dielectric constant (ε_r), remanent polarization (P_r), and coercive electric field (E_c) of various piezoelectric biomaterials with γ-GC/BC composite.

Piezoelectric Biomaterials	Material	Type	ε_r 100 Hz-1MHz	P_r μC/cm^2	E_c kV/cm	Ref
Inorganic piezoelectric materials	PZT	Ceramic	1,250.00	22.75	8.60	[151, 152]
	ZnO	Crystal	4.00	16.31	6.11	[153]
	$BaTiO_3$	Ceramic	1,135.00	12.60	30.00	[154]
	$LiNbO_3$	Ceramic	62.00	-	-	[155]
Organic piezoelectric materials	Chitin nanofiber	Protein	8.00	0.178	62.00	[156]
	Bone	Tissue	9.20	0.620	0.85	[157]
	Eggshell	Tissue	19.00	0.460	20.00	[158]
	Onion skin	Cellulose fibrous	32.80	0.068	10.00	[159]
	Silk	Semi-crystalline	3.40	0.050	35.00	[160]
	β-Glycine-Chitosan	Amino-Protein	3.50	-	-	[161]
	γ-Glycine-BC	Amino-Cellulose	12.00	0.004	1.20	This work

4.4 Conclusion

The present study reports the successful fabrication of γ-GC-BC composite ceramic using CSP. The optimized process was carried out at 120 °C/24 h under applied uniaxial pressure of 2000 kPa, resulting in a high density of 97%. IR and XRD results confirmed the γ-GC phase stabilization without any transformation to the metastable α-GC. The incorporation of BC into the γ-GC matrix led to significant improvements in the Vickers hardness. This improvement can be attributed to the formation of strong hydrogen bonds between the amino acids of γ-GC and the hydroxyl groups of BC. The electrical behavior of the composite was studied by examining temperature-dependent (RT to 150 °C) and frequency-dependent (100 Hz-1 MHz) dielectric properties. The composite exhibited a high dielectric constant of 984 with low tan δ. The ferroelectric properties were also determined by measuring

the P-E hysteresis loop, where the 120 °C/24 h γ-GC-BC composite ceramic exhibited the highest P_s = 0.013 μC/cm2 and P_r = 0.004 μC/cm^2. Our results clearly demonstrate the potential of CSP to successfully fabricate the high-density γ-GC-BC composite ceramics at low temperatures.

CHAPTER 5

THE ROLE of γ- $C_2H_5NO_2$ AS a NEW TRANSIENT LIQUID PHASE IN COLD SINTERING PROCESS OF $BaTiO_3$ COMPOSITES

Based on article published in Journal of Advanced Ceramics

Lead-free piezoelectric materials, like barium titanate-based (BT-based), have excellent piezoelectric properties, but require high temperatures (above 1300 ˚C) for ceramic fabrication, leading to high costs and energy loss. The cold sintering process (CSP) offers a solution to these issues and is gaining worldwide attention as an innovative fabrication route. In this work, we proposed an alternative organic ferroelectric phase, gamma-glycine (γ-GC) that acts as a transient liquid phase to fabricate high-density composites with barium titanate (BT) at low-temperature through a CSP. Our findings show that the density of 15 γ-GC/85BT reached 96.7% when sintered at 120 ˚C for 6 hours (h) under 10,000 kPa uniaxial pressure. The SEM-EDS mapping of the composite suggested that γ-GC completely underwent the precipitation-dissolution process and, therefore, filled between BT particles. Moreover, XRD and FTIR confirmed the preservation of γ-GC without the undesired phase transformation. In addition, the ferroelectric and dielectric properties of the γ-GC/BT composites were reported. The high dielectric constant (ε_r) was 3600, and the low dielectric loss (tan δ) was 1.20 at 200 ˚C, 100kHz, with 15 γ-GC/85BT composite. The hysteresis loop showed a remanent polarization (P_r) of 0.55 μC•cm^{-2} and a coercive field (E_c) of 7.25 kV•cm^{-1}. Our findings reaffirmed that organic ferroelectric material (γ-GC) can act as a transient liquid phase in a CSP that can successfully and sustainably fabricate γ-GC/BT composites at low temperatures while delivering outstandingly high performance.

5.1 Introduction

In recent years, a groundbreaking low-temperature sintering technique known as the cold sintering process (CSP) was discovered by Randall *et al.* [162] at Pennsylvania State University in 2016, has emerged as a highly effective method for producing dense ceramic materials. The CSP involves homogenizing powdered inorganic compounds with a transient liquid phase. This blending process yields a uniform mixture characterized by the presence of a transient liquid phase, typically constituting 1 to 10% of the total volume. Utilizing pressures ranging from 100 MPa to 700 MPa and temperatures below 300°C, CSP facilitates the evaporation of solvents and the densification of inorganic compounds, resulting in the formation of high-density sintered materials [163]. The core processing variables of CSP, including the transient liquid phase, sintering temperature, pressure, and holding time, play pivotal roles in driving the densification process of materials [139]. Of particular significance, the transient liquid phase substantially contributes to the dissolution-precipitation phenomenon within CSP. This mechanism enables the partial dissolution of sharp particle edges, thereby creating spaces for particle rearrangement. Moreover, the liquid phase readily redistributes itself, filling particle interstitials and fostering grain growth [142]. CSP has been successfully applied to water-soluble materials such as sodium chloride (NaCl), where NaCl particles diffuse throughout the water film, filling voids and precipitating through the dissolution-precipitation process inherent to CSP. Consequently, CSP can achieve high relative densities exceeding 90% after 24 h at room temperature and 75% relative humidity. Furthermore, CSP has been effectively employed with various ferroelectric or piezoelectric materials, including KH_2PO_4, $NaNO_2$, CeO_2, and BT [17, 164]. Notably, KH_2PO_4 and $NaNO_2$ exhibit high relative densities (>98%) comparable to conventionally sintered materials, even when treated at temperatures below 120 ˚C under 350 MPa without additional treatment. However, for materials with low water solubility, a tailored liquid solution becomes imperative. In a similar vein, Hanzheng Guo *et al*. [165] employed CSP to fabricate high-density BT ceramic at temperatures below 200 ˚C. By utilizing a 25wt% $Ba(OH)_2/TiO_2$ solution as a transient liquid phase and consolidating at 180°C under 430 MPa pressure, they achieved a relative density of 95%. However, a subsequent annealing step at 900 ˚C, while achieving characteristics comparable to conventionally sintered counterparts,

nullified the advantage of low-temperature manufacturing, preventing the production of new composites below 300 °C. Addressing the limitation, Tsuji *et al.* [166] successfully fabricated dense and high-quality BT materials via cold sintering at 300 °C in single-step using NaOH-KOH eutectic fluxes. Nevertheless, the severe conditions of strong alkaline fluxes at 300 °C restrict the fabrication of innovative composites with additives such as polymers, 2D materials, and fibers due to the necessity of appropriate quick kinetics for the congruent dissolution of the ceramic phase's surface ions to ensure dense ceramic manufacturing.

Despite these challenges, recent studies have demonstrated the feasibility of co-sintering various materials through CSP, enabling the fabrication of novel composite materials. Notably, low melting point materials such as thermoplastic [167], thermosetting [168], and 2D-nanostructured materials [169] can serve as transient liquid phases in CSP, modifying matrix material qualities including density, strength, hardness, and electrical properties [170, 171]. For instance, Jing Guo et al. [169] conducted CSP to manufacture a cold co-sintering process of 2D-MXene and ZnO at 300 °C for 1 h under 250 MPa pressure, resulting in improved electrical conductivity with the addition of up to 5wt% $Ti_3C_2T_x$ MXene. Takao Sada et al. [172] successfully co-sintered BT and PTFE using $Ba(OH)_2{\cdot}8H_2O$ flux, bridging the temperature gap between ferroelectric ceramics and polymers, albeit with challenges related to non-homogeneous polymer distribution. Similarly, Subramaniyan Vinoth and Sea-Fue Wang [173] effectively prepared BT/poly(vinylidene difluoride) nanocomposites, albeit with issues regarding the homogeneity of polymer distribution and unclear ferroelectric properties attributed to grain boundary microstructure [174]. In our previous work, we found that organic ferroelectric materials, including γ-GC, can be fabricated into a composite with bacterial cellulose (BC) powder via CSP and achieved satisfactory ferroelectric effects at conditions 120 ° C/24h [175]. The γ-GC is the thermodynamically most stable phase and exhibited piezoelectric effects at room temperature because it has a winding hydrogen bond network, unlike the other two main phases (α and β phase) [176, 177]. Moreover, its water solubility qualifies it for usage as a transient liquid phase in a CSP [24, 178].

The present study proposes the use of γ-GC phase to fabricate piezoelectric composites via the cold sintering process (CSP). The γ-GC phase is an ideal transient

liquid phase that induces excellent dissolution-precipitation phenomena during the CSP. Moreover, it exhibits remarkable ferroelectric properties that do not interfere with the properties of the primary phase. The focus of this research is to determine the optimized quantity of γ-GC phase for high-density BT composite through the CSP. A comprehensive examination of the time and temperature conditions applied in the CSP is conducted to refine the fabrication process and enhance the overall performance of the resulting composites.

5.2 Experimental procedure

5.2.1 Gamma glycine (γ-GC) preparation

The γ-GC compound was synthesized using a method described in literature [175]. Firstly, 56 g of commercial-grade glycine and 15 g of sodium chloride in a 3:1 molar ratio were dissolved in 100 mL of deionized water (DI water) by stirring for 5 h at room temperature (RT). The resulting mixture was then filtered using vacuum filtration, and the obtained liquid was kept in an oven at 35 ˚C for 25 days. During this aging process, α-G crystals were transformed into γ-GC crystals. The γ-GC crystals were then washed with saturated glycine solution, ground for 3 h using a ball mill, and finally placed in the oven for an additional 2 days. This process resulted in the successful synthesis of γ-GC crystals.

5.2.2 Barium titanate (BT) preparation

Two types of BT powders were employed: (i) as purchased, a commercial product from Inframat Advanced Materials, LLC ($BaTiO_3$ nano-powder, 99.95%), and (ii) Heat-treated commercial BT powder at 1200 ˚C for 12 h in air. Both powders (untreated, and heat-treated) were separately stirred with 1 M acetic acid solution at 80 ˚C for 1 h. Then, the pH of the suspension was adjusted to neutral, and the respective BT powders were filtered prior to drying in an oven at 60 ˚C for 24 h, as schematically shown in Figure 5.1a.

5.2.3 Fabrication of γ-GC/BT composites via CSP

To optimize packing density, a specific ratio of 73.6/26.4, determined by theoretical predictions for dense random packing, was employed for mixing BT particles of both nanometer (untreated particles) and micrometer (heat-treated particles) sizes. Subsequently, the fabrication process of composites involving γ-GC

and BT via CSP was initiated by precisely measuring 2.208 g of heat-treated BT and 0.792 g of untreated BT. These two types of BT were thoroughly combined in a mortar for a duration of 5 minutes to ensure homogeneity. Following this, varying proportions (15%, 30%, 50%, and 90% by weight) of γ-GC powder were incorporated into the BT mixture and meticulously blended manually in the mortar for an additional 5 minutes. Subsequently, 7wt% of DI water was introduced into the blend, which was then ground for an additional 5 minutes to facilitate thorough mixing. Next, 0.3 grams of the resulting γ-GC/BT mixture were meticulously deposited into a tungsten carbide die. In the context of the CSP, the initial mixture undergoes continuous compression via a straightforward uniaxial pressure of 10 MPa. Heating is facilitated by a resistance jacket enveloping the die system within the CS equipment employed. The heating jacket demonstrates the capability to ramp up the temperature at a steady rate of 3 °C per minute, reaching a maximum temperature of 120 °C. The specified heating temperature and duration were maintained for 6 hours. The CSP apparatus utilized in this investigation was constructed as depicted in Figure 5.1b (I-III). Once the process was completed, the cold-sintered γ-GC/BT composite was allowed to cool before being extracted from the block for subsequent characterization analysis.

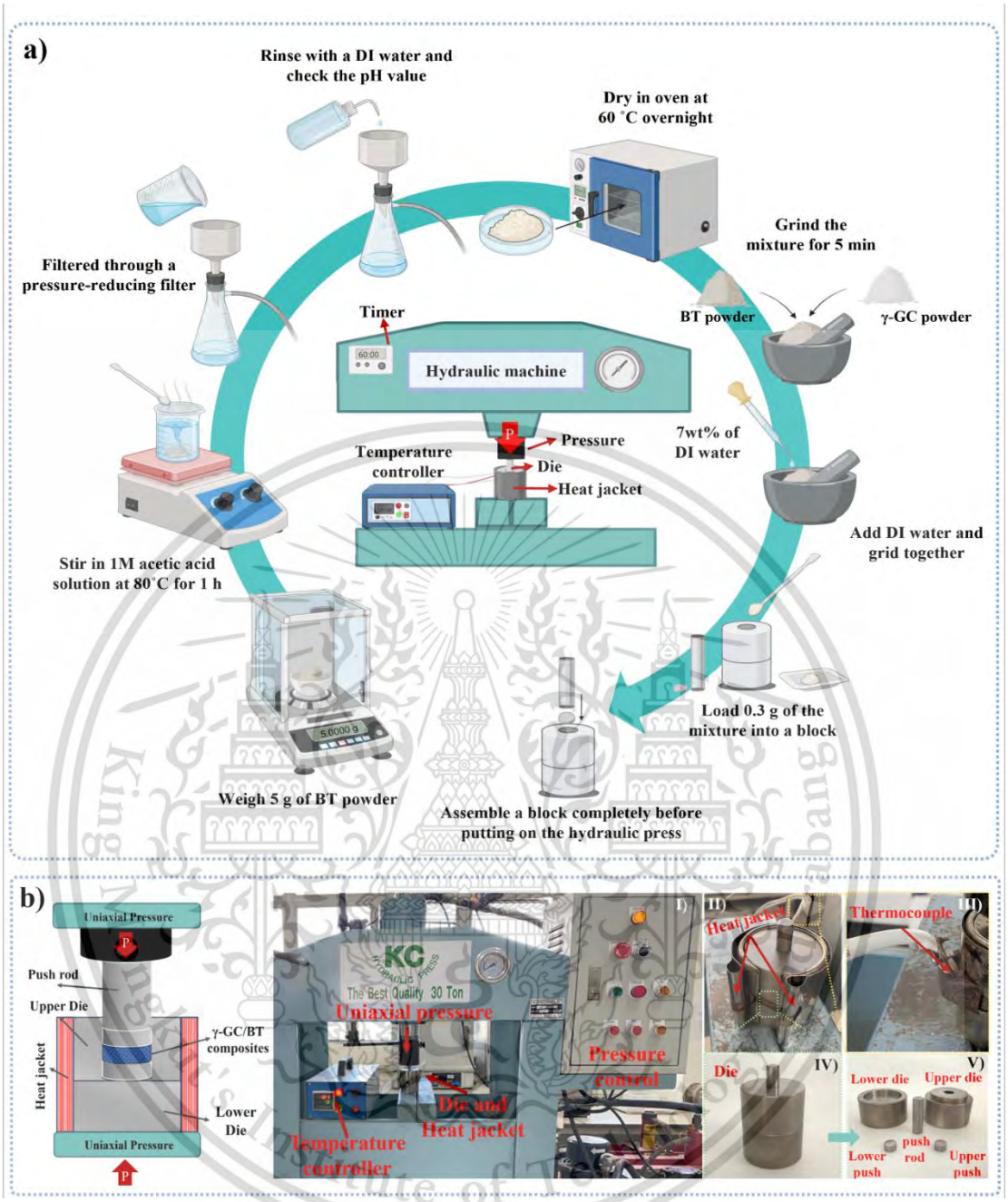

Figure 5.1 Schematic illustration of the fabrication process of the γ-GC/BT composite via CSP.

5.2.4 Characterization

Although the Archimedes method is renowned for its precision in determining density, its utility in our investigation was hampered by the solubility properties of γ-GC in polar solvents. Traditional organic solvents employed in Archimedes' principle, such as water, ethanol, isopropanol, and acetone, were deemed incompatible with

our samples due to their inherent polarity. Moreover, the use of nonpolar solvents posed a risk of altering the phase or stability of γ-GC. Additionally, the metastable nature of γ-GC warranted cautious immersion protocols, as it could lead to phase transitions in glycine. Consequently, we adopted an alternative approach to determine sample density, relying on measurements of mass, thickness, and dimensions. By employing 12 samples, we aimed to account for inherent variations within the sample set, thereby obtaining a more comprehensive representation of density. Densification calculations were performed using Equation 5.1, elucidating the ratio of actual density to theoretical density [175],[179].

$$R = \frac{4m}{(\pi d^2 h \rho)} \times 100\% \quad (5.1)$$

where R is the relative density (%), m is the mass (g) of the pellet, d is the diameter (cm) of the pellet, h is the thickness (cm) of the pellet, and r is the theoretical density calculated from the Equation 5.2.

$$\rho = \frac{m}{(\frac{m_{BT}}{\rho_{BT}} + \frac{m_{\gamma-GC}}{\rho_{\gamma-GC}})} \quad (5.2)$$

where m_{BT} and $m_{\gamma-GC}$ represent the masses of BT and γ-GC in the composite pellet; ρ_{BT} and $\rho_{\gamma-GC}$ represent the theoretical densities of BT and γ-GC, which are 6.02 g/cm^3 and 1.59 g/cm^3, respectively [175, 180].

The phase purity and crystal structure of the cold-sintered γ-GC/BT composite at varying weight ratios from 15% to 90% were identified by X-ray diffraction (XRD, RIGAKU smart lab) with Cu Kα (λ = 1.5418 Å) radiation in the range of 2θ = 10° to 80°. The XRD results were compared to the JCPDS database. Moreover, LeBail refinement of the unit cell parameters was performed using JANA2006 software. The crystallite size estimation calculated for the corresponding phase was done by using the Scherrer Equation 5.3.

$$L = \frac{K\lambda}{(FWHM \times cos\theta)} \quad (5.3)$$

where L refers to the crystallite size, K is the Scherrer constant (K = 0.94), λ is the wavelength of the radiation, θ is the diffraction angle of the peak, and $FWHM$ is the full width at half maximum.

The BT and γ-GC powders were subjected to Fourier-Transform Infrared Spectroscopy (FT-IR, SHI-MADZU, IRTracer-100) measurement in a transmission mode from 400 to 4,000 cm^{-1} with a resolution of 4 cm^{-1} to confirm the presence of functional groups. The morphology, particles size and grain size of untreated / heat-treated particles and cold-sintered γ-GC/BT composite were observed by field emission scanning electron microscopy (FE-SEM, TESCAN, model MIRA) and transmission electron microscopy (TEM, FEI, Model: TECNAI G2 20, Netherlands). In addition, energy dispersive X-ray spectroscopy (EDS-mapping) was performed to analyze the chemical components of materials. Particle size and particle size distribution were measured and analyzed through examination and quantitative analysis using ImageJ software. The three-dimensional (3D) X-ray image of the cold-sintered γ-GC/BT composite was obtained using Synchrotron Radiation X-ray Tomographic Microscopy (SR-XTM) technique at beamline 1.2 W, SLRI, Thailand. X-ray intensity was controlled by attenuating polychromatic X-rays with a 350 μm-thick aluminum foil. X-ray images were captured using a microscopic lens system and recorded by an sCMOS camera with a 1.44-μm pixel size. The X-ray images dataset was converted into sinograms, which were used in the Octopus Reconstruction software. The reconstructed images were visualized using Drishti software. The dielectric behavior including dielectric constant (ε_r) and loss tangent (tan δ) of cold-sintered γ-GC/BT composites was studied using an LCR meter (Agilent E4908A) from RT to 200 °C at frequencies ranging from 100 Hz to 2MHz. The polarization versus electric field hysteresis (P-E) curves of cold-sintered γ-GC/BT composites were measured at RT by a standard ferroelectric test system (RT66A) from Radiant Technologies.

5.3 Results and Discussion

The morphology of the commercial nano-crystallites BT powder (untreated particles) is presented in Figure 5.2a, where SEM imaging showcases randomly distributed particles, with a smaller subset exhibiting homogeneously spherical-shaped particles of smaller size. ImageJ analysis revealed a Gaussian distribution of particle sizes, indicating a relatively uniform particle size population. The mean

particle size was determined to be 75.85 ± 13.65 nm, with a narrow size distribution. The skewness and kurtosis values were close to zero, suggesting symmetry and a moderate peak, respectively. After the heat treatment process, agglomerates of varying sizes became apparent, as depicted in Figure 5.2d. The SEM images revealed a bimodal distribution with peak particle sizes observed at 1.39 ± 0.03 μm and 4.83 ± 0.11 μm. This distribution suggests the presence of two distinct populations of particles within the sample, possibly indicating different stages of aggregation or variations in particle formation mechanisms [181]. It's noteworthy that the heat-treated particles exhibit sizes within the micron range, which are more than 30 times larger compared to the untreated particles. BT particles of both nanometer and micrometer sizes will be mixed at a specific ratio determined by theoretical predictions for dense random packing. The TEM bright field image, the selected area electron diffraction (SAED) pattern, and the high-resolution TEM image (HRTEM) of BT powders before and after heat treatment at 1,200 °C for 12 h are shown in Figure 5.2b-c, e-f. For the untreated powder (Figure 5.2b), the particles appear nearly spherical with an average diameter of 78.14 ± 19.12 nm. The inset SAED pattern shows a polycrystalline diffraction ring made up of separate diffraction spots, indicating the polycrystalline nature of the nanoparticles [182]. Further fringes in BT were detected by HR-TEM. Figure 5.2c exhibits lattice fringe with the interfering distance at 0.287 nm, which corresponds to the crystal plane (110) spacing of the cubic BT phase (JCPDS card no. 075-0213, d (110) = 0.283 nm). In contrast, the BT powder, after heat treatment at 1,200 °C for 12 h (Figure 5.2e), demonstrates particle agglomeration, resulting in a tenfold increase in the average particle size compared to the untreated powder. The inset SAED pattern shows the bright spots assigned to the lattice atoms that were spaced crystallographically with perfect plan orientation of BT, suggesting high crystallinity and structural perfection for the tetragonal perovskite structure [183]. Clear lattice fringes are observed (Figure 5.2f) with the measured interplanar spacing of about 0.286 nm corresponding the crystallographic plane (101) of tetragonal BT (JCPDS card no. 079-2265, $d_{(101)}$ = 0.285) [184, 185]. These results confirmed that a high-temperature calcination results in phase transformation of BT from cubic to tetragonal.

Moreover, the XRD pattern (Figure 5.2g) was consistent with the above results and the LeBail refinement. All the peaks (blue lines) are indexed (JCPDS card no. 079-2265) for cubic phase formation of the space group Pm-3m. The lattice parameters were a=b=c= 4.0067 Å and V = 65.3 Å. The parameters of refinement are R_p = 10.59, R_{wp} = 16.62 and GOF = 2.01. The R factors present a good agreement between refined and experimental XRD profiles for BT. The average crystallite sizes as estimated by Scherrer formula Equation 5.3 was 20.33 nm using the (110) major diffraction peak. After calcination of BT at 1,200 °C/12 h, the diffraction peaks (red line) are sharp and narrow, indicating high crystallinity. All peaks are indexed (JCPDS card no. 075-0213) for tetragonal phase, as judged from the splitting of the (200) diffraction plane into (002) and (200) at 51.02°and 56.3°, respectively. Lattice parameters were a = b = 3.9919 Å, c = 4.0321 Å and V = 64.3 Å, which belongs to space group of P4/mmm [186]. The parameters of refinement are R_p = 11.59, R_{wp} = 17.04 and GOF = 1.97. The average crystallite size was 27.56 ± 3.12 nm. These findings suggest that the tetragonal structure of BT phases is generated through high-temperature calcination.

The BT powder before and after calcination were characterized by FTIR in transmission mode as shown in Figure 5.2h. For the BT powder before calcination, the absorption bands appeared at 3507 cm^{-1}, which corresponded to the stretching mode of O-H groups. The band at 1637 cm^{-1} is characteristic of the O-H bending from the physically adsorbed water on BT nanoparticles. The strong absorption at 487 cm^{-1} is assigned to the bending vibrations of the Ti-O bond in $[TiO_6]^{2-}$ octahedron. It is also a characteristic absorption of BT powder [187]. Notably, the intensity of the O-H stretching vibration bands at 3507 cm^{-1} and 1637 cm^{-1} became weaker as the calcination temperature increased, showing clearly instead the metal-oxygen (Ti-O) band stretching [188-190].

The γ-GC powder and the mixed BT powder were mixed at a varying weight ratio (15, 30, 50, and 90wt% of γ-GC powder) and grounded in a mortar, followed by addition of 7wt% of DI water and another grinding. Then, 0.3 g of the γ-GC/BT mixture was loaded into a tungsten carbide block, and a pressure of 10 MPa was applied. CSP was carried forward for 6 h before heating to 120 °C. At the end of the process, the

tungsten carbide block was cooled, and the γ-GC/BT composite pellets were removed.

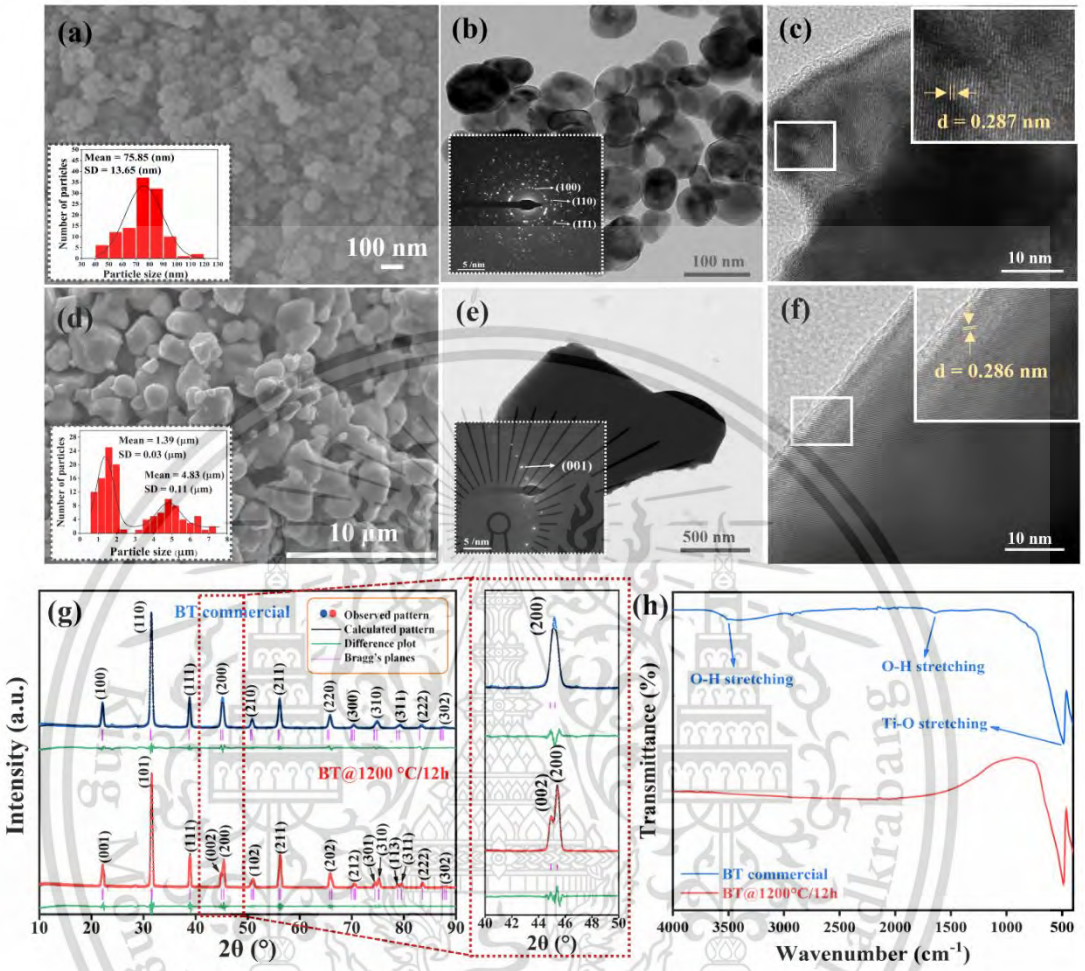

Figure 5.2 SEM images of a) BT commercial powder before calcination and d) BT after calcination at 1,200 ˚C for 12 h. b), e) show TEM images of BT powder before and after calcination at 1200 ˚C for 12 h respectively. The inset shows the corresponding SAED patterns. c), f) the high-resolution TEM and the white frame showing the lattice fringe. g), h) XRD and FTIR results of BT powder before and after calcination at 1200 ˚C for 12 h.

The white pellets, depicted in the inset of Figure 5.3, possess a diameter of 1 cm and a thickness of approximately 0.7 mm. In the case of a composite sintered with 15wt% of γ-GC (Figure 5.3a), the surface predominantly comprises 85wt% BT, resulting in densely packed BT particles and a smooth surface with reduced pore

count. Subsequently, with an increase in γ-GC content to 30% (Figure 5.3b), the surface remains smooth, albeit with small porous areas emerging. Upon further escalation of γ-GC content to 50wt% (Figure 5.3c), the surface manifests large particle clusters, nanoparticle dispersion throughout the matrix, and some filling of gaps, leading to heightened porosity and surface unevenness. The average grain size measures 3.92 ± 1.75 μm. Notably, at 90wt% γ-GC (Figure 5.3d), irregularly arranged large clumps of γ-GC particles, numerous small grain sizes (average grain size of 6.67 ± 4.17 μm), and substantial interparticle voids are observed. Additionally, nanoparticles are dispersed within the matrix. The SEM results underscore that an optimal γ-GC content of 15wt% fosters the formation of dense γ-GC/BT composites.

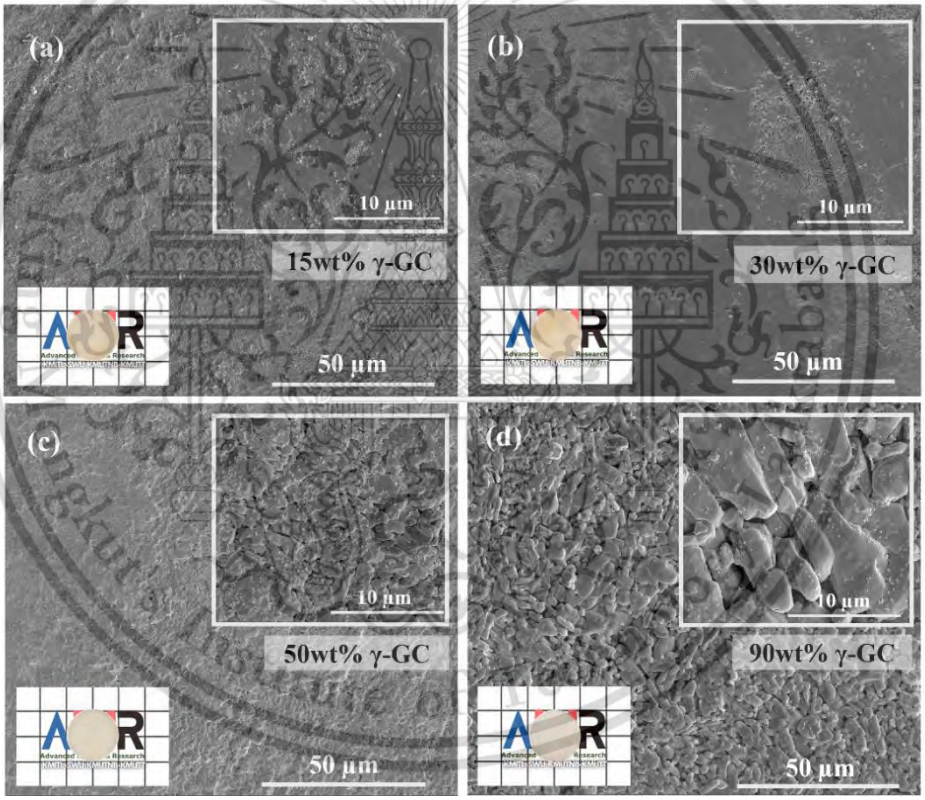

Figure 5.3 SEM images of cold-sintered composites between γ-GC and BT as prepared through CSP at varying amount of γ-GC: a) 15wt% b) 30wt% c) 50wt% and d) 90wt%. The bottom-left insets show the corresponding digital image of the pellet. The white frame on top-right shows morphological features under 10,000 x magnification.

Furthermore, SEM mapping and EDS analysis were conducted to explore the chemical composition of the composites, leveraging X-ray emissions pertaining to the constituent elements. The presence of γ-GC and BT was confirmed by the detection of Ba, Ti, N, C, and O. SEM mapping of 15wt% γ-GC pellets (Figure 5.4) reveals large agglomerations of Ba (Figure 5.4c) and Ti (Figure 5.4d), with gaps between them filled with Nitrogen (N) (Figure 5.4f) and Carbon (C) (Figure 5.4g), elements characteristic of γ-GC. Furthermore, EDS measurement (Figure 5.4h) confirms the presence of Ba, Ti, O, N, and C elements in the composites, with Ba, Ti, and O comprising 41.2%, 18.4%, and 19.6% by weight, respectively. The Ba and Ti signals correspond to the BT content in 15wt% γ-GC pellets, affirming γ-GC's capacity to bind BT and form a ceramic composite via CSP.

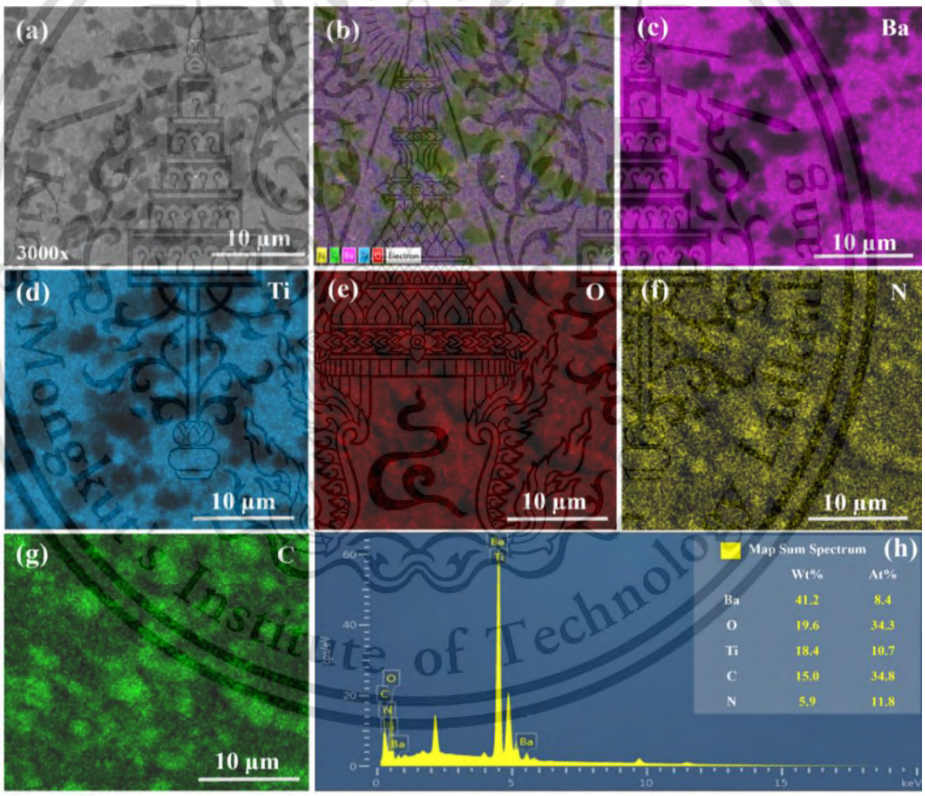

Figure 5.4 The SEM-EDS mapping of 15wt% γ-GC pellet: a) SEM image at a magnification of 3,000x for the composite 15wt% γ-GC/BT. b) All mapping elements. c-g) Mapping image of Ba, Ti, O, N, and C elements in the composites. h) The EDS spectrum with the table in the inset showing a quantitative result obtained for Ba, O, Ti, C, and N.

The XTM images of the composites containing 5wt%, 30wt%, and 90wt% of γ-GC/BT were obtained using Synchrotron Radiation X-ray Tomographic Microscopy (SR-XTM). These images provide a macroscopic view of the 3D distribution of the components, distinguishing between two distinct phases represented by orange (γ-GC) and purple (BT). For the composites containing 5wt% γ-GC (Figure 5.5a) and 30wt% γ-GC (Figure 5.5b), BT acts as the matrix phase, with γ-GC evenly dispersed over the BT surface. Additionally, in certain regions, the γ-GC phase precipitates and fills the gaps between BT particles. However, as the γ-GC content increases to 90wt% (Figure 5.5c), BT becomes uniformly distributed within the γ-GC matrix. The XTM image verifies that the γ-GC phase is dispersed throughout the specimen, with instances of agglomeration and precipitation between BT particles, a finding consistent with SEM observations. These XTM findings offer valuable insights into the spatial arrangement and distribution of γ-GC and BT phases within the composites, shedding light on their microstructural characteristics and providing essential information for understanding the composite's properties and behaviors.

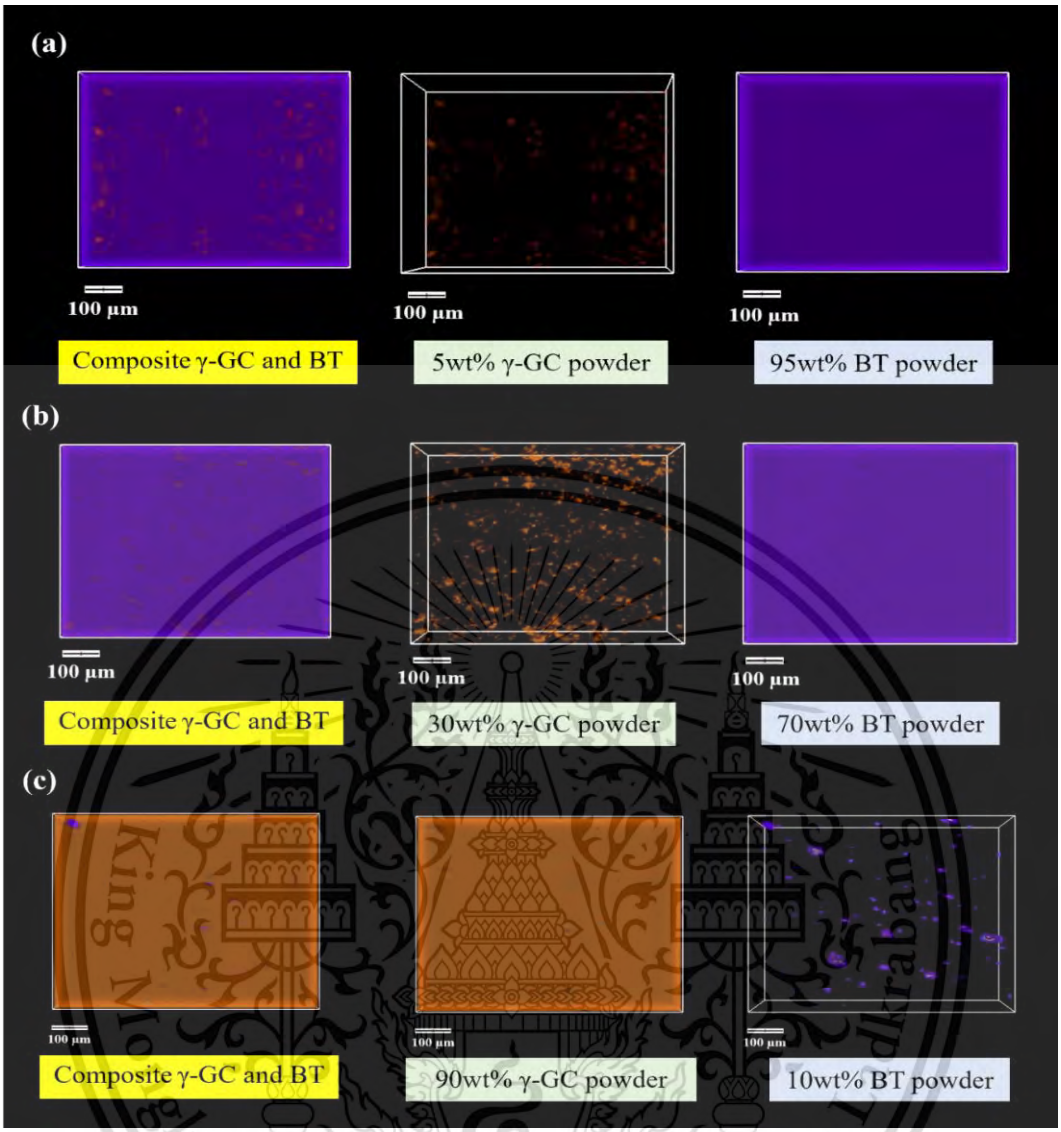

Figure 5.5 X-ray tomographic 3D visualization of γ-GC/BT composites via CSP at varying γ-GC contents a) 5wt% b) 30wt% and c) 90wt% respectively.

The relative density of the γ-GC/BT composites, as determined by Equation 5.1, is illustrated in Figure 5.6a. As the weight percentage of γ-GC increases from 15% to 90%, a corresponding trend of decreasing relative density is observed, declining from 96.7 ± 1.2% to 82.7 ± 1.1%. These findings align closely with the observations from SEM imaging. With a decrease in γ-GC content, the particles of BT exhibit a more compact arrangement compared to the composites containing 90wt% γ-GC, primarily due to the inherently higher density of BT. Furthermore, the presence of γ-GC serves

to fill the interstitial spaces between BT particles, thereby reducing pore formation. This phenomenon contributes to the overall reduction in porosity and subsequent enhancement in relative density. The relative density can be explained by a mechanism as reported in the previous study [175]. It was found that pressure, sintering temperature, holding times, and transient liquid solvent are important factors for the effective CSP. BT powder is known to be thermodynamically unstable in water solutions. Ba^{2+} ions are leached out of the BT powder, producing a TiO_2^- rich amorphous surface layer [191, 192]. The amorphous layer, which is difficult to dissolve in the liquid phase, impedes the dissolution-precipitation process during the CSP, thereby preventing the densification of the BT ceramic. Therefore, the surface of BT powders in this work was treated with acetic acid (CH_3COOH) to generate additional -OH groups on the BT particle surfaces (Figure 5.6b) via hydroxylation reaction [193]. When the γ-GC powder is mixed with (acid-treated) BT particles and fabricated via CSP, hydrogen bond will form between the -COOH groups on the γ-GC chains and the -OH groups on the surfaces of BT particles [194, 195]. An appropriate amount of γ-GC can easily dissolve in water and act as the liquid phase, which enhances the dissolution-precipitation process during CSP. So, γ-GC promotes close packing in the composites and enhances the relative density of composites [196].

Furthermore, to elucidate the structural behavior, X-ray diffraction (XRD) analysis was employed to assess the cold-sintered samples, as depicted in Figure 5.6c. Notably, all sintered samples (15wt%, 30wt%, 50wt%, and 90wt% of γ-GC) manifest sharp diffraction peaks corresponding to two distinct phases: $BaTiO_3$ (tetragonal; JCPDS no. 075-0213) and γ-GC (JCPDS no. 06-230). At 90wt% of γ-GC, two prominent peaks observed at 25.28˚ and 31.57˚ can be unequivocally indexed to the (110) and (101) diffraction planes of γ-GC and BT respectively. As the γ-GC content decreases, notably, the intensity of the γ-GC peak at 25.28˚ undergoes a significant reduction, consistent with expectations. Subsequently, at γ-GC contents of 30wt% and 15wt%, the characteristic peaks associated with γ-GC are conspicuously absent from the diffraction patterns.

The cold-sintered samples underwent characterization using FTIR in transmission mode, with the results presented in Figure 5.6d. Across all sintered

samples, distinct peaks indicative of γ-GC patterns emerged within the range of 1,500-1,200 cm^{-1} [197] . Notably, the highest intensity peak at 1,573 cm^{-1} (peak 1) corresponds to the asymmetric (C=O)O stretching, while the peak at 1,492 cm^{-1} (peak 2) signifies the NH bending vibration of NH_3^+. Additionally, the peak at 1,390 cm^{-1} (peak 3) corresponds to the symmetric (C=O)O stretching, whereas the peak at 1,328 cm^{-1} (peak 4) represents the CH_2 wagging with the lowest intensity. These observations collectively affirm the presence of γ-GC within the samples. However, a notable trend emerges as the γ-GC content decreases: the intensity of the four peaks diminishes significantly, accompanied by peak overlap within the range of 486-684 cm^{-1}. The overlapping peaks are attributed to the carboxylate ion group COO^- of γ-GC and the stretching vibrations of Ti-O of BT, further underscoring the formation of composites between γ-GC and BT. Importantly, no undesired phase transition of γ-GC was observed throughout the analysis, affirming the stability of the composite structure.

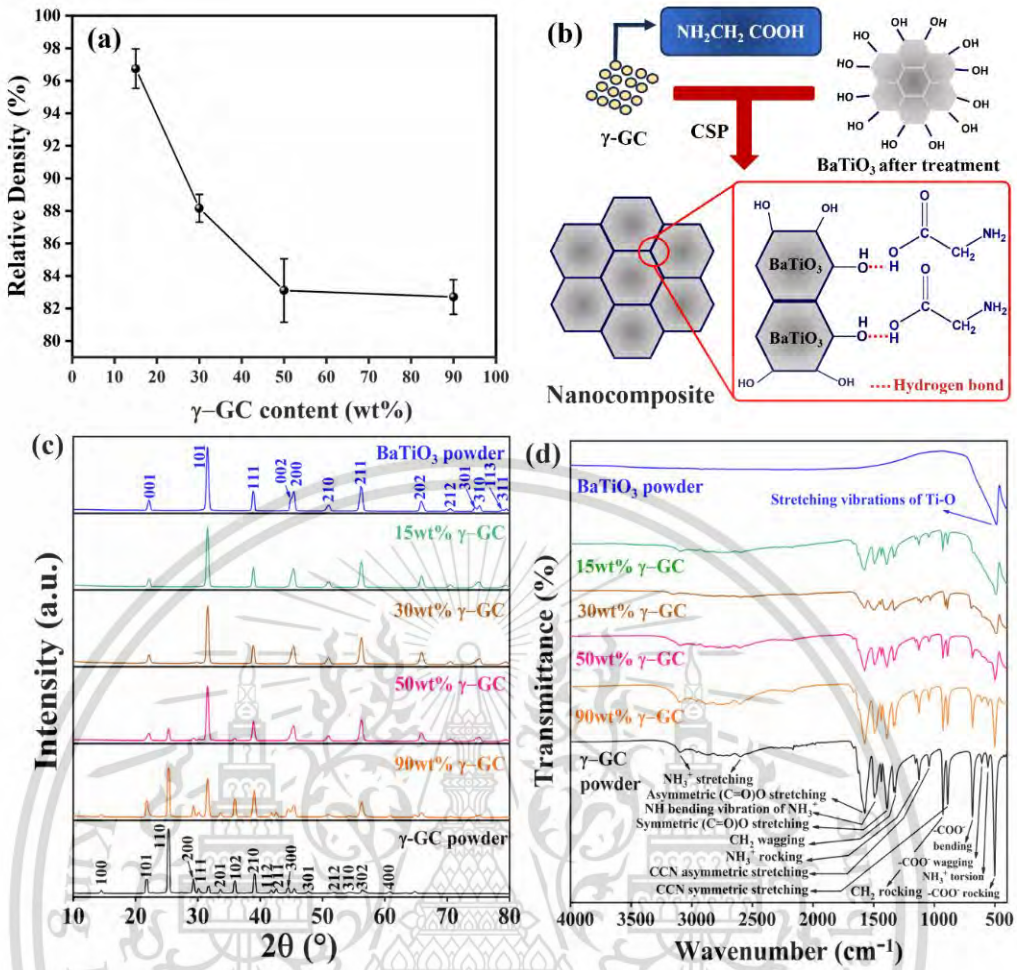

Figure 5.6 The relative density of γ-GC/BT composites after CSP a) variation of the γ-GC contents. b) schematic diagram of BT after treatment with 1 M acetic acid, showing the surface OH group on BT surfaces and the formation of hydrogen bonds in the γ-GC/BT composite, c) XRD patterns and d) FTIR spectrum of γ-GC/BT composites.

The density of composites, as elucidated in Figure 5.7, is expounded through the schematic representation of the cold sintering mechanism across various stages. Initially, the composite material particles (I) comprising γ-GC, BT, and water are densely packed. In the initial stage, a sufficient quantity of the liquid phase (water) is integrated with the composite particles, ensuring homogeneous moisturization. Here, γ-GC particles act as a transient liquid phase, dissolving and diffusing alongside water,

facilitating particle rearrangement (II). Notably, the pink frame in the illustration delineates the intricacies of particle sliding upon the introduction of the liquid phase, creating spaces at the particle-particle contact area. These spaces enable particle sliding and subsequent rearrangement. Densification primarily ensues under external pressure at this juncture, leading to overall sample shrinkage (S_1). Subsequently, in the second stage, a dissolution-precipitation process comes into play. Following particle dissolution, sliding, and rearrangement in the initial stage, mass transfer occurs via the diffusion of γ-GC ions or atoms along the water (III (a-ii)), effectively filling the interstitial gaps between grains. Consequently, precipitates (III(a-iii)) form on crystal sites with lower chemical potential, which are thermodynamically favored and conducive to neck growth. This mass transport process concurrently diminishes the surplus free energy of the surface and mitigates porosity, resulting in the formation of a dense solid and a slight sample shrinkage (S_2). The final stage, characterized by crystal growth (IV-b), is predominantly governed by a robust dynamic process catalyzed by water evaporation. This evaporation induces a supersaturated state of the liquid phase at temperatures slightly above its boiling point, thereby engendering a significant chemical driving force for the solid and liquid phases to attain equilibrium. Upon completion of precipitation, particle-particle contacts are markedly enhanced, facilitating crystal growth via the coalescence of small crystallites (Thickness = T_0) into larger ones (Thickness = T_1). The comprehensive overview of various BT-based ceramics and composites, detailing their raw materials, the presence of transient liquid phases, CSP conditions, achieved densities, and corresponding references is present in Table I. BT ceramics synthesized through solid-state reactions typically undergo high-temperature sintering, yielding densities between 94-96%. Alternatively, employing $Ba(OH)_2{\cdot}8H_2O$ as a transient liquid phase at 180 °C under pressure yields a density of 95%. Composite systems such as BT/ZnO and BT/Polytetrafluoroethylene exhibit densities ranging from 60%-98% and 93.5%, respectively, utilizing specific liquid phase chemistries and CSP conditions. Notably, the γ-GC/BT composites, synthesized at a lower temperature of 120 °C and 10 MPa pressure, demonstrate a density of 96.7±1.6%. These findings highlight the diverse synthesis strategies and optimization approaches employed in the fabrication of BT-based ceramics and composites for various applications.

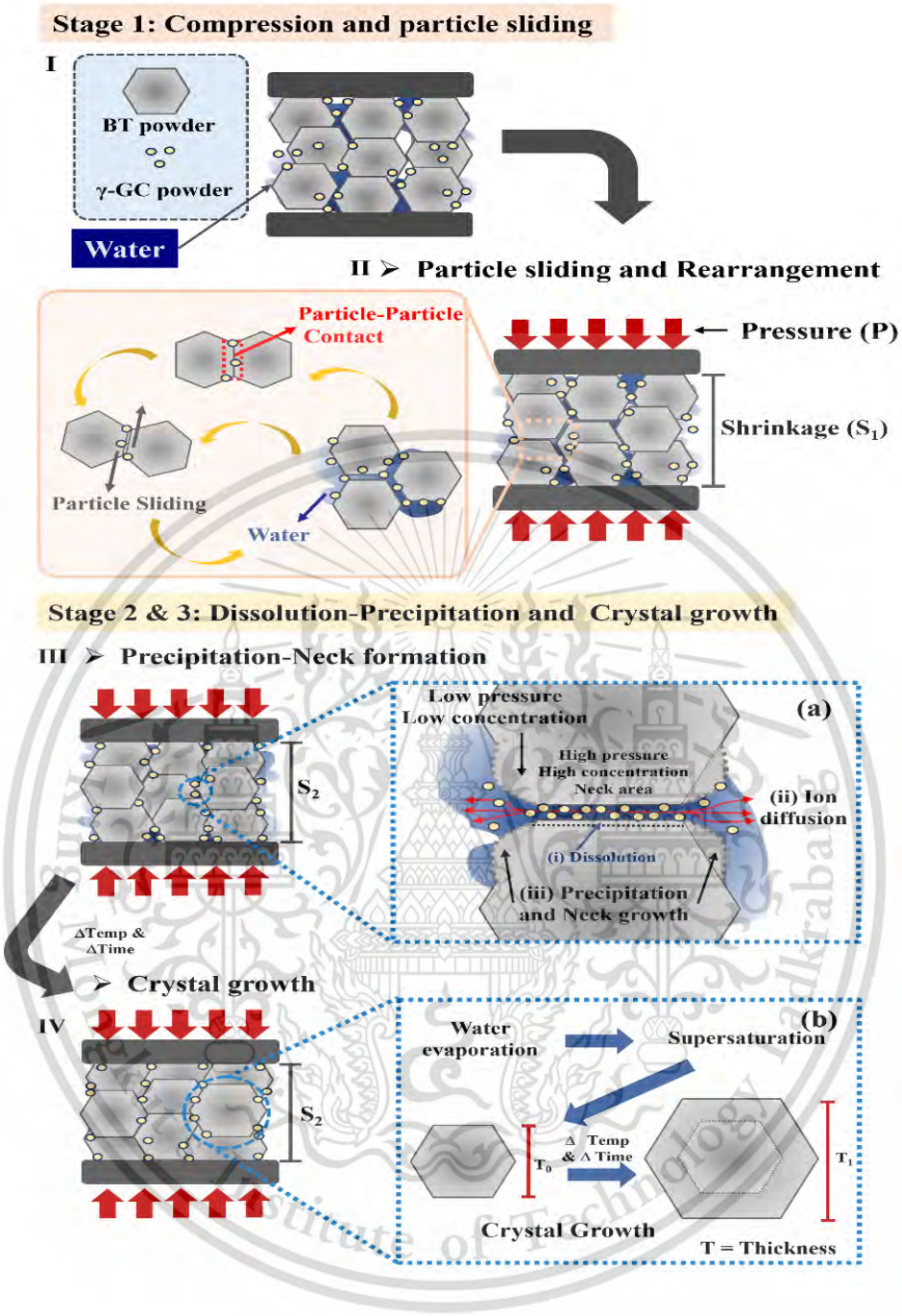

Figure 5.7 Schematics of CSP mechanism at mainly 3 stages adapted from Refs. [14, 175, 198]. Stage 1 involves I. particle compaction of composite consisting of γ-GC, BT, and water, II. Particle sliding and rearrangement. Stage 2 shows the dissolution-precipitation process, III. Precipitation-Neck formation. Details of this stage show in (a) dissolution (i), ion diffusion (ii), precipitation-neck growth (iii). Stage 3 is related to crystal growth (IV) and (b) shows the detail of its stage related to water evaporation and crystal growth.

The dielectric responses of the γ-GC/BT composites were examined as a function of temperatures and frequency. Figure 5.8a shows the temperature dependences of dielectric constant (ε_r) and dielectric loss (tan δ) for all composites from RT to 200 ˚C at 100 kHz. For the composites with 15-90 wt% γ-GC content, the value of ε_r tends to increase with increasing temperature. The maximum ε_r value obtained was 3,600, and the low tan δ was 1.20 for 15wt% γ-GC composite. The increased ε_r value is a result of the addition of ferroelectric ceramic powders primarily caused by the dipolar polarization effect and induced by the permanent dipoles existent in the filler. The permanent dipole of BT is from the uneven distribution of the charge-density between O, Ba, and Ti atom [199].

The frequency-dependences of ε_r and tan δ of the composites are shown in Figure 5.8b at 200 ˚C and the frequency from 100 Hz to 2 MHz. As frequency increases, ε_r decreases until it reaches a near-constant value at the high-frequency region. The high value of ε_r at low frequencies is caused by a combination of polarizations, including atomic, ionic, interfacial, and electronic. However, only electronic polarization affects the ε_r at high frequencies. The results clearly show that when the amount of γ-GC decrease, the dipole of the interface increase due to the BT content increase and leading in an increase ε_r [200]. At 15wt% γ-GC, ε_r = 27,000 and tan δ (which is the lowest) was 1.50 at 100 Hz.

We also demonstrate the beneficial effect of increasing proportion of γ-GC by examining other presentations of AC properties, as depicted in Figure 5.8c, where the positive impact of γ-GC becomes more apparent. The imaginary part of the complex dielectric permittivity e'' (dash line in Figure 5.8c, shown for 90wt% as an example) follows the universal power law [201, 202] $e'' = A \cdot f^{s-1}$, where A and s are the fitting parameters. The parameter s represents the effective dimension of charge carriers, [203, 204] being 1D for s ~ 0.17-0.44. Accordingly, the s values of 0.11 (30wt% γ-GC) and 0.22 (50wt% γ-GC) suggest the 1D nature. Meanwhile, at 90% γ-GC, the low s = 0.03 is close to zero such that e'' follows f^{-1}. This is the “low-frequency dispersion” [205, 206] which points out that very high charge densities are stored, consistent with the well-known capacitive nature of BT.

Figure 5.8d shows the *T*-dependent of the imaginary part of the complex electric modulus $M''\times100$ [$M'' = e''/(e'^2+ e''^2)$]. The electric modulus corresponds to the relaxation of an electric field in the material when the electric displacement remains constant [205] It was found that the sample with 30wt%, 50wt%, and 90wt% γ-GC had a relaxation peak at 87, 154, and 163 °C, respectively. The latter two might be compared to 132 °C obtained from the elastic (mechanical) modulus of BT sintered at 1,300 °C [206]. The different peak temperatures might be explained by different sintering methods (CSP vs traditional) and measurement methods (electric relaxation vs mechanical relaxation). Still, the shift of the relaxation is clear, presumably to the value of BT. Table 5.2 presents a comparison of the dielectric properties of BT and BT composites that were fabricated using CSP and traditional sintering methods. The results indicate that the dielectric properties of traditional sintered BT and γ-GC/BT composite are practically identical. Our study highlights the effectiveness of γ-GC as a transient liquid phase in CSP for the successful and sustainable production of high-density γ-GC/BT composites at relatively low temperatures.

The ferroelectric polarization-electric field (P-E) hysteresis loops of the γ-GC pellet and the γ-GC/BT composite pellets are shown in Figure 5.8e. It is found that the hysteresis loop of γ-GC/BT composite pellets becomes larger with increasing BT contents. Compared with γ-GC, the composite ceramics exhibit good symmetry and a well-saturated shape (see the inset). For 90wt% γ-GC, the surface has porosity, and the addition of BT makes the ferroelectric phase discontinuous as it hinders the domain orientation. However, as the γ-GC content decreases to 15wt%, the porosity is lower, and the ferroelectric property is optimized with easy switching of domains within materials. The measured values of the remnant polarization (P_r) and saturation polarization (P_s) at electric field of 20 kV•cm^{-1} are 0.013 μC•cm^{-2} and 0.025 μC•cm^{-2} for γ-GC, 0.035 μC•cm^{-2} and 0.052 μC•cm^{-2} for 90wt% γ-GC, 0.121 μC•cm^{-2} and 0.276 μC•cm^{-2} for 50wt% γ-GC, 0.554 μC•cm^{-2} and 1.466 μC•cm^{-2} for 15wt% γ-GC, respectively. In contrast, the coercive electric field (E_c) is lowest for pure γ-GC sample but increases for the 90wt% γ-GC. However, it was significantly decreased when the γ-GC content decreased further to 50wt% and 15wt% (Figure 5.8f). Moreover, P_s clearly increases as the BT content increases. These results indicate that γ-GC as a

transient liquid phase in a CSP can be successfully used to sustainably fabricate high-density composites between γ-GC and BT.

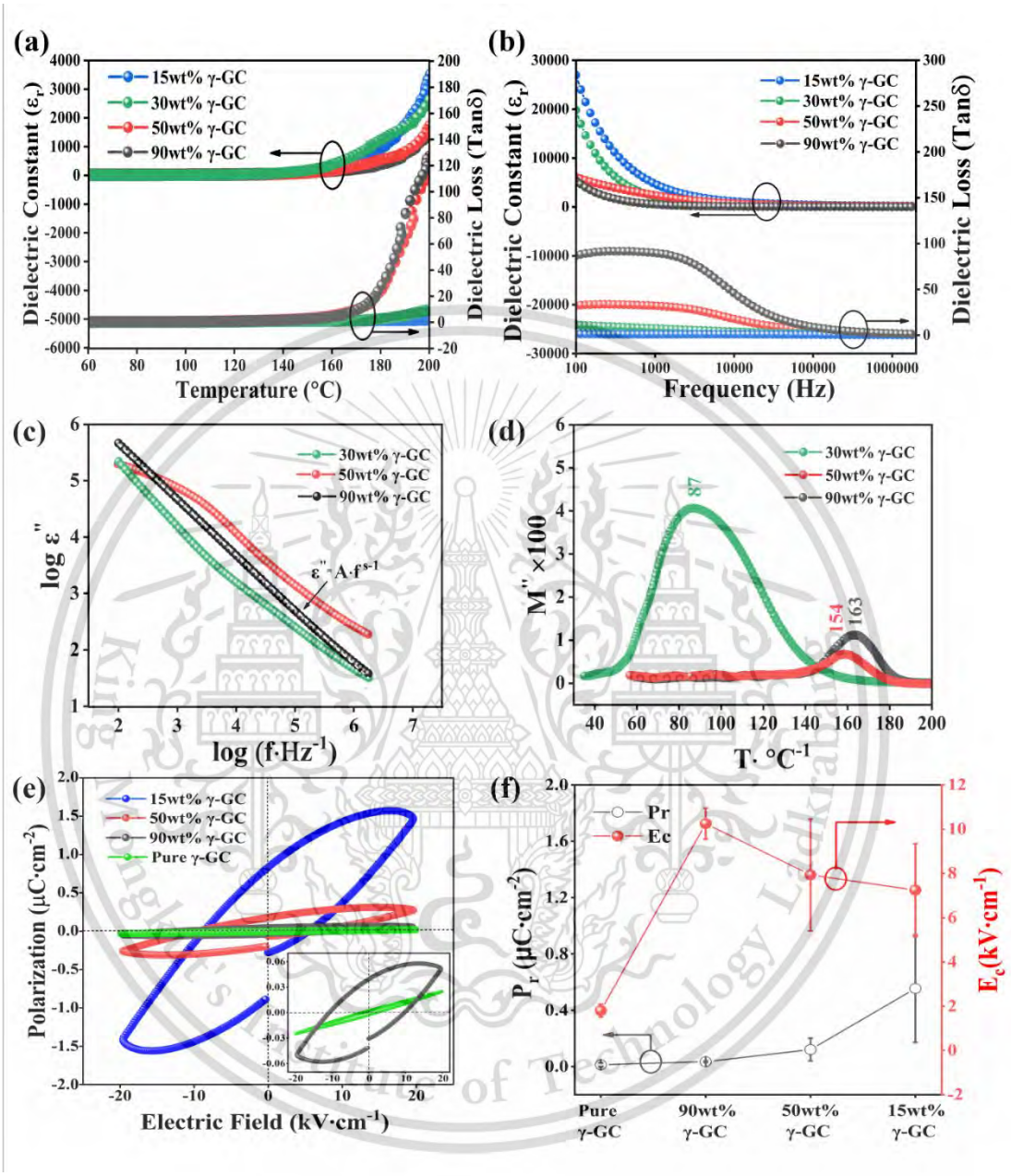

Figure 5.8 Electrical properties of γ-GC/BT composites fabricated via CSP: a) temperature-dependence b) frequency-dependence of the dielectric constant and dielectric loss. c) the *f*-dependent ε″ d) the *T*-dependent *M*″x 100 of the γ-GC/BT composites with γ-GC content of 30, 50, and 90wt%. e) P-E hysteresis loop of γ-GC and the γ-GC/BT composites, at the electric field of 20 kV/cm, and f) the corresponding P_r and E_c values.

Table 5.1 A concise comparison of the raw materials used, the presence of transient liquid phase, and the conditions of the Cold Sintering Process (CSP) for both BT-based ceramics and composites.

BT-based Ceramics/Composite	Raw materials	Transient liquid phase	CSP conditions	density	Reference
$BaTiO_3$ (Solid state reaction)	$BaCO_3$+TiO_2	-	1200-1400 ° C/ 6-24 h (Traditional sintering temperature)	94-96%	[11, 207] [208]
$BaTiO_3$	$Ba(OH)_2$+TiO_2 → $BaTiO_3$	$Ba(OH)_2$ ·$8H_2O$	180 °C/ 15 to 120 mins/430 MPa/annealing 900 ° C	95%	[209]
$BaTiO_3$/ZnO	$BaTiO_3$ + ZnO	CH_3COOH + H_2O	250°C/1h/166 MPa	60%-98%	[210]
$BaTiO_3$/Polytetrafluoroethylene (PTFE) composites	Nano $BaTiO_3$/ polymer PTFE	$Ba(OH)_2$ ·$8H_2O$	225°C/2h/350 MPa	93.5%	[211]
$BaTiO_3$/Polyphenylene oxide nanocomposite	$BaTiO_3$/ polymer PPO	$Ba(OH)_2$ ·$8H_2O$	225°C/12h/350 MPa	96%	[212]
$BaTiO_3$/Poly(vinylidene difluoride)	$BaTiO_3$/ polymer PVDF	H_2O	190°C/160 mins/350 MPa	94.8%	[213]
$BaTiO_3$/ catechol	Nano$BaTiO_3$/ benzenediol organic compound	$Ba(OH)_2$ ·$8H_2O$	200°C/75 mins/350 MPa/annealing 200 °C	93%-95%	[214]
γ-GC/BT composites	Micro/Nano $BaTiO_3$	γ-$C_2H_5NO_2$	120 °C /6 hrs/10 MPa	96.7± 1.6%	This study

Table 5.2 Comparison of Dielectric Properties of BT ceramic and BT-Based Composites prepared by CSP.

System	Fabrication process	Dielectric constant at 1kHz	Dielectric loss at 1kHz	Reference
$BaTiO_3$	Solid state reaction	2900-4500	1.4-2.8	[11, 207] [208]
$BaTiO_3$	CSP	1,800	0.03	[209]
$BaTiO_3$/ZnO	CSP	50.9-7000	0.04-3.13	[210]
$BaTiO_3$/Polytetrafluoroethylene (PTFE) composites	CSP	790 (@ 1 MHz)	1.4 (@ 1 MHz)	[211]
$BaTiO_3$/Polyphenylene oxide nanocomposite	CSP	1,500	0.05	[212]
$BaTiO_3$/Poly(vinylidene difluoride)	CSP	71.1 (@ 1 GHz)	0.04 (@ 1 GHz)	[213]
$BaTiO_3$/ catechol	CSP	700 (@ 1 MHz)	0.04 (@ 1 MHz)	[214]
γ-GC/BT composites	CSP	4500	0.99	This study

5.4 Conclusion

In this study, we have successfully demonstrated the implementation of organic ferroelectric (γ-GC) phase as a transient liquid phase substitute for fabricating the γ-GC/BT composite ceramic through CSP (Cold Sintering Process). Our investigation involved incorporating γ-GC contents ranging from 15% to 90% by weight into BT, followed by CSP with a sintering temperature of 120 °C, a holding time of 6 h, and an applied uniaxial pressure of 10 MPa. The addition of γ-GC resulted in notable enhancements in both relative density and electrical properties of the composites. Particularly, the optimal γ-GC content of 15wt% yielded a remarkable relative density of up to 96.7±1.6%. Our findings were further corroborated by FTIR and XRD analyses, which confirmed the phase stability of γ-GC and its prevention of undesired transformation into the non-piezoelectric phase (α-GC). SEM-EDS mapping revealed the

precipitation-dissolution process of γ-GC in CSP, where it functioned as a filler diffusing into the space surrounding BT particles. XTM images provided a comprehensive 3D distribution of both BT and γ-GC, consistent with SEM observations. Furthermore, we conducted a thorough examination of the electrical properties of the composites across varying temperatures (RT-200 °C) and frequencies (100Hz-2MHz). The dielectric constant (ε_r) exhibited an increase with decreasing γ-GC content. Notably, the 15wt% γ-GC pellet demonstrated the highest ε_r of 3600 coupled with a low dielectric loss (tan δ) of 1.20. The P-E hysteresis loop measurements revealed that the 15wt% γ-GC composite ceramic displayed the highest values of Ps = 1.46 μC•cm^{-2} and P_r = 0.55 μC•cm^{-2}. Our study underscores the efficacy of γ-GC as a transient liquid phase in CSP for successfully and sustainably fabricating high-density γ-GC/BT composites at relatively low temperatures. These results contribute to the advancement of ceramic processing techniques and hold promise for various applications in the fields of electronics, energy, and beyond.

CHAPTER 6

CONCLUSIONS AND SUGGESTION FOR FURTHER WORK

6.1 Conclusions

This work effectively utilized the cold sintering process (CSP) to produce high-density γ-GC ceramics and γ-GC/BT composites at low temperatures. Consequently, this chapter aims to summarize and compare the mechanisms of the cold sintering process with traditional sintering (TSP) and liquid phase sintering process (LPS). Table 6.1 presents a comparison of the mechanisms of various sintering processes.

Table 6.1 Shows a comparison of the mechanisms of the traditional sintering process (TSP), liquid phase sintering process (LPS), and cold sintering process (CSP).

	TSP	LPS	CSP
Sintering mechanism	**1.Stage I:** The particles are first placed in contact with each other; instantaneous neck formation takes place. **2.Stage II:** Once it is formed, the neck grows rapidly by several different mechanisms: 2.1 Diffusion of the atom along the surface to the neck. 2.2 Vapor transport from the surface to the neck. 2.3 Lattice diffusion: materials transported from a particle surface to the neck. 2.4 Atoms from grain boundary to be transported from the grain boundary through the lattice to the neck. 2.5 Atom from grain boundary transport along the grain boundary to a neck region or pore surface. 2.6 Plastic flow occurs due to stresses that develop during sintering and helps densification. **3.Stage III:** The pore phase is continuous and gives cylindrical channels of porosity sitting along the grain edges. **4.Stage IV:** Begins when the pores pinch off and become isolated at the grain corners, they may shrink continuously with time and disappear.	1. **Stage I:** The powder mixture is compacted into a green body with loosely packed particles. During the stages of heating, the particles begin to rearrange. 2. **Stage II:** As the temperature increases, certain components within the powder mixture will melt, leading to the formation of a liquid phase. 3. **Stage III:** The formation of the liquid phase enables capillary action, which draws the liquid into the interparticle voids, promoting particle coalescence and neck formation between adjacent particles. 4. **Stage IV:** With further heating, the liquid phase facilitates the mass transport mechanism such as diffusion, viscous flow, and surface diffusion, leading to the rearrangement of particles and the densification of material. 5. **Stage V:** Final solidification, as the sintering process progresses and the temperature reaches the solidus temperature of the liquid phase, the liquid phase begins to solidify. The necks formed between particles become more rigid. 6. **Stage VI:** Once the sintering process is complete, the materials is allowed to cool down gradually and the solidified microstructure is stabilized.	**1.Stage I: Particle compaction** Particles are separated with a solution. Densification at this stage is mainly from the compaction, external pressure, and rearrangement of particles. The transient solution contributes to the particle rearrangement by acting as a lubricant between particles and assists the rearrangement and sliding process. **2.Stage II: Dissolution-precipitation and grain coarsening** Relies on filling gaps/voids between grains. Mass transport occurs through the transient liquid phase from the surface (high concentration) to the pore (low concentration) to fill the gaps or pore. When the pore has a concentration rise, the solution becomes super-saturated to the point where precipitation begins and leads to necking. Then, temperature and times increase, the solution evaporates, and the coarsening of particles occurs, and the crystal becomes larger.
Final density	65-100%	80-100%	80-100%

6.1.1 Traditional sintering process (TSP) [215]

Sintering, a crucial process in material science and engineering, unfolds through four discernible stages, each characterized by intricate physical and chemical transformations. Initially, during the solid stage, individual particles come into contact, prompting the instantaneous formation of necks between them (refer to Figure 6.1A). These nascent necks serve as nuclei for further growth, initiating a cascade of mechanisms that drive rapid expansion. Notably, this growth phase is propelled by several mechanisms, including surface diffusion, wherein atoms migrate along the material's surface, and lattice diffusion, which involves the movement of atoms within the crystal lattice. Additionally, vapor transport, grain boundary diffusion, and lattice diffusion from the grain boundary, often accompanied by plastic flow, collectively contribute to the neck enlargement process (as depicted in Figure 6.1B).

This stage persists until the neck radius between the particles reaches approximately 0.4-0.5 times the radius of the particles themselves. Concurrently, the material experiences a notable increase in density, reaching around 0.65, accompanied by a linear shrinkage ranging from 3% to 5%. These changes signify the onset of the intermediate stage (illustrated in Figure 6.1C), characterized by the attainment of equilibrium shapes by the pores. These pores, integral to the material's microstructure, form continuous cylindrical channels of porosity along the grain edges, influencing the material's mechanical and thermal properties.

The final stage of sintering (depicted in Figure 6.1D) marks a critical juncture in the process, heralding the completion of densification. Here, the pores, having reached their maximum extent, undergo closure, becoming isolated at the grain boundaries. Over time, these isolated pores may continue to diminish until they vanish entirely, facilitating grain growth and enhancing the material's homogeneity and strength. At this stage, the material achieves a relative density ranging from 65% to 100%, culminating in the formation of a robust and structurally stable material matrix.

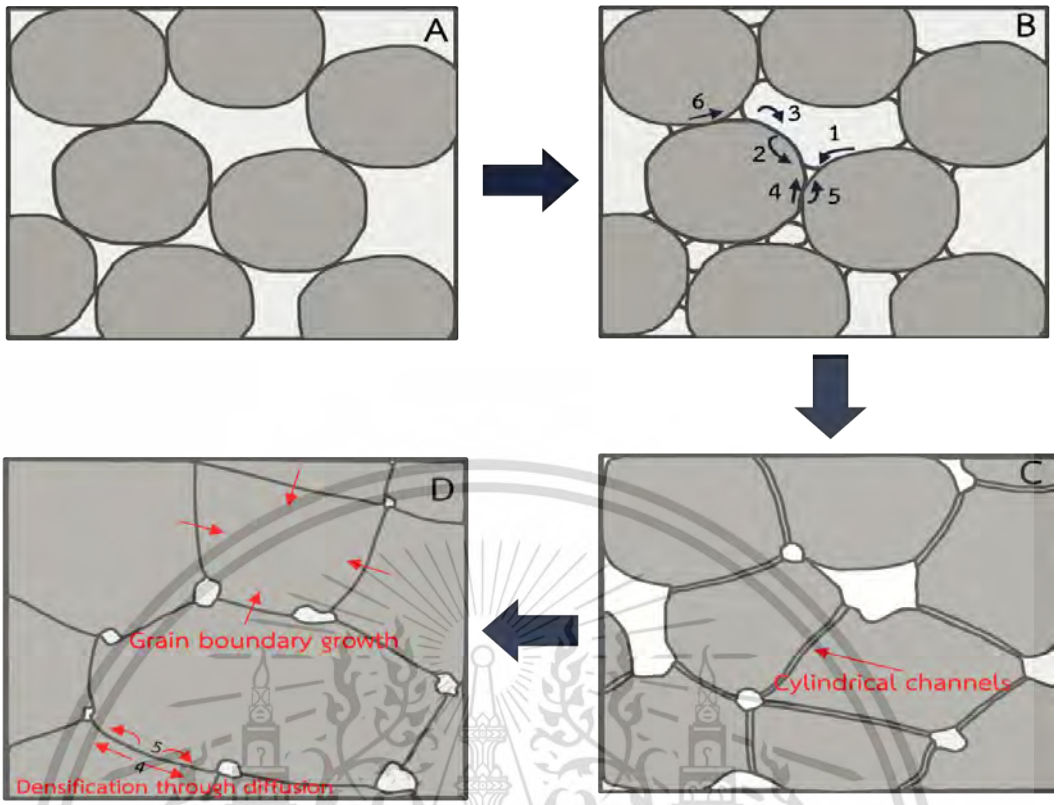

Figure 6.1 The mechanism of the traditional sintering process, A) The particles contact each other, and the formation of the neck occurs. B) the neck grows rapidly through 6 different mechanisms. C) The pore is continuous and gives cylindrical channels of porosity sitting along the grain edges and D) grain growth (Modified from [215]).

6.1.2 Liquid phase sintering (LPS) [216]

Liquid phase sintering (LPS) is a sophisticated process utilized to enhance the densification and mechanical properties of materials, particularly ceramics and metal powders. In LPS, an additive, often referred to as a sintering aid or a liquid phase former, is incorporated into the powder mixture (as depicted in Figure 6.2A). This additive is carefully selected to possess a lower melting point than the main matrix phase, ensuring it liquefies prior to the matrix phase during the heating stage.

As the temperature rises and the liquid phase forms, a remarkable phenomenon known as capillary action comes into play. Capillary action, a consequence of intermolecular forces, causes the liquid to be drawn into the pores within the powder compact. This migration of the liquid phase facilitates wetting of

the particle surfaces, fostering particle rearrangement, coalescence, and the formation of necks between adjacent particles (illustrated in Figure 6.2B). These nascent necks serve as nuclei for further densification and structural development.

Subsequently, during the solution-precipitation stage (depicted in Figure 6.2C), a fascinating interplay of dissolution and precipitation occurs. At the inter-particle contact points, the solubility of the solid in the liquid phase increases, leading to the transfer of material from regions of higher concentration to those of lower concentration. This mass transfer, coupled with precipitation in regions of low energy, drives densification and pore elimination. The liquid phase acts as a medium for the flow of material, effectively removing pores and promoting the formation of a dense, homogeneous structure.

As the sintering process progresses and the temperature approaches the solidus temperature of the liquid phase, the final stage, solidification, commences (as depicted in Figure 6.2D). At this juncture, the once-fluidic necks between particles undergo a transition to a more rigid state as the liquid phase solidifies. This solidification further stabilizes the microstructure, enhancing the mechanical integrity and structural uniformity of the final product.

In essence, liquid phase sintering represents a sophisticated approach to tailor the microstructure and properties of materials, offering unprecedented control over densification kinetics and final product characteristics. Its versatility and efficacy make it a cornerstone technique in the fabrication of advanced ceramics, alloys, and composites across diverse industrial session.

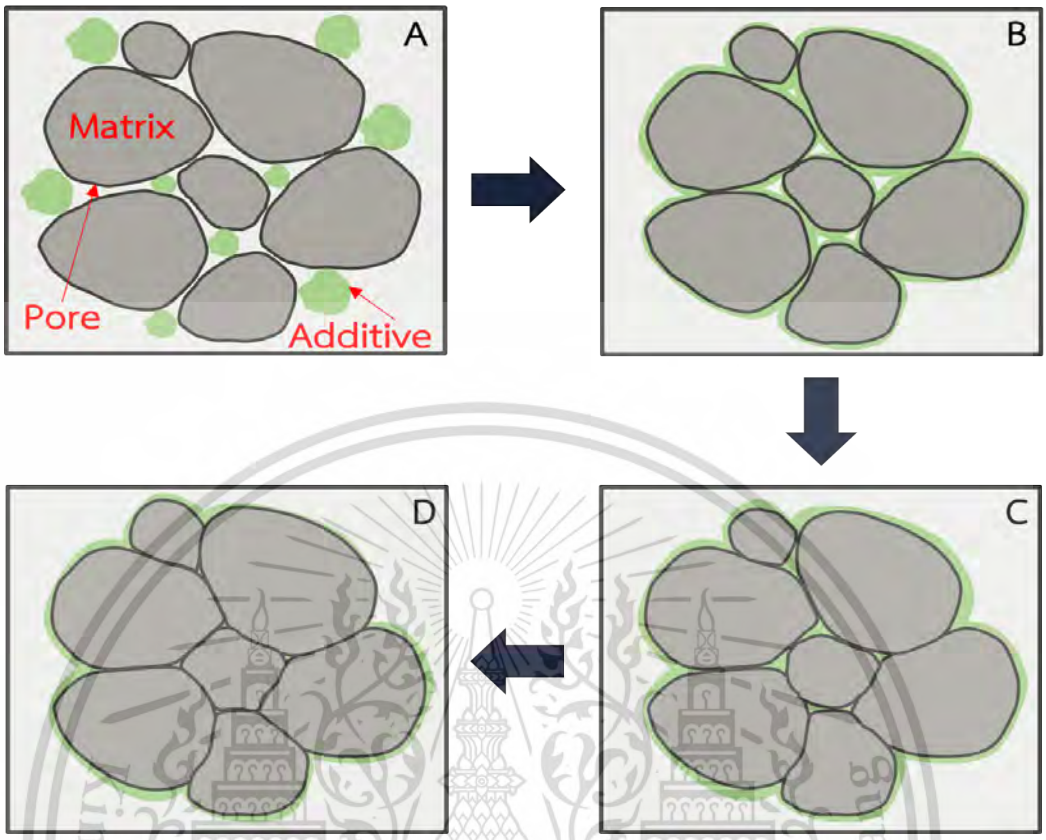

Figure 6.2 The mechanism of liquid phase sintering process by A) mixed powders, B) Liquid formation, spreading and rearrangement, C) solution-reprecipitation (diffusion, grain growth, and shape accommodation), and D) solid-state (pore elimination, grain growth, and contact growth) (Modified from [216]).

6.1.3 Cold sintering process (CSP) [162]

The Cold Sintering Process (CSP) presents a unique approach to fabricating dense ceramic materials at significantly lower temperatures compared to conventional sintering methods. This innovative technique operates through two distinct stages, each contributing to the densification and structural evolution of the material.

In the initial stage of the CSP, particles are dispersed within a solution, typically deionized (DI) water. Densification primarily occurs through compaction, external pressure, and the rearrangement of particles facilitated by the transient liquid phase.

The solution acts as a lubricant, reducing friction between particles and facilitating their movement and reorganization. Mass transport subsequently occurs through the transient liquid phase, as molecules migrate from regions of higher concentration on particle surfaces to regions of lower concentration within pores, effectively filling the gaps between particles. As the concentration within the pores rises, the solution becomes supersaturated, leading to precipitation and the formation of necks between particles, as indicated by the red frame in Figure 6.2.

As temperature and time progress, the solution gradually evaporates, leading to particle coarsening and crystal growth, depicted by the yellow frame in Figure 6.2. Interestingly, in the case of γ-GC/BT composites, the mechanism resembles that of Liquid Phase Sintering (LPS), with γ-GC serving as a transient liquid phase. This phase aids in particle sliding, rearrangement, and precipitation between BT particles, ultimately resulting in the formation of a highly dense ceramic composite.

Comparing the mechanisms of the three sintering processes—Traditional Sintering Process (TSP), Liquid Phase Sintering (LSP), and CSP—reveals significant differences. While TSP and LSP exhibit distinct mechanisms, CSP presents unique characteristics, particularly in the initial and intermediate stages. In TSP, a single-phase ceramic powder remains solid throughout, with mass transfer occurring according to predefined mechanisms. In contrast, LSP involves the melting of solid particles with lower melting points, acting as a liquid phase to drive densification. At the intermediate stage, both LSP and CSP comprise solid particles and a liquid phase, albeit with different characteristics. In LSP, the liquid phase consists of particle melt, promoting particle rearrangement and neck formation. In CSP, the liquid phase comprises DI water, serving as a lubricant and partially dissolving particles to facilitate movement and rearrangement.

Upon completion of the sintering process (final state), TSP results in densely packed solid particles and significant grain growth. In contrast, LSP sees the liquid phase precipitate and solidify between particles, yielding a high-density ceramic with minimal grain growth. Similarly, CSP yields a highly dense solid, with grain growth observed in

pure ceramic compositions, while composite materials exhibit minimal grain growth, akin to LSP. A comprehensive comparison of particle states across various sintering processes at different stages is provided in Table 6.2, including grain growth metrics. This analysis underscores the unique advantages and mechanisms of CSP, offering a promising avenue for the fabrication of advanced ceramic materials with tailored properties and microstructures.

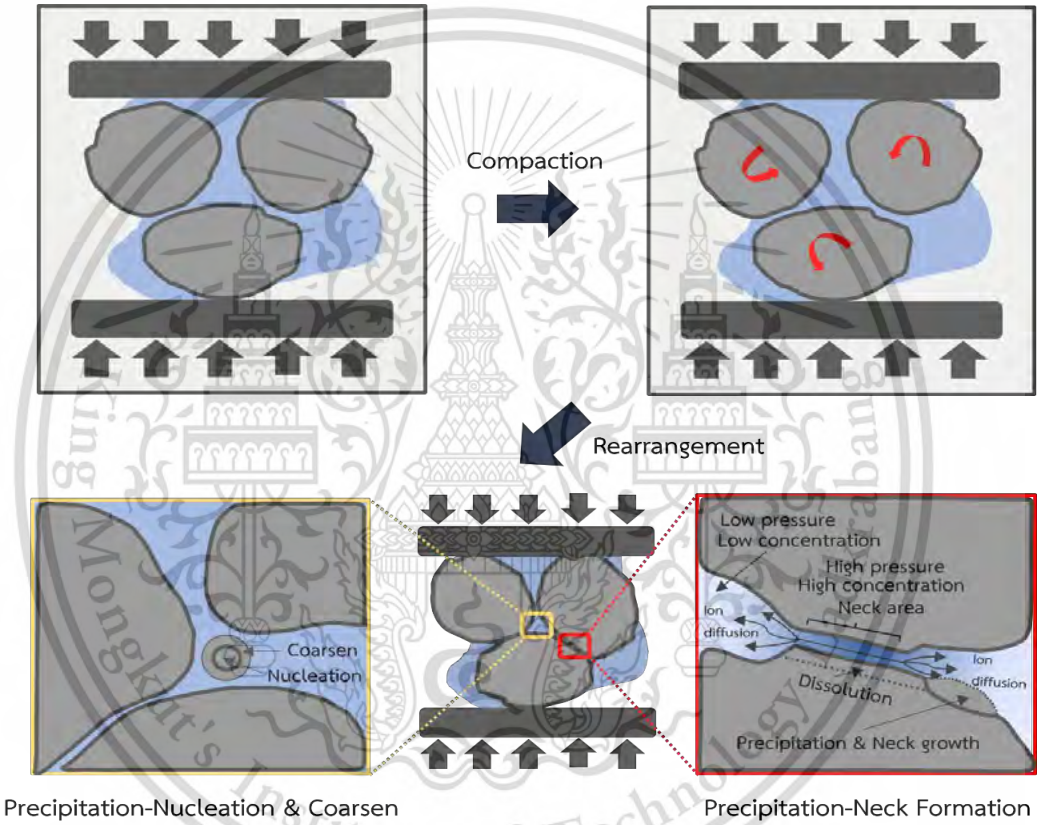

Figure 6.3 The general mechanism of the cold sintering process (Modified from [162]).

Table 6.2 presents the comparison of the particle states of various sintering processes at initial, intermediate, and final state sintering, including grain growth.

Sintering Process	Initial State	Intermediate State	Final State
Traditional Sintering Process (TSP)	Solid-phase particles, compaction under pressure, absence of liquid phase.	Solid-phase particles, diffusion-driven mass transport, minimal grain coarsening.	Densely packed solid particles, significant grain growth due to Ostwald ripening and coalescence.
Liquid Phase Sintering (LSP)	Solid-phase particles, incorporation of liquid phase (e.g., low melting point constituent)	Solid-phase particles with a surrounding liquid phase (particle melt), facilitating particle rearrangement, coalescence, and neck formation.	High-density ceramic with minimal grain growth, liquid phase precipitated and solidified, contributing to enhanced densification.
Cold Sintering Process (CSP)	Solid-phase particles dispersed in a transient liquid phase (e.g., DI water).	Solid-phase particles and surrounding liquid phase (DI water), promoting particle rearrangement, sliding, and mass transport.	Highly dense solid with controlled grain growth, facilitated by transient liquid phase evaporation and particle coarsening.

6.2 Suggestions

6.2.1 Increase sintering temperature and holding time for high density of composites but be careful not to let the sintering temperature exceed the melting point of the material.

6.2.2 Keep the temperature not more than 200 °C because γ-GC can change phase to α-GC and decompose at high temperatures.

6.2.3 Use an appropriate amount of liquid transient (water) such as 7% by weight to satisfy the CSP.

Author biography

Name-Surname	Jitrawan Noisak
Date of birth	2 March 1999
Province	Chai Nat
Education	**B.S.** (Industrial Chemistry, Science), King Mongkut's Institute of Technology Ladkrabang, Bangkok (2020) **M.S.** (Applied Chemistry, Science) King Mongkut's Institute of Technology Ladkrabang, Bangkok (2021-present)
Scholarship	Scholarships to support studies at the master's degree (KRIS), Grant No. KREF016412.

Conference

1. **Jitrawan Noisak,** Natdanai Suktep, Satana Pongampai, Thitirat Charoonsuk, Naratip Vittayakorn "Silk Fibroin Film Fabrication for Transparent Triboelectric Nanogenerator" the Joint International Conference on Applied Physics and Materials Applications & Applied Magnetism and Ferroelectrics (ICAPMA-JMAG-2021), Nongnooch Traditional Hall, Pattaya, Chon Buri, Thailand, December 1-4, 2021. (Poster Presentation)

2. **Jitrawan Noisak,** Utchawadee Pharino, Thitirat Charoonsuk, Satana Pongampai, Wanwilai Vittayakorn, Tosapol Malungnont, Naratip Vittayakorn "Biocompatible and biodegradable Gamma Glycine Treated Bacterial Cellulose Nanofibils Based on Hybrid Piezoelectric-Triboelectric Nanogenerator" The International Conference on Science and Technology of Emerging Materials (STEMa 2022), Holiday Inn Pattaya, Pattaya, Chon Buri, Thailand, August 4-6, 2022. (Oral presentation award)

3. **Jitrawan Noisak,** Thitirat Charoonsuk, Satana Pongampai, Naratip Vittayakorn "Cold Sintering Process for Fabricating Composite of Bacterial Cellulose Nanofibrils and

Gamma Glycine" IEEE Magnetic Society Conference 2022 (IMagSoc 2022), The Bangkok Marriott Sukhumvit, Bangkok, Thailand, November 16-18, 2022. (Poster Presentation)

4. **Jitrawan Noisak,** Thitirat Charoonsuk, Satana Pongampai, Naratip Vittayakorn "Cold Sintering Process for Fabricating Composite of Bacterial Cellulose Nanofibrils and Gamma Glycine" International Conference and Exhibition on Science, Technology and Engineering of Materials (ISTEM 2022), Nongnooch Traditional Hall, Pattaya, Chon Buri, Thailand, November 29- December 2, 2022. (Oral Presentation)

International publications

1. "The Role of γ-$C_2H_5NO_2$ as a New Transient Liquid Phase in Cold Sintering Process of $BaTiO_3$ Composites" **J. Noisak**, P. Ieamviteevanich, T. Charoonsuk, P. Pakawanit, N. Pinpru, W. Vittayakorn, T. Maluangnont, P. Seeharaj, T. Chiu, N. Vittayakorn. **Journal of Advanced Ceramics,** IF 16.9, Q1, Top 10%.

2."Towards the preparation of organic ferroelectric composites: fabrication of a gamma-glycine-bacterial cellulose composite via cold sintering process" **J. Noisak**, T. Charoonsuk, S. Pongampai, N. Pinpru, P. Pakawanit, W. Vittayakorn, T. Maluangnont, T. Chiu, N. Vittayakorn, **Journal of Materials Research and Technology.** Volume 25, 3rd July 2023, IF 6.4, Q1, Tire 1.

3."Silk Fibroin/Amino Acid Hybrid Organic Piezoelectric-Triboelectric Nanogenerator" N. Suktep, **J. Noisak**, S. Pongampai, P. Pakawanit, T. Bongkarn, T. Charoonsuk, and N. VIttayakorn, **Intrgrated Ferroelectrics**, 29th September 2023, IF 0.79, Q4.

References

[1] Curie, J. and P. Curie, *Développement par compression de l'électricité polaire dans les cristaux hémièdres à faces inclinées.* Bulletin de minéralogie, 1880. **3**(4): p. 90-93.

[2] Gallego-Juarez, J.A., *Piezoelectric ceramics and ultrasonic transducers.* Journal of Physics E: Scientific Instruments, 1989. **22**(10): p. 804.

[3] Cho, S.-B., et al., *Low temperature hydrothermal synthesis and formation mechanisms of lead titanate (PbTiO3) particles using tetramethylammonium hydroxide: thermodynamic modelling and experimental verification.* Journal of the European Ceramic Society, 2003. **23**(13): p. 2323-2335.

[4] Funsueb, N., A. Limpichaipanit, and A. Ngamjarurojana, *Effect of sintering temperature on phase formation and dielectric property of modified PLZT ceramics with addition of BT and PZN.* Phase Transitions, 2022. **95**(5): p. 363-371.

[5] Schäufele, A.B. and K. Heinz Härdtl, *Ferroelastic Properties of Lead Zirconate Titanate Ceramics.* Journal of the American Ceramic Society, 1996. **79**(10): p. 2637-2640.

[6] Panda, P. and B. Sahoo, *PZT to lead free piezo ceramics: A review.* Ferroelectrics, 2015. **474**.

[7] Shrout, T.R. and S.J. Zhang, *Lead-free piezoelectric ceramics: Alternatives for PZT?* Journal of Electroceramics, 2007. **19**: p. 113-126.

[8] Koruza, J., K.V. Lalitha, and B. Malic, *Lead-free perovskite ferroelectrics*. 2018. p. 51-69.

[9] Hong, K., et al., *Perspectives and challenges in multilayer ceramic capacitors for next generation electronics.* Journal of Materials Chemistry C, 2019. **7**(32): p. 9782-9802.

[10] N George, C., et al., *Characterization, sintering and dielectric properties of nanocrystalline barium titanate synthesized through a modified combustion process.* Materials Characterization - MATER CHARACT, 2009. **60**: p. 322-326.

[11] Kim, H.T. and Y.H. Han, *Sintering of nanocrystalline BaTiO3.* Ceramics International, 2004. **30**(7): p. 1719-1723.

[12] Maiwa, H., *Preparation and Properties of BaTiO3 Ceramics by Spark Plasma Sintering.* Japanese Journal of Applied Physics, 2008. **47**.

[13] Takahashi, H., et al., *Lead-Free Barium Titanate Ceramics with Large Piezoelectric Constant Fabricated by Microwave Sintering.* Japanese Journal of Applied Physics, 2006. **45**(1L): p. L30.

[14] Guo, H., et al., *Cold Sintering Process: A Novel Technique for Low-Temperature Ceramic Processing of Ferroelectrics.* Journal of the American Ceramic Society, 2016. **99**(11): p. 3489-3507.

[15] Guo, J., et al., *Cold sintering: a paradigm shift for processing and integration of ceramics.* Angewandte Chemie, 2016. **128**(38): p. 11629-11633.

[16] Anindy, U., M. Indro, and I. Husein, *Piezoelectric properties: cerium oxide (CeO 2) doped barium titanate (BaTiO 3) film on ITO substrate.* Ferroelectrics, 2021. **570**: p. 162-175.

[17] Kalugina, S.G., et al., *Fundamental optical spectra of ferroelectric NaNO2.* Inorganic Materials, 2009. **45**(8): p. 925-929.

[18] Atashfaraz, M., et al., *Effect of titanium dioxide solubility on the formation of BaTiO3 nanoparticles in supercritical water.* Fluid Phase Equilibria, 2007. **257**(2): p. 233-237.

[19] Induja, I.J. and M.T. Sebastian, *Microwave dielectric properties of mineral sillimanite obtained by conventional and cold sintering process.* Journal of the European Ceramic Society, 2017. **37**(5): p. 2143-2147.

[20] Anbu Arasi, M., M. Alagar, and M. Raja Pugalenthi, *Growth of γ-glycine single crystals using the tailored additive of potassium chloride and L-Proline and analyzing micro structural, optical, mechanical and electrical parameters.* Chemical Physics Letters, 2021. **765**: p. 138301.

[21] Jiang, Q., et al., *Non-Topotactic Phase Transformations in Single Crystals of β-Glycine.* Crystal Growth & Design, 2015. **15**: p. 150507145213005.

[22] Guerin, S., et al., *Control of piezoelectricity in amino acids by supramolecular packing.* Nature Materials, 2018. **17**.

[23] Hu, P., et al., *Bioferroelectric properties of glycine crystals.* The Journal of Physical Chemistry Letters, 2019. **10**(6): p. 1319-1324.

[24] Yang, X., X. Wang, and C. Ching, *Solubility of Form α and Form γ of Glycine in Aqueous Solutions.* Journal of Chemical and Engineering Data - J CHEM ENG DATA, 2008. **53**.

[25] Mason, W.P., *Piezoelectricity, its history and applications.* The Journal of the Acoustical Society of America, 1981. **70**(6): p. 1561-1566.

[26] Katzir, S., *The Discovery of the Piezoelectric Effect.* Archive for History of Exact Sciences, 2003. **57**(1): p. 61-91.

[27] Dineva, P., et al., *Piezoelectric materials*. 2014: Springer.

[28] Arnau, A. and D. Soares, *Fundamentals of piezoelectricity*, in *Piezoelectric transducers and applications*. 2009, Springer. p. 1-38.

[29] Zhang, Q. *Properties of Ferroelectric Perovskite Structures under Non-equilibrium Conditions*. 2012.

[30] Bhalla, A.S., R. Guo, and R. Roy, *The perovskite structure – a review of its role in ceramic science and technology.* Material Research Innovations, 2000. **4**(1): p. 3-26.

[31] Goldschmidt, V.M., *Die Gesetze der Krystallochemie.* Naturwissenschaften, 1926. **14**(21): p. 477-485.

[32] Travis, W., et al., *On the application of the tolerance factor to inorganic and hybrid halide perovskites: a revised system.* Chemical Science, 2016. **7**(7): p. 4548-4556.

[33] Bhalla, A.S., R. Guo, and R. Roy, *The perovskite structure—a review of its role in ceramic science and technology.* Materials Research Innovations, 2000. **4**(1): p. 3-26.

[34] Xu, P., et al., *Search for ABO3 Type Ferroelectric Perovskites with Targeted Multi-Properties by Machine Learning Strategies.* Journal of Chemical Information and Modeling, 2022. **62**(21): p. 5038-5049.

[35] Sawaguchi, E., *Ferroelectricity versus Antiferroelectricity in the Solid Solutions of PbZrO3 and PbTiO3.* Journal of the Physical Society of Japan, 1953. **8**(5): p. 615-629.

[36] Lu, J., et al., *Microstructure and electrical properties of Pb(Zr, Ti)O3 thick film prepared by electrostatic spray deposition.* Sensors and Actuators A: Physical, 2003. **108**: p. 2-6.

[37] Guo, R., et al., *Origin of the high piezoelectric response in PbZr1-xTixO3.* Phys Rev Lett, 2000. **84**(23): p. 5423-6.

[38] Stølen, S., E. Bakken, and C. Mohn, *Oxygen-Deficient Perovskites: Linking Structure, Energetics and Ion Transport.* Physical chemistry chemical physics : PCCP, 2006. **8**: p. 429-47.

[39] Park, S.-E. and T.R. Shrout, *Ultrahigh strain and piezoelectric behavior in relaxor based ferroelectric single crystals.* Journal of Applied Physics, 1997. **82**(4): p. 1804-1811.

[40] Shrout, T. and S. Zhang, *Lead-Free Piezoelectric Ceramics: Alternatives for PZT?* Journal of Electroceramics, 2007. **19**: p. 113-126.

[41] Noblanc, O., P. Gaucher, and G. Calvarin, *Structural and dielectric studies of Pb(Mg1/3Nb2/3)O3–PbTiO3 ferroelectric solid solutions around the morphotropic boundary.* Journal of Applied Physics, 1996. **79**(8): p. 4291-4297.

[42] Zhang, S., et al., *Piezoelectric shear coefficients of Pb (Zn1/3Nb2/3) O3–PbTiO3 single crystals.* Japanese journal of applied physics, 2002. **41**(10A): p. L1099.

[43] Pramanik, S., B. Pingguan-Murphy, and N.A. Abu Osman, *Developments of Immobilized Surface Modified Piezoelectric Crystal Biosensors for Advanced Applications.* International journal of electrochemical science, 2013. **8**: p. 8863-8892.

[44] Saito, Y., et al., *Lead-free piezoceramics.* Nature, 2004. **432**(7013): p. 84-7.

[45] Shirane, G., R.E. Newnham, and R. Pepinsky, *Dielectric Properties and Phase Transitions of NaNbO3 and (Na,K)NbO3.* Physical Review, 1954.

[46] Jaffe, H., *Piezoelectric ceramics.* Journal of the American Ceramic Society, 1958. **41**(11): p. 494-498.

[47] Smolenskii, G., *New ferroelectrics of complex composition. IV.* Soviet Physics-Solid State, 1961. **2**: p. 2651-2654.

[48] Qiao, X., X. Chao, and Z. Yang, *Bi0.5Na0.5TiO3-based ceramics with high energy storage density and good thermal stability.* Journal of Materials Science: Materials in Electronics, 2021. **33**.

[49] Li, Y., et al., *Dielectric and piezoelecrtic properties of lead-free (Na0.5Bi0.5)TiO3-NaNbO3 ceramics.* Materials Science and Engineering B-advanced Functional Solid-state Materials, 2004. **112**: p. 5-9.

[50] Jia, W., et al., *Superior temperature‐stable dielectrics for MLCC s based on Bi0. 5Na0. 5TiO3‐NaNbO3 system modified by CaZrO3.* Journal of the American Ceramic Society, 2018. **101**(8): p. 3468-3479.

[51] Wul, B. and J. Goldman, *Ferroelectric switching in BaTiO3 ceramics.* CR Acad. Sci. URSS, 1946. **51**: p. 21.

[52] Vijatović Petrović, M.M., J.D. Bobić, and B. Stojanović, *History and Challenges of Barium Titanate: Part II.* Science of Sintering, 2008. **40**.

[53] Korkmaz, S. and a. Kariper, *BaTiO3-Based Nanogenerators: Fundamentals and Current Status.* Journal of Electroceramics, 2021.

[54] Cho, W.-S., *Structural evolution and characterization of BaTiO3 nanoparticles synthesized from polymeric precursor.* Journal of Physics and Chemistry of Solids, 1998. **59**(5): p. 659-666.

[55] Vijatović Petrović, M.M., J.D. Bobić, and B. Stojanović, *History and Challenges of Barium Titanate: Part I.* Science of Sintering, 2008. **40**.

[56] Rout, S., *Phase Formation and Dielectric Studies of Some $BaO-TiO_2-ZrO_2$ Based Perovskite System.* 2023.

[57] Karvounis, A., et al., *Barium Titanate Nanostructures and Thin Films for Photonics.* Advanced Optical Materials, 2020. **8**(24): p. 2001249.

[58] Guo, L., et al., *Microwave hydrothermal synthesis of barium titanate powders.* Materials Letters, 2006. **60**(24): p. 3011-3014.

[59] Philippot, G., et al., *Supercritical fluid technology: A reliable process for high quality BaTiO3 based nanomaterials.* Advanced Powder Technology, 2014. **25**.

[60] Benlahrache, M.T., et al., *Influence of polarization electric field on the dielectric properties of BaTiO3-based ceramics.* Materials Science in Semiconductor Processing, 2006. **9**: p. 1115-1118.

[61] Boulos, M., et al., *Hydrothermal Synthesis of Nanosized BaTiO3 Powders and Dielectric Properties of Corresponding Ceramics.* Solid State Ionics, 2005. **176**: p. 1301-1309.

[62] Norfarina, N., et al., *Synthesis of BaTiO3 Nanoparticles via Hydrothermal Method.* Solid State Phenomena, 2017. **268**: p. 172-176.

[63] Siddiqui, M.A., et al., *Effect of Calcination and Sintering Temperatures on Physical Properties of Barium Titanate Ceramic.* Int. J. Electroactive Mater, 2018. **6**: p. 42-47.

[64] Simon-Seveyrat, L., et al., *Re-investigation of synthesis of BaTiO3 by conventional solid-state reaction and oxalate coprecipitation route for piezoelectric applications.* Ceramics International, 2007. **33**(1): p. 35-40.

[65] Jaffe, H., *Titanate Ceramics for Electromechanical Purposes.* Industrial & Engineering Chemistry, 1950. **42**(2): p. 264-268.

[66] Gao, J., et al., *Recent Progress on BaTiO3-Based Piezoelectric Ceramics for Actuator Applications.* Actuators, 2017. **6**(3): p. 24.

[67] Pithan, C., D. Hennings, and R. Waser, *Progress in the synthesis of nanocrystalline BaTiO3 powders for MLCC.* International Journal of Applied Ceramic Technology, 2005. **2**(1): p. 1-14.

[68] Bailliez, S. and A. Nzihou, *The kinetics of surface area reduction during isothermal sintering of hydroxyapatite adsorbent.* Chemical Engineering Journal, 2004. **98**(1-2): p. 141-152.

[69] Aytimur, A., S. Kocyigit, and I. Uslu, *Calcia Stabilized Ceria Doped Zirconia Nanocrystalline Ceramic.* Journal of Inorganic and Organometallic Polymers and Materials, 2014. **24**: p. 927-932.

[70] Rahaman, M.N., *Sintering of ceramics*. 2007: CRC press.

[71] Somiya, S. and Y. Moriyoshi, *Sintering key papers*. 2012: Springer Science & Business Media.

[72] Trzaskowska, M., V. Vivcharenko, and A. Przekora, *The Impact of Hydroxyapatite Sintering Temperature on Its Microstructural, Mechanical, and Biological Properties.* International Journal of Molecular Sciences, 2023. **24**(6): p. 5083.

[73] German, R.M., P. Suri, and S.J. Park, *Review: liquid phase sintering.* Journal of Materials Science, 2009. **44**(1): p. 1-39.

[74] Somiya, S., *Hydrothermal reactions for materials science and engineering: an overview of research in Japan.* 2012.

[75] HIRANO, S.-I. and S. SOMIYA, *Hydrothermal Reaction Sintering of Pure Cr2O3.* Journal of the American Ceramic Society, 1976. **59**(11-12): p. 534-534.

[76] Yanagisawa, K., Q. Feng, and N. Yamasaki, *Preparation of ceramics by hydrothermal hot-pressing.* High Pressure Research, 2001. **20**(1-6): p. 343-349.

[77] Yamasaki, N., et al., *A hydrothermal hot-pressing method: apparatus and application*, in *Hydrothermal Reactions for Materials Science and Engineering: An Overview of Research in Japan*, S. S**ō**miya, Editor. 1989, Springer Netherlands: Dordrecht. p. 423-424.

[78] Matamoros-Veloza, Z., et al., *Low temperature preparation of porous materials from TV panel glass compacted via hydrothermal hot pressing.* Ceramics International, 2015. **41**(10, Part A): p. 12700-12709.

[79] Yamasaki, N., W. Tang, and J. Ke, *Low-temperature sintering of calcium carbonate by a hydrothermal hot-pressing technique.* Journal of Materials Science Letters, 1992. **11**(13): p. 934-936.

[80] Anselmi-Tamburini, U., *Spark Plasma Sintering*, in *Encyclopedia of Materials: Technical Ceramics and Glasses*, M. Pomeroy, Editor. 2021, Elsevier: Oxford. p. 294-310.

[81] Suárez, M., et al., *Challenges and opportunities for spark plasma sintering: a key technology for a new generation of materials.* Sintering applications, 2013. **13**: p. 319-342.

[82] Kganakga, M., et al., *Erosion wear behavior of spark plasma-sintered Ti-6Al-4V reinforced with TiN nanoparticles.* The International Journal of Advanced Manufacturing Technology, 2020. **110**: p. 1-10.

[83] Leszczy**ń**ska-Madej, B., M. Madej, and D. Garbiec, *Tribological Properties of Spark Plasma Sintered Al-SiC Composites.* Materials, 2020. **13**(21): p. 4969.

[84] Xu, Z. *Study on microwave sintering process and surface texture characteristics of ceramic materials*. in *IOP Conference Series: Materials Science and Engineering*. 2019. IOP Publishing.

[85] Savani, S., et al., *Microwave sintering of ZrB2-based ceramics: A review.* Synthesis and Sintering, 2023. **3**(3): p. 143-152.

[86] Takahashi, H., et al., *Piezoelectric properties of BaTiO3 ceramics with high performance fabricated by microwave sintering.* Japanese journal of applied physics, 2006. **45**(9S): p. 7405.

[87] Ramarao, S.D., S.R. Kiran, and V.R.K. Murthy, *Structural, morphological and microwave dielectric studies on microwave sintered ZnWO4 ceramic compounds.* Ceramics International, 2023. **49**(14, Part A): p. 23075-23081.

[88] Yu, T., et al., *Current understanding and applications of the cold sintering process.* Frontiers of Chemical Science and Engineering, 2019. **13**(4): p. 654-664.

[89] Leng, H., et al., *Cold sintering and ionic conductivities of Na3.256Mg0.128Zr1.872Si2PO12 solid electrolytes.* Journal of Power Sources, 2018. **391**: p. 170-179.

[90] Funahashi, S., et al., *Demonstration of the cold sintering process study for the densification and grain growth of ZnO ceramics.* Journal of the American Ceramic Society, 2017. **100**(2): p. 546-553.

[91] Thomson, J., *XLII. On certain curious motions observable at the surfaces of wine and other alcoholic liquors.* The London, Edinburgh, and Dublin Philosophical Magazine and Journal of Science, 1855. **10**(67): p. 330-333.

[92] Guo, J., et al., *Cold Sintering: A Paradigm Shift for Processing and Integration of Ceramics.* Angewandte Chemie International Edition, 2016. **55**(38): p. 11457-11461.

[93] al, K.A.e. *Structure and Function-Amino Acids*. 2020; Available from: https://bio.libretexts.org/Bookshelves/Biochemistry/Book%3A_Biochemistry_Free_For_All_(Ahern_Rajagopal_and_Tan)/02%3A_Structure_and_Function/202%3A_Structure__Function_-_Amino_Acids.

[94] Randy. *Amino Acids Are Organic Compounds Consisting of an Amino Group*. 2023; Available from: https://lifeline-hospital.com/amino-acids-are-organic-compounds-consisting-of-an-amino-group/.

[95] Han, G., P. Chow, and R. Tan, *Understanding the Salt-Dependent Outcome of Glycine Polymorphic Nucleation.* Pharmaceutics, 2021. **13**: p. 262.

[96] Heredia, A., et al., *Nanoscale Ferroelectricity in Crystalline γ-Glycine.* Advanced Functional Materials, 2012. **22**(14): p. 2996-3003.

[97] Rodríguez, J.S., et al., *Structural and Optoelectronic Properties of the α-, β-, and γ-Glycine Polymorphs and the Glycine Dihydrate Crystal: A DFT Study.* Crystal Growth & Design, 2019. **19**(9): p. 5204-5217.

[98] Han, G., P.S. Chow, and R.B.H. Tan, *Effects of Common Inorganic Salts on Glycine Polymorphic Transformation: An Insight into Salt-Dependent Polymorphic Selectivity.* Crystal Growth & Design, 2016. **16**(11): p. 6499-6505.

[99] Bhat, M.N. and S.M. Dharmaprakash, *Growth of nonlinear optical γ-glycine crystals.* Journal of Crystal Growth, 2002. **236**(1): p. 376-380.

[100] Iitaka, Y., *The crystal structure of γ-glycine.* Acta Crystallographica, 1961. **14**(1): p. 1-10.

[101] Peter, M.E. and P. Ramasamy, *Growth of gamma glycine crystal and its characterisation.* Spectrochim Acta A Mol Biomol Spectrosc, 2010. **75**(5): p. 1417-21.

[102] Guerin, S., et al., *Control of piezoelectricity in amino acids by supramolecular packing.* Nat Mater, 2018. **17**(2): p. 180-186.

[103] กีรติเสวี, ห., ภาพรวมของวัสดุเชิงประกอบ. วิศวกรรมสาร มก., 2009. **22**(70): p. 18-32.

[104] Advani, S.G. and K.-T. Hsiao, *Manufacturing techniques for polymer matrix composites (PMCs)*. 2012: Elsevier.

[105] Alexander, J., *MECHANICAL PROPERTY IMPROVEMENT OF CARBON FIBER REINFORCED POLYMERIC COMPOSITES BY FILLER DISPERSION: A REVIEW.* The Journal of the Mississippi Academy of Sciences, 2016. **61**: p. 242-248.

[106] Clyne, T.W., *4.1 An Introductory Overview of Metal Matrix Composites Systems, Types and Developments*, in *Comprehensive Composite Materials II*, P.W.R. Beaumont and C.H. Zweben, Editors. 2018, Elsevier: Oxford. p. 1-21.
Bansal, N.P. and J. Lamon, *Ceramic matrix composites: materials, modeling and technology*. 2014: John Wiley & Sons.

[107] Guo, N., H.-Z. Shen, and P. Shen, *Cold sintering of chitosan/hydroxyapatite composites.* Materialia, 2022. **21**: p. 101294.

[108] Zhou, W., et al., *Fundamentals of Scanning Electron Microscopy (SEM)*. 2006. p. 1-40.

[109] Li, Z., et al., *Defect Engineering in Lead Zirconate Titanate Ferroelectric Ceramic for Enhanced Electromechanical Transducer Efficiency.* Advanced Functional Materials, 2021. **31**(1): p. 2005012.

[110] Jackson, N., L. Keeney, and A. Mathewson, *Flexible-CMOS and biocompatible piezoelectric AlN material for MEMS applications.* Smart Materials and Structures, 2013. **22**(11): p. 115033.

[111] Pongampai, S., et al., *Sensing layer combination of vertically aligned ZnO nanorods and graphene oxide for ultrahigh sensitivity IDE capacitive humidity sensor.* IEEJ Transactions on Electrical and Electronic Engineering, 2020. **15**(6): p. 965-975.

[112] Charoonsuk, T., et al., *Tetragonal BaTiO3 Nanowires: A Template-Free Salt-Flux-Assisted Synthesis and Its Piezoelectric Response Based on Mechanical Energy Harvesting.* Journal of Materials Chemistry C, 2019. **7**: p. 8277-8286.

[113] Pongampai, S., et al., *Triboelectric-piezoelectric hybrid nanogenerator based on BaTiO3-Nanorods/Chitosan enhanced output performance with self-charge-pumping system.* Composites Part B: Engineering, 2021. **208**: p. 108602.

[114] Sriphan, S., et al., *Piezoelectric Energy Harvesting for Low-Power Smart Electronics*, in *Encyclopedia of Materials: Electronics*, A.S.M.A. Haseeb, Editor. 2023, Academic Press: Oxford. p. 369-404.

[115] Sriphan, S. and N. Vittayakorn, *Hybrid piezoelectric-triboelectric nanogenerators for flexible electronics: Recent advances and perspectives.* Journal of Science: Advanced Materials and Devices, 2022. **7**(3): p. 100461.

[116] Yan, X., et al., *Recent progress on piezoelectric materials for renewable energy conversion.* Nano Energy, 2020. **77**: p. 105180.

[117] Charoonsuk, T., et al., *Achieving a highly efficient chitosan-based triboelectric nanogenerator via adding organic proteins: Influence of morphology and molecular structure.* Nano Energy, 2021. **89**: p. 106430.

[118] Guerin, S., et al., *Control of piezoelectricity in amino acids by supramolecular packing.* Nature Materials, 2018. **17**(2): p. 180-186.

[119] Khare, D., B. Basu, and A.K. Dubey, *Electrical stimulation and piezoelectric biomaterials for bone tissue engineering applications.* Biomaterials, 2020. **258**: p. 120280.

[120] Chorsi, M.T., et al., *Piezoelectric biomaterials for sensors and actuators.* Advanced Materials, 2019. **31**(1): p. 1802084.

[121] Kholkin, A., et al., *Strong Piezoelectricity in Bioinspired Peptide Nanotubes.* ACS Nano, 2010. **4**(2): p. 610-614.

[122] Pongampai, S., et al. *Ultrahigh Linear Sensitivity of Capacitive Humidity Sensor Base on Bilayer Structure of Graphene Oxide*. in *2019 7th International Electrical Engineering Congress (iEECON)*. 2019.

[123] Charoonsuk, T., et al., *Simple enhanced charge density of chitosan film by the embedded ion method for the flexible triboelectric nanogenerator.* Carbohydrate Polymers, 2022. **297**: p. 120070.

[124] Kim, D., et al., *Biomolecular Piezoelectric Materials: From Amino Acids to Living Tissues.* Advanced Materials, 2020. **32**(14): p. 1906989.

[125] Shin, D.-M., S.W. Hong, and Y.-H. Hwang *Recent Advances in Organic Piezoelectric Biomaterials for Energy and Biomedical Applications*. Nanomaterials, 2020. **10**, DOI: 10.3390/nano10010123.

[126] Yang, F., et al., *Wafer-scale heterostructured piezoelectric bio-organic thin films.* Science, 2021. **373**(6552): p. 337-342.

[127] Jiang, Q., et al., *Non-Topotactic Phase Transformations in Single Crystals of β-Glycine.* Crystal Growth & Design, 2015. **15**(6): p. 2568-2573.

[128] Han, G., P.S. Chow, and R.B.H. Tan, *Understanding the Salt-Dependent Outcome of Glycine Polymorphic Nucleation.* Pharmaceutics, 2021. **13**(2): p. 262.

[129] Wang, R., J. Sui, and X. Wang, *Natural Piezoelectric Biomaterials: A Biocompatible and Sustainable Building Block for Biomedical Devices.* ACS Nano, 2022. **16**(11): p. 17708-17728.

[130] Heredia, A., et al., *Nanoscale Ferroelectricity in Crystalline γ-glycine.* Adv. Funct. Mater., 2012. **22**: p. 2996.

[131] Charoonsuk, T., et al., *Enhancing the densification of ceria ceramic at low temperature via the cold sintering assisted two-step sintering process.* Ceramics International, 2018. **44**: p. S54-S57.

[132] Jin, D.H., et al., *Boosting densification and microwave dielectric properties in cold sintered BaF2 ceramics for 5.8 GHz WLAN applications.* Journal of Alloys and Compounds, 2021. **886**: p. 161141.

[133] Liu, B., et al., *Enhancement of densification and microwave dielectric properties in LiF ceramics via a cold sintering and post-annealing process.* Journal of the European Ceramic Society, 2021. **41**(2): p. 1726-1729.

[134] Liu, B., et al., *Novel transparent LiF ceramics enabled by cold sintering at 150 °C.* Scripta Materialia, 2022. **220**: p. 114917.

[135] Biesuz, M., et al., *A theoretical analysis of cold sintering.* Advances in Applied Ceramics, 2020. **119**(2): p. 75-89.

[136] Galotta, A. and V.M. Sglavo, *The cold sintering process: A review on processing features, densification mechanisms and perspectives.* Journal of the European Ceramic Society, 2021. **41**(16): p. 1-17.

[137] Hajizadeh, Z., R. Taheri-Ledari, and F.R. Asl, *3 - Identification and analytical methods*, in *Heterogeneous Micro and Nanoscale Composites for the Catalysis of Organic Reactions*, A. Maleki, Editor. 2022, Elsevier. p. 33-51.

[138] Yu, T., et al., *Current understanding and applications of the cold sintering process.* Frontiers of Chemical Science and Engineering, 2019. **13**: p. 654-664.

[139] Guo, J., et al., *Cold sintering process: a new era for ceramic packaging and microwave device development.* Journal of the American Ceramic Society, 2017. **100**(2): p. 669-677.

[140] Gundersen, E., et al., *Coupling between pressure solution creep and diffusive mass transport in porous rocks: Journal of Geophysical Research B.* Solid Earth, 2002. **107**.

[141] Wang, D., et al., *Cold sintering of microwave dielectric ceramics and devices.* Journal of Materials Research, 2021. **36**(2): p. 333-349.

[142] Marom, N., et al., *Many-Body Dispersion Interactions in Molecular Crystal Polymorphism.* Angewandte Chemie International Edition, 2013. **52**(26): p. 6629-6632.

[143] Polat, S. and P. Sayan, *The characterization and polymorphism of α-Glycine in the presence of butyric acid.* Advanced Powder Technology, 2018. **29**(9): p. 1968-1976.

[144] Liu, Z., et al., *Crystallization of metastable β glycine from gas phase via the sublimation of α or γ form in vacuum.* Biophysical Chemistry, 2008. **132**(1): p. 18-22.

[145] Surma-Ślusarska, B., S. Presler, and D. Danielewicz, *Characteristics of Bacterial Cellulose Obtained from Acetobacter xylinum Culture for Application in Papermaking.* Fibres and Textiles in Eastern Europe, 2008. **16**: p. 108-111.

[146] Tylczyński, Z. and P. Busz, *Low-temperature Phase Transition in γ-glycine Single Crystal. Pyroelectric, Piezoelectric, Dielectric and Elastic Properties.* Mater. Chem. Phys., 2016. **183**: p. 254.

[147] Tylczyński, Z. and P. Busz, *Transformation from γ to α modification in glycine crystal.* Phase Transitions, 2014. **87**(10-11): p. 1157-1164.

[148] Boldyreva, E., T. Drebushchak, and E. Shutova, *Structural distortion of the α,β, and γ polymorphs of glycine on cooling.* Zeitschrift fur Kristallographie, 2003. **218**: p. 366-376.

[149] Anbu Chudar Azhagan, S. and V.S. Kathiravan, *Selective crystallization of gamma glycine for NLO applications using magnesium sulfate (MgSO) as an additive.* Materials Science-Poland, 2019. **37**(2): p. 265-279.

[150] Wu, D., et al., *Dielectric and Piezoelectric Properties of PZT Composite Thick Films with Variable Solution to Powder Ratios.* J Am Ceram Soc, 2009. **92**(6): p. 1276-1279.

[151] Li, H., et al., *Improved ferroelectric properties of (100)-oriented PZT thin films deposited on stainless steel substrates with La0.5Sr0.5CoO3 buffer layers.* Journal of Materials Science: Materials in Electronics, 2018. **29**(17): p. 14651-14656.

[152] Gupta, M.K., et al., *Piezoelectric, dielectric, optical and electrical characterization of solution grown flower-like ZnO nanocrystal.* Materials Letters, 2009. **63**(22): p. 1910-1913.

[153] Sharma, H. and A. Mansingh, *Sol-gel processed barium titanate ceramics and thin films.* Journal of materials science, 1998. **33**: p. 4455-4459.

[154] Vaněk, P., et al., *Electrical activity of ferroelectric biomaterials and its effects on the adhesion, growth and enzymatic activity of human osteoblast-like cells.* Journal of Physics D: Applied Physics, 2016. **49**(17): p. 175403.

[155] Hoque, N.A., et al., *Biowaste crab shell-extracted chitin nanofiber-based superior piezoelectric nanogenerator.* Journal of Materials Chemistry A, 2018. **6**(28): p. 13848-13858.

[156] Halperin, C., et al., *Piezoelectric Effect in Human Bones Studied in Nanometer Scale.* Nano Letters, 2004. **4**(7): p. 1253-1256.

[157] Karan, S.K., et al., *A new insight towards eggshell membrane as high energy conversion efficient bio-piezoelectric energy harvester.* Materials Today Energy, 2018. **9**: p. 114-125.

[158] Maiti, S., et al., *Bio-waste onion skin as an innovative nature-driven piezoelectric material with high energy conversion efficiency.* Nano Energy, 2017. **42**: p. 282-293.

[159] Sohn, C., et al., *Generating electricity from molecular bonding-correlated piezoresponse of biodegradable silk nanofibers.* Nano Energy, 2022. **103**: p. 107844.

[160] Hosseini, E.S., et al., *Glycine–Chitosan-Based Flexible Biodegradable Piezoelectric Pressure Sensor.* ACS Applied Materials & Interfaces, 2020. **12**(8): p. 9008-9016.

[161] Guo, H., et al., *Cold Sintering Process: A Novel Technique for Low-Temperature Ceramic Processing of Ferroelectrics.* Journal of the American Ceramic Society, 2016. **99**.

[162] Maria, J.-P., et al., *Cold sintering: Current status and prospects.* Journal of Materials Research, 2017. **32**(17): p. 3205-3218.

[163] Anindy, U., M. Nur Indro, and I. Husein, *Piezoelectric properties: cerium oxide (CeO2) doped barium titanate (BaTiO3) film on ITO substrate.* Ferroelectrics, 2021. **570**(1): p. 162-175.

[164] Guo, H., et al., *Protocol for ultralow-temperature ceramic sintering: an integration of nanotechnology and the cold sintering process.* ACS nano, 2016. **10**(11): p. 10606-10614.

[165] Tsuji, K., et al., *Single Step Densification of High Permittivity BaTiO3 Ceramics at 300 ºC.* Journal of the European Ceramic Society, 2019. **40**.

[166] Kang, S., et al., *Barium titanate/poly (vinylidene fluoride) nanocomposites with core–shell structure with high dielectric constant and temperature stability prepared via a cold sintering process.* Journal of Materials Science: Materials in Electronics, 2020. **31**.

[167] Ndayishimiye, A., et al., *Thermosetting polymers in cold sintering: The fabrication of ZnO-polydimethylsiloxane composites.* Journal of the American Ceramic Society, 2020. **103**(5): p. 3039-3050.

[168] Guo, J., et al., *Cold Sintered Ceramic Nanocomposites of 2D MXene and Zinc Oxide.* Advanced Materials, 2018. **30**(32): p. 1801846.

[169] Alter, H., *Filler particle size and mechanical properties of polymers.* Journal of Applied Polymer Science, 1965. **9**(4): p. 1525-1531.

[170] Zhao, Y., et al., *Cold-Sintered V2O5-PEDOT:PSS Nanocomposites for Negative Temperature Coefficient Materials.* Journal of the European Ceramic Society, 2018. **39**.

[171] Sada, T., et al., *High permittivity BaTiO3 and BaTiO3-polymer nanocomposites enabled by cold sintering with a new transient chemistry: Ba (OH) 2· 8H2O.* Journal of the European Ceramic Society, 2021. **41**(1): p. 409-417.

[172] Vinoth, S. and S.-F. Wang, *Cold Sintering Process for a BaTiO3/Poly (vinylidene difluoride) Ceramic–Polymer Composite: Evaluation of the Structural and Microwave Dielectric Properties.* Inorganic Chemistry, 2023.

[173] Sada, T., et al., *Highly Reliable BaTiO3-Polyphenylene Oxide Nanocomposite Dielectrics via Cold Sintering.* Advanced Materials Interfaces, 2021. **8**(18): p. 2100963.

[174] Noisak, J., et al., *Towards the preparation of organic ferroelectric composites: fabrication of a gamma-glycine-bacterial cellulose composite via cold sintering process.* Journal of Materials Research and Technology, 2023. **25**: p. 4749-4760.

[175] Peter, M.E. and P. Ramasamy, *Growth of gamma glycine crystal and its characterisation.* Spectrochimica Acta Part A: Molecular and Biomolecular Spectroscopy, 2010. **75**(5): p. 1417-1421.

[176] Ukasi, S., et al., *Gamma glycine enhances efficiency of organic hybrid piezoelectric-triboelectric nanogenerators.* Nano Energy, 2024. **119**: p. 109045.

[177] Bouchard, A., G.W. Hofland, and G.-J. Witkamp, *Solubility of Glycine Polymorphs and Recrystallization of β-Glycine.* Journal of Chemical & Engineering Data, 2007. **52**(5): p. 1626-1629.

[178] Ning Guo, H.-Z.S., Ping Shen, *Cold sintering of chitosan/hydroxyapatite composites.* Materialia, 2022. **21**(2589-1529).

[179] Chandrasekaran, K., et al., *X-ray structure of barium titanate - missed opportunities.* Acta crystallographica. Section B, Structural science, 2000. **56 (Pt 5)**: p. 918-9.

[180] Su, J. and J. Zhang, *Recent development on modification of synthesized barium titanate (BaTiO3) and polymer/BaTiO3 dielectric composites.* Journal of Materials Science: Materials in Electronics, 2019. **30**.

[181] Fuentes, S., et al., *Synthesis and characterization of BaTiO3 nanoparticles in oxygen atmosphere.* Journal of Alloys and Compounds, 2010. **505**(2): p. 568-572.

[182] Vasudevan, R., et al., *Effect of microwave sintering on the structural, optical and electrical properties of BaTiO3 nanoparticles.* Journal of Materials Science: Materials in Electronics, 2014. **25**.

[183] Hu, Z., et al., *Facile fabrication of tetragonal phase single-crystalline BaTiO3 terrace-like dendrite by a simple solvothermal method and its piezocatalytic properties.* Materials Chemistry and Physics, 2023. **293**: p. 126911.

[184] Luo, G., et al., *Synthesis of tetragonal BaTiO3 powder with size and dispersity optimization via synergy mechanisms of combined dispersants.* Journal of Alloys and Compounds, 2023. **944**: p. 169079.

[185] Luan, S., et al., *Fabrication of BaTiO3 nanopowders with high tetragonality via two-step assisted rotary furnace calcination for MLCC applications.* Ceramics International, 2023. **49**(8): p. 12529-12539.

[186] Phan, T.T.M., et al., *Enhancement of polarization property of silane-modified BaTiO3 nanoparticles and its effect in increasing dielectric property of epoxy/BaTiO3 nanocomposites.* Journal of Science: Advanced Materials and Devices, 2016. **1**(1): p. 90-97.

[187] Lee, D.Y., et al., *Effect of calcination temperature and atmosphere on crystal structure of BaTiO3 nanofibers.* Metals and Materials International, 2010. **16**(3): p. 453-457.

[188] Hao, S., et al., *Preparation and Characterization of Ag-Doped BaTiO3 Conductive Powders.* International Journal of Inorganic Chemistry, 2011. **2011**.

[189] Nakhaei, M. and A. Bahari, *Synthesis and investigation of temperature effects on barium titanate (BaTiO3) nanostructural and electrical properties.* Journal of Materials Science: Materials in Electronics, 2016. **27**(6): p. 5899-5908.

[190] Chiang, C.-W. and J.-H. Jean, *Effects of barium dissolution on dispersing aqueous barium titanate suspensions.* Materials Chemistry and Physics, 2003. **80**(3): p. 647-655.

[191] Tripathy, S.S. and A.M. Raichur, *Dissolution properties of BaTiO3 nanoparticles in aqueous suspensions.* Journal of Experimental Nanoscience, 2011. **6**(2): p. 127-137.

[192] Chang, S.-J., et al., *An efficient approach to derive hydroxyl groups on the surface of barium titanate nanoparticles to improve its chemical modification ability.* Journal of Colloid and Interface Science, 2009. **329**(2): p. 300-305.

[193] Nawanil, C., et al. *Effect of surface treatment on electrical properties of barium titanate/carbon nanotube/polydimethylsiloxane nanocomposites*. in *AIP Conference Proceedings*. 2018. AIP Publishing.

[194] Chen, L., et al., *Mechanical, thermal, and dielectric properties of polyvinylidene fluoride nanocomposites fabricated by introducing functional MWCNTs/barium titanate compounding dielectric nanofillers.* Polymer Composites, 2021. **42**(3): p. 1383-1395.

[195] Kang, S., et al., *Influence of surface coating on the microstructures and dielectric properties of BaTiO3 ceramic via a cold sintering process.* RSC Advances, 2020. **10**(51): p. 30870-30879.

[196] R, E.V., et al., *Crystal growth, optical and thermal studies of nonlinear optical-glycine single crystal grown from lithium nitrate.* Optik - International Journal for Light and Electron Optics, 2012. **123**: p. 409-413.

[197] Wang, D., et al., *Cold sintering of microwave dielectric ceramics and devices.* Journal of Materials Research, 2021. **36**.

[198] Stefanescu, E.A., et al., *Multifunctional fiberglass-reinforced PMMA-BaTiO3 structural/dielectric composites.* Polymer, 2011. **52**: p. 2016-2024.

[199] Chao, F., et al., *Study of dielectric property on BaTiO3/BADCy composite.* Materials Chemistry and Physics, 2008. **108**: p. 306-311.

[200] Maluangnont, T., et al., *Electrochemical and electrical characteristics of ball milled Cs2Ti6O13 modified by the surface-to-bulk migration of hydroxyl groups.* Dalton Transactions, 2023. **52**(34): p. 11815-11825.

[201] Sriphan, S., et al., *Effect of Adsorbed Water and Temperature on the Universal Power Law Behavior of Lepidocrocite-Type Alkali Titanate Ceramics.* The Journal of Physical Chemistry C, 2021. **125**(23): p. 12910-12920.

[202] Dyre, J.C., et al., *Fundamental questions relating to ion conduction in disordered solids.* Reports on Progress in Physics, 2009. **72**(4): p. 046501.

[203] Sidebottom, D.L., *Dimensionality Dependence of the Conductivity Dispersion in Ionic Materials.* Physical Review Letters, 1999. **83**(5): p. 983-986.

[204] Liu, J., et al., *Dielectric Permittivity and Electric Modulus in Bi2Ti4O11.* The Journal of Chemical Physics, 2003. **119**: p. 2812-2819.

[205] Cheng, B.L., et al., *Mechanical loss and elastic modulus associated with phase transitions of barium titanate ceramics.* Journal of Alloys and Compounds, 1994. **211-212**: p. 352-355.

[206] Shao, S., et al., *High piezoelectric properties and domain configuration in BaTiO3 ceramics obtained through the solid-state reaction route.* Journal of Physics D: Applied Physics, 2008. **41**(12): p. 125408.

[207] Chaisan, W., *Effect of sintering temperature on the hysteresis properties of barium titanate ceramic.* NU. International Journal of Science, 2007. **4**(2): p. 132-139.

[208] Guo, H., et al., *Hydrothermal-Assisted Cold Sintering Process: A New Guidance for Low-Temperature Ceramic Sintering.* ACS Appl Mater Interfaces, 2016. **8**(32): p. 20909-15.

[209] Coutinho, L., R. Aredes, and E. Antonelli, *Cold sintering and electric characterization of ZnO-BaTiO 3 composites.* Cerâmica, 2021. **67**: p. 105-110.

[210] Sada, T., et al., *High permittivity BaTiO3 and BaTiO3-polymer nanocomposites enabled by cold sintering with a new transient chemistry: Ba(OH)2·8H2O.* Journal of the European Ceramic Society, 2021. **41**(1): p. 409-417.

[211] Sada, T., et al., *Highly Reliable BaTiO3-Polyphenylene Oxide Nanocomposite Dielectrics via Cold Sintering.* Advanced Materials Interfaces, 2021. **8**(18): p. 2100963.

[212] Vinoth, S. and S.-F. Wang, *Cold Sintering Process for a BaTiO3/Poly (vinylidene difluoride) Ceramic–Polymer Composite: Evaluation of the Structural and Microwave Dielectric Properties.* Inorganic Chemistry, 2023. **62**(21): p. 8326-8333.

[213] Sada, T., et al., *Surface modification of BaTiO3 with catechol surfactant and effects on cold sintering.* Journal of Applied Physics, 2021. **129**(18).

[214] Yoon, S.H., et al., *Sintering and consolidation of silver nanoparticles printed on polyimide substrate films.* Macromolecular Research, 2009. **17**(8): p. 568-574.

[215] Kang, S.J.L., *5 - Liquid phase sintering*, in *Sintering of Advanced Materials*, Z.Z. Fang, Editor. 2010, Woodhead Publishing. p. 110-129.

JOURNAL OF MATERIALS RESEARCH AND TECHNOLOGY 2023;25:4749–4760

Available online at www.sciencedirect.com

jmr&t Journal of Materials Research and Technology

journal homepage: www.elsevier.com/locate/jmrt

Towards the preparation of organic ferroelectric composites: fabrication of a gamma-glycine-bacterial cellulose composite via cold sintering process

Jitrawan Noisak [a,b], *Thitirat Charoonsuk* [c], *Satana Pongampai* [d], *Nattapong Pinpru* [e], *Phakkhananan Pakawanit* [f], *Wanwilai Vittayakorn* [g], *Tosapol Maluangnont* [g], *Te-Wei Chiu* [h], *Naratip Vittayakorn* [a,b,*]

[a] *Advanced Materials Research Unit, School of Science, King Mongkut's Institute of Technology Ladkrabang, Bangkok 10520, Thailand*

[b] *Department of Chemistry, School of Science, King Mongkut's Institute of Technology Ladkrabang, Bangkok 10520, Thailand*

[c] *Department of Materials Science, Faculty of Science, Srinakharinwirot University, Sukhumvit 23, Wattana, Bangkok 10110, Thailand*

[d] *Department of Physics, Faculty of Science, King Mongkut's University of Technology Thonburi, Bangkok 10140, Thailand*

[e] *Nanohybrids and Innovation Coating (NHIC), National Nanotechnology Center (NANOTEC), National Science and Technology Development Agency (NSTDA), Khlong Luang, Pathumthani 12120, Thailand*

[f] *Synchrotron Research and Applications Division, Synchrotron Light Research Institute, 111 University Avenue, Muang District, Nakhon Ratchasima, 30000, Thailand*

[g] *Electroceramics Research Laboratory, College of Materials Innovation and Technology, King Mongkut's Institute of Technology Ladkrabang, Bangkok 10520*

[h] *Department of Materials and Mineral Resources Engineering, National Taipei University of Technology, Taipei, 106 Taiwan*

ARTICLE INFO

Article history:
Received 18 May 2023
Accepted 28 June 2023
Available online 3 July 2023

Keywords:
Bacterial cellulose
γ-glycine
Cold sintering process

ABSTRACT

The cold sintering process (CSP) has emerged as a revolutionary technique for low-temperature processing of ceramics and composites, enabling high-density fabrication at low temperatures. In this study, we demonstrated the implementation of CSP in fabricating the γ-glycine (γ-G)-bacterial cellulose (BC) composite and evaluated the effect of sintering temperature and holding time on the microstructure and electrical properties. Our findings revealed that an increase in sintering temperature and holding time leads to grain growth, as the transient solvent (water) facilitates the closely-packed microstructure. Moreover, the addition of BC as a filler into the γ-G matrix leads to a composite with a 10% increase in hardness when BC was uniformly distributed in γ-G. The composite with a relative density of 97% was successfully obtained at 120 °C/24 h, preserving the γ polymorph of glycine without the unwanted transformation commonly observed with traditional sintering. We also reported the dielectric and ferroelectric properties of the γ-G-BC composite, exhibiting

* Corresponding author. Advanced Materials Research Unit, School of Science, King Mongkut's Institute of Technology Ladkrabang, Bangkok 10520, Thailand.
E-mail address: naratip.vi@kmitl.ac.th (N. Vittayakorn).

https://doi.org/10.1016/j.jmrt.2023.06.259

a remanent polarization of 0.004 μC/cm^2 and a coercive field of 1.201 kV/cm. Our findings suggest that CSP is a promising approach for low-temperature processing and fabrication of ceramics, especially when incorporating structurally sensitive filler such as organic ferroelectric, to achieve high-performance composites.

1. Introduction

Piezoelectric materials have the unique property of converting mechanical forces into electricity and vice versa. Inorganic piezoelectric materials, such as lead zirconated titanate (PZT) [1], aluminum nitride (AlN) [2], zinc oxide (ZnO) [3], and barium titanate ($BaTiO_3$) [4,5], exhibit this effect due to ions rearrangement within their crystal structures which lack the inversion symmetry [6,7]. These materials are commonly used as ultrasonic motors and actuators, precision motion control and positioning devices, microfluidics, implantable medical devices, and piezoelectric nanogenerators [6–9]. However, inorganic piezoelectric materials have some drawbacks, including limited strength and durability, poor temperature stability, high cost and difficulty of processing, inflexibility, poor biocompatibility, potential toxicity to the environment and human health, making them less attractive for biomedical and related applications [6,7].

Recently, organic piezoelectric materials, including glycine [10], collagen [11], silk [12], self-assembled diphenylalanine peptide nanotubes (PNTs) [13], graphene [14] and chitosan [15], are attracting increasing attention due to their notable advantages [16] such as high biocompatibility, flexibility, and processability. However, they have relatively low piezoelectric coefficients and poor mechanical properties [17]. Despite these limitations, organic piezoelectric materials hold great promise in the field of biomedicine, particularly for implantable devices and sensors, due to the reduced risk of adverse biological responses. Improvements in the fabrication techniques, molecular design, and characterization methods are necessary to address these challenges and to expand their potential applications in various fields [18,19]. Among organic piezoelectric materials, glycine has gained considerable attention due to its simplicity as the simplest amino acid found in proteins [19,20]. It crystallizes into three polymorphs depending on crystallization conditions: α, β, and γ. The metastable α-glycine (α-G) phase has a centrosymmetric structure and possesses no piezoelectricity, while the unstable β-glycine (β-G) phase has a non-centrosymmetric structure and consequently shows piezoelectricity [21]. The addition of inorganic salts (such as NaCl) significantly promotes the secondary nucleation of the piezoelectric γ-G while simultaneously inhibiting the α-G primary nucleation. This is possible due to ion-glycine interaction and the formation of linear head-to-tail glycine chains [22]. Despite initial reports of low piezoelectric coefficients, recent studies [23,24] have shown that glycine exhibits strong piezoelectric properties, with piezoelectric coefficients comparable to or better than those of conventional organic piezoelectric materials [25]. In 2012, Heredia et al. [26] reported robust and continuous nanoscale ferroelectricity in piezoelectric γ-G for the first time. Additionally, the polarization of γ-G is about five times stronger than that of β-G due to spirally aligned dipoles along the axis, as opposed to randomly oriented dipoles in β-G [27]. However, when compared to inorganic piezoelectric materials, γ-G still possess a lower piezoelectric output.

However, the synthesis of γ-G crystals through traditional re-crystallization processes does not allow doping or compositing. While the properties could be improved when γ-G ceramics is composited with other materials, the transformation of γ-G at high temperatures remains a challenge that affects its piezoelectric and ferroelectric properties. The current limitation regarding the densification of ceramics can be addressed by utilizing the cold sintering process (CSP) [28–31]. This innovative low-temperature sintering approach has proven to be effective in densifying ceramic materials. The recent study conducted by Randall et al. [32] reported that the CSP is capable of delivering high relative densities (>98%) of potassium dihydrogen phosphate (KH_2PO_4) below 300 °C, with a processing duration of around 1 h. This finding highlights the potential of CSP as a promising alternative, based on the "*dissolution-precipitation*" phenomenon, to conventional high-temperature sintering methods [33,34]. Accordingly, CSP is an innovative, promising approach for the preparation of γ-G composites by utilizing the low-temperature processing conditions which could impede the conventional γ-G transformation typically at >200 °C [20,21]. This research seeks to improve the density, mechanical, piezoelectric, and ferroelectric properties of γ-G, an organic piezoelectric/ferroelectric material. Additionally, the study aims to explore new methods for the fabrication of high-performance composites using biomaterial-based fillers such as bacterial cellulose, thereby expanding the range of their potential applications.

2. Experimental procedure

2.1. *Gamma glycine (γ-G) preparation*

Fig. 1a Shows a schematic illustration of the γ-G synthesis via a recrystallization process. An amount of 56 g of commercial-grade glycine (NH_2COOH, 99% purity from Sigma-Aldrich) and 15 g of sodium chloride (NaCl, analytical-grade from Carlo Erba) in a 3:1 mol ratio were dissolved in 100 mL deionized water (DI water), stirred for 5 h at room temperature (RT), then filtered with a vacuum filtration twice. The obtained liquid was kept in an oven at 35 °C for 25 days for the α-to-γ transformation. The γ-G crystals were obtained after 25 days,

which were ground using a ball mill apparatus for 3 h to make the γ-G powder.

2.2. Bacterial cellulose (BC) preparation

BC powder was prepared by washing and soaking 700 g of nata de coco from the local manufacturer (Bifern, ASP Inter Food Co., Ltd) in 1000 mL of boiled water, with the water replaced every 30 min until pH 5. Then, the obtained nata de coco paste was blended in a wet blender, poured into trays, and freeze-dried at −40 °C for 24 h.

2.3. Fabrication of γ-G-BC composites via CSP

Fig. 1b Illustrates the fabrication of γ-G-BC composite via CSP. γ-G powder and BC powder were mixed in a mortar for 2 min. Then, DI water was added, and the mixture was ground in a pestle and mortar for 2 min. The weight ratio of γ-G: BC: DI water was 92:1:7. Next, 0.1 g of the γ-G-BC mixture was placed in a tungsten carbide block and subjected to uniaxial pressure of 2000 kPa at RT-120 °C for 6–24 h for densification. After cooling, the cold-sintered γ-G-BC composite was removed from the block for characterization. For comparison, the traditional sintering process (TSP) was also employed. The γ-G powder underwent uniaxial pressing at a pressure of 2000 kPa, followed by sintering in air at a temperature of 200 °C for a duration of 24 h.

2.4. Characterization

The relative density of γ-G-based composites was calculated by measuring mass and dimensions of the cold-sintered pellet. The degree of densification, or the ratio of actual density to theoretical density, was calculated using Eq. (1) [35]:

$$\rho_r = \frac{4m}{\left(\pi d^2 h \rho_t\right)} \times 100\% \quad (1)$$

where: ρ_r is the relative density (%), m is mass of γ-G-BC composites (g), d and h are diameter (cm) and thickness (cm) of the pellet, respectively; and ρ_t is the theoretical density (g/cm^3) which was calculated using Eq. (2):

$$\rho_t = \frac{m}{\left(\frac{m_1}{\rho_1}\right) + \left(\frac{m_2}{\rho_2}\right)} \quad (2)$$

where m_1 and m_2 are the masses of γ-G and BC, respectively; ρ_1 and ρ_2 are the theoretical densities (g/cm^3) of γ-G and BC, respectively, which were calculated according to Eq. (3):

$$\rho = \frac{nA}{V_c N_A} \quad (3)$$

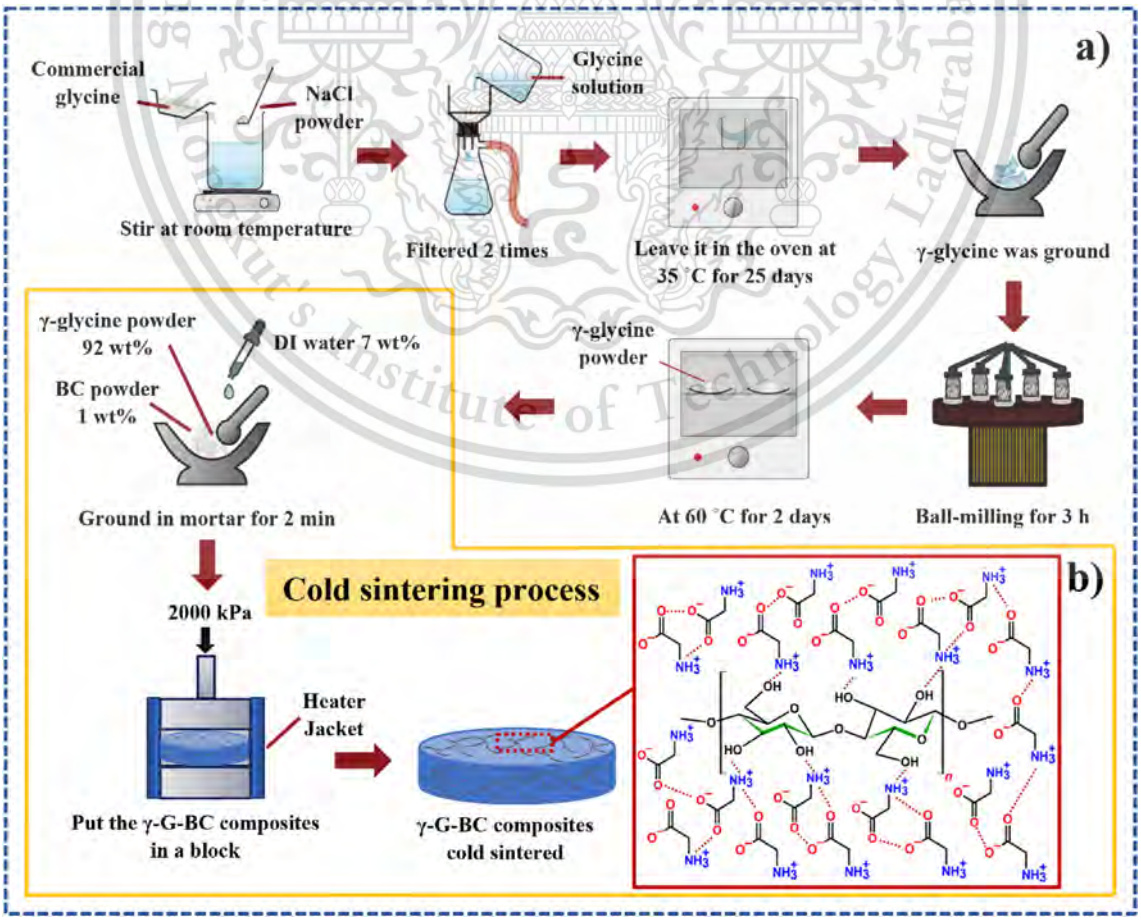

Fig. 1 – Schematic illustrations of (a) preparation of γ-G, and (b) fabrication of the γ-G-BC composites via CSP.

where n is the number of molecules per unit cell, A is the formula weight (g/mol), V_c is the volume per unit cell (cm^3/unit cell), and $N_A = 6.023 \times 10^{23}$/mol.

Fourier-transform infrared spectroscopy (FT-IR, SHIMADZU, IRTracer-100) in an attenuated total reflectance (ATR) mode was recorded between 700 and 4000 cm^{-1} and the resolution 4 cm^{-1} with 45 accumulation scans. Crystal structure of the composite was characterized by X-ray diffraction (XRD, RIGAKU smart lab, $2\theta = 5–50°$) and compared to the JCPDS database. LeBail refinement of the unit cell parameters was performed using JANA2006 software. The average crystallite size of γ-G-BC composites was calculated using Debye-Scherrer Eq. (4):

$$D = \frac{K\lambda}{\beta \cos \Theta} \tag{4}$$

where D is the crystallite size, K is known as the Scherer's constant ($K = 0.94$), λ is wavelength of X-ray radiation (1.5418 Å), β is a full width at half maximum (FWHM) of the diffraction peak, and Θ is the angle of diffraction [36]. A simultaneous XRD-DSC instrument (Rigaku Co., Tokyo, Japan) was also utilized to further characterize the γ-G-BC composite. The instrument merges a heat-flux type DSC with an X-ray diffractometer (Cu K_α, 40 kV, 30 mA; and $2\theta = 10–40°$) to obtain accurate readings. The composite was placed on an aluminum square-shaped stage (8 mm × 8 mm), and the temperature was increased from RT to 300 °C at a heating rate of 40 °C/min. The morphology and grain size of the γ-G-BC composite were observed using an SEM (Quanta FEG-250, FEI). SR-XTM was conducted at beamline 1.2 W, SLRI, Thailand. X-ray projections of the sample were collected for a complete dataset, spanning 180° with 0.1-degree increments. Artifacts were minimized by attenuating polychromatic X-rays with a 350-micron-thick aluminum foil, averaging at 11.5 keV. Projections were captured using a sCMOS camera with 1.44-μm pixel size. Data was pre-processed and reconstructed in 3D using the Octopus Reconstruction software. The reconstructed images were visualized using Drishti software. The Vickers test was examined using a micro hardness tester (Shimadzu HMV-2T, 1 kg load). Hardness values were calculated using Vickers hardness Eq. (5):

$$HV = \frac{1.854 \times F}{d^2} \tag{5}$$

where HV represents a Vickers hardness (kg/mm^2), F is the applied load (g), and d is the diagonal length (mm) of the indentation cavity. To determine the dielectric properties of the γ-G-based composite, top and bottom surfaces of the pellet were coated with silver paste and dried in air at 100 °C for 30 min. The dielectric constant (ε_r) and loss tangent (tan δ) of the γ-G-BC composites were recorded using an LCR meter (Agilent E4908A) from 100 Hz to 1 MHz at RT, 50, 100 and 150 °C. Polarization versus electric field hysteresis loops of selected samples were recorded at RT using a standard ferroelectric test system (RT66A) from Radiant Technologies.

3. Results and discussion

Fig. 2 is the SEM images showing the microstructure of the γ-G-BC composites compressed at 2000 kPa and sintered at varying temperatures (RT, 60, and 120 °C) for a duration of 6–24 h. After removal from the tungsten carbide block, the composites appeared as white pellets with a diameter of 1 cm and a thickness of approximately 1 mm. Firstly, at the fixed holding time of 24 h, the γ-G-BC composite sintered at RT had a porous and uneven surface, with a small grain size of approximately 1.45 ± 0.73 μm (Fig. 2a). With increasing sintering temperature to 60 °C (Figs. 2b) and 120 °C (Fig. 2c), the surface became smoother, and the grain size increased to 1.76 ± 1.20 μm and 2.27 ± 0.99 μm, respectively. In other experiments where the temperature was fixed at RT and the time was varied, the composite sintered for 6 h had a small grain size of 1.42 ± 0.81 μm (Fig. 2d) and a porous surface. The grain size increased with increasing holding time to 2.01 ± 1.02 μm (12 h, Figs. 2e) and 2.39 ± 1.48 μm (24 h, Fig. 2f). Clearly, the sintering temperature and holding time both affect the grain size and densification, as they play important

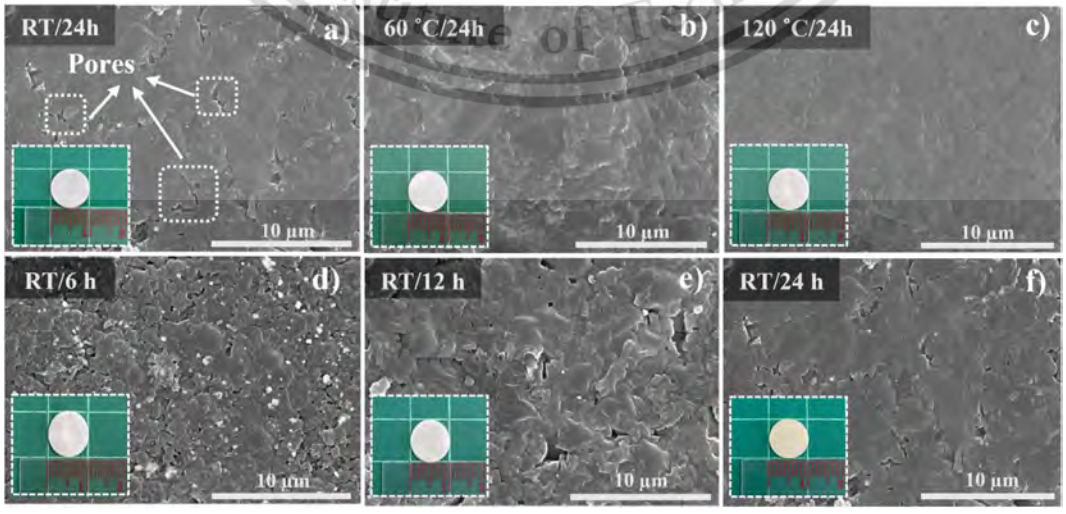

Fig. 2 – SEM images of the cold-sintered γ-G-BC composites prepared at different conditions: (a) RT/24 h (b) 60 °C/24 h (c) 120 °C/24 h (d) RT/6 h (e) RT/12 h and (f) RT/24 h. The insets show the corresponding digital image of the pellet.

roles in accelerating the density and the densification process [37].

The mechanism of CSP is depicted in Fig. 3, consisting of two stages. At stage I, the homogenized ensembles of the γ-G-BC composite was added with a liquid phase, which can be water or water with volatile solute (i) [38,39]. The liquid phase serves as a lubricant and smooths the particle surface. The added liquid is beneficial to particle rearrangement (ii) as it partially dissolves sharp particles edges, leading to spaces for particles sliding. The densification at this stage is mainly

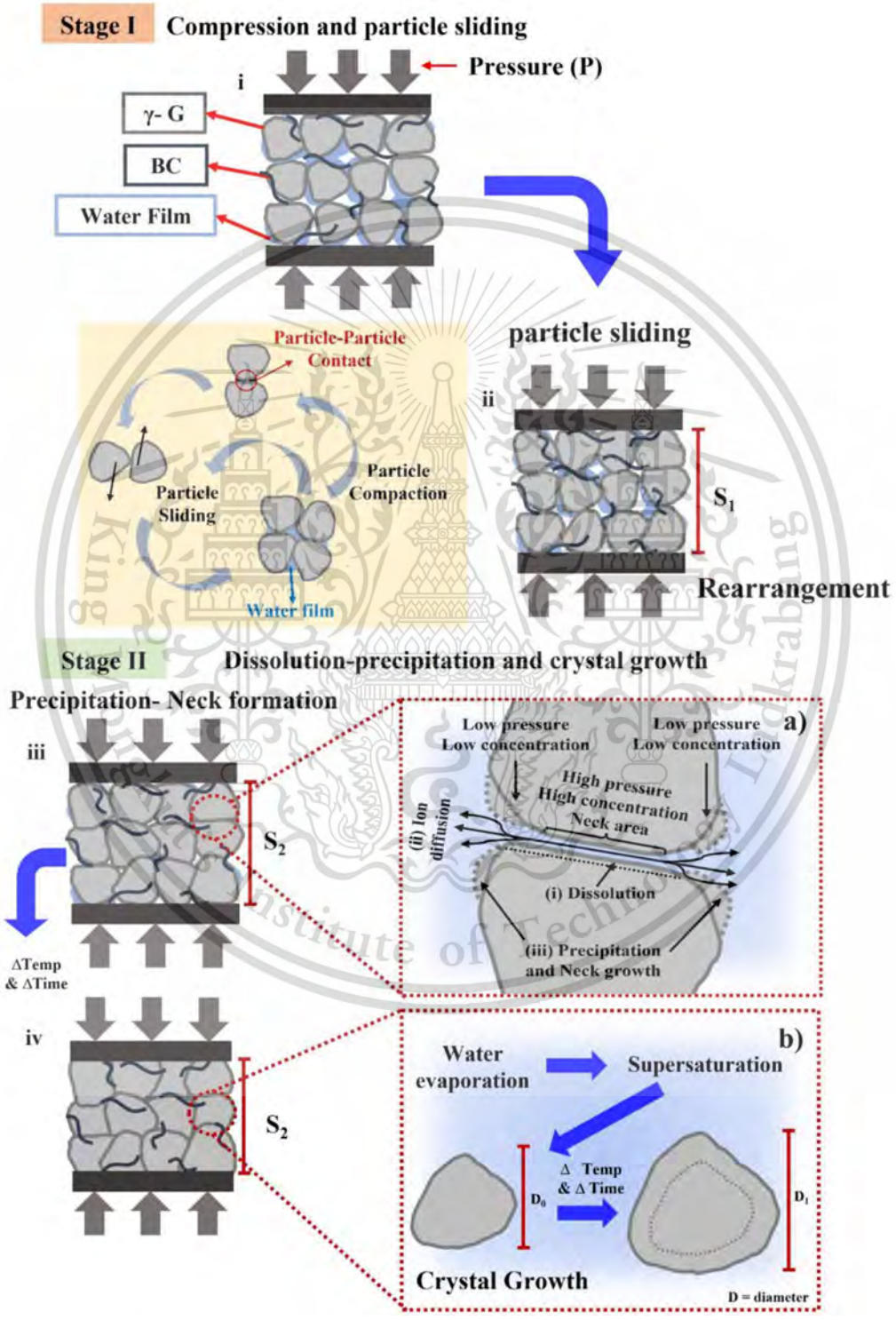

Fig. 3 – Schematics of CSP mechanism at various stages adapted from Refs. [32,38,54]. Stage I involves compression and particle sliding: i) particle compaction, ii) particle sliding and rearrangement. Stage II involves the dissolution-precipitation and crystal growth shown in iii) and iv). Details of the these two steps of Stage II are shown in a) incorporating dissolution, ion diffusion, precipitation-neck formation; and b) water evaporation and crystal growth.

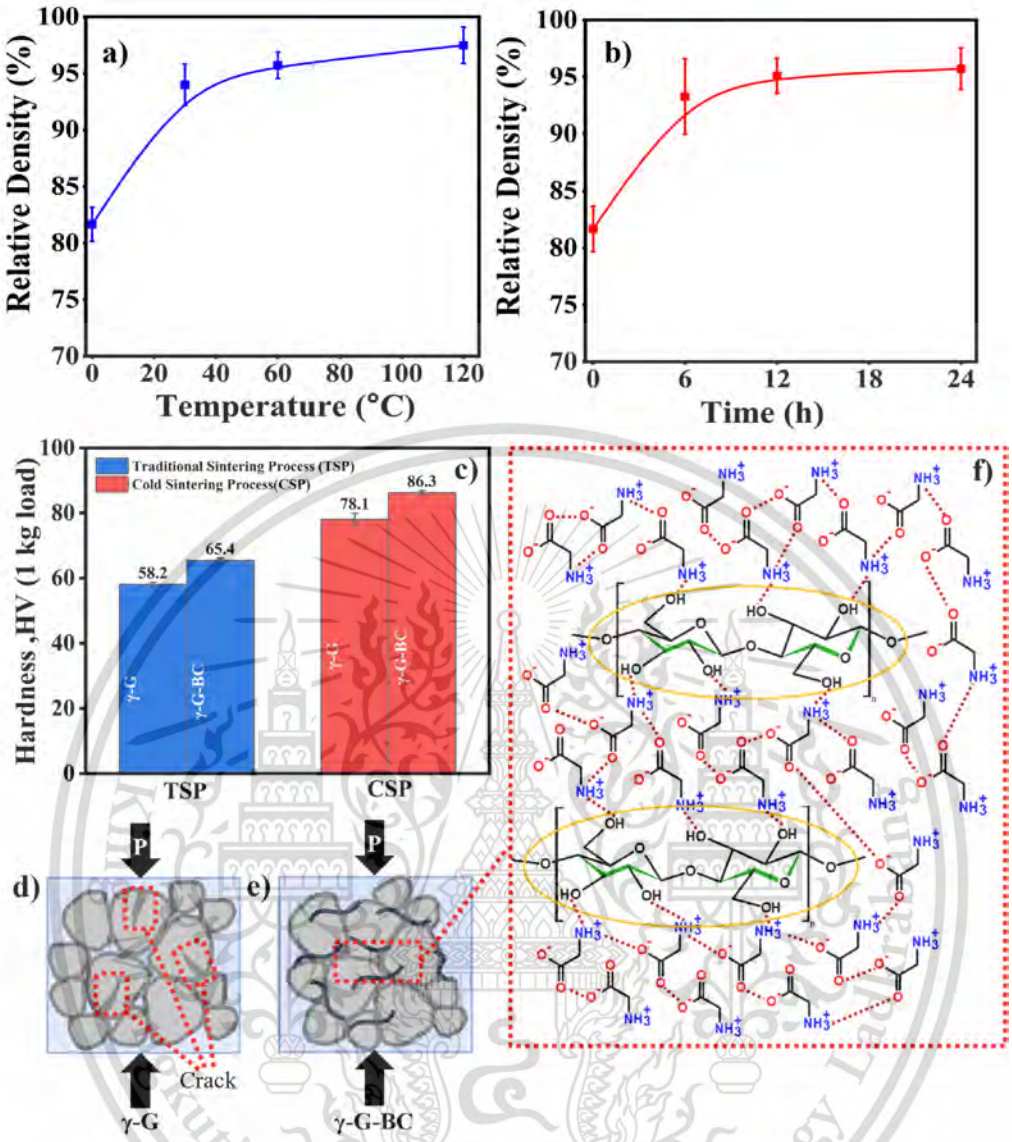

Fig. 4 – The relative density of γ-G-BC composite after CSP at (a) various sintering temperatures and (b) various holding times. (c) Vickers hardness number (HV, 1 kg load) of the γ-G-BC composites via TSP (blue) and the 120 °C/24 h via CSP (red). CSP diagram of (d) γ-G via CSP, and (e) after adding BC; (f) the chemical structure showing hydrogen bonds between amino acid groups of γ-G and hydroxyl groups of BC.

through the external pressure, where the liquid phase readily redistributes itself and fills into particle interstitials. Accordingly, this early stage of sintering results in the initial particle compaction (yellow frame), contributing mostly to the total sample shrinkage (S1) [40].

Next, stage II begins at the solid-solid interface [41], involving dissolution at intergranular interfaces and mass transport through diffusion. Here, the ions (dissolved from the particles) diffuse through the water film (iii (a-ii)), causing gradual dilution of solute concentration away from the solid surfaces. Subsequently, precipitation occurs in pores (iii(a-iii)) and lead to neck growth at grain-grain interstitials. As a result, the sample undergoes a slight shrinkage (S2). When the temperature and time are raised, the liquid volume is substantially reduced. Once precipitation is completed, the number of particle-particle contacts is significantly increased; crystal growth may occur via the coalescence of small crystallites into relatively larger ones. Notably, the crystal growth stages (iv-b) are strongly dynamic in nature, being driven by water evaporation and a supersaturated liquid at the temperature right above its boiling point. This triggers a large chemical driving force for the solid and liquid phases to reach an equilibrium state. Accordingly, temperature and time play a crucial role in this stage, as they enhance solubility while speeding up dissolution and grain growth. During the grain growth state, the initial grain undergoes a gradual and controlled increase in size, influenced by factors such as temperature and time. Throughout this process, the average grain size transitions from an initial value of D_0 to a final value of D_1. The densification rate varies with temperature, initially

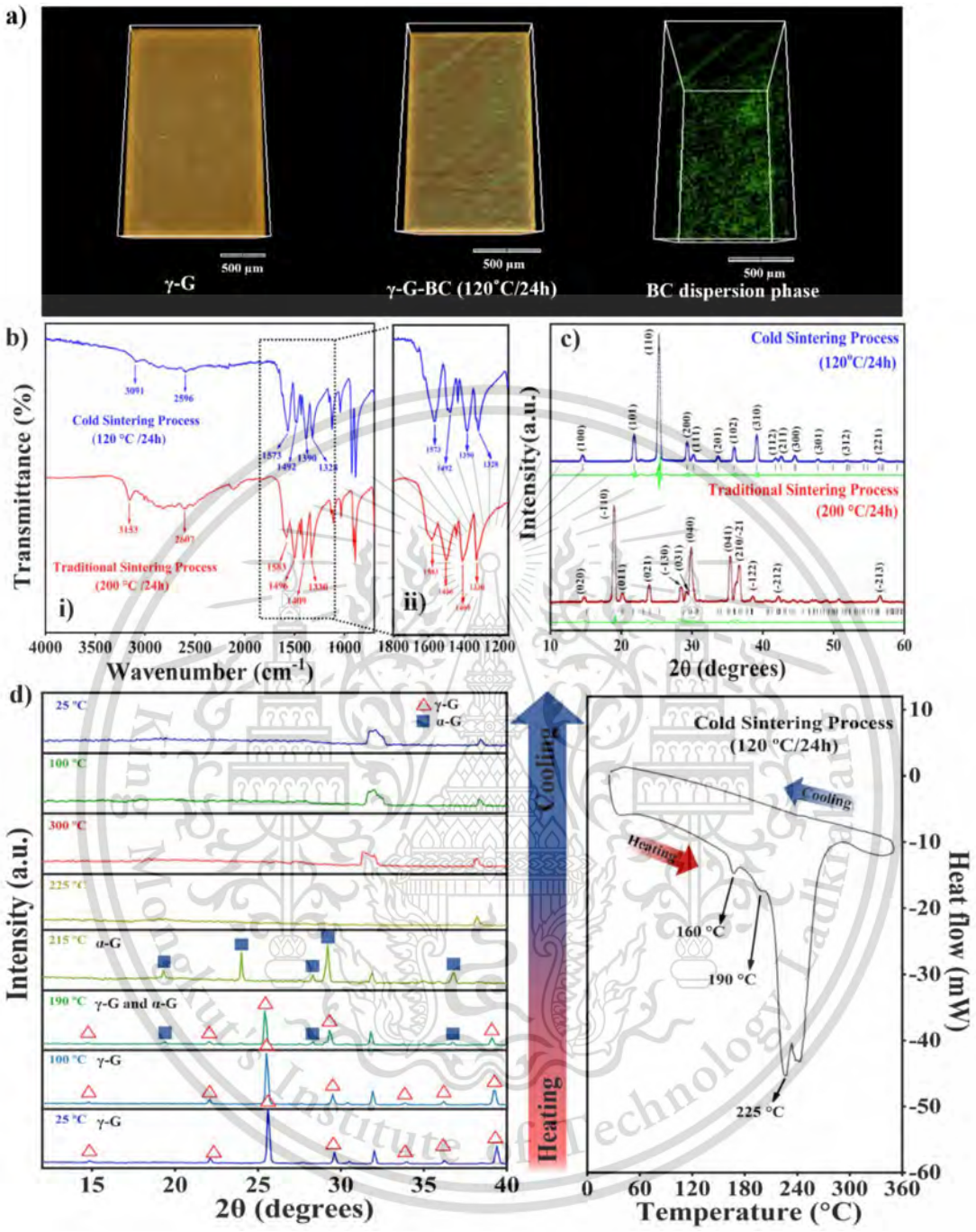

Fig. 5 – (a) X-ray tomographic 3D visualization of γ-G-BC composites via TSP and the 120 °C/24 h via CSP (c) and BC dispersion phase (b) i. ATR-IR spectrum and ii. The zoom-in; (c) LeBail refinement of the XRD patterns of the γ-G-BC composites via TSP and the 120 °C/24 h via CSP; and (d) in-situ XRD patterns and the simultaneous heal flow curve of the 120 °C/24 h γ-G-BC composites.

rising rapidly before becoming constant. The densification process may slow down at high temperatures due to evaporation [42,43].

The relative density of the γ-G-BC composites was plotted in Fig. 4a and b, illustrating its dependence on CSP parameters such as sintering temperatures and holding times. The results revealed that increasing the sintering temperature in CSP from RT to 120 °C (Fig. 4a) increased the relative density from 93.9 ± 1.8% to 97.4 ± 1.5%. This is attributed to the improved mass transport and composite deformation at elevated temperature, leading to the improved bonding between particles and elimination of pores. The holding time also affected the relative density, as shown in Fig. 4b. It is rationalized that a longer holding time allows for the enhanced dissolution of ions into DI water, and for a greater amount of precipitates around grain boundaries, thereby decreasing the local

Table 1 – LeBail refinement parameters and calculated data from XRD pattern using JANA2006 software.

Samples	Lattice parameters				structure	polymorph	R-parameters
	a (Å)	*b* (Å)	*c* (Å)	Angles (°)			
TSP	5.492(5)	11.704(9)	5.125(4)	$\alpha = 90.0$ $\beta = 111.3$ $\gamma = 90.0$	Monoclinic	Alpha (α)	$R_p = 9.12$ $R_{wp} = 16.76$ $R_{exp} = 5.61$ $GOF = 2.26$
CSP	7.031(1)	7.031(1)	5.478(1)	$\alpha = 90.0$ $\beta = 90.0$ $\gamma = 120.0$	Hexagonal	Gamma (γ)	$R_p = 7.92$ $R_{wp} = 10.47$ $R_{exp} = 7.87$ $GOF = 1.33$

distance between particles and promoting mass transport [32,38,44] The relative density of γ-G-BC composites via CSP (97%, 120 °C, 24 h) was found to be higher than that from the traditional sintering process (TSP, 85%, 200 °C, 24 h).

The densification of the γ-G-BC composite was also correlated with hardness, as seen from the micro-hardness test (Fig. 4c) which is suitable for small scale samples. We observed an increase in hardness value from 58.2 ± 0.56 (TSP) to 78.1 ± 1.88 (CSP) for γ-G. However, these values are smaller than 86.3 ± 0.66 for the γ-G-BC composites prepared via CSP, presenting an increase of approximately 10%. The Vickers hardness of the γ-G can be attributed to the H-bonded chains of which are interconnected by lateral NH···O H bonds, resulting in a three-dimensional network. However, the brittle γ-G is prone to cracking by pressure as depicted in Fig. 4d [45]. The addition of BC filler increased the hardness of the γ-G-BC composite due to strong crosslinking between the amine groups of γ-G and the hydroxyl groups of BC as demonstrated in Fig. 4e–f. The 3D distribution of the γ-G-BC composite on a macroscale was confirmed using Synchrotron Radiation X-ray Tomographic Microscopy (SR-XTM), which showed that BC was evenly distributed over the γ-G surface (Fig. 5a).

The different γ-G-BC composites were also characterized using ATR-FTIR. The NH_3^+ stretching vibrations were observed in all spectra as the broad band at 3091 cm^{-1}, as depicted in Fig. 5b–i. The zoom-in in Fig. 5b–ii shows a strong asymmetrical (C]O)O stretching with the highest intensity at 1573 cm^{-1} (peak 1), NH bending vibration of NH_3^+ at 1492 cm^{-1} (peak 2), (C]O)O symmetrical stretching at 1390 cm^{-1} (peak 3), and CH_2 wagging with the lowest intensity among four peaks at 1328 cm^{-1} (peak 4). The ratio of the intensity (*I*) of these four peaks, where $I_3 > I_4 > I_2 > I_1$, and $I_2/I_1 = 1.27$ is unique to α-glycine [46]. For β-G, the characteristics intensity sequence is $I_1 > I_2 > I_4 > I_3$, and $I_2/I_3 = 1.02$ [47]. Lastly, the characteristics intensity sequence for γ-G is $I_1 > I_3 > I_2 > I_4$, with $I_2/I_3 = 0.96$ [48]. Therefore, if I_1 is maximum, and I_2/I_3 ratios are between 0.96 and 1.02, glycine is presumably a mixed phase between β-G and γ-G. Note that β-G can rapidly transform to α-G and γ-G in the presence of moisture at room temperature, but it is metastable in dry air. It is deduced from the sequence of intensities and the calculated I_2/I_1 of 1.36, that the glycine in the γ-G-BC (TSP) composite is α-G. On the other hand, the ATR-FTIR results of the γ-G-BC composite prepared via CSP indicated that glycine is in the γ-G form ($I_2/I_3 = 0.76$) without phase transformation commonly observed with the TSP employing higher temperatures (>200 °C). The presence of the carboxylic acid group resulted in the donation of its proton to the amino group, forming a dipolar ion with a strong hydrogen bond viz. $H_3N^+CH_2COO$. These zwitterions adopt an antiparallel arrangement and subsequently the non-centrosymmetric cell with piezoelectric/ferroelectric properties.

The X-ray diffraction (XRD) patterns of the γ-G-BC composites prepared through TSP and CSP are presented in Fig. 5c. Consistent with ATR-FTIR results, all peaks of the sample prepared through TSP corresponded to the standard data in JCPDS number 32–1702 of α-G. This contrasts with the γ-G phase (JCPDS 06–230) for the composites prepared through CSP. In addition, LeBail refinement using the JANA2006 software was performed, and the results are shown in Fig. 5c (calculated peak, black line; observed peak, +; shift patterns, green line; and the Bragg peak positions, black). The refinement parameters are selectively tabulated in Table 1. The lattice parameters obtained for the sample prepared through TSP were $a = 5.492(5)$ Å, $b = 11.704(9)$ Å, and $c = 5.125(4)$ Å, confirming the monoclinic structure of the α polymorph. The lattice parameters of the sample obtained from CSP were $a = b = 7.031(1)$ Å and $c = 5.478(1)$ Å, indicating a hexagonal structure characteristic of the γ polymorph. Accordingly, XRD analysis confirmed that the CSP successfully preserved the γ polymorph of glycine which would provide the piezoelectric properties. The crystalline size, estimated using Eq. (4), is not significantly different between CSP (23.8 nm) and TSP (21.4 nm).

To further investigate the temperature-dependent phase transformation of the γ-G-BC composite, the simultaneous differential scanning calorimetry (DSC) and XRD analyses were performed. The heat flow curve, as depicted in Fig. 5d, show three distinct steps at 160, 190, and 225 °C. The first one corresponds to the melting of BC [49]. Next, the other two steps reflect the γ-G transformation. At 190 °C, the mixture of γ-G and α-G was formed, resulting from the breaking of the 3D network of H-bonds in the crystal lattice [21,50]. This temperature is comparable to 185.5 °C [51] and 187 °C [52], in the literature, and is complete at 215 °C, as confirmed by X-ray diffraction. Accordingly, the third DSC peak at 225 °C indicates the decomposition of glycine [53]. The temperature dependence of the phase transformation explains why TSP which requires a higher sintering temperature of >200 °C will not preserve the γ polymorph of glycine.

The dielectric responses of the γ-G-BC composites were investigated as a function of temperatures and frequencies. The temperature dependences of the ε_r and tan δ for the

120 °C/24 h γ-G-BC composites from RT to 150 °C at selected frequencies are shown in Fig. 6a–b. Fig. 6a indicated that ε_r increases gradually with increasing temperature due to the increased mobility of the polar segments. Specifically, the cellulose sub-unit comprises of polar −OH groups in gluco-pyranose rings oriented in the equatorial direction. Meanwhile, γ-G exists as a dipolar ion as discussed above. The alignment of these polar groups from two components contributes to an increase in orientation polarization, resulting in a higher dielectric constant of the composite. Fig. 6b Illustrates the temperature-dependence of tan δ at different frequencies. At 100 Hz, the tan δ peak is observed at 105 °C, with the peak shifting to higher temperatures as frequency increases. The maximum tan δ values are found to be 123 °C and 140 °C for 1 kHz and 10 kHz, respectively. The tan δ peak corresponds to the transition from a crystalline to an amorphous phase of BC. The results agree well with the DSC results shown in Fig. 5d. However, the different temperature occurrence may be attributed to the use of different measurement techniques.

Fig. 6c Illustrates the frequency-dependent variation of the ε_r at different temperatures ranging from RT to 150 °C. At low frequencies, the ε_r value is high, typical for space charge polarization at the grain boundaries. As the frequency increases, the ε_r decreases for all temperatures, indicating a decrease in polarization due to the dielectric dispersion behavior. This behavior is influenced by the distribution of charges and the statistical motion of interfacial polarization effects. Fig. 6d Demonstrates the effect of frequency on tan δ at different temperatures. At 50 °C, the tan δ peak is identified around 10^3 Hz. This peak shifts to higher frequencies as the temperature increases. The maximum is formed due to the dielectric relaxation, which is mainly found in organic molecules through ionic motion and molecular dynamic motion. It is noteworthy that at 150 °C, a rapid increase in tan δ is observed at low frequencies, suggesting the onset of direct current conduction.

An electric field can induce polarization reversal/switching in ferroelectric materials, which is one of their most significant characteristics. This switching of domains within ferroelectric materials is responsible for the occurrence of ferroelectric hysteresis loops. Fig. 6e shows the polarization-electric field (P-E) hysteresis loops of the γ-G-BC composites prepared under different conditions, i.e., RT/24 h, 60 °C/24 h, and 120 °C/24 h, where the voltage ranges from −5 to 5 kV. The polarization (P_r) is similar in the RT/24 h and 60 °C/24 h samples, but it significantly increases in the 120 °C/24 h sample. In contrast, the coercive electric field (E_c) remains constant for the RT/24 h and 60 °C/24 h samples but significantly decreases for the 120 °C/24 h sample (Fig. 6f). It can be observed that the hysteresis loop is saturated, especially for the 120 °C/24 h γ-G-BC composite, indicating good ferroelectric characteristics with saturated polarization (P_s), P_r and E_c of 0.013 μC/cm^2,

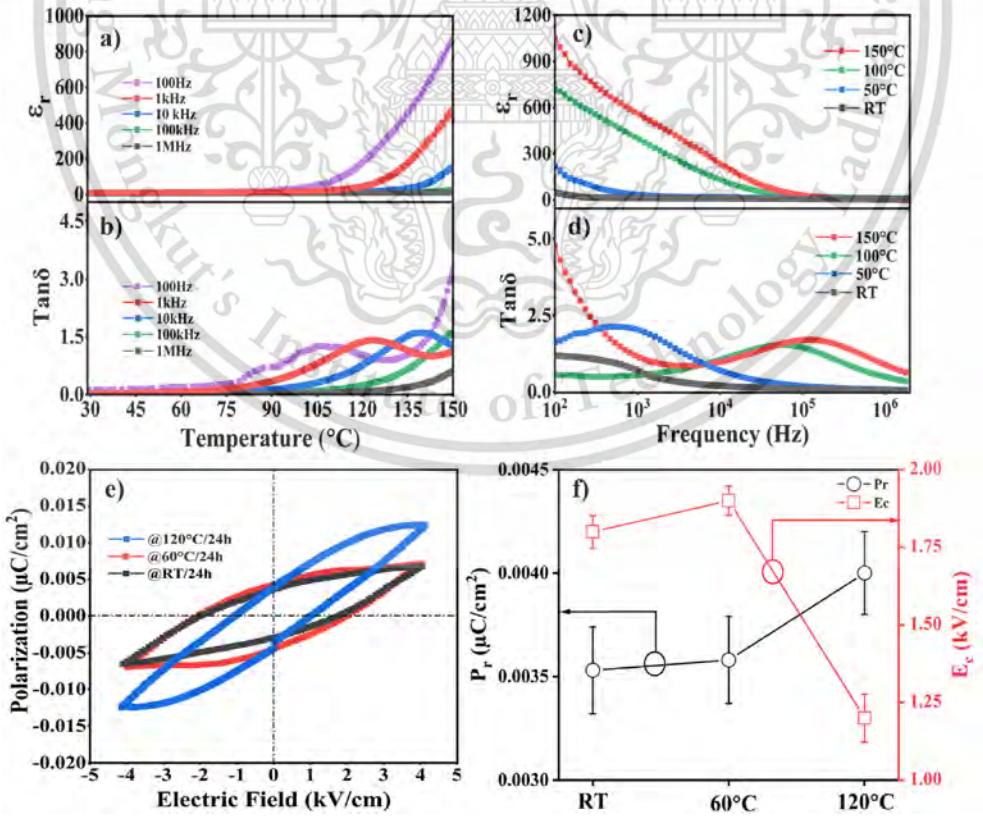

Fig. 6 – Temperature dependence of (a) the dielectric constant and (b) loss tangent; and the frequency dependence of (c) the dielectric constant and (d) loss tangent of the 120 °C/24 h γ-G-BC composite; (e) the ferroelectric properties of γ-G-BC composites prepared at the conditions RT/24 h, 60 °C/24 h and 120 °C/24 h, at the electric field of 5 kV/cm. And (f) the corresponding P_r and E_c values.

Table 2 – A comparison of dielectric constant (ε_r), remanent polarization (P_r), and coercive electric field (E_c) of various piezoelectric biomaterials with γ-G-BC composite.

Piezoelectric Biomaterials	Material	Type	ε_r (at 100 Hz-1MHz)	P_r (μC/cm^2)	E_c (kV/cm)	Ref
Inorganic piezoelectric materials	PZT	Ceramic	1250.00	22.75	8.60	[55,56]
	ZnO	Crystal	4.00	16.31	6.11	[57]
	$BaTiO_3$	Ceramic	1135.00	12.60	30.00	[58]
	$LiNbO_3$	Ceramic	62.00	–	–	[59]
Organic piezoelectric materials	Chitin nanofiber	Protein	8.00	0.178	62.00	[60]
	Bone	Tissue	9.20	0.620	0.85	[61]
	Eggshell membrane	Tissue	19.00	0.460	20.00	[62]
	Onion skin	Cellulose fibrous	32.80	0.068	10.00	[63]
	Silk	Semi-crystalline	3.40	0.050	35.00	[64]
	β-Glycine-Chitosan	Amino-Protein	3.50	–	–	[65]
	γ-Glycine-BC	Amino-Cellulose	12.00	0.004	1.20	This work

0.004 μC/cm^2 and 1.201 kV/cm, respectively. Table 2 presents a comprehensive comparison between the ε_r, P_r and E_c of diverse piezoelectric biomaterials and the γ-G-BC composite. The experimental results provide evidence of a direct relationship between the density of the sample and its mechanical, dielectric, and ferroelectric properties, substantiating the successful fabrication of high-density γ-G-BC composite ceramics by CSP.

4. Conclusion

The present study reports the successful fabrication of γ-G-BC composite ceramic using CSP. The optimized process was carried out at 120 °C/24 h under applied uniaxial pressure of 2000 kPa, resulting in a high density of 97%. IR and XRD results confirmed the γ-G phase stabilization without any transformation to the metastable α-G. The incorporation of BC into the γ-G matrix led to significant improvements in the Vickers hardness. This improvement can be attributed to the formation of strong hydrogen bonds between the amino acids of γ-G and the hydroxyl groups of BC. The electrical behavior of the composite was studied by examining temperature-dependent (RT to 150 °C) and frequency-dependent (100 Hz–1 MHz) dielectric properties. The composite exhibited a high dielectric constant of 984 with low tan δ. The ferroelectric properties were also determined by measuring the P-E hysteresis loop, where the 120 °C/24 h γ-G-BC composite ceramic exhibited the highest P_S = 0.013 μC/cm^2 and P_r = 0.004 μC/cm^2. Our results clearly demonstrate the potential of CSP to successfully fabricate the high-density γ-G-BC composite ceramics at low temperatures.

Declaration of competing interest

The authors declare that they have no known competing financial interests or personal relationships that could have appeared to influence the work reported in this paper.

Acknowledgements

This study was financially supported by KMITL through [Grant No. KREF116501]. The research by Jitrawan Noisak was funded by [Grant No. KREF016412], while that by Satana Pongampai was supported by King Mongkut's Institute of Technology Ladkrabang (KMITL) under [Grant number KREF146411]. Thitirat Charoonsuk's contribution to the study was supported by the National Research Council of Thailand (NRCT) through [Grant Number N42A650220]. The collaboration between N. Vittayakorn and Te-Wei Chiuh was supported by the TUT-KMITL-Joint Research Program [Grant No. KREF016412]. We acknowledged the facilities and technical assistance from Nanotechnology and Materials Analytical Instrument Service Unit (NMIS) of College of Materials Innovation and Technology, KMITL.

REFERENCES

[1] Li Z, et al. Defect engineering in lead zirconate titanate ferroelectric ceramic for enhanced electromechanical transducer efficiency. Adv Funct Mater 2021;31(1):2005012.
[2] Jackson N, Keeney L, Mathewson A. Flexible-CMOS and biocompatible piezoelectric AlN material for MEMS applications. Smart Mater Struct 2013;22(11):115033.
[3] Pongampai S, et al. Sensing layer combination of vertically aligned ZnO nanorods and graphene oxide for ultrahigh sensitivity IDE capacitive humidity sensor. IEEJ Trans Electr Electron Eng 2020;15(6):965–75.
[4] Charoonsuk T, Sriphan S, Nawanil C, Chanlek N, Vittayakorn W, Vittayakorn N. Tetragonal BaTiO3 nanowires: a template-free salt-flux-assisted synthesis and its piezoelectric response based on mechanical energy harvesting. J Mater Chem C 2019;7:8277–86.
[5] Pongampai S, et al. Triboelectric-piezoelectric hybrid nanogenerator based on BaTiO3-Nanorods/Chitosan enhanced output performance with self-charge-pumping system. Compos B Eng 2021;208:108602.
[6] Sriphan S, Charoonsuk T, Maluangnont T, Vittayakorn N. Piezoelectric energy harvesting for low-power smart electronics. In: Haseeb ASMA, editor. Encyclopedia of materials: electronics. Oxford: Academic Press; 2023. p. 369–404.
[7] Sriphan S, Vittayakorn N. Hybrid piezoelectric-triboelectric nanogenerators for flexible electronics: recent advances and perspectives. J Sci: Advanced Materials and Devices 2022;7(3):100461.
[8] Yan X, Li G, Wang Z, Yu Z, Wang K, Wu Y. Recent progress on piezoelectric materials for renewable energy conversion. Nano Energy 2020;77:105180.

[9] Charoonsuk T, Pongampai S, Pakawanit P, Vittayakorn N. Achieving a highly efficient chitosan-based triboelectric nanogenerator via adding organic proteins: influence of morphology and molecular structure. Nano Energy 2021;89:106430.
[10] Guerin S, et al. Control of piezoelectricity in amino acids by supramolecular packing. Nat Mater 2018;17(2):180–6.
[11] Khare D, Basu B, Dubey AK. Electrical stimulation and piezoelectric biomaterials for bone tissue engineering applications. Biomaterials 2020;258:120280.
[12] Chorsi MT, et al. Piezoelectric biomaterials for sensors and actuators. Adv Mater 2019;31(1):1802084.
[13] Kholkin A, Amdursky N, Bdikin I, Gazit E, Rosenman G. Strong piezoelectricity in bioinspired peptide nanotubes. ACS Nano 2010;4(2):610–4.
[14] Pongampai S, Pengpad P, Meananeatra R, Chaisriratanakul W, Thitirungraung W, Muanghlua R. Ultrahigh linear sensitivity of capacitive humidity sensor base on bilayer structure of graphene oxide. 2019 7th international electrical engineering congress (iEECON); 2019.
[15] Charoonsuk T, et al. Simple enhanced charge density of chitosan film by the embedded ion method for the flexible triboelectric nanogenerator. Carbohydr Polym 2022;297:120070.
[16] Guerin S, Tofail SAM, Thompson D. Organic piezoelectric materials: milestones and potential. NPG Asia Mater 2019;11(1):10.
[17] Kim D, Han SA, Kim JH, Lee J-H, Kim S-W, Lee S-W. Biomolecular piezoelectric materials: from amino acids to living tissues. Adv Mater 2020;32(14):1906989.
[18] Shin D-M, Hong SW, Hwang Y-H. Recent advances in organic piezoelectric biomaterials for energy and biomedical applications. Nanomaterials 2020;10. https://doi.org/10.3390/nano10010123.
[19] Yang F, et al. Wafer-scale heterostructured piezoelectric bio-organic thin films. Science 2021;373(6552):337–42.
[20] Anbu Arasi M, Alagar M, Raja Pugalenthi M. Growth of γ-glycine single crystals using the tailored additive of potassium chloride and L-Proline and analyzing micro structural, optical, mechanical and electrical parameters. Chem Phys Lett 2021;765:138301.
[21] Jiang Q, Shtukenberg AG, Ward MD, Hu C. Non-topotactic phase transformations in single crystals of β-Glycine. Cryst Growth Des 2015;15(6):2568–73.
[22] Han G, Chow PS, Tan RBH. Understanding the salt-dependent outcome of Glycine polymorphic nucleation. Pharmaceutics 2021;13(2):262.
[23] Wang R, Sui J, Wang X. Natural piezoelectric biomaterials: a biocompatible and sustainable building block for biomedical devices. ACS Nano 2022;16(11):17708–28.
[24] Hu P, et al. Bioferroelectric properties of glycine crystals. J Phys Chem Lett 2019;10(6):1319–24.
[25] Guerin S, et al. Control of piezoelectricity in amino acids by supramolecular packing. Nat Mater 2018;17(2):180–6.
[26] Heredia A, et al. Nanoscale ferroelectricity in crystalline γ-Glycine. Adv Funct Mater 2012;22.
[27] Rodríguez JS, et al. Structural and optoelectronic properties of the α-, β-, and γ-Glycine polymorphs and the Glycine dihydrate crystal: a dft study. Cryst Growth Des 2019;19(9):5204–17.
[28] Charoonsuk T, Sukkha U, Kolodiazhnyi T, Vittayakorn N. Enhancing the densification of ceria ceramic at low temperature via the cold sintering assisted two-step sintering process. Ceram Int 2018;44:S54–7.
[29] Jin DH, et al. Boosting densification and microwave dielectric properties in cold sintered BaF2 ceramics for 5.8 GHz WLAN applications. J Alloys Compd 2021;886:161141.
[30] Liu B, et al. Enhancement of densification and microwave dielectric properties in LiF ceramics via a cold sintering and post-annealing process. J Eur Ceram Soc 2021;41(2):1726–9.
[31] Liu B, et al. Novel transparent LiF ceramics enabled by cold sintering at 150 °C. Scripta Mater 2022;220:114917.
[32] Guo H, Baker A, Guo J, Randall CA. Cold sintering process: a novel technique for low-temperature ceramic processing of ferroelectrics. J Am Ceram Soc 2016;99(11):3489–507.
[33] Biesuz M, et al. A theoretical analysis of cold sintering. Adv Appl Ceram 2020;119(2):75–89.
[34] Galotta A, Sglavo VM. The cold sintering process: a review on processing features, densification mechanisms and perspectives. J Eur Ceram Soc 2021;41(16):1–17.
[35] Guo N, Shen H-Z, Shen P. Cold sintering of chitosan/hydroxyapatite composites. Materialia 2022;21:101294.
[36] Hajizadeh Z, Taheri-Ledari R, Asl FR. 3 - identification and analytical methods. In: Maleki A, editor. Heterogeneous micro and nanoscale composites for the catalysis of organic reactions. Elsevier; 2022. p. 33–51.
[37] Reitz W. Ceramic processing and sintering by M. N. Rahaman. Mater Manuf Process 1997;12(3):555–6.
[38] Tong Yu JC, Li L, Sun B, Bao X, Zhang H. Current understanding and applications of the cold sintering process. Front Chem Sci Eng 2019;13(4):654–64.
[39] Guo J, Guo H, Baker AL, Lanagan MT, Kupp ER, Messing GL, et al. Cold sintering: a paradigm shift for processing and integration of ceramics. Angew Chem 2016;128(38):11629–33.
[40] Guo J, Baker AL, Guo H, Lanagan M, Randall CA. Cold sintering process: a new era for ceramic packaging and microwave device development. J Am Ceram Soc 2017;100(2):669–77.
[41] Gundersen E, Renard F, Dysthe DK, Bjørlykke K, Jamtveit B. Coupling between pressure solution creep and diffusive mass transport in porous rocks. J Geophys Res Solid Earth 2002;107(B11):19–21.
[42] Leng H, Huang J, Nie J, Luo J. Cold sintering and ionic conductivities of Na3.256Mg0.128Zr1.872Si2PO12 solid electrolytes. J Power Sources 2018;391:170–9.
[43] Funahashi S, et al. Demonstration of the cold sintering process study for the densification and grain growth of ZnO ceramics. J Am Ceram Soc 2017;100(2):546–53.
[44] Guo H, Baker A, Guo J, Randall CA. Protocol for ultralow-temperature ceramic sintering: an integration of Nanotechnology and the cold sintering process. ACS Nano 2016;10(11):10606–14.
[45] Marom N, et al. Many-body dispersion interactions in molecular crystal polymorphism. Angew Chem Int Ed 2013;52(26):6629–32.
[46] Polat S, Sayan P. The characterization and polymorphism of α-Glycine in the presence of butyric acid. Adv Powder Technol 2018;29(9):1968–76.
[47] Liu Z, Zhong L, Ying P, Feng Z, Li C. Crystallization of metastable β glycine from gas phase via the sublimation of α or γ form in vacuum. Biophys Chem 2008;132(1):18–22.
[48] Peter ME, Ramasamy P. Growth of gamma glycine crystal and its characterisation. Spectrochim Acta Mol Biomol Spectrosc 2010;75(5):1417–21.
[49] Surma-Ślusarska B, Presler S, Danielewicz D. Characteristics of bacterial cellulose obtained from acetobacter xylinum culture for application in papermaking. Fibres Text East Eur 2008;16:108–11.
[50] Tylczyński Z, Busz P. Low-temperature phase transition in γ-glycine single crystal. Pyroelectric, piezoelectric, dielectric and elastic properties. Mater Chem Phys 2016;183:254.
[51] Tylczynski Z, Busz P. Transformation from γ to α modification in glycine crystal. Phase Transitions A Multinatl J 2014;87.

[52] Boldyreva E, Drebushchak T, Shutova E. Structural distortion of theα,β, andγpolymorphs of glycine on cooling. Zeitschrift fur Kristallographie 2003;218:366–76.
[53] Anbu Chudar Azhagan S, Kathiravan VS. Selective crystallization of gamma glycine for NLO applications using magnesium sulfate (MgSO) as an additive. Materials Science-Poland 2019;37(2):265–79.
[54] Wang D, et al. Cold sintering of microwave dielectric ceramics and devices. J Mater Res 2021;36.
[55] Wu D, Zhou Q, Shung KK, Bharadwaja SN, Zhang D, Zheng H. Dielectric and piezoelectric properties of PZT composite thick films with variable solution to powder ratios. J Am Ceram Soc 2009;92(6):1276–9.
[56] Li H, et al. Improved ferroelectric properties of (100)-oriented PZT thin films deposited on stainless steel substrates with La0.5Sr0.5CoO3 buffer layers. J Mater Sci Mater Electron 2018;29(17):14651–6.
[57] Gupta MK, Sinha N, Singh BK, Singh N, Kumar K, Kumar B. Piezoelectric, dielectric, optical and electrical characterization of solution grown flower-like ZnO nanocrystal. Mater Lett 2009;63(22):1910–3.
[58] Sharma H, Mansingh A. Sol-gel processed barium titanate ceramics and thin films. J Mater Sci 1998;33:4455–9.
[59] Vaněk P, et al. Electrical activity of ferroelectric biomaterials and its effects on the adhesion, growth and enzymatic activity of human osteoblast-like cells. J Phys Appl Phys 2016;49(17):175403.
[60] Hoque NA, et al. Biowaste crab shell-extracted chitin nanofiber-based superior piezoelectric nanogenerator. J Mater Chem 2018;6(28):13848–58.
[61] Halperin C, et al. Piezoelectric effect in human bones studied in nanometer scale. Nano Lett 2004;4(7):1253–6.
[62] Karan SK, et al. A new insight towards eggshell membrane as high energy conversion efficient bio-piezoelectric energy harvester. Mater Today Energy 2018;9:114–25.
[63] Maiti S, Kumar Karan S, Lee J, Kumar Mishra A, Bhusan Khatua B, Kon Kim J. Bio-waste onion skin as an innovative nature-driven piezoelectric material with high energy conversion efficiency. Nano Energy 2017;42:282–93.
[64] Sohn C, Kim H, Han J, Lee K-T, Šutka A, Jeong CK. Generating electricity from molecular bonding-correlated piezoresponse of biodegradable silk nanofibers. Nano Energy 2022;103:107844.
[65] Hosseini ES, Manjakkal L, Shakthivel D, Dahiya R. Glycine–Chitosan-Based flexible biodegradable piezoelectric pressure sensor. ACS Appl Mater Interfaces 2020;12(8):9008–16.

https://doi.org/10.26599/JAC.2024.9220908

Research Article

The role of γ-$C_2H_5NO_2$ as a new transient liquid phase in cold sintering process of $BaTiO_3$ composites

Jitrawan Noisak [a,b], Pimchanok Ieamviteevanich [a], Thitirat Charoonsuk [c], Phakkhananan Pakawanit [d], Nattapong Pinpru [e], Wanwilai Vittayakorn [f], Tosapol Maluangnont [f], Panpailin Seeharaj [a], Theerachai Bongkarn [g,h], Te-Wei Chiu [i], Naratip Vittayakorn [a,b *]

[a] *Advanced Materials Research Unit, School of Science, King Mongkut's Institute of Technology Ladkrabang, Bangkok 10520, Thailand*

[b] *Department of Chemistry, School of Science, King Mongkut's Institute of Technology Ladkrabang, Bangkok 10520, Thailand*

[c] *Department of Materials Science, Faculty of Science, Srinakharinwirot University, Sukhumvit 23, Wattana, Bangkok 10110, Thailand*

[d] *Synchrotron Research and Applications Division, Synchrotron Light Research Institute, 111 University Avenue, Muang District, Nakhon Ratchasima 30000, Thailand*

[e] *Sustainability Centre, Plastics Market Intelligent Department, Plastics Institute of Thailand, Bangkok 10110, Thailand*

[f] *Electroceramics Research Laboratory, College of Materials Innovation and Technology, King Mongkut's Institute of Technology Ladkrabang, Bangkok 10520, Thailand*

[g] *Department of Physics, Faculty of Science, Naresuan University, Phitsanulok 65000, Thailand*

[h] *Research Center for Academic Excellence in Applied Physics, Faculty of Science, Naresuan University, Phitsanulok 65000, Thailand*

[i] *Department of Materials and Mineral Resources Engineering, "National" Taipei University of Technology, Taipei 106, Taiwan, China*

*****Corresponding author.

E-mail: naratip.vi@kmitl.ac.th

Received: March 03, 2024; Revised: April 12, 2024; Accepted: May 01, 2024

Abstract: Dielectric materials, like barium titanate-based (BT-based), have excellent dielectric properties but require high temperatures (above 1300 ˚C) for ceramic fabrication, leading to high costs and energy loss. The cold sintering process (CSP) offers a solution to these issues and is gaining worldwide attention as an innovative fabrication route. In this work, we proposed an alternative organic ferroelectric phase, gamma-glycine (γ-GC) that acts as a transient liquid phase to fabricate high-density composites with barium titanate (BT) at low-temperature through a CSP. Our findings show that the density of 15γ-GC/85BT reached 96.7±1.6% when sintered at 120 ˚C for 6 hours (h) under 10MPa uniaxial pressure. The SEM-EDS mapping of the composite suggested that γ-GC completely underwent the precipitation-dissolution process and, therefore, filled between BT particles. Moreover, XRD and FTIR confirmed the preservation of γ-GC without the undesired phase transformation. In addition, the ferroelectric and dielectric properties of the γ-GC/BT composites were reported. The high dielectric constant (ε_r) was 3600, and the low dielectric loss (tan δ) was 1.20 at 200 ˚C, 100 kHz, with 15γ-GC/85BT composite. The hysteresis loop showed a remanent polarization (P_r) of 0.55 μC.cm^{-2} and a coercive field (E_c) of 7.25 kV.cm^{-1}. Our findings reaffirmed that organic ferroelectric material (γ-GC) can act as a transient liquid phase in a CSP that can successfully and sustainably fabricate γ-GC/BT composites at low temperatures while delivering outstandingly high performance.

Keywords: γ-GC, barium titanate; cold sintering process; Organic Ferroelectric Materials; Dielectric properties; Ferroelectric properties

1 Introduction

In recent years, a groundbreaking low-temperature sintering technique known as the cold sintering process (CSP) was discovered by Randall *et al.* [1] at Pennsylvania State University in 2016, has emerged as a highly effective method for producing dense ceramic materials. The CSP involves homogenizing powdered inorganic compounds with a transient liquid phase. This blending process yields a uniform mixture characterized by the presence of a transient liquid phase, typically constituting 1 to 10% of the total volume. Utilizing pressures ranging from 100 MPa to 700 MPa and temperatures below 300°C, CSP facilitates the evaporation of solvents and the densification of inorganic compounds, resulting in the formation of high-density sintered materials [2] . The core processing variables of CSP, including the transient liquid phase, sintering temperature, pressure, and holding time, play pivotal roles in driving the densification process of materials [3]. Of particular significance, the transient liquid phase substantially contributes to the dissolution-precipitation phenomenon within CSP. This mechanism enables the partial dissolution of sharp particle edges, thereby creating spaces for particle rearrangement. Moreover, the liquid phase readily redistributes itself, filling particle interstitials and fostering grain growth [4]. CSP has been successfully applied to water-soluble materials such as sodium chloride (NaCl), where NaCl particles diffuse throughout the water film, filling voids and precipitating through the dissolution-precipitation process inherent to CSP. Consequently, CSP can achieve high relative densities exceeding 90% after 24 h at room temperature and 75% relative humidity. Furthermore, CSP has been effectively employed with various metal oxide and dielectric materials, including KH_2PO_4, $NaNO_2$, and $BaTiO_3$; BT [5, 6]. Notably, KH_2PO_4 and $NaNO_2$ exhibit high relative densities (>98%) comparable to conventionally sintered materials, even when treated at temperatures below 120 ˚C under 350 MPa without additional treatment.

However, for materials with low water solubility, a tailored liquid solution becomes imperative. In a similar vein, Hanzheng Guo *et al*. [7] employed CSP to fabricate high-density BT ceramic at temperatures below 200 ˚C. By utilizing a 25wt% $Ba(OH)_2/TiO_2$ solution as a transient liquid phase and consolidating at 180°C under 430 MPa pressure, they achieved a relative density of 95%. However, a subsequent annealing step at 900 ˚C, while achieving characteristics comparable to conventionally sintered counterparts, nullified the advantage of low-temperature manufacturing, preventing the production of new composites below 300 ˚C. Addressing the limitation, Tsuji *et al.* [8] successfully fabricated dense and high-quality BT materials via cold sintering at 300 ˚C in single-step using NaOH-KOH eutectic fluxes. Nevertheless, the severe conditions of strong alkaline fluxes at 300 ˚C restrict the fabrication of innovative composites with additives such as polymers, 2D materials, and fibers due to the necessity of appropriate quick kinetics for the congruent dissolution of the ceramic phase's surface ions to ensure dense ceramic manufacturing.

Despite these challenges, recent studies have demonstrated the feasibility of co-sintering various materials through CSP, enabling the fabrication of novel composite materials. Notably, low melting point materials such as thermoplastic [9], thermosetting [10], and 2D-nanostructured materials [11] can serve as transient liquid phases in CSP, modifying matrix material qualities including density, strength, hardness, and electrical properties [12, 13]. For instance, Jing Guo et al. [11] conducted CSP to manufacture a cold co-sintering process of 2D-MXene and ZnO at 300 ˚C for 1 hour under 250 MPa pressure, resulting in improved electrical conductivity with the addition of up to 5wt% $Ti_3C_2T_x$ MXene. Takao Sada *et al.* [14] successfully co-sintered BT and PTFE using $Ba(OH)_2 \cdot 8H_2O$ flux, bridging the temperature gap between ferroelectric ceramics and polymers, albeit with challenges related to non-homogeneous polymer distribution. Similarly,

Subramaniyan Vinoth and Sea-Fue Wang [15] effectively prepared BT/poly(vinylidene difluoride) nanocomposites, albeit with issues regarding the homogeneity of polymer distribution and unclear ferroelectric properties attributed to grain boundary microstructure [16]. In our previous work, we found that organic ferroelectric materials, including γ-GC, can be fabricated into a composite with bacterial cellulose (BC) powder via CSP and achieved satisfactory ferroelectric effects at conditions 120 ˚ C/24h [17]. The γ-GC is the thermodynamically most stable phase and exhibits piezoelectric effects at room temperature because it has a winding hydrogen bond network, unlike the other two main phases (α and β phase) [18, 19]. Moreover, its water solubility qualifies it for usage as a transient liquid phase in a CSP [20, 21].

The present study proposes the use of γ-GC phase to fabricate ferroelectric composites via the cold sintering process (CSP). The γ-GC phase is an ideal transient liquid phase that induces excellent dissolution-precipitation phenomena during the CSP. Moreover, it exhibits remarkable ferroelectric properties that do not interfere with the properties of the primary phase. The focus of this research is to determine the optimized quantity of γ-GC phase for high-density BT composite through the CSP. A comprehensive examination of the time and temperature conditions applied in the CSP is conducted to refine the fabrication process and enhance the overall performance of the resulting composites.

2 Experimental

2.1 Gamma glycine (γ-GC) preparation

The γ-GC compound was synthesized using a method described in literature [17]. Firstly, 56 g of commercial-grade glycine and 15 g of sodium chloride in a 3:1 molar ratio were dissolved in 100 mL of deionized water (DI water) by stirring for 5 h at room temperature (RT). The resulting mixture was then filtered using vacuum filtration, and the obtained liquid was kept in an oven at

35 ˚C for 25 days. During this aging process, α-GC crystals were transformed into γ-GC crystals. The γ-GC crystals were then washed with saturated glycine solution, ground for 3 h using a ball mill, and finally placed in the oven for an additional 2 days. This process resulted in the successful synthesis of γ-GC crystals.

2.2 Barium titanate (BT) preparation

Two types of BT powders were employed: (i) as purchased, a commercial product from Inframat Advanced Materials, LLC ($BaTiO_3$ nano-powder, 99.95%), and (ii) Heat-treated commercial BT powder at 1200 ˚C for 12 h in air. Both powders (untreated, and heat-treated) were separately stirred with 1 M acetic acid solution at 80 ˚C for 1 h. Then, the pH of the suspension was adjusted to neutral, and the respective BT powders were filtered prior to drying in an oven at 60 ˚C for 24 h, as schematically shown in Fig. 1a.

2.3 Fabrication of γ-GC/BT composites via CSP

To optimize packing density, a specific ratio of 73.6/26.4, determined by theoretical predictions for dense random packing, was employed for mixing BT particles of both nanometer (untreated particles) and micrometer (heat-treated particles) sizes. Subsequently, the fabrication process of composites involving γ-GC and BT via CSP was initiated by precisely measuring 2.208 g of heat-treated BT and 0.792 g of untreated BT. These two types of BT were thoroughly combined in a mortar for a duration of 5 minutes to ensure homogeneity. Following this, varying proportions (15%, 30%, 50%, and 90% by weight) of γ-GC powder were incorporated into the BT mixture and meticulously blended manually in the mortar for an additional 5 minutes. Subsequently, 7wt% of DI water was introduced into the blend, which was then ground for an additional 5 minutes to facilitate thorough mixing. Next, 0.3 grams of the resulting γ-GC/BT

mixture were meticulously deposited into a tungsten carbide die. In the context of the CSP, the initial mixture undergoes continuous compression via a straightforward uniaxial pressure of 10 MPa. Heating is facilitated by a resistance jacket enveloping the die system within the CS equipment employed. The heating jacket demonstrates the capability to ramp up the temperature at a steady rate of 3°C per minute, reaching a maximum temperature of 120°C. The specified heating temperature and duration were maintained for 6 hours. The CSP apparatus utilized in this investigation was constructed as depicted in Figure 1b (I-III). Once the process was completed, the cold-sintered γ-GC/BT composite was allowed to cool before being extracted from the block for subsequent characterization analysis.

2.4 Characterization

Although the Archimedes method is renowned for its precision in determining density, its utility in our investigation was hampered by the solubility properties of γ-GC in polar solvents. Traditional organic solvents employed in Archimedes' principle, such as water, ethanol, isopropanol, and acetone, were deemed incompatible with our samples due to their inherent polarity. Moreover, the use of nonpolar solvents posed a risk of altering the phase or stability of γ-GC. Additionally, the metastable nature of γ-GC warranted cautious immersion protocols, as it could lead to phase transitions in glycine. Consequently, we adopted an alternative approach to determine sample density, relying on measurements of mass, thickness, and dimensions. By employing 12 samples, we aimed to account for inherent variations within the sample set, thereby obtaining a more comprehensive representation of density. Densification calculations were performed using Equation (1), elucidating the ratio of actual density to theoretical density [17, 22].

$$R = \frac{4m}{(\pi d^2 h \rho)} \times 100\% \quad (1)$$

where R is the relative density (%), m is the mass (g) of the pellet, d is the diameter (cm) of the pellet, h is the thickness (cm) of the pellet, and ρ is the theoretical density calculated from the Eq. (2)

$$\rho = \frac{m}{(\frac{m_{BT}}{\rho_{BT}} + \frac{m_{\gamma-GC}}{\rho_{\gamma-GC}})} \quad (2)$$

where m_{BT} and $m_{\gamma-GC}$ represent the masses of BT and γ-GC in the composite pellet; ρ_{BT} and $\rho_{\gamma-GC}$ represent the theoretical densities of BT and γ-GC, which are 6.02 g·cm^{-3} and 1.59 g·cm^{-3}, respectively [17, 23].

The phase purity and crystal structure of the cold-sintered γ-GC/BT composite at varying weight ratios from 15% to 90% were identified by X-ray diffraction (XRD, RIGAKU smart lab) with Cu Kα (λ = 1.5418 Å) radiation in the range of 2θ = 10˚ to 80˚. The XRD results were compared to the JCPDS database. Moreover, LeBail refinement of the unit cell parameters was performed using JANA2006 software. The crystallite size estimation calculated for the corresponding phase was done by using the Scherrer Eq. (3)

$$L = \frac{K\lambda}{(FWHM \times cos\theta)} \quad (3)$$

where L refers to the crystallite size, K is the Scherrer constant (K = 0.94), λ is the wavelength of the radiation, θ is the diffraction angle of the peak, and $FWHM$ is the full width at half maximum.

The BT and γ-GC powders were subjected to Fourier-Transform Infrared Spectroscopy (FT-IR, SHI-MADZU, IRTracer-100) measurement in a transmission mode from 400 to 4000 cm^{-}

^{1} with a resolution of 4 cm^{-1} to confirm the presence of functional groups. The morphology, particles size and grain size of untreated / heat-treated particles and cold-sintered γ-GC/BT composite were observed by field emission scanning electron microscopy (FE-SEM, TESCAN, model MIRA) and transmission electron microscopy (TEM, FEI, Model: TECNAI G2 20, Netherlands). In addition, energy dispersive X-ray spectroscopy (EDS-mapping) was performed to analyze the chemical components of materials. Particle size and particle size distribution were measured and analyzed through examination and quantitative analysis using ImageJ software. The three-dimensional (3D) X-ray image of the cold-sintered γ-GC/BT composite was obtained using Synchrotron Radiation X-ray Tomographic Microscopy (SR-XTM) technique at beamline 1.2 W, SLRI, Thailand. X-ray intensity was controlled by attenuating polychromatic X-rays with a 350 μm-thick aluminum foil. X-ray images were captured using a microscopic lens system and recorded by an sCMOS camera with a 1.44-μm pixel size. The X-ray images dataset was converted into sinograms, which were used in the Octopus Reconstruction software. The reconstructed images were visualized using Drishti software. The dielectric behavior, including dielectric constant (ε_r) and loss tangent (tan δ) of cold-sintered γ-GC/BT composites, was studied using an LCR meter (Agilent E4908A) from RT to 200 ˚ C at frequencies ranging from 100 Hz to 2MHz. The polarization versus electric field hysteresis (P-E) curves of cold-sintered γ-GC/BT composites were measured at RT by a standard ferroelectric test system (RT66A) from Radiant Technologies.

3 Results and Discussion

The morphology of the commercial nano-crystallites BT powder (untreated particles) is presented in Fig. 2(a), where SEM imaging showcases randomly distributed particles, with a smaller subset exhibiting homogeneously spherical-shaped particles of smaller size. ImageJ

analysis revealed a Gaussian distribution of particle sizes, indicating a relatively uniform particle size population. The mean particle size was determined to be 75.85 ± 13.65nm, with a narrow size distribution. The skewness and kurtosis values were close to zero, suggesting symmetry and a moderate peak, respectively. After the heat treatment process, agglomerates of varying sizes became apparent, as depicted in Fig. 2(d). The SEM images revealed a bimodal distribution with peak particle sizes observed at 1.39 ± 0.03 μm and 4.83 ± 0.11 μm. This distribution suggests the presence of two distinct populations of particles within the sample, possibly indicating different stages of aggregation or variations in particle formation mechanisms [24]. It's noteworthy that the heat-treated particles exhibit sizes within the micron range, which are more than 30 times larger compared to the untreated particles. BT particles of both nanometer and micrometer sizes will be mixed at a specific ratio determined by theoretical predictions for dense random packing. The TEM bright field image, the selected area electron diffraction (SAED) pattern, and the high-resolution TEM image (HRTEM) of BT powders before and after heat treatment at 1200 ˚ C for 12 h are shown in Fig 2(b)-(c), (e)-(f). For the untreated powder (Fig.2(b)), the particles appear nearly spherical with an average diameter of 78. 14 ± 19.12 nm. The inset SAED pattern shows a polycrystalline diffraction ring made up of separate diffraction spots, indicating the polycrystalline nature of the nanoparticles [25]. Further fringes in BT were detected by HR-TEM. Fig.2(c) exhibits lattice fringe with the interfering distance at 0.287 nm, which corresponds to the crystal plane (110) spacing of the cubic BT phase (JCPDS card no. 075-0213, $d_{(110)} = 0.283$ nm). In contrast, the BT powder, after heat treatment at 1200°C for 12 hours (Fig. 2e), demonstrates particle agglomeration, resulting in a tenfold increase in the average particle size compared to the untreated powder. The inset SAED pattern shows the bright spots assigned to the lattice atoms that were spaced crystallographically with perfect plan orientation of BT, suggesting high

crystallinity and structural perfection for the tetragonal perovskite structure [26]. Clear lattice fringes are observed (Fig.2(f)) with the measured interplanar spacing of about 0.286 nm corresponding to the crystallographic plane (101) of tetragonal BT (JCPDS card no. 079-2265, $d_{(101)}$ = 0.285) [27, 28]. These results confirmed that a high-temperature calcination results in the phase transformation of BT from cubic to tetragonal.

Moreover, the XRD pattern (Fig.2(g)) was consistent with the above results and the LeBail refinement. All the peaks (blue lines) are indexed (JCPDS card no. 079-2265) for cubic phase formation of the space group Pm-3m. The lattice parameters were a=b=c= 4.0067 Å and V = 65.3 Å. The parameters of refinement are R_p = 10.59, R_{wp} = 16.62 and GOF = 2.01. The R factors present a good agreement between refined and experimental XRD profiles for BT. The average crystallite sizes as estimated by Scherrer formula Eq. (3) was 20.33 nm using the (110) major diffraction peak. After calcination of BT at 1200 ˚C/12 h, the diffraction peaks (red line) are sharp and narrow, indicating high crystallinity. All peaks are indexed (JCPDS card no. 075-0213) for tetragonal phase, as judged from the splitting of the (200) diffraction plane into (002) and (200) at 51.02˚and 56.3˚, respectively. Lattice parameters were a = b = 3.9919 Å, c = 4.0321 Å and V = 64.3 Å, which belongs to space group of P4/mmm [29]. The parameters of refinement are R_p = 11.59, R_{wp} = 17.04 and GOF = 1.97. The average crystallite size was 27.56 ± 3.12 nm. These findings suggest that the tetragonal structure of BT phases is generated through high-temperature calcination.

The BT powder before and after calcination were characterized by FTIR in transmission mode as shown in Fig. 2(h). For the BT powder before calcination, the absorption bands appeared at 3507 cm^{-1}, which corresponded to the stretching mode of O-H groups. The band at 1637 cm^{-1} is characteristic of the O-H bending from the physically adsorbed water on BT nanoparticles. The

strong absorption at 487 cm^{-1} is assigned to the bending vibrations of the Ti-O bond in $[TiO_6]^{2-}$ octahedron. It is also a characteristic absorption of BT powder [30]. Notably, the intensity of the O-H stretching vibration bands at 3507 cm^{-1} and 1637 cm^{-1} became weaker as the calcination temperature increased, showing clearly instead the metal-oxygen (Ti-O) band stretching [31-33].

The γ-GC powder and the mixed BT powder were mixed at a varying weight ratio (15, 30, 50, and 90wt% of γ-GC powder) and grounded in a mortar, followed by addition of 7wt% of DI water and another grinding. Then, 0.3 g of the γ-GC/BT mixture was loaded into a tungsten carbide block, and a pressure of 10 MPa was applied. CSP was carried forward for 6 h before heating to 120 ˚C. At the end of the process, the tungsten carbide block was cooled, and the γ-GC/BT composite pellets were removed.

The white pellets, depicted in the inset of Fig. 3, possess a diameter of 1 cm and a thickness of approximately 0.7 mm. In the case of a composite sintered with 15wt% of γ-GC (Fig. 3(a)), the surface predominantly comprises 85wt% BT, resulting in densely packed BT particles and a smooth surface with reduced pore count. Subsequently, with an increase in γ-GC content to 30% (Fig. 3(b)), the surface remains smooth, albeit with small porous areas emerging. Upon further escalation of γ-GC content to 50wt% (Fig. 3(c)), the surface manifests large particle clusters, nanoparticle dispersion throughout the matrix, and some filling of gaps, leading to heightened porosity and surface unevenness. The average grain size measures 3.92 ± 1.75 μm. Notably, at 90wt% γ-GC (Fig. 3(d)), irregularly arranged large clumps of γ-GC particles, numerous small grain sizes (average grain size of 6.67 ± 4.17 μm), and substantial interparticle voids are observed. Additionally, nanoparticles are dispersed within the matrix. The SEM results underscore that an optimal γ-GC content of 15wt% fosters the formation of dense γ-GC/BT composites. Furthermore, SEM mapping and EDS analysis were conducted to explore the

chemical composition of the composites, leveraging X-ray emissions pertaining to the constituent elements. The presence of γ-GC and BT was confirmed by the detection of Ba, Ti, N, C, and O. SEM mapping of 15wt% γ-GC pellets (Fig. 4) reveals large agglomerations of Ba (Fig. 4(c)) and Ti (Fig. 4(d)), with gaps between them filled with Nitrogen (N) (Fig. 4(f)) and Carbon (C) (Fig. 4(g)), elements characteristic of γ-GC. Furthermore, EDS measurement (Fig. 4(h)) confirms the presence of Ba, Ti, O, N, and C elements in the composites, with Ba, Ti, and O comprising 41.2%, 18.4%, and 19.6% by weight, respectively. The Ba and Ti signals correspond to the BT content in 15wt% γ-GC pellets, affirming γ-GC's capacity to bind BT and form a ceramic composite via CSP.

The XTM images of the composites containing 5wt%, 30wt%, and 90wt% of γ-GC/BT were obtained using Synchrotron Radiation X-ray Tomographic Microscopy (SR-XTM). These images provide a macroscopic view of the 3D distribution of the components, distinguishing between two distinct phases represented by orange (γ-GC) and purple (BT). For the composites containing 5wt% γ-GC (Fig. 5(a)) and 30wt% γ-GC (Fig. 5(b)), BT acts as the matrix phase, with γ-GC evenly dispersed over the BT surface. Additionally, in certain regions, the γ-GC phase precipitates and fills the gaps between BT particles. However, as the γ-GC content increases to 90wt% (Fig. 5(c)), BT becomes uniformly distributed within the γ-GC matrix. The XTM image verifies that the γ-GC phase is dispersed throughout the specimen, with instances of agglomeration and precipitation between BT particles, a finding consistent with SEM observations. These XTM findings offer valuable insights into the spatial arrangement and distribution of γ-GC and BT phases within the composites, shedding light on their microstructural characteristics and providing essential information for understanding the composite's properties and behaviors.

The relative density of the γ-GC/BT composites, as determined by Eq. (1), is illustrated in Fig. 6(a). As the weight percentage of γ-GC increases from 15% to 90%, a corresponding trend of decreasing relative density is observed, declining from 96.7 ± 1.2% to 82.7 ± 1.1%. These findings align closely with the observations from SEM imaging. With a decrease in γ-GC content, the particles of BT exhibit a more compact arrangement compared to the composites containing 90wt% γ-GC, primarily due to the inherently higher density of BT. Furthermore, the presence of γ-GC serves to fill the interstitial spaces between BT particles, thereby reducing pore formation. This phenomenon contributes to the overall reduction in porosity and subsequent enhancement in relative density. The relative density can be explained by a mechanism as reported in the previous study [17]. It was found that pressure, sintering temperature, holding times, and transient liquid solvent are important factors for the effective CSP. BT powder is known to be thermodynamically unstable in water solutions. Ba^{2+} ions are leached out of the BT powder, producing a TiO_2-rich amorphous surface layer [34, 35]. The amorphous layer, which is difficult to dissolve in the liquid phase, impedes the dissolution-precipitation process during the CSP, thereby preventing the densification of the BT ceramic. Therefore, the surface of BT powders in this work was treated with acetic acid (CH_3COOH) to generate additional -OH groups on the BT particle surfaces (Fig. 6(b)) via hydroxylation reaction [36]. When the γ-GC powder is mixed with (acid-treated) BT particles and fabricated via CSP, hydrogen bond will form between the -COOH groups on the γ-GC chains and the -OH groups on the surfaces of BT particles [37, 38]. An appropriate amount of γ-GC can easily dissolve in water and act as the liquid phase, which enhances the dissolution-precipitation process during CSP. So, γ-GC promotes close packing in the composites and enhances the relative density of composites [39].

Furthermore, to elucidate the structural behavior, X-ray diffraction (XRD) analysis was employed to assess the cold-sintered samples, as depicted in Fig. 6(c). Notably, all sintered samples (15wt%, 30wt%, 50wt%, and 90wt% of γ-GC) manifest sharp diffraction peaks corresponding to two distinct phases: $BaTiO_3$ (tetragonal; JCPDS no. 075-0213) and γ-GC (JCPDS no. 06-230). At 90wt% of γ-GC, two prominent peaks observed at 25.28˚ and 31.57˚ can be unequivocally indexed to the (110) and (101) diffraction planes of γ-GC and BT respectively. As the γ-GC content decreases, notably, the intensity of the γ-GC peak at 25.28˚ undergoes a significant reduction, consistent with expectations. Subsequently, at γ-GC contents of 30wt% and 15wt%, the characteristic peaks associated with γ-GC are conspicuously absent from the diffraction patterns.

The cold-sintered samples underwent characterization using FTIR in transmission mode, with the results presented in Fig. 6(d). Across all sintered samples, distinct peaks indicative of γ-GC patterns emerged within the range of 1500-1200 cm^{-1}[40] . Notably, the highest intensity peak at 1573 cm^{-1} (peak 1) corresponds to the asymmetric (C=O)O stretching, while the peak at 1492 cm^{-1} (peak 2) signifies the NH bending vibration of NH_3^+. Additionally, the peak at 1390 cm^{-1} (peak 3) corresponds to the symmetric (C=O)O stretching, whereas the peak at 1328 cm^{-1} (peak 4) represents the CH_2 wagging with the lowest intensity. These observations collectively affirm the presence of γ-GC within the samples. However, a notable trend emerges as the γ-GC content decreases: the intensity of the four peaks diminishes significantly, accompanied by peak overlap within the range of 486-684 cm^{-1}. The overlapping peaks are attributed to the carboxylate ion group COO^- of γ-GC and the stretching vibrations of Ti-O of BT, further underscoring the formation of composites between γ-GC and BT. Importantly, no undesired phase transition of γ-GC was observed throughout the analysis, affirming the stability of the composite structure.

The density of composites, as elucidated in Fig. 7, is expounded through the schematic representation of the cold sintering mechanism across various stages. Initially, the composite material particles (I) comprising γ-GC, BT, and water are densely packed. In the initial stage, a sufficient quantity of the liquid phase (water) is integrated with the composite particles, ensuring homogeneous moisturization. Here, γ-GC particles act as a transient liquid phase, dissolving and diffusing alongside water, facilitating particle rearrangement (II). Notably, the pink frame in the illustration delineates the intricacies of particle sliding upon the introduction of the liquid phase, creating spaces at the particle-particle contact area. These spaces enable particle sliding and subsequent rearrangement. Densification primarily ensues under external pressure at this juncture, leading to overall sample shrinkage (S_1). Subsequently, in the second stage, a dissolution-precipitation process comes into play. Following particle dissolution, sliding, and rearrangement in the initial stage, mass transfer occurs via the diffusion of γ-GC ions or atoms along the water (III (a-ii)), effectively filling the interstitial gaps between grains. Consequently, precipitates (III(a-iii)) form on crystal sites with lower chemical potential, which are thermodynamically favored and conducive to neck growth. This mass transport process concurrently diminishes the surplus free energy of the surface and mitigates porosity, resulting in the formation of a dense solid and a slight sample shrinkage (S_2). The final stage, characterized by crystal growth (IV-b), is predominantly governed by a robust dynamic process catalyzed by water evaporation. This evaporation induces a supersaturated state of the liquid phase at temperatures slightly above its boiling point, thereby engendering a significant chemical driving force for the solid and liquid phases to attain equilibrium. Upon completion of precipitation, particle-particle contacts are markedly enhanced, facilitating crystal growth via the coalescence of small crystallites (Thickness = T_0) into larger ones (Thickness = T_1). The comprehensive overview of various BT-based ceramics and

composites, detailing their raw materials, the presence of transient liquid phases, CSP conditions, achieved densities, and corresponding references is present in Table I. BT ceramics synthesized through solid-state reactions typically undergo high-temperature sintering, yielding densities between 94-96%. Alternatively, employing $Ba(OH)_2 \cdot 8H_2O$ as a transient liquid phase at 180°C under pressure yields a density of 95%. Composite systems such as BT/ZnO and BT/Polytetrafluoroethylene exhibit densities ranging from 60%-98% and 93.5%, respectively, utilizing specific liquid phase chemistries and CSP conditions. Notably, the γ-GC/BT composites, synthesized at a lower temperature of 120°C and 10 MPa pressure, demonstrate a density of 96.7±1.6%. These findings highlight the diverse synthesis strategies and optimization approaches employed in the fabrication of BT-based ceramics and composites for various applications.

The dielectric responses of the γ-GC/BT composites were examined as a function of temperatures and frequency. Fig. 8(a) shows the temperature dependences of dielectric constant (ε_r) and dielectric loss (tan δ) for all composites from RT to 200 ˚C at 100 kHz. For the composites with 15-90 wt% γ-GC content, the value of ε_r tends to increase with increasing temperature. The maximum ε_r value obtained was 3600, and the low tan δ was 1.20 for 15wt% γ-GC composite. The increased ε_r value is a result of the addition of ferroelectric ceramic powders primarily caused by the dipolar polarization effect and induced by the permanent dipoles existent in the filler. The permanent dipole of BT is from the uneven distribution of the charge-density between O, Ba, and Ti atom [41].

The frequency-dependences of ε_r and tan δ of the composites are shown in Fig. 8(b) at 200 ˚C and the frequency from 100 Hz to 2 MHz. As frequency increases, ε_r decreases until it reaches a near-constant value at the high-frequency region. The high value of ε_r at low frequencies is caused by a combination of polarizations, including atomic, ionic, interfacial, and electronic.

However, only electronic polarization affects the ε_r at high frequencies. The results clearly show that when the amount of γ-GC decreases, the dipole of the interface increases due to the BT content increase and leading in an increase ε_r [42]. At 15wt% γ-GC, ε_r = 27,000 and tan δ (which is the lowest) was 1.50 at 100 Hz.

We also demonstrate the beneficial effect of increasing proportion of γ-GC by examining other presentations of AC properties, as depicted in Figure 8c, where the positive impact of γ-GC becomes more apparent. The imaginary part of the complex dielectric permittivity e'' (dash line in Figure 8c, shown for 90wt% as an example) follows the universal power law[43, 44] $e'' = A \cdot f^{s-1}$, where A and s are the fitting parameters. The parameter s represents the effective dimension of charge carriers,[45, 46] being 1D for s ~ 0.17-0.44. Accordingly, the s values of 0.11 (30wt% *g*-GC) and 0.22 (50wt% *g*-GC) suggest the 1D nature. Meanwhile, at 90% *g*-GC, the low s = 0.03 is close to zero such that e'' follows f^{1}. This is the "low-frequency dispersion" [47, 48] which points out that very high charge densities are stored, consistent with the well-known capacitive nature of BT.

Figure 8d shows the T-dependent of the imaginary part of the complex electric modulus $M''\times100$ [$M'' = e''/(e'^2 + e''^2)$]. The electric modulus corresponds to the relaxation of an electric field in the material when the electric displacement remains constant.[47] It was found that the sample with 30wt%, 50wt%, and 90wt% g-GC had a relaxation peak at 87, 154, and 163 °C, respectively. The latter two might be compared to 132 °C obtained from the elastic (mechanical) modulus of BT sintered at 1300 °C.[48] The different peak temperatures might be explained by different sintering methods (CSP vs traditional) and measurement methods (electric relaxation vs mechanical relaxation). Still, the shift of the relaxation is clear, presumably to the value of BT. Table 2 presents a comparison of the dielectric properties of BT and BT composites that were

fabricated using CSP and traditional sintering methods. The results indicate that the dielectric properties of traditional sintered BT and γ-GC/BT composite are practically identical. Our study highlights the effectiveness of γ-GC as a transient liquid phase in CSP for the successful and sustainable production of high-density γ-GC/BT composites at relatively low temperatures.

The ferroelectric polarization-electric field (P-E) hysteresis loops of the γ-GC pellet and the γ-GC/BT composite pellets are shown in Fig. 8(e). It is found that the hysteresis loop of γ-GC/BT composite pellets becomes larger with increasing BT contents. Compared with γ-GC, the composite ceramics exhibit good symmetry and a well-saturated shape (see the inset). For 90wt% γ-GC, the surface has porosity, and the addition of BT makes the ferroelectric phase discontinuous as it hinders the domain orientation. However, as the γ-GC content decreases to 15wt%, the porosity is lower, and the ferroelectric property is optimized with easy switching of domains within materials. The measured values of the remnant polarization (P_r) and saturation polarization (P_s) at electric field of 20 $kV \cdot cm^{-1}$ are 0.013 $\mu C \cdot cm^{-2}$ and 0.025 $\mu C \cdot cm^{-2}$ for γ-GC, 0.035 $\mu C \cdot cm^{-2}$ and 0.052 $\mu C \cdot cm^{-2}$ for 90wt% γ-GC, 0.121 $\mu C \cdot cm^{-2}$ and 0.276 $\mu C \cdot cm^{-2}$ for 50wt% γ-GC, 0.554 $\mu C \cdot cm^{-2}$ and 1.466 $\mu C \cdot cm^{-2}$ for 15wt% γ-GC, respectively. In contrast, the coercive electric field (E_c) is lowest for pure γ-GC sample but increases for the 90wt% γ-GC. However, it was significantly decreased when the γ-GC content decreases further to 50wt% and 15wt% (Fig. 8(f)). Moreover, P_s clearly increases as the BT content increases. These results indicate that γ-GC as a transient liquid phase in a CSP can be successfully used to sustainably fabricate high-density composites between γ-GC and BT.

4 Conclusion

In this study, we have successfully demonstrated the implementation of organic ferroelectric (γ-GC) phase as a transient liquid phase substitute for fabricating the γ-GC/BT composite ceramic through CSP (Cold Sintering Process). Our investigation involved incorporating γ-GC contents ranging from 15% to 90% by weight into BT, followed by CSP with a sintering temperature of 120 ˚C, a holding time of 6 h, and an applied uniaxial pressure of 10 MPa. The addition of γ-GC resulted in notable enhancements in both relative density and electrical properties of the composites. Particularly, the optimal γ-GC content of 15wt% yielded a remarkable relative density of up to 96.7±1.6%. Our findings were further corroborated by FTIR and XRD analyses, which confirmed the phase stability of γ-GC and its prevention of undesired transformation into the non-piezoelectric phase (α-GC). SEM-EDS mapping revealed the precipitation-dissolution process of γ-GC in CSP, where it functioned as a filler diffusing into the space surrounding BT particles. XTM images provided a comprehensive 3D distribution of both BT and γ-GC, consistent with SEM observations. Furthermore, we conducted a thorough examination of the electrical properties of the composites across varying temperatures (RT-200 ˚C) and frequencies (100Hz-2MHz). The dielectric constant (ε_r) exhibited an increase with decreasing γ-GC content. Notably, the 15wt% γ-GC pellet demonstrated the highest ε_r of 3600 coupled with a low dielectric loss (tan δ) of 1.20. The P-E hysteresis loop measurements revealed that the 15wt% γ-GC composite ceramic displayed the highest values of P_s = 1.46 μC·cm^{-2} and P_r = 0.55 μC·cm^{-2}. Our study underscores the efficacy of γ-GC as a transient liquid phase in CSP for successfully and sustainably fabricating high-density γ-GC/BT composites at relatively low temperatures. These results contribute to the advancement of ceramic processing techniques and hold promise for various applications in the fields of electronics, energy, and beyond.

Acknowledgments

This study was financially supported by King Mongkut's Institute of Technology Ladkrabang (KMITL) under Grant Nos. KREF116501 and 2567-02-05-020. Jitrawan Noisak's work was funded by Grant No. KREF016412. Thitirat Charoonsuk's contributions were supported by the National Research Council of Thailand (NRCT) through Grant Number N42A650220. Pimchanok Ieamviteevanich's work received support from the School of Science at King Mongkut's Institute of Technology Ladkrabang. T. Bongkarn acknowledges financial assistance from Naresuan University, the National Science, Research, and Innovation Fund (NSRF) under Grant No. R2567B001, and the Global and Frontier Research University Fund at Naresuan University (NU) under Grant No. R2567C001. The collaboration between N. Vittayakorn and Te-Wei Chiu was facilitated by the NTU-KMITL-Joint Research Program under Grant No. KREF016412. We extend our appreciation to the Nanotechnology and Materials Analytical Instrument Service Unit (NMIS) at the College of Materials Innovation and Technology, KMITL, for their invaluable support and technical assistance.

Declaration of competing interest.

The authors have no competing interests to declare that are relevant to the content of this article.

References

1. Guo, H., et al., *Cold Sintering Process: A Novel Technique for Low-Temperature Ceramic Processing of Ferroelectrics.* Journal of the American Ceramic Society, 2016. **99**(11): p. 3489-3507.
2. Maria, J.-P., et al., *Cold sintering: Current status and prospects.* Journal of Materials Research, 2017. **32**(17): p. 3205-3218.

3. Yu, T., et al., *Current understanding and applications of the cold sintering process.* Frontiers of Chemical Science and Engineering, 2019. **13**: p. 654-664.
4. Wang, D., et al., *Cold sintering of microwave dielectric ceramics and devices.* Journal of Materials Research, 2021. **36**.
5. Anindy, U., M. Nur Indro, and I. Husein, *Piezoelectric properties: cerium oxide (CeO_2) doped barium titanate ($BaTiO_3$) film on ITO substrate.* Ferroelectrics, 2021. **570**(1): p. 162-175.
6. Kalugina, S.G., et al., *Fundamental optical spectra of ferroelectric $NaNO_2$.* Inorganic Materials, 2009. **45**(8): p. 925-929.
7. Guo, H., et al., *Protocol for ultralow-temperature ceramic sintering: an integration of nanotechnology and the cold sintering process.* ACS nano, 2016. **10**(11): p. 10606-10614.
8. Tsuji, K., et al., *Single Step Densification of High Permittivity $BaTiO_3$ Ceramics at 300 ºC.* Journal of the European Ceramic Society, 2019. **40**.
9. Kang, S., et al., *Barium titanate/poly (vinylidene fluoride) nanocomposites with core–shell structure with high dielectric constant and temperature stability prepared via a cold sintering process.* Journal of Materials Science: Materials in Electronics, 2020. **31**.
10. Ndayishimiye, A., et al., *Thermosetting polymers in cold sintering: The fabrication of ZnO ‐ polydimethylsiloxane composites.* Journal of the American Ceramic Society, 2020. **103**(5): p. 3039-3050.
11. Guo, J., et al., *Cold sintered ceramic nanocomposites of 2D MXene and zinc oxide.* Advanced Materials, 2018. **30**(32): p. 1801846.
12. Alter, H., *Filler particle size and mechanical properties of polymers.* Journal of Applied Polymer Science, 1965. **9**(4): p. 1525-1531.
13. Zhao, Y., et al., *Cold-Sintered V_2O_5-PEDOT:PSS Nanocomposites for Negative Temperature Coefficient Materials.* Journal of the European Ceramic Society, 2018. **39**.
14. Sada, T., et al., *High permittivity $BaTiO_3$ and $BaTiO_3$-polymer nanocomposites enabled by cold sintering with a new transient chemistry: $Ba(OH)_2 \cdot 8H_2O$.* Journal of the European Ceramic Society, 2021. **41**(1): p. 409-417.
15. Vinoth, S. and S.-F. Wang, *Cold Sintering Process for a $BaTiO_3$/Poly (vinylidene difluoride) Ceramic–Polymer Composite: Evaluation of the Structural and Microwave Dielectric Properties.* Inorganic Chemistry, 2023.

16. Sada, T., et al., *Highly Reliable $BaTiO_3$ - Polyphenylene Oxide Nanocomposite Dielectrics via Cold Sintering.* Advanced Materials Interfaces, 2021. **8**(18): p. 2100963.
17. Noisak, J., et al., *Towards the preparation of organic ferroelectric composites: fabrication of a gamma-glycine-bacterial cellulose composite via cold sintering process.* Journal of Materials Research and Technology, 2023. **25**: p. 4749-4760.
18. Peter, M.E. and P. Ramasamy, *Growth of gamma glycine crystal and its characterisation.* Spectrochimica Acta Part A: Molecular and Biomolecular Spectroscopy, 2010. **75**(5): p. 1417-1421.
19. Ukasi, S., et al., *Gamma glycine enhances efficiency of organic hybrid piezoelectric-triboelectric nanogenerators.* Nano Energy, 2024. **119**: p. 109045.
20. Bouchard, A., G.W. Hofland, and G.-J. Witkamp, *Solubility of Glycine Polymorphs and Recrystallization of β-Glycine.* Journal of Chemical & Engineering Data, 2007. **52**(5): p. 1626-1629.
21. Yang, X., X. Wang, and C. Ching, *Solubility of Form α and Form γ of Glycine in Aqueous Solutions.* Journal of Chemical and Engineering Data - J CHEM ENG DATA, 2008. **53**.
22. Guo, N., H.-Z. Shen, and P. Shen, *Cold sintering of chitosan/hydroxyapatite composites.* Materialia, 2022. **21**: p. 101294.
23. Evans, H., *An X-ray diffraction study of tetragonal barium titanate.* Acta Crystallographica, 1961. **14**(10): p. 1019-1026.
24. Su, J. and J. Zhang, *Recent development on modification of synthesized barium titanate ($BaTiO_3$) and polymer/$BaTiO_3$ dielectric composites.* Journal of Materials Science: Materials in Electronics, 2019. **30**(3): p. 1957-1975.
25. Fuentes, S., et al., *Synthesis and characterization of $BaTiO_3$ nanoparticles in oxygen atmosphere.* Journal of Alloys and Compounds, 2010. **505**(2): p. 568-572.
26. Vasudevan, R., et al., *Effect of microwave sintering on the structural, optical and electrical properties of $BaTiO_3$ nanoparticles.* Journal of Materials Science: Materials in Electronics, 2014. **25**.
27. Hu, Z., et al., *Facile fabrication of tetragonal phase single-crystalline $BaTiO_3$ terrace-like dendrite by a simple solvothermal method and its piezocatalytic properties.* Materials Chemistry and Physics, 2023. **293**: p. 126911.

28. Luo, G., et al., *Synthesis of tetragonal $BaTiO_3$ powder with size and dispersity optimization via synergy mechanisms of combined dispersants.* Journal of Alloys and Compounds, 2023. **944**: p. 169079.
29. Luan, S., et al., *Fabrication of $BaTiO_3$ nanopowders with high tetragonality via two-step assisted rotary furnace calcination for MLCC applications.* Ceramics International, 2023. **49**(8): p. 12529-12539.
30. Thi Tuyet Mai, P., et al., *Enhancement of Polarization Property of Silane-Modified $BaTiO_3$ Nanoparticles and Its Effect in Increasing Dielectric Property of Epoxy/$BaTiO_3$ Nanocomposites.* Journal of Science: Advanced Materials and Devices, 2016. **1**: p. 90-97.
31. Lee, D., et al., *Effect of calcination temperature and atmosphere on crystal structure of $BaTiO_3$ nanofibers.* Metals and Materials International - MET MATER INT, 2010. **16**: p. 453-457.
32. Hao, S., et al., *Preparation and Characterization of Ag-Doped $BaTiO_3$ Conductive Powders.* International Journal of Inorganic Chemistry, 2011. **2011**.
33. Nakhaei, M. and A. Bahari, *Synthesis and investigation of temperature effects on barium titanate ($BaTiO_3$) nanostructural and electrical properties.* Journal of Materials Science: Materials in Electronics, 2016. **27**.
34. Chiang, C.-W. and J.-H. Jean, *Effects of barium dissolution on dispersing aqueous barium titanate suspensions.* Materials Chemistry and Physics, 2003. **80**(3): p. 647-655.
35. Tripathy, S.S. and A.M. Raichur, *Dissolution properties of $BaTiO_3$ nanoparticles in aqueous suspensions.* Journal of Experimental Nanoscience, 2011. **6**(2): p. 127-137.
36. Chang, S.-J., et al., *An efficient approach to derive hydroxyl groups on the surface of barium titanate nanoparticles to improve its chemical modification ability.* Journal of Colloid and Interface Science, 2009. **329**(2): p. 300-305.
37. Nawanil, C., et al. *Effect of surface treatment on electrical properties of barium titanate/carbon nanotube/polydimethylsiloxane nanocomposites*. in *AIP Conference Proceedings*. 2018. AIP Publishing.
38. Chen, L., et al., *Mechanical, thermal, and dielectric properties of polyvinylidene fluoride nanocomposites fabricated by introducing functional MWCNTs/barium titanate compounding dielectric nanofillers.* Polymer Composites, 2021. **42**(3): p. 1383-1395.

39. Kang, S., et al., *Influence of surface coating on the microstructures and dielectric properties of $BaTiO_3$ ceramic via a cold sintering process.* RSC Advances, 2020. **10**(51): p. 30870-30879.
40. R, E.V., et al., *Crystal growth, optical and thermal studies of nonlinear optical-glycine single crystal grown from lithium nitrate.* Optik - International Journal for Light and Electron Optics, 2012. **123**: p. 409-413.
41. Stefanescu, E.A., et al., *Multifunctional fiberglass-reinforced PMMA-$BaTiO_3$ structural/dielectric composites.* Polymer, 2011. **52**(9): p. 2016-2024.
42. Chao, F., et al., *Study of dielectric property on $BaTiO_3$/BADCy composite.* Materials Chemistry and Physics, 2008. **108**: p. 306-311.
43. Maluangnont, T., et al., *Electrochemical and electrical characteristics of ball milled $Cs_2Ti_6O_{13}$ modified by the surface-to-bulk migration of hydroxyl groups.* Dalton Trans., 2023. **52**: p. 11815-11825.
44. Sriphan, S., et al., *Effect of adsorbed water and temperature on the universal power law behavior of lepidocrocite-type alkali titanate ceramics.* J. Phys. Chem. C, 2021. **125**: p. 12910–12920.
45. Dyre, J.C., et al., *Fundamental questions relating to ion conduction in disordered solids.* Rep. Prog. Phys., 2009. **72**: p. 046501.
46. Sidebottom, D.L., *Dimensionality dependence of the conductivity dispersion in ionic materials.* Phys. Rev. Lett., 1999. **83**: p. 983-986.
47. Liu, J., et al., *Dielectric permittivity and electric modulus in $Bi_2Ti_4O_{11}$* J. Chem. Phys., 2003. **119**: p. 2812-2819.
48. Cheng, B.L., et al., *Mechanical loss and elastic modulus associated with phase transitions of barium titanate ceramics.* J. Alloys Compd., 1994. **211/212**: p. 352-355.
49. Shao, S., et al., *High piezoelectric properties and domain configuration in $BaTiO_3$ ceramics obtained through the solid-state reaction route.* Journal of Physics D: Applied Physics, 2008. **41**(12): p. 125408.
50. Kim, H.T. and Y.H. Han, *Sintering of nanocrystalline $BaTiO_3$.* Ceramics International, 2004. **30**(7): p. 1719-1723.
51. Chaisan, W., *Effect of sintering temperature on the hysteresis properties of barium titanate ceramic.* NU. International Journal of Science, 2007. **4**(2): p. 132-139.

52. Guo, H., et al., *Hydrothermal-Assisted Cold Sintering Process: A New Guidance for Low-Temperature Ceramic Sintering.* ACS Appl Mater Interfaces, 2016. **8**(32): p. 20909-15.
53. Coutinho, L., R. Aredes, and E. Antonelli, *Cold sintering and electric characterization of ZnO-$BaTiO_3$ composites.* Cerâmica, 2021. **67**: p. 105-110.
54. Sada, T., et al., *High permittivity $BaTiO_3$ and $BaTiO_3$-polymer nanocomposites enabled by cold sintering with a new transient chemistry: $Ba(OH)_2{\cdot}8H_2O$.* Journal of the European Ceramic Society, 2021. **41**(1): p. 409-417.
55. Sada, T., et al., *Highly Reliable $BaTiO_3$-Polyphenylene Oxide Nanocomposite Dielectrics via Cold Sintering.* Advanced Materials Interfaces, 2021. **8**(18): p. 2100963.
56. Vinoth, S. and S.-F. Wang, *Cold Sintering Process for a $BaTiO_3$/Poly (vinylidene difluoride) Ceramic–Polymer Composite: Evaluation of the Structural and Microwave Dielectric Properties.* Inorganic Chemistry, 2023. **62**(21): p. 8326-8333.
57. Sada, T., et al., *Surface modification of $BaTiO_3$ with catechol surfactant and effects on cold sintering.* Journal of Applied Physics, 2021. **129**(18).

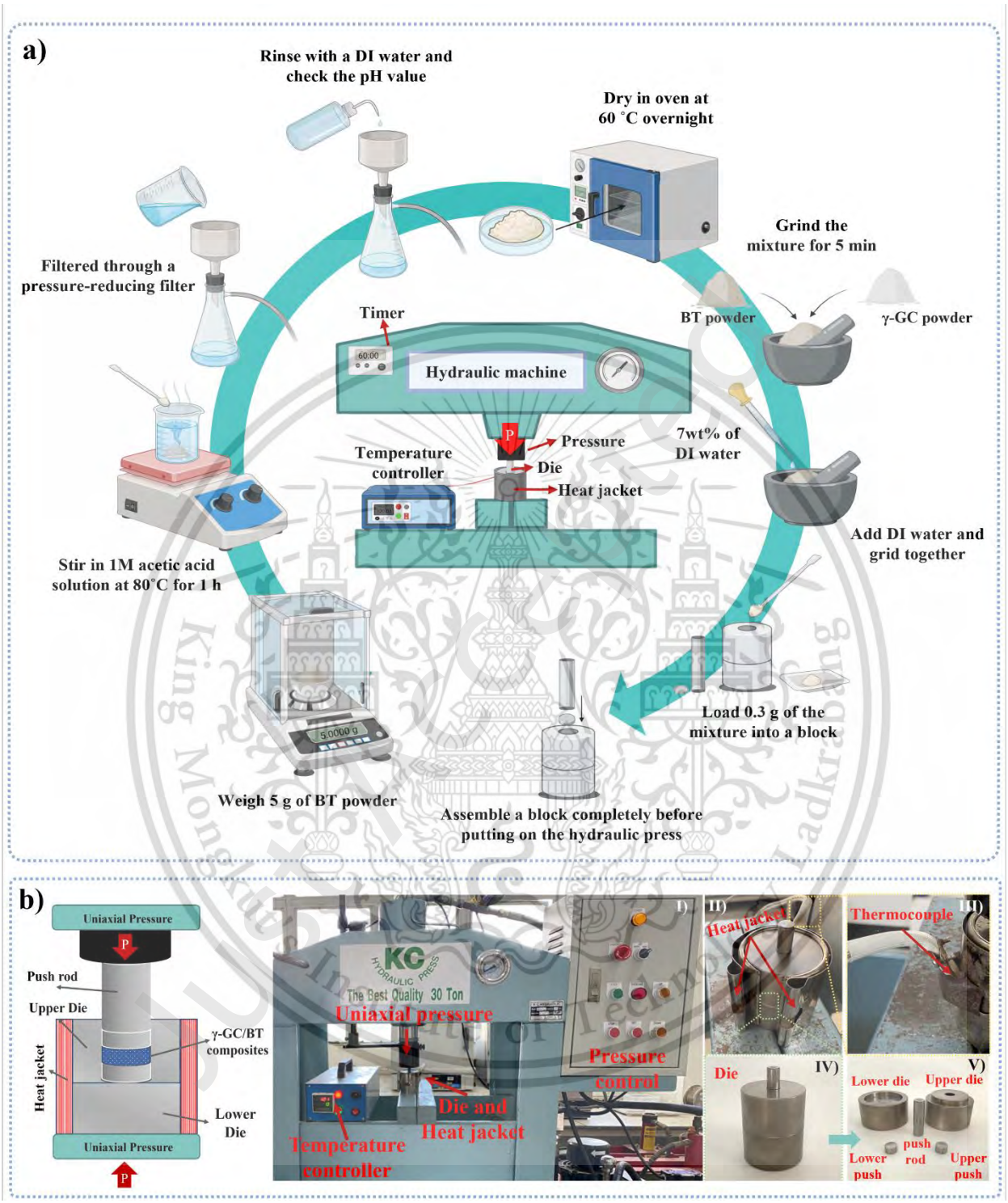

Fig. 1 Schematic illustration of the fabrication process of the γ-GC/BT composite via CSP.

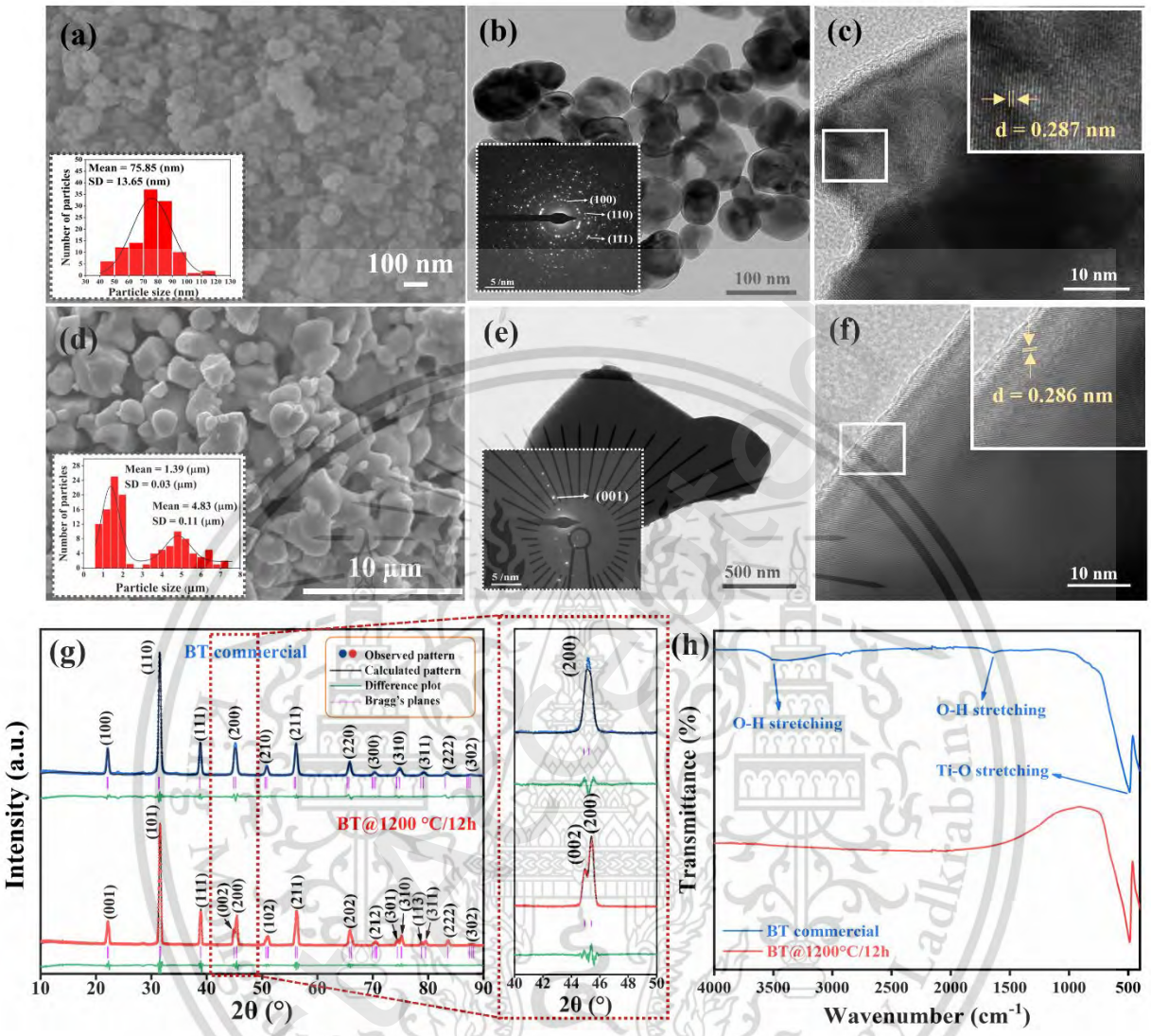

Fig. 2 SEM images of (a) BT commercial powder before calcination and (d) BT after calcination at 1200 ˚C for 12 h. (b), (e) show TEM images of BT powder before and after calcination at 1200 ˚C for 12 h respectively. The inset shows the corresponding SAED patterns. (c), (f) the high-resolution TEM and the white frame showing the lattice fringe. (g), (h) XRD and FTIR results of BT powder before and after calcination at 1200 ˚C for 12 h.

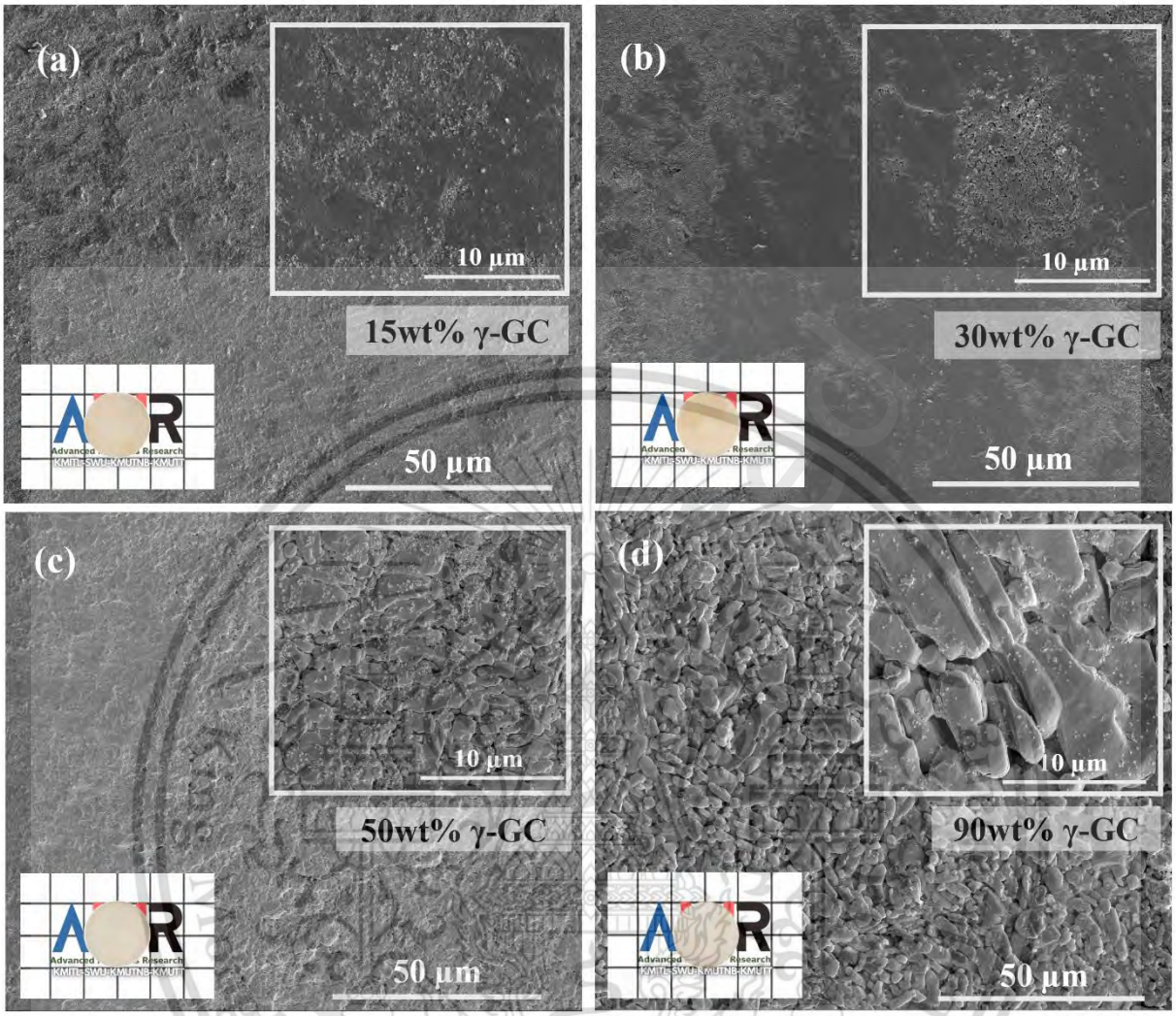

Fig. 3 SEM images of cold-sintered composites between γ-GC and BT as prepared through CSP at varying amount of γ-GC: (a) 15wt% (b) 30wt% (c) 50wt% and (d) 90wt%. The bottom-left insets show the corresponding digital image of the pellet. The white frame on top-right shows morphological features under 10,000 x magnification.

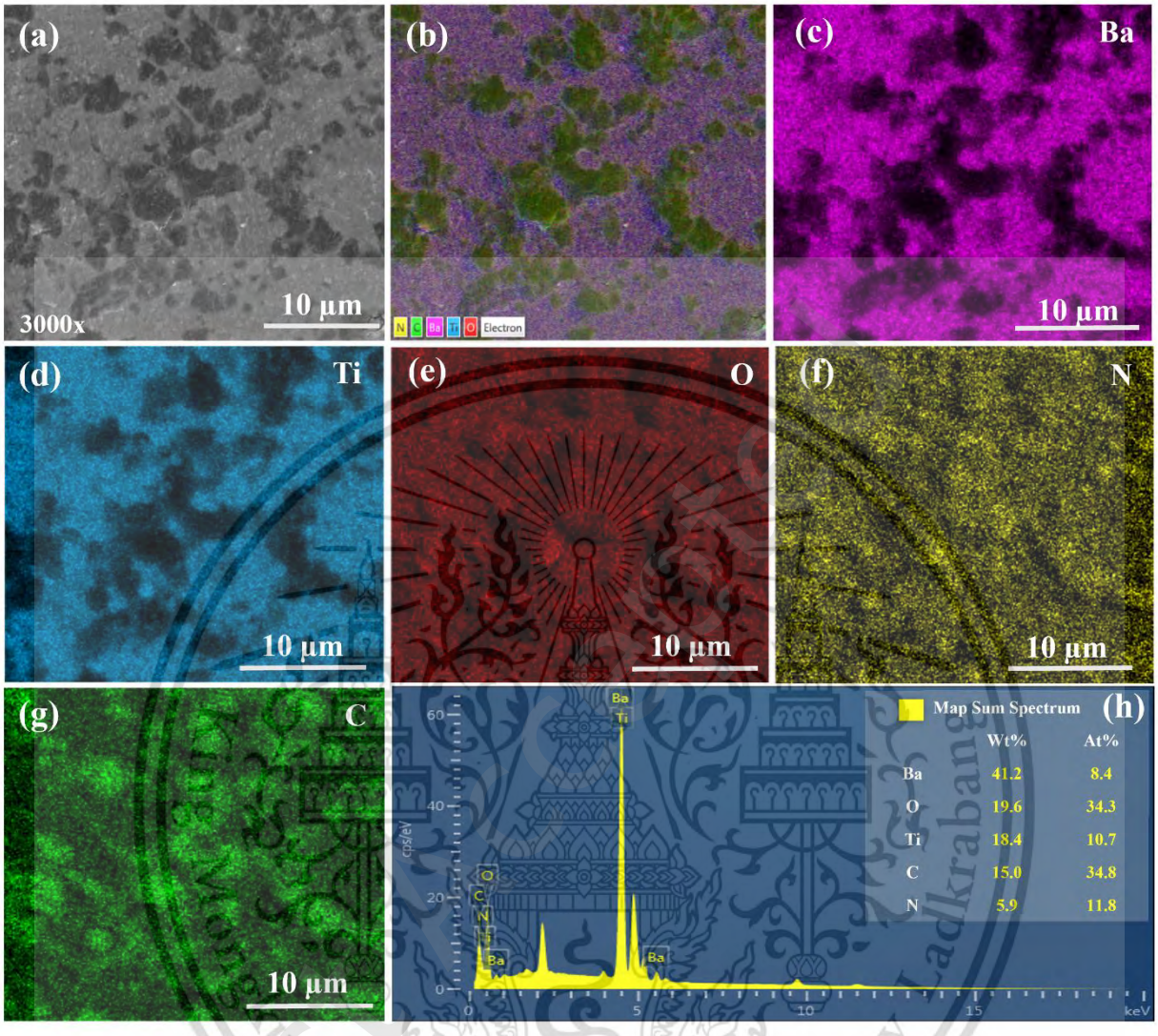

Fig. 4 The SEM-EDS mapping of 15wt% γ-GC pellet: (a) SEM image at a magnification of 3000x for the composite 15wt% γ-GC/BT. (b) All mapping elements. (c-g) Mapping image of Ba, Ti, O, N, and C element in the composites. (h) The EDS spectrum with the table in the inset showing a quantitative result obtained for Ba, O, Ti, C, and N.

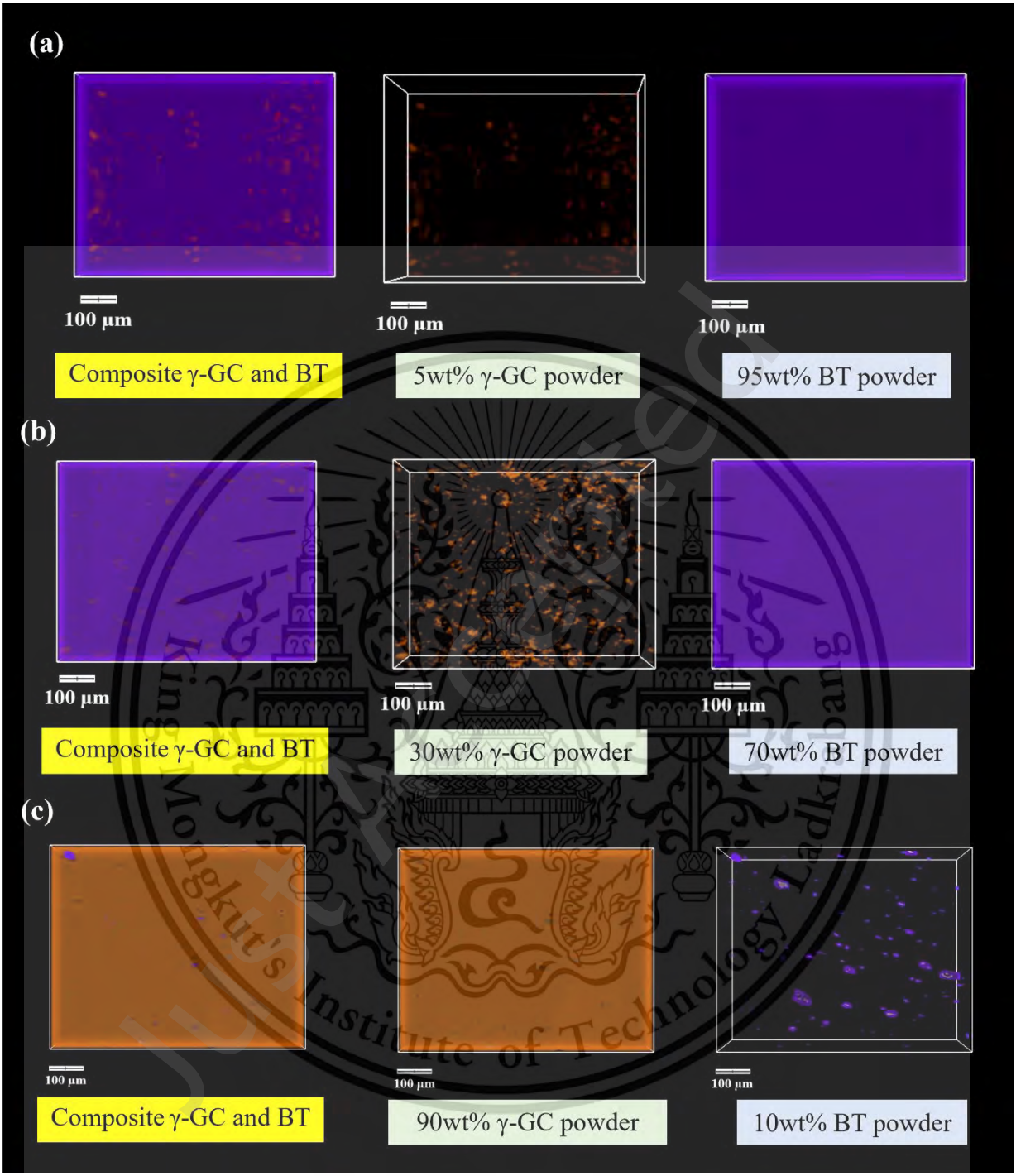

Fig. 5 X-ray tomographic 3D visualization of γ-GC/BT composites via CSP at varying γ-GC contents (a) 5wt% (b) 30wt% and (c) 90wt% respectively.

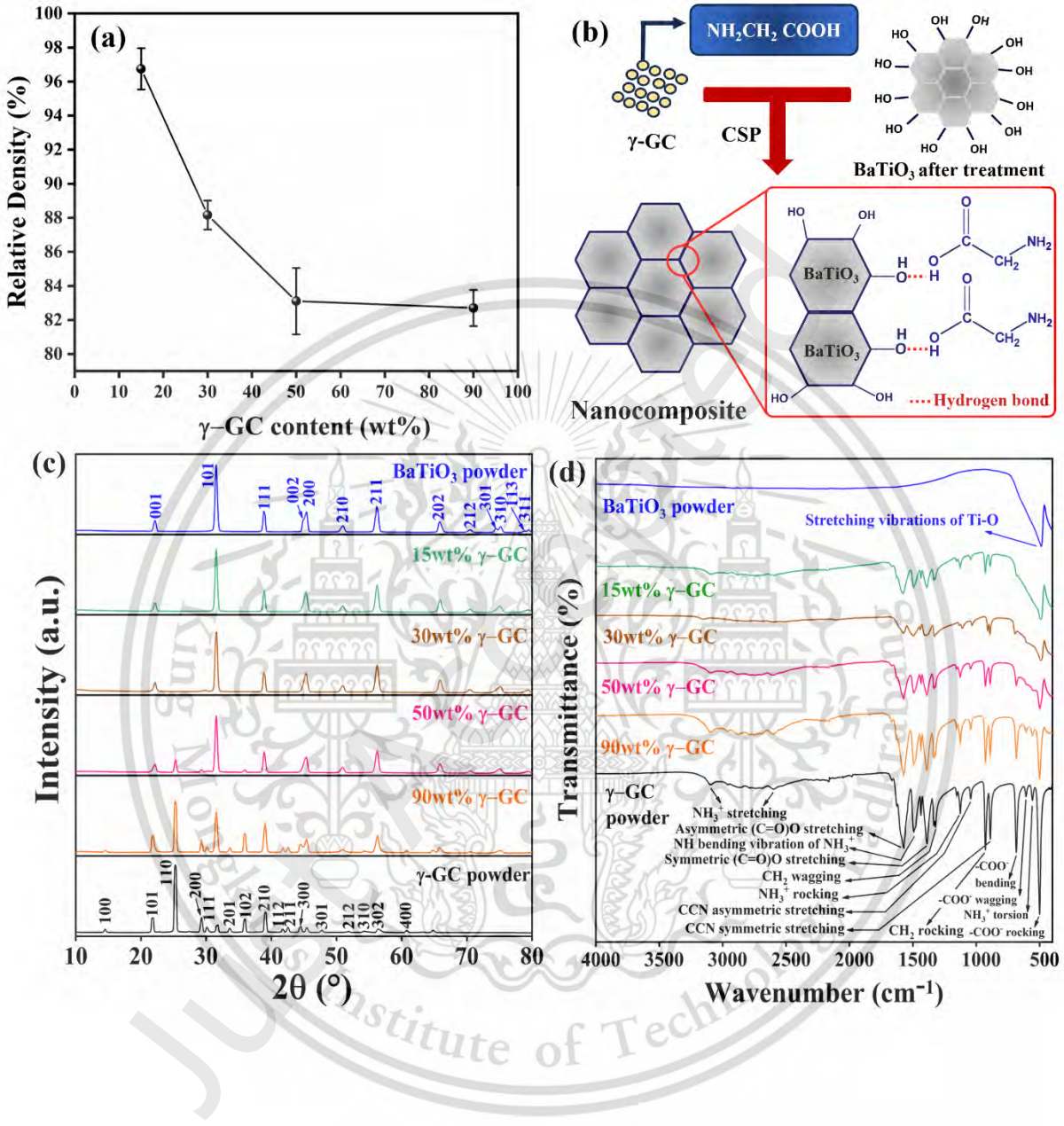

Fig. 6 The relative density of γ-GC/BT composites after CSP (a) variation of the γ-GC contents. (b) schematic diagram of BT after treatment with 1 M acetic acid, showing the surface OH group on BT surfaces and the formation of hydrogen bond in the γ-GC/BT composite, (c) XRD patterns and (d) FTIR spectrum of γ-GC/BT composites.

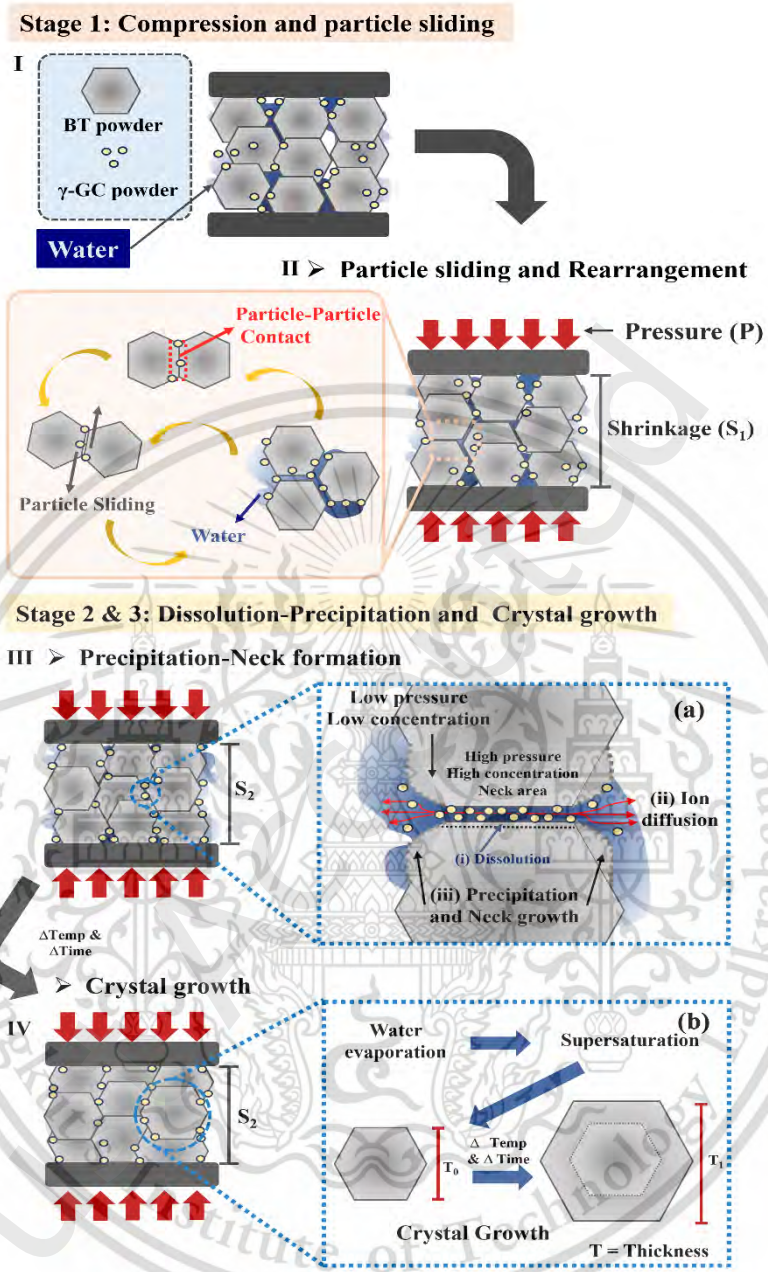

Fig. 7 Schematics of CSP mechanism at mainly 3 stages adapted from Refs.[1, 4, 17]. Stage 1 involves I. particle compaction of composite consisting of γ-GC, BT, and water, II. Particle sliding and rearrangement. Stage 2 shows the dissolution-precipitation process, III. Precipitation-Neck formation. Details of this stage show in (a) dissolution (i), ion diffusion (ii), precipitation-neck growth (iii). Stage 3 related to crystal growth (IV) and (b) show the detail of its stage related to water evaporation and crystal growth.

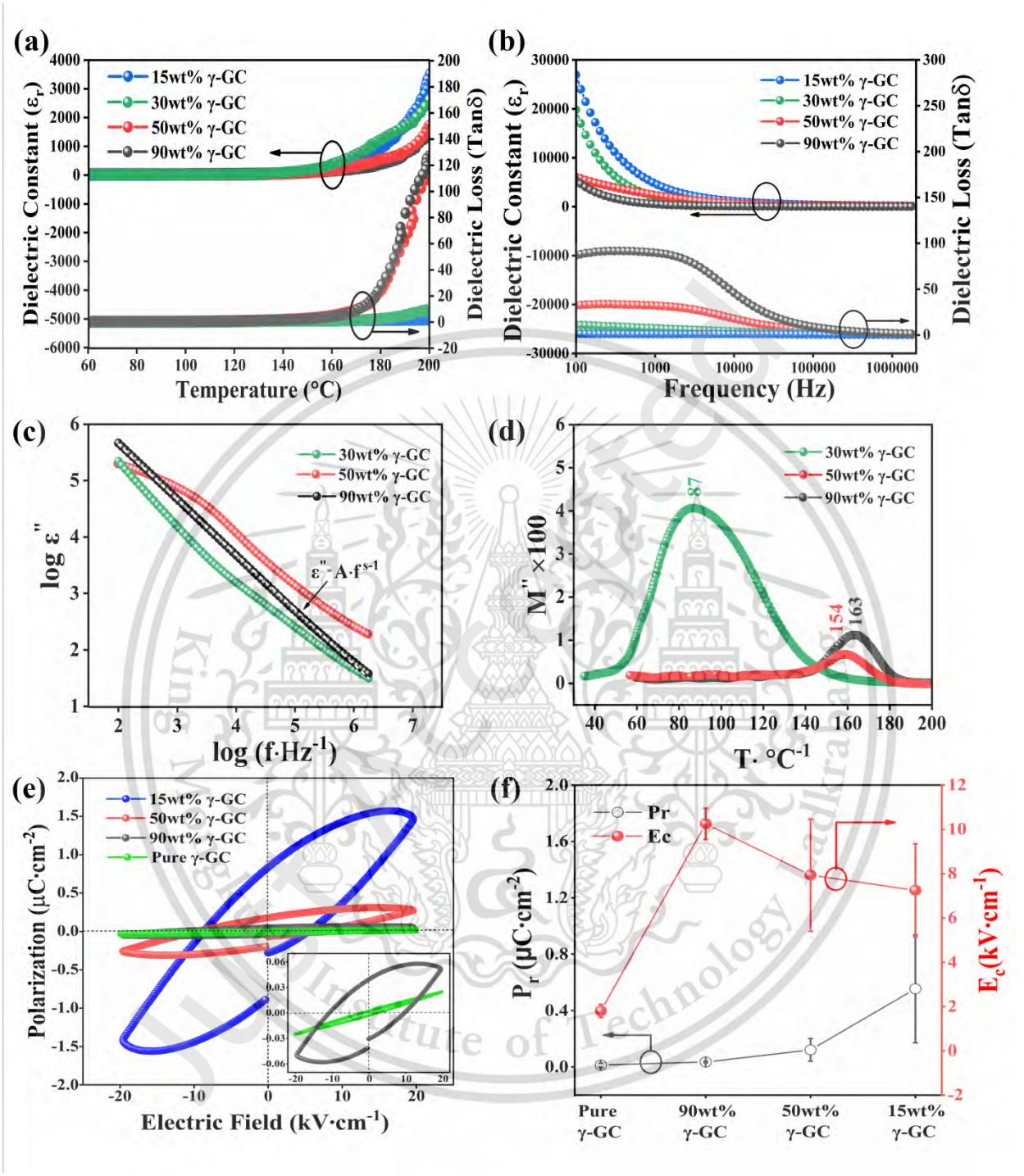

Fig. 8 Electrical properties of γ-GC/BT composites fabricated via CSP: (a) temperature-dependence (b) frequency-dependence of the dielectric constant and dielectric loss. (c) P-E hysteresis loop of γ-GC and the γ-GC/BT composites, at the electric field of 20 kV/cm, and (d) the corresponding P_r and E_c values.

Table 1. A concise comparison of the raw materials used, the presence of transient liquid phase, and the conditions of the Cold Sintering Process (CSP) for both BT-based ceramics and composites.

BT-based Ceramics/Composite	Raw materials	Transient liquid phase	CSP conditions	density	Reference
$BaTiO_3$ (Solid state reaction)	$BaCO_3$+TiO_2	-	1200-1400 ˚ C/ 6-24 h (Traditional sintering temperature)	94-96%	[49, 50] [51]
$BaTiO_3$	$Ba(OH)_2$+TiO_2 → $BaTiO_3$	$Ba(OH)_2 \cdot 8H_2O$	180 ˚ C/ 15 to 120 mins/430 MPa/annealing 900 ˚ C	95%	[52]
$BaTiO_3$/ZnO	$BaTiO_3$ + ZnO	CH_3COOH + H_2O	250˚C/1h/166 MPa	60%-98%	[53]
$BaTiO_3$/Polytetrafluoroethylene (PTFE) composites	Nano $BaTiO_3$/polymer PTFE	$Ba(OH)_2 \cdot 8H_2O$	225˚C/2h/350 MPa	93.5%	[54]
$BaTiO_3$/Polyphenylene oxide nanocomposite	$BaTiO_3$/polymer PPO	$Ba(OH)_2 \cdot 8H_2O$	225˚C/12h/350 MPa	96%	[55]
$BaTiO_3$/Poly(vinylidene difluoride)	$BaTiO_3$/polymer PVDF	H_2O	190˚C/160 mins/350 MPa	94.8%	[56]
$BaTiO_3$/ catechol	Nano$BaTiO_3$/benzenediol organic compound	$Ba(OH)_2 \cdot 8H_2O$	200˚C/75 mins/350 MPa/annealing 200 ˚ C	93%-95%	[57]
γ-GC/BT composites	Micro/Nano $BaTiO_3$	γ-$C_2H_5NO_2$	120 ˚C /6 hrs/10 MPa	96.7±1.6%	This study

Table 2. Comparison of Dielectric Properties of BT ceramic and BT-Based Composites prepared by CSP.

System	Fabrication process	Dielectric constant at 1kHz	Dielectric loss at 1kHz	Reference
$BaTiO_3$	Solid state reaction	2900-4500	1.4-2.8	[49, 50] [51]
$BaTiO_3$	CSP	1,800	0.03	[52]
$BaTiO_3$/ZnO	CSP	50.9-7000	0.04-3.13	[53]
$BaTiO_3$/Polytetrafluoroethylene (PTFE) composites	CSP	790 (@ 1 MHz)	1.4 (@ 1 MHz)	[54]
$BaTiO_3$/Polyphenylene oxide nanocomposite	CSP	1,500	0.05	[55]
$BaTiO_3$/Poly(vinylidene difluoride)	CSP	71.1 (@ 1 GHz)	0.04 (@ 1 GHz)	[56]
$BaTiO_3$/ catechol	CSP	700 (@ 1 MHz)	0.04 (@ 1 MHz)	[57]
γ-GC/BT composites	CSP	4500	0.99	This study